

Accelerated Non-contrast-enhanced
Morphological and Functional
Magnetic Resonance Angiography
Beschleunigte kontrastmittelfreie
morphologische und funktionelle
Magnetresonanzangiographie

Der Technischen Fakultät
der Friedrich-Alexander-Universität
Erlangen-Nürnberg

zur

Erlangung des Doktorgrades Dr.-Ing.

vorgelegt von

Jana Hutter

aus

Erlangen, Deutschland

Als Dissertation genehmigt
von der Technischen Fakultät
der Friedrich-Alexander-Universität Erlangen-Nürnberg

Tag der mündlichen Prüfung:	09.05.2014
Vorsitzende des Promotionsorgans:	Prof. Dr.-Ing. habil M. Merklein
Gutachter:	Prof. Dr.-Ing. J. Hornegger Prof. Dr. D. Rückert

Abstract

Cardiovascular diseases such as stroke, stenosis, peripheral or renal artery disease require accurate angiographic visualization techniques both for diagnosis and treatment planning. Beside the morphological imaging, the in-vivo acquisition of blood flow information gained increasing clinical importance in recent years. Non-contrast-enhanced Magnetic Resonance Angiography (nceMRA) provides techniques for both fields. For morphological imaging, Time of Flight (TOF) and magnetization-prepared balanced Steady State Free Precession (mp-bSSFP) offer non-invasive, ionizing-radiation free and user independent alternatives to clinically established methods such as Digital Subtraction Angiography, Computed Tomography or Ultrasound. In the field of functional imaging, unique novel possibilities are given with three-directional velocity fields, acquired simultaneously to the morphological information using Phase Contrast Imaging (PCI). But the wider clinical use of nceMRA is still hampered by long acquisition times. Thus, accelerating nceMRA is a problem of high relevance and with great potential clinical impact. In this thesis, acceleration strategies based on k -space sampling below the Nyquist limit and adapted reconstruction techniques, combining parallel MRI (pMRI) methods with Compressed Sensing (CS), are developed for both types of nceMRA methods. This includes contributions to all relevant parts of the reconstruction algorithms, the sampling strategy, the regularization technique and the optimization method.

For morphological imaging, a novel analytical pattern combining aspects of pMRI and CS, called the MICCS pattern, is proposed in combination with an adapted Split Bregman algorithm. This allows for a reduction in the acquisition time for peripheral TOF imaging of the entire lower vasculature from over 30 minutes to less than 8 minutes. Further acceleration is achieved for 3-D free-breathing renal angiography using mp-bSSFP, where the entire volume can be acquired in less than 1 minute instead of over 8 minutes. In addition, organ based evaluations including the vessel sharpness at important positions show the diagnostic usability and the increased accuracy over clinically established acceleration methods.

For PCI, advances are achieved with a dedicated novel sampling strategy, called I-VT sampling, including interleaved variations for all dimensions. Furthermore, two novel regularization techniques for PCI are developed in this thesis. First, a novel temporally masked and weighted strategy focusing on enhanced temporal fidelity, referred to as TMW, is developed. This fully automatic approach uses dynamic and static vessel masks to guide the influence specifically to the static areas. Second, the low rank and sparse decomposition model, is extended to PCI, combined with adapted sparsity assumptions and the unconstrained Split Bregman algorithm. These methods are successfully applied to the carotid bifurcation, a region with a huge demand of significant acceleration as well high spatial and temporal accuracy of the flow values. But all algorithmic contributions exploit inherent properties of the acquisition technique, and thus can be applied for further applications.

In summary, the main contribution of this thesis is significant acceleration of nceMRA achieved with novel sampling, regularization and optimization elements.

Kurzübersicht

Kardiovaskuläre Erkrankungen wie Schlaganfall, Gefäßverengungen und Gefäß-erkrankungen erfordern sowohl für die Diagnose als auch die Planung operativer Eingriffe akkurate angiographische Bildgebung. Neben den morphologischen Techniken gewinnen Techniken, die die Aufnahme von Flussinformationen ermöglichen, zunehmend an klinischer Bedeutung. Kontrastmittelfreie Magnetresonanzangiographie bietet für beide Bereiche Techniken. Für morphologische Bildgebung stehen mit *Time of Flight* und *magnetization-prepared balanced Steady State Free Precession* nicht invasive strahlungsfreie Alternativen zu klinisch etablierten Verfahren wie Digitale Subtraktionsangiographie, Computer Tomographie und Ultraschall zur Verfügung. Im Bereich der funktionellen bildgebenden Verfahren ermöglicht Phasenkontrastbildgebung die gleichzeitige Aufnahme dreidimensionaler Geschwindigkeitsfelder und morphologischer Information. Ein Nachteil kontrastmittelfreier Verfahren sind lange Aufnahmezeiten, die noch immer ihre weitere klinische Nutzung verhindern. Deswegen ist die Beschleunigung dieser Methoden ein Problem mit hoher Bedeutung und großem klinischen Nutzen. In dieser Arbeit werden für beide Arten kontrastmittelfreier Angiographie Strategien zur Beschleunigung entwickelt, die auf einer Unterabtastung des k-Raums und geeigneten Rekonstruktionsverfahren (parallele MR Bildgebungstechniken und *Compressed Sensing*) basieren.

Für die morphologische Bildgebung wird ein neuartiges analytisches Abtastmuster (MICCS), das Aspekte der parallelen MR Bildgebung mit den Anforderungen von *Compressed Sensing* vereint, in Verbindung mit einem angepassten *Split Bregman* Algorithmus vorgestellt. Diese Methode erlaubt die Reduktion der Aufnahmezeit für eine TOF basierte Darstellung der Beinarterien von 30 zu weniger als acht Minuten. Weiterhin wurde bei 3D Nierenbildgebung unter freier Atmung für das gesamte Volumen eine Aufnahmezeit von unter einer statt über acht Minuten erzielt. Darüber hinaus zeigen organbasierte Auswertemethoden wie die Schärfe der Gefäßränder eine erhöhte Genauigkeit im Vergleich zu klinische etablierten Methoden.

Im Bereich der Phasenkontrastbildgebung wurden Fortschritte erzielt mit einer neuartigen Abtaststrategie, die Variation in alle vorhandenen Dimensionen erlaubt. Weitergehend wurden zwei neuartige Regularisierungsstrategien entwickelt. Erstens wurde eine neue zeitlich maskierte und gewichtete Strategie, mit dem Fokus die zeitliche Datentreue zu erhalten, entwickelt. Dieser komplett automatisierte Ansatz verwendet dynamische und statische Adermasken um den Einfluss der Regularisierung auf die statischen Bereiche zu beschränken. Die zweite Methode erweitert das sogenannte *low rank-sparse model* auf Phasenkontrastdaten und verwendet den *Split Bregman* Algorithmus zur Lösung. Diese Methoden wurden erfolgreich auf Aufnahmen der Halsschlagadern angewandt. Dieser Bereich erfordert hohe Beschleunigung sowie räumliche und zeitliche Genauigkeit der Flussgeschwindigkeiten. Alle algorithmischen Beiträge beruhen auf intrinsischen Eigenschaften von Phasenkontrast und können somit auf weitere Körperregionen angewandt werden. Zusammenfassend ist der Hauptbeitrag dieser Arbeit die signifikante Beschleunigung kontrastmittelfreier Magnetresonanzangiographie mittels neuartigen Abtast-, Regularisierungs- und Optimierungselementen.

Acknowledgments

There were a number of people involved in writing this thesis, both regarding the contents and the motivation.

First, I would like to thank Prof. Joachim Hornegger for the great opportunity to be part of his lab for the last three years and for the motivation and help he gave me.

Special thanks go to Peter Schmitt, who helped me enormously with the discussions we had, his ideas and enthusiasm. I am especially grateful for the hours he spent with proof reading my publications and this dissertation. I would also like to thank Dr. Andreas Greiser, especially for his help in the PCI part regarding data acquisition, theory and proof reading. I would also like to thank the entire Cardiovascular Team at Siemens MR, and especially Dr. Edgar Mueller for the enjoyable environment I had the chance to work in. I would also like to thank Prof. Dr. Griswold for the chance to spend some weeks in his lab.

I thank Prof. Rückert, Prof. Stamminger and Prof. Bäuerle for joining my examination committee. I would also thank all members of the pattern recognition lab, whom I spent an amazing time with. This goes especially to the MR group, to Eva and Kerstin for surviving the Medical Engineering lecture together with me, to Hannes, Johannes, Martin, Andre for the money lost and won and to Juergen, Simone and Felix for sharing an office. Further thanks go to the students I had the chance to work with, especially Juergen, Monica and Markus.

Special thanks go to Dr. Alexander Brost, Lisa Klausmann, Paula Schaller and Rebecca Ramb for their proof reading efforts.

For the motivation part, I would like to thank Barbara for making the lamb dream real, the Tuesday team and everyone else whom I had the chance to spend so important relaxing time with.

Last but not least, I would like to thank my family, especially my parents Birgitt and Michael and my brother Paul, for their love, ongoing encouragement and acceptance of my changing moods, as well as Andreas for providing me with food and love.

This thesis is dedicated to Helga Hutter.

London, May 8th, 2014

Jana Hutter

Contents

Chapter 1 Introduction	1
1.1 Motivation	1
1.1.1 Clinical Background.	2
1.1.2 Diagnostic Angiography	3
1.2 Thesis Overview	6
1.2.1 Focus of Research and Scientific Contributions	6
1.2.2 Organization of the Thesis	8
I Background	11
Chapter 2 Magnetic Resonance Angiography	13
2.1 From Spin to Image - MRI in a Nutshell	13
2.1.1 Spins and Magnetization	13
2.1.2 Echo Generation	17
2.1.3 K-space and Spatial Encoding.	19
2.2 Non-contrast-enhanced MRA Methods	21
2.2.1 Time of Flight	22
2.2.2 Magnetization Prepared Balanced Steady State Free Precession	22
2.2.3 Velocity Encoded Phase Contrast Imaging.	23
2.3 Summary Conclusions	25

Chapter 3	Compressed Sensing MRI Reconstruction	27
3.1	MRI Reconstruction: Signal Equation to Discrete Finite Sampling	27
3.1.1	Discrete Formulation	28
3.1.2	Discrete Sampling and Aliasing	30
3.1.3	Finite Sampling and Resolution	32
3.2	Parallel MRI and Extensions to Spatio-Temporal Correlations	33
3.2.1	Spatial sensitivity information	33
3.2.2	SENSE reconstruction as a linear problem	36
3.3	Compressed Sensing in MRI	38
3.3.1	Compressed Sensing	38
3.3.2	Sparsity and Incoherence in MRI	40
3.4	Parallel MRI Reconstruction in Compressed Sensing	41
3.4.1	Problem Formulation	42
3.4.2	State of the Art	42
3.5	Summary and Conclusions	44
II	Compressed Sensing in MR Angiography	45
Chapter 4	Highly Accelerated Static NceMRA	47
4.1	Motivation	47
4.2	State of the Art	48
4.3	Regularization and Sampling Strategy	49
4.3.1	Regularization	49
4.3.2	MICCS Sampling Strategy	51
4.4	Reconstruction Algorithms	54
4.4.1	Gradient Based Optimization	54
4.4.2	Split Bregman Algorithm	57
4.4.3	Formulation of Split Bregman for the pMRI CS Problem	59
4.5	Implementation	61
4.5.1	Complexity Analysis	62
4.5.2	Parameter Choices	65
4.6	Summary and Conclusion	65

Chapter 5 Accelerated 2-D Peripheral NceMRA	67
5.1 Motivation	67
5.2 Data and Evaluation	68
5.2.1 Peripheral TOF Data Acquisition	68
5.2.2 Volume Based Evaluation.	68
5.2.3 Organ Based Evaluation.	69
5.3 Evaluation of the MICCS Sampling Strategy	70
5.3.1 Experimental Setup	70
5.3.2 Results	71
5.4 Highly Accelerated NceMRA of the Peripheral Arteries	72
5.4.1 Experimental Setup	73
5.4.2 Results	73
5.5 Summary and Conclusions	74
Chapter 6 Accelerated 3-D Renal NceMRA	77
6.1 Motivation	77
6.2 Data and Evaluation	78
6.2.1 Renal mp-bSSFP Data Acquisition	78
6.2.2 Evaluation Strategy	78
6.3 Acceleration Study	79
6.4 Highly Accelerated NceMRA of the Renal Arteries	80
6.4.1 Experimental Setup	80
6.4.2 Results	81
6.5 Comparison With Clinical State of the Art	81
6.5.1 Experimental Setup	81
6.5.2 Results	82
6.6 Discussion	83
6.7 Summary and Conclusion	83
III Compressed Sensing in MR Phase Contrast	89
Chapter 7 Processing Pipeline and State of the Art in Phase Contrast MRI	91
7.1 Motivation	91
7.2 From Moving Magnetization to Physiological Values	92
7.2.1 Acquisition and Reconstruction	93
7.2.2 Postprocessing.	94
7.3 State of the Art in Accelerated PCI Reconstruction	96
7.3.1 Non-iterative Reconstruction	96
7.3.2 Iterative Methods	96
7.3.3 Sampling.	97
7.4 Summary and Conclusion	98

Chapter 8	Experimental Setup	99
8.1	Motivation for Carotid PCI	99
8.2	Data	100
8.2.1	Phantom Experiment	100
8.2.2	In-vivo Study	100
8.2.3	Patient Cases	101
8.3	Evaluation Strategy	103
8.3.1	Volume Based Evaluation	103
8.3.2	Physiology Based Evaluation	103
8.4	Summary and Conclusion	104
Chapter 9	Iterative Reconstruction for PCI	107
9.1	Joint Regularized Iterative Reconstruction	107
9.1.1	Joint Iterative Reconstruction	108
9.1.2	Regularization Strategy	109
9.2	Interleaved Velocity Encoding and Temporal Sampling	111
9.2.1	Pattern Formulation	111
9.2.2	Interleaved Central k-Space Sampling	112
9.2.3	Peripheral Decreased Density Sampling	113
9.3	Implementation	114
9.4	Summary and Conclusion	114
Chapter 10	Multi-dimensional Flow-Preserving Compressed Sensing (MuFloCoS)	117
10.1	Motivation	117
10.2	MuFloCoS	118
10.2.1	Vessel Masked and Temporal Weighted L1 Regularization	118
10.2.2	Anatomy Based Sub Division	122
10.3	Implementation and Experiments	124
10.3.1	MuFloCoS Implementation Details	124
10.3.2	Quantitative and Physiological Evaluation of the TMW Regularization	127
10.3.3	Comparison Against State of the Art in CS for Carotid PCI	128
10.3.4	Parameter and Robustness	128
10.4	Results	129
10.4.1	Quantitative and Physiological Evaluation	129
10.4.2	Comparison against Carotid PCI State of the Art	131
10.4.3	Robustness and Acceleration Studies	132
10.4.4	Patient Cases	133
10.5	Discussion	134
10.5.1	Quantitative Evaluation	134
10.5.2	Evaluation of I-VT, Shared Coil Profiles and TMW	137
10.6	Summary and Conclusion	141

Chapter 11	Low Rank Sparse Decomposition based Compressed Sensing (LoSDeCoS)	143
11.1	Motivation	143
11.2	LoSDeCoS	144
11.2.1	Influence of the Sampling on the Rank Minimization	144
11.2.2	Low Rank Assumption.	144
11.2.3	Rank Minimization Using the Nuclear Norm.	146
11.2.4	Objective Function	148
11.2.5	Minimization Using the Split Bregman Algorithm	149
11.3	Implementation and Experiments.	151
11.3.1	LoSDeCoS Implementation Details	151
11.3.2	Sparsity and Parameter Study.	151
11.4	Results	155
11.4.1	Sparsity and Parameter Study.	155
11.4.2	Comparison.	158
11.5	Discussion	159
11.5.1	Parameter Choices and Comparison	159
11.5.2	Limitations	161
11.6	Summary and Conclusion	162
IV	Summary and Outlook	163
Chapter 12	Summary	165
Chapter 13	Outlook	169
List of Figures		173
List of Abbreviations and Symbols		177
List of Tables		182
Bibliography		185

Introduction

1.1 Motivation	1
1.2 Thesis Overview	6

This thesis develops novel reconstruction methods for different applications in the field of non-contrast enhanced Magnetic Resonance Angiography (nceMRA) based on parallel MRI (pMRI) and Compressed Sensing (CS) . The clinical background and the commonly used diagnostic angiographic methods are presented in this chapter, along with their advantages and disadvantages. Furthermore, the contributions of this thesis are introduced and an overview of the following chapters is given.

1.1 Motivation

The blood vessels as part of cardiovascular system are essential for maintaining human life as they ensure the vital supply of cells and organs with nutrients and oxygen. The high prevalence of diseases and malformations associated with the vascular system and their mortality explains the importance of diagnosis and treatment options and consequently the availability of fast angiographic imaging.

NceMRA provides an excellent and non-invasive imaging modality to assess both the morphology and functionality of the blood vessels. Furthermore, it offers a wide range of options to influence the image contrast, allowing to emphasize on different features and to visualize physiological parameters, e.g the blood flow velocities. In contrast to other imaging modalities, the patient is not exposed to ionizing radiation or invasive procedures such as the injection of contrast agents. But despite those unique advantages, its clinical use is still limited due to its rather long acquisition times. A scan for of the lower peripheral vasculature could take for example about 30 minutes, a scan of the renal arteries over 8 minutes, always depending also on the heart cycle, breathing pattern, required imaging volume and the chosen acquisition technique. First of all, the slow imaging process is inconvenient for patients, particularly in combination with the limited space within the Magnetic Resonance (MR) scanner bore. But the long acquisition also limits the clinically desirable and technically achievable spatial and temporal resolution. Furthermore, motion-affected examinations, such as the assessment of aortic flow or the visualization of renal arteries, often require breath holds or specific physiological triggering and would highly profit from shorter scan times. Therefore,

there is an important clinical need for reducing the MR scan time in a wide range of angiographic nceMRA examinations to provide faster diagnostic imaging. As a consequence, acceleration is an important research focus in Magnetic Resonance Imaging (MRI) since its invention. Hardware-based improvements, which facilitate the acquisition of more image information in a shorter time, improved the imaging speed to a point where physiological and physical limitations such as nerve stimulation, maximal slew rate, and gradient strength play an important role for future technological advanced [Wrig97]. Another option are MR scan sequence-based improvements, which focus on reducing the amount of acquired data without compromising the image quality after reconstruction. These methods, relying heavily on prior knowledge and redundancies in the data, include partial Fourier techniques and parallel acquisition methods. While partial Fourier techniques exploit the symmetry of the k -space, pMRI methods accelerate by acquiring only a subset of k -space points simultaneously with spatially separated coils. The sub-sampled data is then reconstructed by adding prior knowledge of the spatial coil sensitivity distribution.

A new development made in the last decade was the use of CS techniques for MRI. CS methods were originally developed for domains such as video compression, but rapidly showed its applicability to a wide range of fields. Here, the principles of sparsity, incoherent sampling, and iterative non-linear reconstruction are combined to achieve faster acquisitions. Combinations of pMRI and CS techniques have been proposed [Cand08, Lust10] and led to a significant acceleration in MRI. Currently, CS based MRI is an active research field, still awaiting its clinical acceptance. Over the last five years, numerous concepts and novel techniques were proposed for a growing range of possible applications. Important steps include the data acquisition, the iterative reconstruction, and the modelling of sparsity assumptions for individual applications. The present thesis features advances in the iterative reconstruction algorithms, the accelerated sampling and in the development and the modelling process of sparsity in different, both morphological and functional, nceMRA examinations.

1.1.1 Clinical Background

The human vascular system is a closed system with the vessels acting as pathways. Blood is circulated around the body through the pumping action of the heart. The blood vessels are categorized by their respective function within the system into arteries, veins, and capillaries. The function of the arterial system is the transport of oxygenated blood from the lung to the entire body and the maintenance of the pressure-driven blood flow. Exceptions are the pulmonary arteries carrying deoxygenated blood and the pulmonary veins, where the blood arrives oxygenated from the lungs. Arteries experience high pressure values and variations over the cardiac cycle as they experience the direct action of the beating heart [Ufla06]. The ventricular contraction and the successive ejection of blood into the aorta in systole leads to a sharp rise in arterial blood pressure and to an expansion of the arterial walls. They contract almost immediately when the ventricles relax, implying a pressure drop during diastole. These pressure variations result in a highly

pulsatile arterial blood flow. Veins differ from arteries regarding their function and, in consequence, structure. They carry de-oxygenated blood back towards the heart and are therefore less influenced by the heart contractions. Unlike arteries, they do not use muscular action to maintain the lumen diameter but rather collapse in the absence of blood. Valves are used to maintain the blood flow direction within the veins. Capillaries assure the connection between arteries and veins and ensure the exchange between the vascular system and the body tissues through the capillary walls. The most important parts of the vascular system are shown in Figure 1.1, where the regions of interest for this work are highlighted. The carotid arteries (a) ensure the supply of the neck and head with oxygenated blood. After originating from the brachiocephalic trunk on the right side and the aortic arch on the left, the common carotid artery (CCA) bifurcates into the internal and external carotid arteries (ICA/ECA) [Ufla 06, Gray 01]. A further region of interest for this thesis are the renal arteries (b), originating from the abdominal aorta and branching into typically three to five branches to supply the entire kidneys with blood. Finally, the arteries in the legs (c) are typically summarized under peripheral arteries [Kand 08]. After emerging from the aorta, the common iliac arteries bifurcate into internal and external iliac, the latter leading into the femoral arteries. These extend until becoming the popliteal arteries, which then bifurcate into the anterior and posterior tibial arteries, supplying the crus and foot with blood.

1.1.2 Diagnostic Angiography

The importance of the cardiovascular system correlates with its leading position within the causes of global mortality. Cardiovascular diseases and acute events such as stroke or heart attack originating within the cardiovascular system account for about 30% of the annual deaths. These diseases include, specifically for the vascular system, peripheral artery disease, coronary artery disease, thrombosis, embolism and aneurysms. A common vascular diagnosis is arterial stenosis, often causing peripheral or coronary artery disease and known to be one of the main origins of strokes [Orga 13, U Ki 09]. While possible reasons include congenital or inflammatory diseases, most stenoses result from atherosclerosis, the formation of plaque within the arteries. Most common are carotid, coronary, aortic, renal or peripheral artery stenosis. The collection of plaque in the arteries is a slow continuous process. Occurring in all humans over their lives, it is dramatically influenced by behavioural factors such as the consumption of tobacco and alcohol, a fat and unhealthy diet as well as the lack of physical activity [Rubi 12]. The earlier the plaque formation is detected, the earlier appropriate actions can be taken.

Most common treatment possibilities for vascular lesions are operative procedures such as angioplasty, atherectomy and revascularization, all aiming to re-establish the blood supply and to expand the lumen [Gonz 11]. The invasiveness and the associated risks demand a careful evaluation of risks and benefits and give raise to the need for precise diagnostic imaging, able to evaluate the stage and degree of vascular lesions and diseases. Vascular imaging can be divided into morphological and functional imaging. While morphological imaging focuses on the anatomy of the vascular system, the vessel lumen and vessel walls, functional

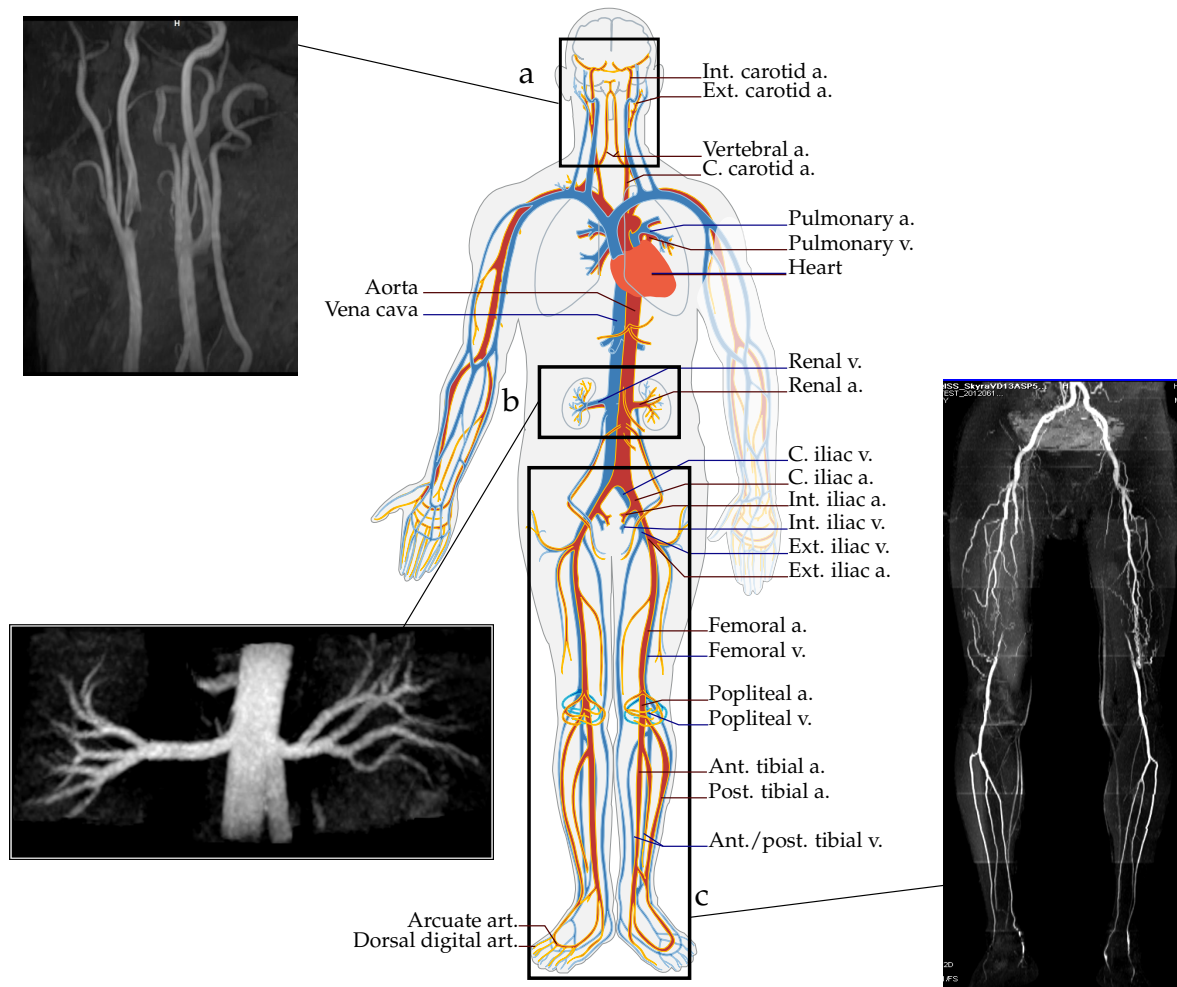


Figure 1.1: The human vascular system, highlighting the (a) carotid arteries, (b) renal arteries and (c) the peripheral arteries. Image adapted from [Gray 01].

imaging assesses the main functionalities of the vascular system, blood pressure and blood flow. The latter two are often referred to as hemodynamics.

At present, vascular imaging is still mainly restricted to morphological imaging but functional imaging gains more and more importance. Three important aspects of functional imaging need to be considered. First, knowledge about flow velocities and patterns within aneurysms and stenosis can impact the evaluation of the state and progress of diseases. The assessment of the peak velocity or the turbulences within the aneurysmic bulb helps to estimate rupture probabilities and the need for invasive treatment. A significant velocity rise within a low grade carotid artery stenosis can be an indicator for a substantial stroke risk [Chen 06]. Second, treatment planning benefits due to hemodynamics evaluation were reported for transcatheter aortic valve implantation [Sher 11] and for the risk of re-stenosis after stenting [Rich 04]. The last aspect is the influence of the hemodynamics on the formation of plaque. The etiology of atherosclerosis is not fully understood, but a tendency to amplified deposition in bifurcations or curved arteries shows the influence of hemodynamics [Chen 06]. Recently, research has identified elevated wall shear stress as one of the promoting factors [Stal 08]. Hence, vascular imag-

ing could greatly benefit from the combination of morphological and functional imaging.

Morphological imaging modalities include Digital Subtraction Angiography (DSA), Computed Tomography Angiography (CTA), Ultrasound (US) and MRA. DSA is a computer-assisted X-ray technique involving the injection of a contrast agent to visualize the vessel tree. The generated contrast relies on the subtraction of two images, one acquired before and one after the contrast agent is administered. Newer developments include 3-D DSA and rotational angiography (DynaCT) [Al Q09]. However, 2-D DSA [Rubi 12] is still the gold standard for most pathologies such as carotid artery stenosis [U Ki 09] and peripheral artery disease [Al Q09]. Its main benefits are high spatial and temporal resolution images and a large field of view paired with a relatively quick acquisition protocol. However, significant drawbacks need to be taken into account. These include the highly invasive intra-arterial injection of nephrotoxic contrast agent requiring experienced staff, the exposition to ionizing radiation for both the medical team and the patient as well as a risk for neurological complications, especially in the case of carotid artery DSA.

CTA is an X-Ray-based technique generating vascular contrast through peripheral injection of a iodine-based contrast agent. It is quick, widely available and offers an excellent 3-D resolution. Multi-center studies reported its high accuracy compared to DSA as a reference for the carotid arteries [U Ki 09, McKi 05, Bart 06] and the peripheral arteries [Rubi 12]. The drawbacks are, however, the injection of contrast agent and the use of ionizing radiation. Furthermore, signal problems in the presence of calcified plaque or metal fragments may lead to overestimation of a stenosis [Al Q09].

US is widely accepted as a non-invasive, inexpensive, and portable imaging modality for a wide range of vascular diseases. Based on sound waves produced by piezoelectric transducers, no ionizing radiation or invasive procedure is required, which makes US an ideal screening modality. However, its high inter-user variability, the restriction to a local assessment rather than a visualization of the entire region of interest and its dependence on a good acoustic window limit its clinical use. In addition, the image acquisition is often hampered by the presence of bowel gas, calcification or post-operational dressings [Coll 07].

A non-invasive alternative is MRA, offering visualization of the vascular structure without the drawbacks of ionizing radiation, user dependency or the need for highly invasive procedures. In addition to the established contrast-enhanced MRA techniques (ceMRA) [Lein 05], involving gadolinium-based agents, nceMRA techniques have emerged. The occurrence of gadolinium induced nephrotoxic systemic fibrosis [Prin 09] and a significant patient population with contraindications to the injection of gadolinium-based contrast agents limit the use of ceMRA. The commonly used nceMRA acquisition methods include Time of Flight (TOF) and magnetization-prepared balanced Steady State Free Precession (mp-bSSFP).

Functional imaging modalities measuring hemodynamic information in-vivo include Doppler Ultrasound (DUS), nceMRA and Fractional Flow Reserve (FFR).

DUS is an US-based technique, relying on the Doppler effect to measure blood velocities [Gibs 94]. In addition to the mentioned disadvantages of US, the accuracy of flow measurements with DUS is very sensitive to the transducer angle and the exact positioning on the narrowest location within the stenosis [U Ki 09].

NceMRA provides alternatives to DUS with Fourier velocity encoding and velocity-encoded Phase Contrast Imaging (PCI). PCI offers a larger anatomical coverage, the encoding of velocity in all three directions as well as the simultaneous acquisition of morphological and functional imaging. However, important drawbacks are long acquisition times limiting both the spatial and temporal resolution as well as physical limitations such as partial volume effects, registration artefacts, and eddy current effects.

Fractional Flow Reserve (FFR) describes the measurement of pressure gradients, mainly in the coronary arteries, using a catheter-mounted sensor [Toni 09]. Further techniques such as laser Doppler and laser speckle are not suited for diagnostic in-vivo imaging [Daly 13]. Another direction of research in hemodynamics are computational fluid dynamics simulations. These include either models or patient specific information, such as vessel geometries, the heart rate as well as blood pressure as input parameters. They generate, however, only simulations rather than actual in-vivo velocity information.

1.2 Thesis Overview

This thesis reports several methodological developments in the field of CS and multiple applications for nceMRA and blood flow imaging.

1.2.1 Focus of Research and Scientific Contributions

The main scientific focus of this work was to develop algorithms which significantly reduce the acquisition time for different applications in the field of morphological and functional nceMRA. The developed algorithms are applied to three major types of angiographic examinations, but are not by any means restricted to those. This thesis provides scientific contributions regarding all three steps of the CS-pMRI reconstruction pipeline, sampling, sparsity transform and the optimization algorithm as shown in Figure 1.2. It provides contributions to the community of MRI reconstruction. In the following section, the major scientific contributions are summarized.

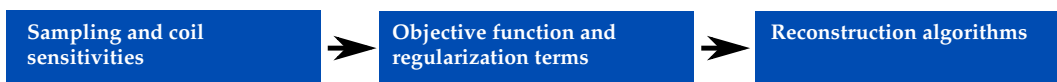


Figure 1.2: Reconstruction algorithm pipeline.

Morphological imaging

- A novel **Multi-Coil Compressed Sensing (MICCS) sampling strategy**, combining the ideas of pMRI and CS in the Cartesian case was designed

to achieve high acceleration factors. Its benefits were shown compared to state of the art approaches when applied to both 2-D and 3-D problems. This approach has been published in [Hutt 11a], [Hutt 13d] and is also used in [Hutt 14d, Hutt 11b, Hutt 13b, Hutt 12a, Hutt 12b, Hutt 13a, Hutt 13e, Hutt 14c, Hutt 14b].

- **Split Bregman-based optimization** schemes were adapted to the pMRI-CS reconstruction problem, combined with different sparsity assumptions and evaluated in comparison to gradient-based optimization methods.
- **Multi-slice** regularization strategies for peripheral TOF were developed, including the vessel prior knowledge strategy presented in [Hutt 11b] and [Hutt 12b] and different TV based variants as published in [Hutt 13c]. These are not within the scope of this thesis.
- **2-D peripheral Time of Flight angiography** was accelerated significantly using the MICCS k -space under sampling pattern and pMRI-CS algorithm reducing scan times from about 30 min to under 3 minutes for a scan of the entire lower peripheral vasculature. The results with evaluation of the pattern were presented in [Hutt 14a].
- **3-D renal free-breathing balanced steady state free precession angiography** were accelerated significantly using the described MICCS k -space sampling strategy and the Split Bregman-based pMRI-CS algorithm reducing scan times from over 8 minutes to below 1 minute for a fully non-invasive free-breathing renal scan. The results and comparison to clinical methods were presented in [Hutt 12a] and [Hutt 14b].
- **A fully automatic segmentation algorithm** was presented for Time of Flight data from the carotid arteries. One of the major problems in this nceMRA application, signal voids in areas of irregular flow patterns, was addressed by proposing a novel 3-D level set based method. The algorithm for completely automatically vessel tree segmentation was presented at [Hutt 12c]. It was shown that this algorithm provided a segmentation with significantly increased accuracy and sensitivity compared to state of the art level set algorithms. However, this work is not in the scope of this thesis.

Blood flow imaging

- **Multi-dimensional interleaved velocity encoding temporal sampling** for Phase Contrast Imaging was proposed, taking all available dimensions into account including the temporal and particularly the velocity encoding dimension. This new approach goes beyond conventional and state of the art implementations, allows to enlarge incoherence, extends the benefits of temporal regularization and enables a fully internal coil sensitivity calculation scheme. Both the pattern and the coil profile sampling strategy were proposed and used in [Hutt 14c], [Hutt 14d], [Hutt 13e] and [Hutt 13b].

- **Anatomical vessel maps as prior knowledge for temporal regularization** were combined with temporal weighting and a static-dynamic map calculation approach to a novel regularization, which proved to be capable of preserving flow dynamics. This was presented in [Hutt 13b], [Hutt 13a] and in [Hutt 14d]. Evaluation against state of the art methods showed significant improvements regarding the flow profile accuracy and the image quality.
- **The low-rank sparse decomposition model**, previously proposed for time resolved MRI was extended to 4-D PCI by tensor unfolding. The emerging reconstruction problem was solved with a novel version of the unconstrained Split Bregman algorithm. Results were presented in [Hutt 13e] and [Hutt 14c].
- **Comprehensive evaluation and comparison** using different regularization terms and optimizers for PCI was presented, including image based and physiological parameters.

1.2.2 Organization of the Thesis

This section details the structure of the thesis and presents the individual chapters. A graphical overview is given in Figure 1.3. Three main parts divide the thesis into content-based entities. The first part focuses on the background and lays the foundations for the second and third part. These parts are formed based on the targeted application, static nceMRA techniques in Part II and blood flow imaging in Part III. In the following, the chapters will be individually presented.

The background Part I consists of two chapters. Chapter 2 introduces the physical bases of MRI, focusing on spins, echo generation and contrast mechanisms as well as the spatial localization in k -space and specifically the contrast mechanisms of the used nceMRA acquisition techniques TOF, bSSFP and PCI. In its first section, Chapter 3 presents the basics of MRI data sampling including the limits leading to aliasing or resolution losses. Second, the principles of pMRI and CS are introduced. Finally, the combined reconstruction problem is formulated and important state of the art techniques are reviewed.

Part II, presenting reconstruction techniques for static nceMRA, is divided into three chapters. Chapter 4 details the developed MICCS sampling strategy and formulates both gradient-based optimization and the Split Bregman algorithm for the given reconstruction algorithm. Implementation details, including the developed framework, are presented.

Chapter 5 presents the first application for the developed algorithm, 2-D peripheral TOF, where the novel MICCS pattern and the Split Bregman-based method were applied in order to decrease the acquisition time and improve reconstruction quality. The image- and organ based evaluation strategy and experiment design are given. Finally, the results for different patterns and algorithms are presented and discussed for both high resolution data sets and data from the entire lower vasculature.

Finally, Chapter 6 reports the achieved acceleration results for 3-D free-breathing mp-bSSFP renal angiography. The image- and organ based evaluation strategy

and experiment design are given. The results of an acceleration study, the algorithm evaluation and comparison against clinically used methods are presented and discussed.

Part III focuses on reconstruction techniques for PCI. It consists of five chapters, with Chapter 7 detailing the specific properties of PCI reconstruction and post processing. Chapter 8 presents the acquired data including the volunteer and phantom study as well as the considered patient cases and the strategy developed for evaluation. The joint iterative reconstruction for PCI as well as the novel I-VT data sampling strategy is developed in Chapter 9. The remaining two Chapters present dedicated reconstruction algorithms, combining novel regularization strategies with the presented methodological elements of Chapter 9.

The first algorithm, called MuFloCoS, is introduced in Chapter 10. Its main parts are the use of an anatomically motivated sub-division using adaptively calculated vessel masks to guide the regularization and the temporal weighted regularization strategy. These elements are motivated and derived, the experiments are introduced, the results are presented and discussed.

Finally, the second developed algorithm for PCI reconstruction, entitled LoSDeCoS, is explained in Chapter 11. The decomposition of the image matrix into a low rank and a sparse part is developed here for multi-dimensional PCI data. Firstly, the construction of the joint vector space is motivated and demonstrated, and the used sparsity and low rank assumptions are explained. Secondly, the unconstrained Split Bregman algorithm is extended to incorporate the sparsity and low rank assumptions for PCI and the used proximal operators are developed. The experimental setup is explained and the results are presented and discussed. The thesis is concluded with Part IV, consisting of the summary in Chapter 12 and the outlook in Chapter 13 presenting future possible directions of research.

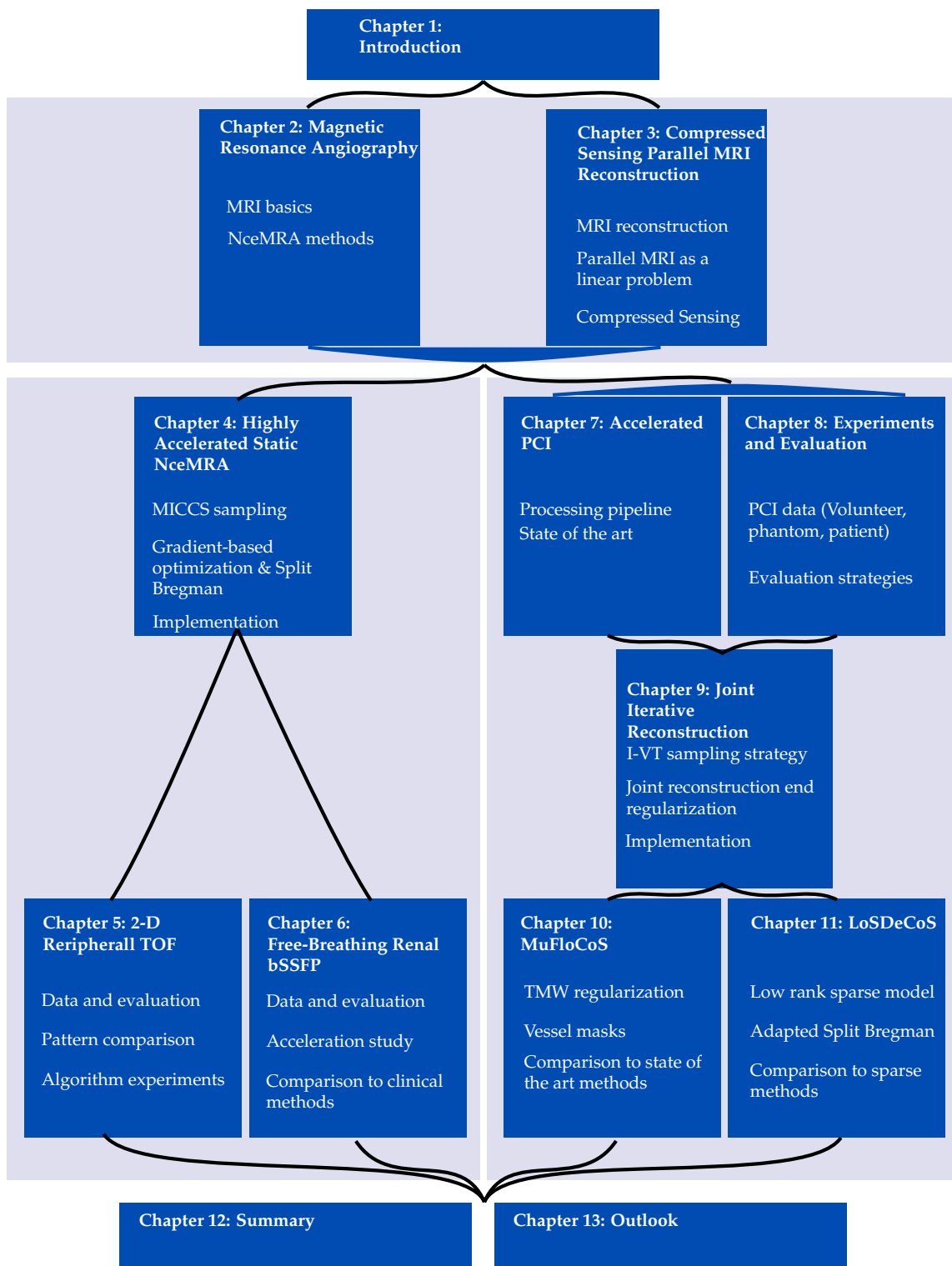


Figure 1.3: Organization of the thesis

Part I
Background

Magnetic Resonance Angiography

2.1 From Spin to Image - MRI in a Nutshell	13
2.2 Non-contrast-enhanced MRA Methods	21
2.3 Summary Conclusions	25

This chapter presents the bases of MRI imaging, detailing the required steps from spin to image including the spin properties, echo generation and spatial localization. In the second part, the used nceMRA acquisition techniques are detailed, focusing on the respective contrast generation methods.

2.1 From Spin to Image - MRI in a Nutshell

The principle of nuclear magnetic resonance, investigated first in bulk matter by Bloch and Purcell in 1946, is based on the alignment and precession of atomic nuclei when exposed to an external static magnetic field and describes the phenomenon occurring when exposed to a second oscillating field. The spin of nuclei is considered as a small magnetic moment on the microscopic scale, precessing with frequency f , which is related to the spatially dependent static field $\mathbf{B}(\mathbf{r})$ and the proton-specific gyromagnetic ratio γ by the Larmor equation:

$$f(\mathbf{r}) = \gamma B(\mathbf{r}). \quad (2.1)$$

Thereby, \mathbf{r} denotes the 3-D spatial position and \mathbf{B} the three-dimensional field. For hydrogen protons ^1H with $\gamma_{^1\text{H}} = 42.6\text{MHz/T}$ and a homogeneous \mathbf{B}_0 field of 3 Tesla, the Larmor frequency equals to 127.8MHz. The high water content of the human body, and therefore the high density of hydrogen protons, leads to their frequent use in human MRI.

2.1.1 Spins and Magnetization

The \mathbf{B}_0 field leads to precession with constant z-component either parallel or anti-parallel along the field. The favourable lower energy-state of the parallel alignment leads to a slight extent of parallel aligned spins, approximately in the ratio of 10 to 1 million, and to a measurable parallel magnetic moment of the spin

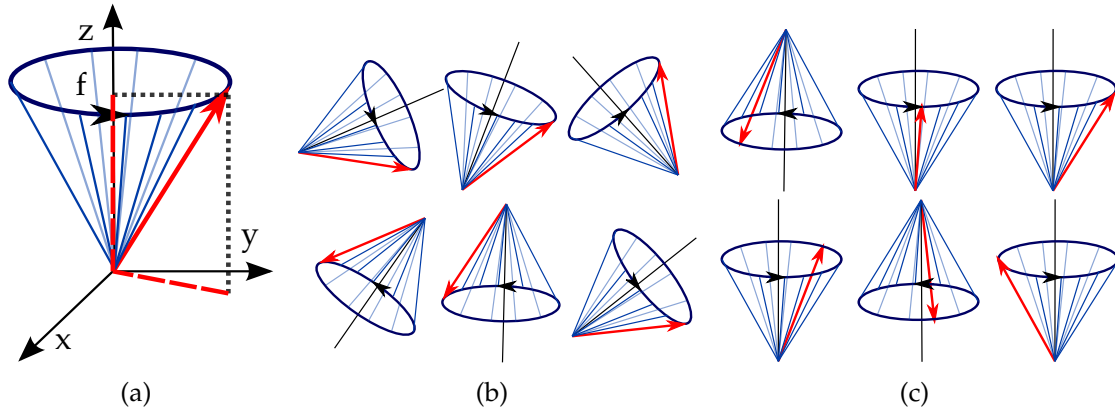


Figure 2.1: The concept of spins is illustrated. (a) Representation of a spin, rotating with frequency f . While random orientation and frequency can be observed (b) without the influence of the magnetic field, the spins are aligned along the main axis either parallel or anti-parallel (c) under the influence of the field.

ensemble. The spins can be represented by 3-D vectors in a standard reference frame. Figure 2.1(a) illustrates a spin rotating with frequency f around the z -axis, by convention the direction of the main magnetic field. Figure 2.1(b) illustrates an ensemble of spins without, Figure 2.1(c) with the influence of the external field. MRI is described on the macroscopic rather than microscopic level, considering an ensemble of spins, represented by a magnetization vector, which corresponds to the vector of the individual magnetic moments. In the thermal equilibrium, the observed magnetization in the main field is longitudinal, as the transversal components of the individual magnetic moments cancel out for the ensemble due to the phase incoherence. An additional influence from specific fields, as detailed below, can transform the longitudinal magnetization $\mathbf{M}_z(\mathbf{r}, t)$ into transversal magnetization $\mathbf{M}_{xy}(\mathbf{r}, t) = M_x(\mathbf{r}, t)\mathbf{e}_x + M_y(\mathbf{r}, t)\mathbf{e}_y$. The magnitude of \mathbf{M}_{xy} will be referred to by $M_{xy} = |\mathbf{M}_{xy}|$. The general description of the magnetization equals

$$\mathbf{M}(\mathbf{r}, t) = \begin{pmatrix} M_x(\mathbf{r}, t) \\ M_y(\mathbf{r}, t) \\ M_z(\mathbf{r}, t) \end{pmatrix} = M_x(\mathbf{r}, t)\mathbf{e}_x + M_y(\mathbf{r}, t)\mathbf{e}_y + M_z(\mathbf{r}, t)\mathbf{e}_z. \quad (2.2)$$

Another important variable is the phase, which is described by the angle Φ between the y -axis and the \mathbf{M}_{xy} magnetization vector. The frequency describes the rate of change of phase. Different frequencies will lead to changes of phase differing over time, but also spins precessing with the same frequency can be out-of-phase.

The generation of a measurable signal in the receiver coils relies on electromagnetic induction and requires transversal magnetization, which originates from phase-coherent spins and is achieved in MRI by radio frequency (RF) pulses. RF pulses are time-dependent magnetic fields. The MR-relevant \mathbf{B}_1 field can be seen as a rotating field in the xy plane, perpendicular to the \mathbf{B}_0 field. Important pulse

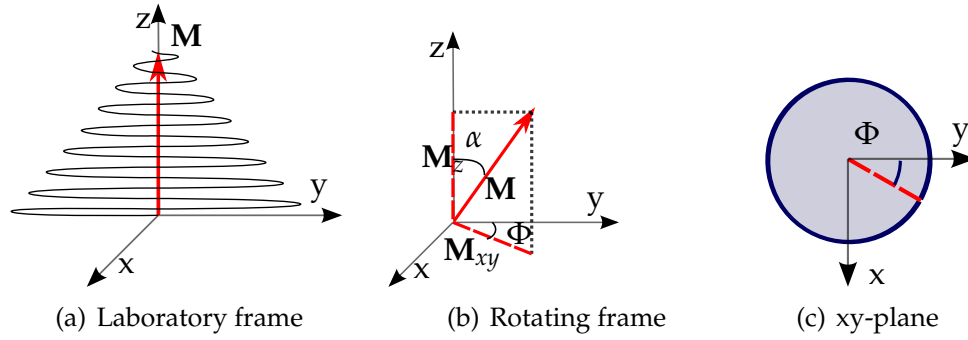


Figure 2.2: Illustration of the influence of a 90° pulse on the magnetization vector in different representations. (a) The spin precesses around the z -axis when visualized in the laboratory frame. (b) The rotating frame is introduced to omit visualization of precession around the z -axis. (c) The phase is typically studied in the xy -plane rather than the 3-D representation.

parameters are the amplitude B_1 of the pulse, the time t during which the RF pulse is applied and the frequency ω_0 :

$$\mathbf{B}_1(t) = B_1 \begin{pmatrix} \cos(\omega_0 t) \\ -\sin(\omega_0 t) \\ 0 \end{pmatrix}. \quad (2.3)$$

Due to the resonance condition, only protons precessing at the frequency ω_0 are affected by the RF pulse. The excitation leads to a forced precession of the magnetization around the field $\mathbf{B}(\mathbf{r}, t) = \mathbf{B}_0(\mathbf{r}, t) + \mathbf{B}_1(t)$. The time and the pulse amplitude define the tilt angle of the magnetization, referred to as flip angle α . The precession during an RF pulse that tilts the magnetization into the transverse plane ($\alpha = 90^\circ$) in a laboratory frame is illustrated in Figure 2.2(a). The magnetization vector spirals down into the xy -plane. Precession is, however, more frequently studied in a rotating frame, rotating at frequency ω_0 , in which the precession around the z -axis is not present. In the rotating frame, the B_1 field strength equals

$$\mathbf{B}_1(t) = \begin{pmatrix} B_1 \\ 0 \\ 0 \end{pmatrix}. \quad (2.4)$$

The RF pulse tips the magnetization by the flip angle α , depending on the time t and the strength B_1 , as illustrated in Figure 2.2(b). The phase of the magnetization is often described using the xy -plane representation as shown in Figure 2.2(c) because the longitudinal magnetization does not influence it.

The mathematical connection between the applied \mathbf{B} -field and the magnetization \mathbf{M} is given through the Bloch equation:

$$\frac{d}{dt}\mathbf{M}(\mathbf{r}, t) = \mathbf{M}(\mathbf{r}, t) \times \gamma\mathbf{B}(\mathbf{r}, t) \quad (2.5)$$

After an RF pulse with flip angle α , resulting in a net magnetization of $M_z(\mathbf{r}, 0) = M(\mathbf{r}, 0) \cos(\alpha)$ and $M_{xy}(\mathbf{r}, 0) = M(\mathbf{r}, 0) \sin(\alpha)$ the spins are freely precessing and

Parameter	Muscle	Fat	Arterial blood
T_1	900	250	1200
T_2	50	60	200

Table 2.1: T_1 and T_2 values for muscle, fat and arterial blood

returning to equilibrium. The corresponding period is called free induction delay (FID). This phenomenon is referred to as relaxation. Interactions between the spins and the surrounding lattice allow recovery of the longitudinal relaxation at a rate proportional to the difference. This is formulated as

$$\frac{dM_z(\mathbf{r}, t)}{dt} = \frac{1}{T_1}(M_z(\mathbf{r}, 0) - M(\mathbf{r}, 0)), \quad (2.6)$$

where T_1 is referred to as longitudinal relaxation time. The evolution of the magnetization towards equilibrium is described by

$$M_z(\mathbf{r}, t) = M(\mathbf{r}, 0) \cos(\alpha) e^{-t/T_1} + M(\mathbf{r}, 0)(1 - e^{-t/T_1}). \quad (2.7)$$

The transversal magnetization is influenced by tissue properties, the spin-spin interaction and magnetic field inhomogeneities, leading to a loss of phase coherence between spins over time with $M_{xy} = M_0 \sin(\alpha) e^{-(t/T_2)}$ and with the characteristic tissue-specific T_2 relaxation constant.

The modified Bloch equation taking relaxation into account equals

$$\frac{d}{dt} \mathbf{M}(\mathbf{r}, t) = \mathbf{M}(\mathbf{r}, t) \times \gamma \mathbf{B}(\mathbf{r}, t) - \frac{M_x(\mathbf{r}, t) \mathbf{e}_x + M_y(\mathbf{r}, t) \mathbf{e}_y}{T_2} - \frac{(M_z(\mathbf{r}, t) - M_z(\mathbf{r}, 0)) \mathbf{e}_z}{T_1}. \quad (2.8)$$

Both mechanisms are extremely important in the contrast generation as they allow to differentiate between tissues by their distinct T_1 and T_2 values. Table 2.1 illustrates typical values for muscle, fat and arterial blood [Haac 99]. Furthermore, to generate vascular contrast in ceMRA techniques, the T_1 values of blood can be altered using contrast agents. The T_1 value of blood is influenced most frequently with contrast agents containing Gadolinium (Gd^{3+}). After injection and propagating through the vascular system, neighbour protons are influenced by the paramagnetic properties of the contrast agent.

The spatial dependency of the frequency on the magnetic field in the Larmor equation Eq. (2.1) can be exploited to vary the magnetization locally by influencing the $\mathbf{B}(\mathbf{r}, t)$ field using gradient coils. This is employed both in the signal generation process and for spatial localization. A field \mathbf{B}_G , varying linearly in x -direction is added to the main field, resulting in

$$\mathbf{B}(\mathbf{r}, t) = \mathbf{B}_0(\mathbf{r}) + \mathbf{B}_G = \mathbf{B}_0(\mathbf{r}) + \begin{pmatrix} xG(t) \\ 0 \\ 0 \end{pmatrix}. \quad (2.9)$$

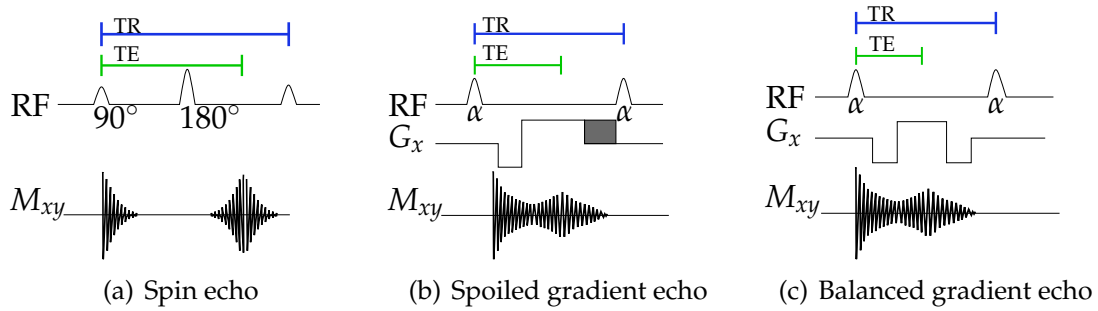


Figure 2.3: Sequence diagrams illustrating the main echo generation mechanisms. (a) The principle of a spin echo is shown with the excitation and refocusing pulse and the resulting echo. (b) A spoiled gradient echo sequence, consisting of the RF pulse, the pre- and rephasing gradients and the spoiler gradient is illustrated. (c) The balanced gradient echo sequence, using a balanced gradient scheme instead of a spoiler, is shown.

$G(t)$ equals the gradient $\partial \mathbf{B} / \partial x(\mathbf{r}, t)$. The frequency changes results in $\omega_G(\mathbf{x}, t) = \gamma x G(t)$. Gradients are time-dependent and vary typically during an MR experiment for a fixed time interval $[0, T]$. The gradient leads to a phase of

$$\Phi_G(\mathbf{r}, t) = - \int_0^T \omega_G(\mathbf{r}, \tau) d\tau = \gamma x \int_0^T G(\tau) d\tau. \quad (2.10)$$

2.1.2 Echo Generation

Both gradient fields and RF pulses are employed for signal generation. The two most fundamental principles, those of gradient and spin echo sequences are briefly explained here.

Spin Echo sequences influence the magnetization with a 90° excitation RF pulse, followed by a 180° refocusing RF pulse. The decay of transverse magnetization in the FID resulting from the first pulse is recovered partly by the second. The effect of spatial field inhomogeneities on the spins, accounting for T_2' losses in phase coherence, is reversed by the refocusing pulse. The phases of magnetization at different frequencies in the xy plane is reverted and the subsequent inverse influence of the inhomogeneities lead to recovery of phase coherence, see Figure 2.3(a). The transverse magnetization, however, does not reach its original value as the tissue-dependent T_2 -induced signal losses are not restored.

The image contrast mainly depends on the echo time (TE), referring to the time between the RF pulse and the echo, and the repetition time (TR), which denotes the time between subsequent 90° pulses. The combination of both influences the final image contrast and allows to generate either T_1 -weighted contrast with short TE of $< 20\text{ms}$ and short TR of $500 - 800\text{ms}$ or T_2 -weighted contrast with long TE of $> 80\text{ms}$ and long TR of $> 1200\text{ms}$. The acquisition time in spin echo sequences is determined by the TR. Methods to reduce the time are fast spin echos (FSE) or multi-slice techniques. FSE sequences capture multiple echos using repeated 180° pulses after the initial 90° pulse. Multi-slice sequences fill the TR needed for recovery with the acquisition of multiple, separate slices.

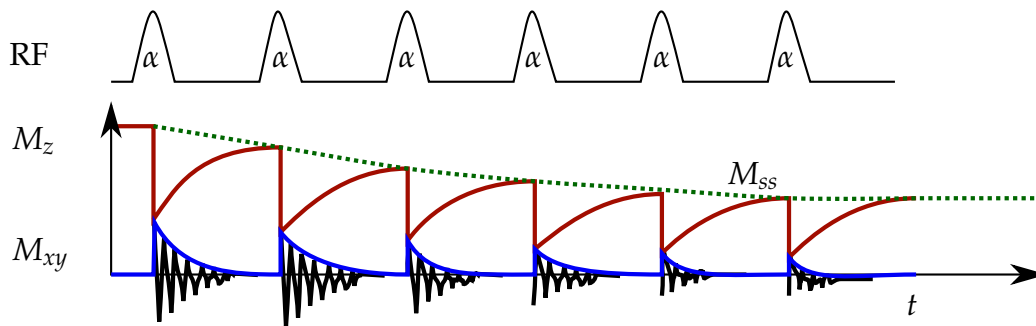


Figure 2.4: The generation of the steady state is shown based on a basic sequence diagram considering only the FID magnetization. The transversal magnetization is shown in blue, the longitudinal in red. The steady state magnetization M_{ss} is obtained after a sufficiently high number of consecutive RF pulses.

Gradient Echo sequences do, in contrast to spin echo techniques, not employ $90^\circ/180^\circ$ RF pulse sequences, but rather de- and rephasing gradients to recover the signal. The accelerated dephasing in the FID caused by the first gradient shape is reversed by a rephasing gradient of opposite polarity as illustrated in Figure 2.3(b). Maximal recovery is reached after TE, when the additive effects of both gradients cancel out. The phase dispersion Φ induced by gradients is proportionally dependent on the amplitude G and the duration t of the gradient [Mark 12].

Spoiled and balanced gradient echo Within the gradient echo sequences, another differentiation between spoiled and balanced steady-state gradient techniques is based on the influence of the sequence on the transverse magnetization after the read-out. A common method to cancel out remaining transverse magnetization is the use of a spoiler gradient resulting in a faster loss of remaining phase coherence as illustrated in Figure 2.3(b). The contrast of spoiled gradient echo sequences is either T_1 - or T_2^* -weighted. In contrast to that, balanced gradient echo techniques rely on keeping the transverse magnetization in phase by using balanced rewinder gradients, see Figure 2.3(c). The contrast is influenced positively by T_2 and negatively by T_1 and therefore called $\frac{T_2}{T_1}$ -weighted. T_1 influence is negative, as longer T_1 leads to slow relaxation of the longitudinal magnetization and to a lower measurable signal. Longer T_2 values, in contrast, allow higher signal as the transverse magnetization is not fully lost before the next pulse is applied, assuming a sufficiently short TR.

Steady State imaging is another important concept in gradient echo imaging, describing the balance between the recovery and loss of longitudinal magnetization between subsequent excitations. An example for the FID signal is shown in Figure 2.4. The steady state magnetization M_{ss} depends on the employed TR, the flip angle and the tissue-dependent T_1 value. The maximal signal for a certain T_1 is obtained using the Ernst angle α_E defined by $\cos \alpha_E = e^{-TR/T_1}$. This equation states the optimal flip angle α_E for a given TR. If the flip angle is chosen higher,

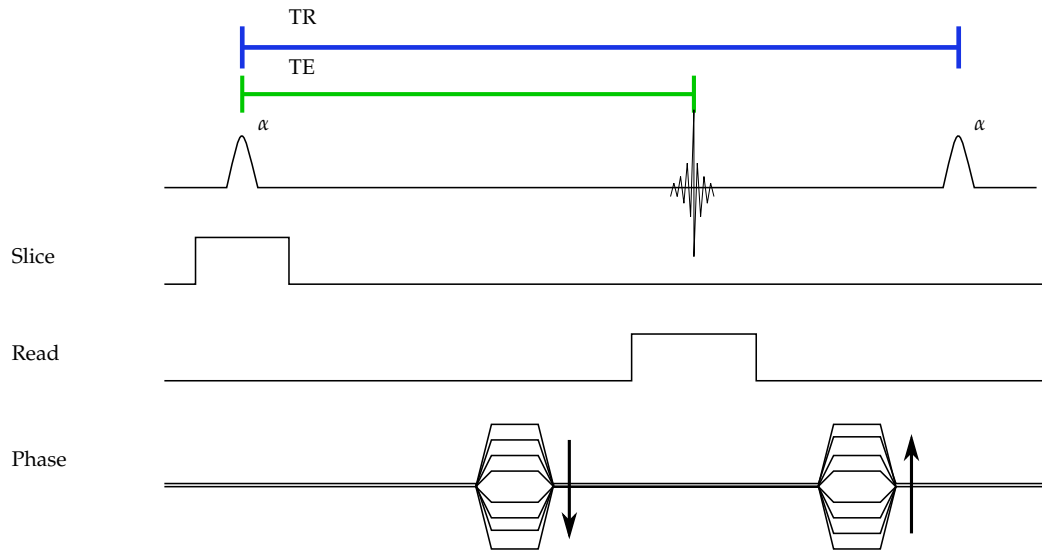


Figure 2.5: Classical sequence diagram focusing on the spatial localization. The slice (Slice), read-out (Read) and phase (Phase) gradients are shown along with the RF pulse and the resulting echo. The echo time TE is depicted in green, the repetition time TR in blue.

saturation occurs as not enough recovery time is given. This leads to a lower signal.

2.1.3 K-space and Spatial Encoding

The spatial localization of the MR signal obtained in the receiver coils is a prerequisite to obtain images and volume data. This is achieved in two steps by the use of the gradient coils. In the following, slice-selective excitation is explained followed by frequency-encoding and phase-encoding gradients. All parts are summarized in the sequence diagram in Figure 2.5.

The localization in slice-direction is based on the resonance condition for RF pulses. Only spins precessing at frequencies within the bandwidth of the applied RF pulse are influenced. The magnetic field is thus slightly changes by gradients with strength B applied in the same time than the RF pulses to limit the RF pulse effects to a certain slice of thickness Δd . Taking the gradient $G = \frac{\Delta B}{\Delta d}$ and the bandwidth Δf into account, the resulting slice thickness equals

$$\Delta d = \frac{\Delta f}{G\gamma}. \quad (2.11)$$

Within the slice, frequency-encoding and phase-encoding gradients allow spatial encoding. The frequency-encoding gradient is applied during the signal readout as shown in Figure 2.5. By manipulating the magnetization in a spatially dependent manner, the sampled data can be localized using a Fourier transform. In contrary to the read-out gradients, phase-encoding gradients are applied before the echo is sampled and influence the phase of the magnetization, which than depends on the position. While frequency-encoding gradients sample k -space data at

multiple data points along a read-out k -space trajectory, the use of a certain phase-encoding gradient corresponds to a k -space offset, which affects the whole subsequent readout. The phase-encoding needs to be repeated for all desired phase-encoding steps with repetition time TR. The time between excitations depends on the magnetization manipulation and the desired contrast and largely contributes to the long MRI acquisition time. The number of frequency steps in each excitation is not time-critical but limited by the decay of magnetization, allowing only a restricted acquisition window. While acquisitions have been proposed [Craw 92], that sample the entire k -space with a single trajectory, this can lead to significant image artefacts or restricted resolution [Lust 07].

In the Cartesian case, phase encoding gradients are applied in multiple steps and orthogonal to the slice encoding and read-out gradients as depicted in Figure 2.5. By storing the acquired echos depending on the applied phase encoding gradient, a two dimensional k -space is filled.

The phase-encoding gradients also allow so a practical explanation for the properties of k -space. Higher phase-encoding gradients result in more dephasing and thus lower signal intensity. Phase-encoding gradients lead to signals with low amplitude, highlighting only the structures with a substantial amount of intensity difference, such as they occur at edges. The obtained k -space can be transformed by inverse Fourier Transform to a spatially localized signal, resulting in an image.

The measured signal, considering the influence of all gradients $G_x t \gamma$, $G_y t \gamma$ and $G_z t \gamma$, equals to the original signal distribution on the spatial domain $\rho(x, y, z)$ multiplied by a sinusoidal function with frequencies

$$(k_x, k_y, k_z) = (G_x t \gamma, G_y t \gamma, G_z t \gamma). \quad (2.12)$$

The measured signal $m(k_x, k_y, k_z)$, summed up over the entire imaging area in the receiver coils is then given as

$$\begin{aligned} m(k_x, k_y, k_z) &= \int_x \int_y \int_z \rho(x, y, z) (\cos(k_x x + k_y y + k_z z) \\ &\quad + i \sin(k_x x + k_y y + k_z z)) dx dy dz \\ &= \int_x \int_y \int_z \rho(x, y, z) e^{-i2\pi(k_x x + k_y y + k_z z)} dx dy dz \end{aligned} \quad (2.13)$$

It is typically written in its vector form as

$$m(\mathbf{k}) = \int \rho(\mathbf{r}) e^{-i2\pi(\mathbf{k}^T \mathbf{r})} d\mathbf{r}, \quad (2.14)$$

with $\mathbf{k} = (k_x, k_y, k_z)$ and $\mathbf{r} = (x, y, z)$. Besides Cartesian sampling of k -space, illustrated in Figure 2.6(a), the read-out may follow different paths such as radial in Figure 2.6(b) or spiral in Figure 2.6(c). In general, non-Cartesian trajectories offer higher flexibility and denser sampling in the center, but come with the drawback of a computational intensive gridding step in the reconstruction, i.e. the interpolation to a Cartesian grid.

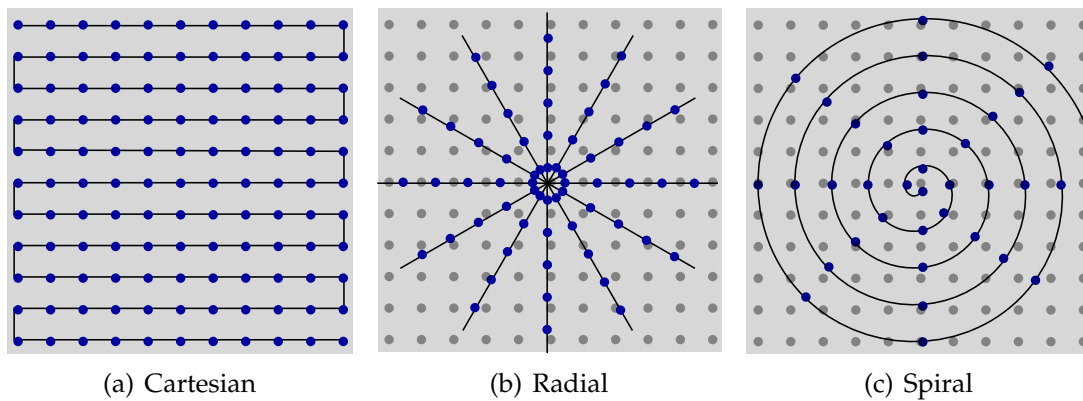


Figure 2.6: Different k -space sampling trajectories: (a) Sequential Cartesian, (b) radial and (c) spiral sampling shown with the corresponding grid.

Method	TOF	mp-bSSFP	PCI
Sequence Type	Spoiled GRE	bSSFP	Spoiled GRE
Inherent Contrast	T_1	T_2/T_1	Spin-density
Contrast mechanism	Inflow during acquisition	Inflow between inversion/acquisition	Velocity translated into phase
Flip angle	50° (2-D), 20° (3-D)	$50-90^\circ$	20° (2-D), 10° (3-D)
TR	20-25ms	3-4ms	15ms

Table 2.2: The properties of the investigated nceMRA methods in different categories are analysed.

2.2 Non-contrast-enhanced MRA Methods

In contrary to most MR examinations, where measures are taken to limit the influence of blood flow-induced artefacts, nceMRA methods exploit the movement of blood to generate vascular contrast.

The contrast mechanisms for commonly used techniques such as Time of Flight (TOF), magnetization-prepared balanced steady state free precession (mp-bSSFP) and velocity-encoded PCI are described in the following section. An overview over the most important sequence parameters is given in Table 2.2.

The dynamic behaviour of blood flow over the cardiac cycle, especially the pulsation of arterial blood flow, has to be considered for some angiographic examinations. Either only data acquired during specific periods of the cardiac cycle are combined to ensure a static and motion-free image, or the dynamics are resolved using segmented acquisition, where separate k -space data sets are sampled for different phases over multiple heart beats. The synchronisation of the acquisition to the patient-specific cardiac cycle is typically done using electrocardiography (ECG) or pulse triggering.

2.2.1 Time of Flight

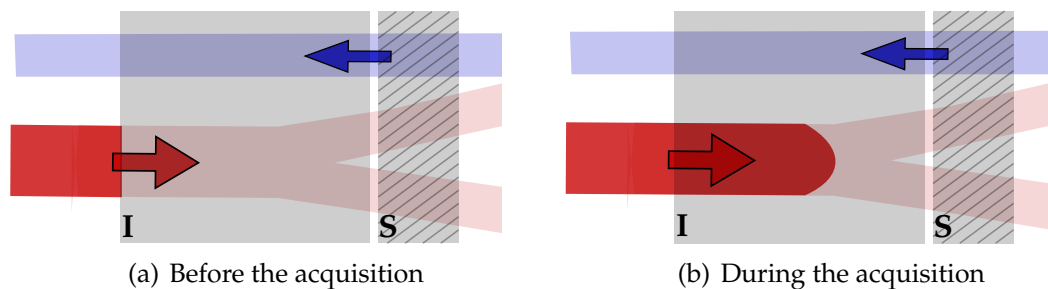


Figure 2.7: The mechanism of flow-related enhancement, basis for the Time-of-Flight contrast is illustrated with a model containing a vein (blue) and an artery (red). The imaging and the saturation slab are pictured in grey and shaded grey, respectively. (a) The contrast situation before the inflow of unsaturated spins is shown, both arterial and venous blood as well as the static tissue is suppressed. (b) The inflowing arterial blood (red) leads to contrast generation, while the static tissue and the venous blood are still suppressed.

In TOF imaging, vascular contrast relies on flow-related enhancement [Whea 12]. This concept describes signal gain in the imaging plane originating from the inflow of blood. It is used in combination with gradient echo sequences with short TR. By application of multiple RF pulses, e.g. in a continuous 3-D acquisition, static tissues are saturated and low signal saturation is obtained. The inflowing spins, illustrated with arrows in Figure 2.7, are less influenced by the repeated pulses. Their longitudinal magnetization, as a consequence, generates high signal intensity when affected by RF pulses [Carr 12]. Relevant parameters for the balance of background suppression and flow-enhancement are the TR, the flip angle and the slice thickness as well as the vessel orientation. The typically short TR and high flip angles assure sufficient background suppression. The saturation of moving spins is scaled by their time within the imaging plane. Thus, ideal contrast can be obtained by positioning imaging planes orthogonal to vessels, for high velocities, and for rather thin slices. To ensure that high signal is exclusively obtained from arterial vessels, the venous inflow signal can be suppressed by adding a slice-selective distal saturation band, illustrated by the hatched area in Figure 2.7. TOF is used in both 2-D and 3-D, while for 3-D the stronger saturation of moving spins due to the thicker slab typically leads to the use of smaller flip angles of 10° - 20° and the use of special shaped tilted optimized non-saturating excitation (TONE) pulses [Atki 94, Kim 12b]. Main applications of TOF are 3-D cranial and carotid imaging as well as 2-D peripheral MRA.

2.2.2 Magnetization Prepared Balanced Steady State Free Precession

The inherent $\frac{T_2}{T_1}$ contrast of bSSFP sequences is well suited for vascular contrast as it tends to highlight blood and suppress most surrounding tissues. Vascular, and specifically arterial contrast can be further enhanced using preparation pulses

inverting the magnetization of the tissue in the imaging region. Imaging after the inversion time (TI), chosen such that the relaxing inverted magnetization reaches values close to zero, results in enhanced contrast of the fresh blood, which was not influenced by the inversion pulse. The inversion slab is typically chosen larger than the imaging plane to ensure inversion of inflowing venous blood and thus uniquely arterial contrast [Kato 04]. The mechanism is illustrated in Figure 2.8(a) for a renal artery acquisition after an inversion pulse and in Figure 2.8(b) at the time of TI. The longitudinal magnetization is depicted in Figure 2.8c.

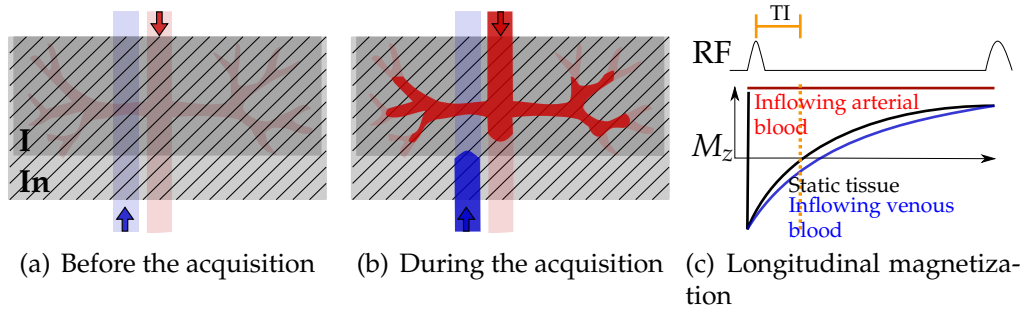


Figure 2.8: The contrast generation for inversion recovery balanced steady-state free precession sequences (bSSFP) is illustrated. (a-b) The renal vasculature is shown with both arteries and veins as well as the imaging slab (I) and the inversion slab (In). The magnetization of static tissues, veins and arteries is inverted at the start of the inversion time TI. After TI, the contrast differences between static tissue and venous blood and the arterial blood are visible. (c) The corresponding curves for the longitudinal magnetization after the inversion pulse allow for the differentiation between the tissues and arteries of interest.

2.2.3 Velocity Encoded Phase Contrast Imaging

Velocity-encoded Phase Contrast Imaging (PCI) relies on bipolar gradients, which are able to map velocity of moving magnetization to phase during the MRI acquisition [Mark 11]. Figure 2.9 illustrates the effect of an idealized bipolar gradient, consisting of a de- and a re-phasing lobe, on static and moving spins respectively. While the phase is cancelled out for static spins after the second lobe, moving spins gain a phase shift.

Sensitivity in arbitrary directions is achieved by repeating the acquisition with different bipolar gradient settings. In a typical experiment, sensitive to the velocities in three orthogonal directions, bipolar gradients are added to the slice encoding, the read and the phase-encoding direction in subsequent acquisitions. The mechanism is illustrated in the following assuming a bipolar gradient field $\mathbf{B}_G(\mathbf{r}, t)$ along the x -direction with

$$\mathbf{B}_G(\mathbf{r}, t) = \begin{pmatrix} xG(t) \\ 0 \\ 0 \end{pmatrix}. \quad (2.15)$$

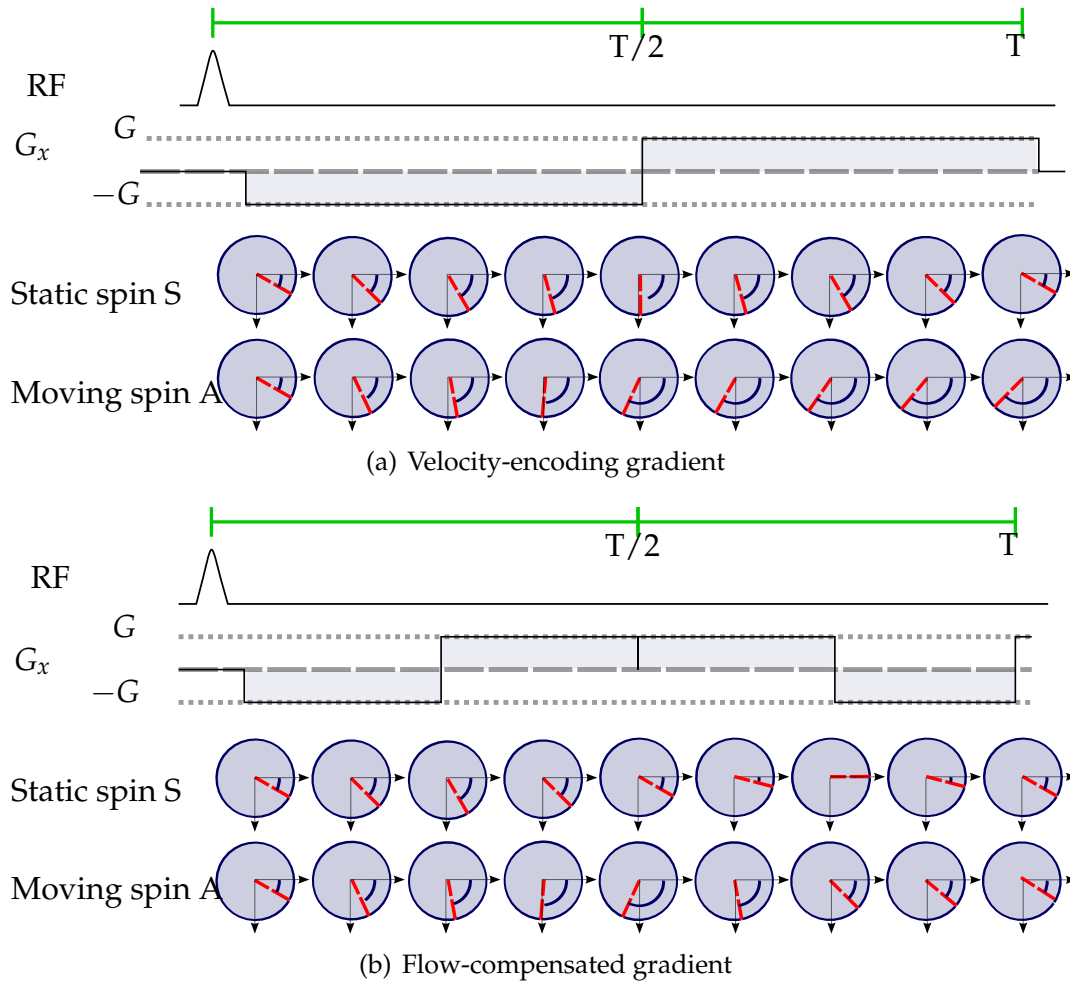


Figure 2.9: Both the velocity-encoding and flow-compensated gradients used for PCI acquisition and their effects on a static spin S and a moving spin A are shown. (a) The bipolar velocity-encoded gradient, consisting of two slopes with equal time $T/2$ and magnitude G but inverse polarity, lead to a different phase evolution for static and moving spins. (b) The flow-compensated gradient, consisting of three slopes, does not affect the phase of the moving or static spins.

The accumulated phase at the end of an acquisition interval $[0, T]$ is calculated by

$$\phi(x, t) = \int_0^T (\gamma B_0 + \gamma x(t)G(t)) dt, \quad (2.16)$$

the total field regarding the x -direction including the bipolar linear gradient equals

$$B(x, t) = B_0(x, t) + B_G(x, t). \quad (2.17)$$

Assuming constant velocity v , the position $x(t)$ of a magnetization moving along x -direction is obtained as $x(t) = x_0 + vt$. Thus, a linear dependence of the phase of the velocity v becomes evident:

$$\phi(x, t) = \int_0^T (\gamma B_0 + \gamma (x_0 + vt)G(t)) dt = \gamma B_0 T - v \gamma G (T/2)^2. \quad (2.18)$$

To compensate for phase effects unrelated to flow such as field inhomogeneities, an additional velocity-compensated reference acquisition using a flow-compensated gradient is required. The flow-compensated gradient compensates for the phase shift as depicted in Figure 2.9. For typical three-directional velocity maps, either reference acquisitions for each encoding, or a reference used for all three encodings are used. The latter is known as the 4-point encoding scheme [Pelc 91]. To obtain absolute velocities, encoded in phase shifts between $-\pi$ and $+\pi$, the encoding velocity ν is fixed to the highest expected velocity. If the choice of ν does not fit the flow dynamics within the imaging slab, either aliasing effects occur or a limited velocity resolution can be observed. Aliasing results from phase wrapping of velocities outside the encoded range $[-\nu, +\nu]$.

2.3 Summary Conclusions

The basic mechanisms used for MRI have been detailed. This includes an introduction of the spin and precession effects exploited for MRI, as well as echo generation principles and k -space localization techniques. Furthermore, the acquisition techniques for non-contrast-enhanced MRA, which were used to generate the data in this thesis, have been introduced.

Compressed Sensing MRI Reconstruction

3.1 MRI Reconstruction: Signal Equation to Discrete Finite Sampling	27
3.2 Parallel MRI and Extensions to Spatio-Temporal Correlations	33
3.3 Compressed Sensing in MRI	38
3.4 Parallel MRI Reconstruction in Compressed Sensing	41
3.5 Summary and Conclusions	44

The duration of an MRI examination for a given region of interest depends on the time required to acquire a certain portion of k -space samples and on the total number of sampled k -space points. Technical possibilities to accelerate the acquisition using hardware or sequence optimizations are limited by physical and physiological constraints [Chro01]. Further acceleration can be achieved by acquiring a lower amount of k -space samples and by using reconstruction methods that restore the missing information. Two families of techniques to reconstruct MR images from sub-sampled k -space data, parallel MRI (pMRI) and Compressed Sensing (CS), were introduced.

This chapter first introduces the influence of sampling for the MRI. In the second part, pMRI reconstruction is formulated as a linear problem. Third, the basic principles of CS and their application within the context of MRI are introduced. Finally, in the forth section, both methods are combined, relevant state of the art is reviewed and the problem formulation used within this thesis is introduced.

3.1 MRI Reconstruction: Signal Equation to Discrete Finite Sampling

The k -space signal $m(\mathbf{k})$ of a 3-D object collected with three orthogonal gradients within an MRI measurement, as described in detail in section 2.1.3 and Eq. (2.14), is given by the following expression

$$m(\mathbf{k}) = \int \rho(\mathbf{r}) e^{-i2\pi(\mathbf{k}^T \mathbf{r})} d\mathbf{r}. \quad (3.1)$$

where $\mathbf{k}, \mathbf{r} \in \mathbb{R}^3$ denote the position in k -space and in the image domain, respectively. Thereby $\rho(\mathbf{r})$ stands for the spin density of the object. Relaxation effects are

neglected in the given formulas.

An inverse Fourier Transform is employed to obtain $\rho(\mathbf{r})$ from the k -space signal:

$$\rho(\mathbf{r}) = \int m(\mathbf{k}) e^{i2\pi(\mathbf{k}^T \mathbf{r})} d\mathbf{k} = \mathcal{F}^{-1}(m(\mathbf{k})). \quad (3.2)$$

The sampling in MRI is discrete and finite, rather than continuous and infinite. Therefore, the basic notation of the discrete formulation used throughout this thesis will be introduced. Furthermore, the discrete sampling with the associated problem of aliasing and the finite sampling and its implications for the image resolution will be detailed in the following subsections.

3.1.1 Discrete Formulation

The basic discrete formulation of the considered reconstruction approach will be introduced here. The volume of interest is discretized in all spatial dimensions. The total number of volume elements N equals $N = N_x \cdot N_y \cdot N_z$. The volume elements are indexed by $\iota_x \in \{1, \dots, N_x\}$, $\iota_y \in \{1, \dots, N_y\}$ and $\iota_z \in \{1, \dots, N_z\}$ for the three spatial dimensions. An index $\iota \in \{1, \dots, N\}$ is introduced to refer to all N voxels, such that ρ_ι represents the spin density at the ι 'th voxel. The entire discretized spin density within the volume of interest may be written as

$$\rho = \begin{pmatrix} \rho_1 \\ \vdots \\ \rho_N \end{pmatrix}. \quad (3.3)$$

In the following, the emerging problem will be formulated using matrix-vector notation wherever appropriate. Therefore, vectors are formed by concatenating data from different dimensions which requires precise definitions of the indexing system within vectors and matrices. In principle, the ι th element of vector $\mathbf{x} \in \mathbb{C}^N$ will be addressed by x_ι or equivalently by $(\mathbf{x})_\iota$. For the element in the κ th row and ι th column of matrix $\mathbf{E} \in \mathbb{C}^{N_k \times N}$ the notation $e_{\kappa, \iota}$ or $(\mathbf{E})_{\kappa, \iota}$ will be used.

But to better illustrate the used data elements for concatenated vectors with different dimensions, the elements will also be addressed by the indices of the individual dimensions instead of the global vector index. For a vector $\mathbf{m} \in \mathbb{C}^{N_\gamma N_k}$, containing N_γ vectors with length N_k , the element $m_{(\gamma, \kappa)}$ corresponds to the element $m_{(\gamma-1)N_k + \kappa}$ with index $(\gamma-1)N_k + \kappa$ in the global index notation. The same applies for matrices, where either one or multiple dimensions are concatenated. For a matrix $\mathbf{E} \in \mathbb{C}^{N_\gamma N_k \times N}$ where $\gamma \in \{1, \dots, N_\gamma\}$, $\kappa \in \{1, \dots, N_k\}$ and $\iota \in \{1, \dots, N\}$, the element in the row corresponding to γ and κ and in column ι is addressed by $e_{(\gamma, \kappa), \iota}$.

The mapping for the frequently used spatial dimensions is described as an example in the following. The arrangement of the coefficients is described by the mappings \mathcal{M} and \mathcal{M}^{-1} as

$$\mathcal{M} : (\iota_x, \iota_y, \iota_z) \rightarrow \iota \text{ with } \iota = \iota_z N_x N_y + \iota_y N_y + \iota_x \text{ and} \quad (3.4)$$

$$\begin{aligned} \mathcal{M}^{-1} : \iota &\rightarrow (\iota_x, \iota_y, \iota_z) \text{ with } \iota_z = \text{mod}(\iota, N_x N_y) \\ \iota_y &= \text{mod}((\iota - N_x N_y), N_y) \text{ and } \iota_x = \iota - N_x N_y - \iota_y N_y. \end{aligned} \quad (3.5)$$

The spatial position of voxel ι , assuming a spacing of $(\Delta_x, \Delta_y, \Delta_z)$, equals $\mathbf{r}_\iota = (\iota_x \Delta_x, \iota_y \Delta_y, \iota_z \Delta_z)$. The size of the volume of interest equals to $N_x \Delta_x \cdot N_y \Delta_y \cdot N_z \Delta_z$, which is referred to as the Field of View (FOV).

The k -space is discretely sampled, the samples are indexed by $\kappa_x \in \{1, \dots, N_{k_x}\}$, $\kappa_y \in \{1, \dots, N_{k_y}\}$ and $\kappa_z \in \{1, \dots, N_{k_z}\}$, resulting in a total of $N_k = N_{k_x} \cdot N_{k_y} \cdot N_{k_z}$ sampling points. An index $\kappa \in \{1, \dots, N_k\}$ is introduced to refer to all N_k voxels, such that k_κ represents the frequency at the ' κ 'th voxel.

The mapping is calculated accordingly by

$$\mathcal{M} : (\kappa_x, \kappa_y, \kappa_z) \rightarrow \kappa \text{ with } \kappa = \kappa_z N_{k_x} N_{k_y} + \kappa_y N_{k_y} + \kappa_x \text{ and} \quad (3.6)$$

$$\begin{aligned} \mathcal{M}^{-1} : \kappa &\rightarrow (\kappa_x, \kappa_y, \kappa_z) \text{ with } \kappa_z = \text{mod}(\kappa, N_{k_x} N_{k_y}) \\ \kappa_y &= \text{mod}((\kappa - N_{k_x} N_{k_y}), N_{k_y}) \text{ and } \kappa_x = \kappa - N_{k_x} N_{k_y} - \kappa_y N_{k_y}. \end{aligned} \quad (3.7)$$

The spatial position of k -space point κ , assuming a spacing of $(\Delta k_x, \Delta k_y, \Delta k_z)$, equals to $\mathbf{k}_\kappa = (\kappa_x \Delta k_x, \kappa_y \Delta k_y, \kappa_z \Delta k_z)$.

For the Cartesian case, the dimensions will be used such that k_x corresponds to the read-out or frequency encoding, while k_y and k_z address the phase-encoding directions. Sub-sampling in the seek of time reduction is thus meaningful only by reducing the number of phase encoding steps to a lower number, i.e. $N'_{k_y} N'_{k_z} < N_{k_y} N_{k_z}$.

The presented notation is used in the following to introduce discrete finite sampling. For this purpose, a 1-D signal $m(k_x)$ of a 1-D object $\hat{\rho}(x)$ will be regarded. A practical example is a 1-D line through a 2-D object such as a 2-D TOF slice through the tibia, featuring schematically the anterior, posterior tibial and fibular arteries. This model is illustrated in Figure 3.1. For the 1-D case Eqs. (3.1) - (3.2) equal

$$m(k_x) = \int \rho(x) e^{-i2\pi(k_x x)} dx = \mathcal{F}(\rho(x)) \text{ and} \quad (3.8)$$

$$\rho(x) = \int m(k_x) e^{i2\pi(k_x x)} dk_x = \mathcal{F}^{-1}(m(k_x)). \quad (3.9)$$

Discrete and finite sampling in MRI correspond to a multiplication of the continuous infinite measured signal $m(k_x)$ with the sampling function $u_\infty(k_x)$ and a windowing function $w(k_x)$:

$$\underbrace{\hat{m}(k_x)}_{\text{Discrete finite signal}} = \underbrace{m(k_x)}_{\text{Continuous infinite signal}} \cdot \underbrace{u_\infty(k_x)}_{\text{Sampling}} \cdot \underbrace{w(k_x)}_{\text{Windowing}} = \underbrace{m_\infty(k_x)}_{\text{Discrete signal}} \cdot w(k_x). \quad (3.10)$$

The use of the sampling function is detailed in section 3.1.2, the windowing function in section 3.1.3.

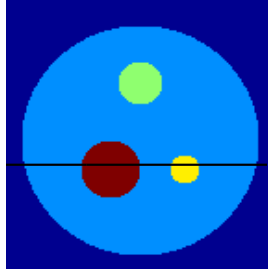


Figure 3.1: Line through a simulated 2-D phantom to illustrate the concepts for aliasing and resolution.

3.1.2 Discrete Sampling and Aliasing

The sampling function $u_\infty(k_x)$, also referred to as comb function, is composed from a sequence of infinite but uniformly distributed Dirac delta functions:

$$u_\infty(k_x) = \Delta k_x \sum_{\kappa=-\infty}^{+\infty} \delta(k_x - \kappa \Delta k_x). \quad (3.11)$$

This allows to represent equidistant Cartesian sampling with spacing Δk_x [Haac 99] where the discrete position equals $k_x = \kappa \Delta k_x$. The sampled discrete signal $\hat{m}_\infty(k_x)$ is obtained by multiplying the signal with the sampling function:

$$\hat{m}_\infty(k_x) = m(k_x) \cdot u_\infty(k_x) = \Delta k_x \sum_{\kappa=-\infty}^{+\infty} m(\kappa \Delta k_x) \delta(k_x - \kappa \Delta k_x). \quad (3.12)$$

Included into Eq. (3.9), the corresponding spin density is obtained as

$$\hat{\rho}_\infty(x) = \int_{-\infty}^{\infty} \hat{m}_\infty(k_x) e^{i2\pi(k_x x)} dk_x \quad (3.13)$$

$$= \int_{-\infty}^{\infty} \left[\Delta k_x \sum_{\kappa=-\infty}^{+\infty} m(\kappa \Delta k_x) \delta(k_x - \kappa \Delta k_x) \right] e^{i2\pi(k_x x)} dk_x \quad (3.14)$$

$$= \Delta k_x \sum_{\kappa=-\infty}^{+\infty} m(\kappa \Delta k_x) e^{i2\pi \kappa \Delta k_x x}. \quad (3.15)$$

The Fourier relation in Eqs. (3.8-3.9), and application of the convolution theorem yields a representation of the infinite spin density as a convolution of the spin density with the inverse Fourier transform of the sampling function $U(x)$:

$$\begin{aligned} \hat{\rho}_\infty(x) &= \mathcal{F}^{-1}(\hat{m}_\infty(k_x)) = \mathcal{F}^{-1}(m(k_x) \cdot u_\infty(k_x)) \\ &= \mathcal{F}^{-1}(m(k_x)) * \mathcal{F}^{-1}(u_\infty(k_x)) \\ &= \rho(x) * \mathcal{F}^{-1}(u_\infty(k_x)). \end{aligned} \quad (3.16)$$

$U(x)$ equals $U(x) = \mathcal{F}^{-1}(u_\infty(k_x))$ and corresponds to a comb function with $U(x) = \sum_{l_x=-\infty}^{\infty} \delta(x - \frac{l_x}{\Delta k_x})$. Finally, the sampled spin density $\hat{\rho}_\infty(x)$ equals

$$\hat{\rho}_\infty(x) = \sum_{l_x=-\infty}^{\infty} \rho(x - \frac{l_x}{\Delta k_x}). \quad (3.17)$$

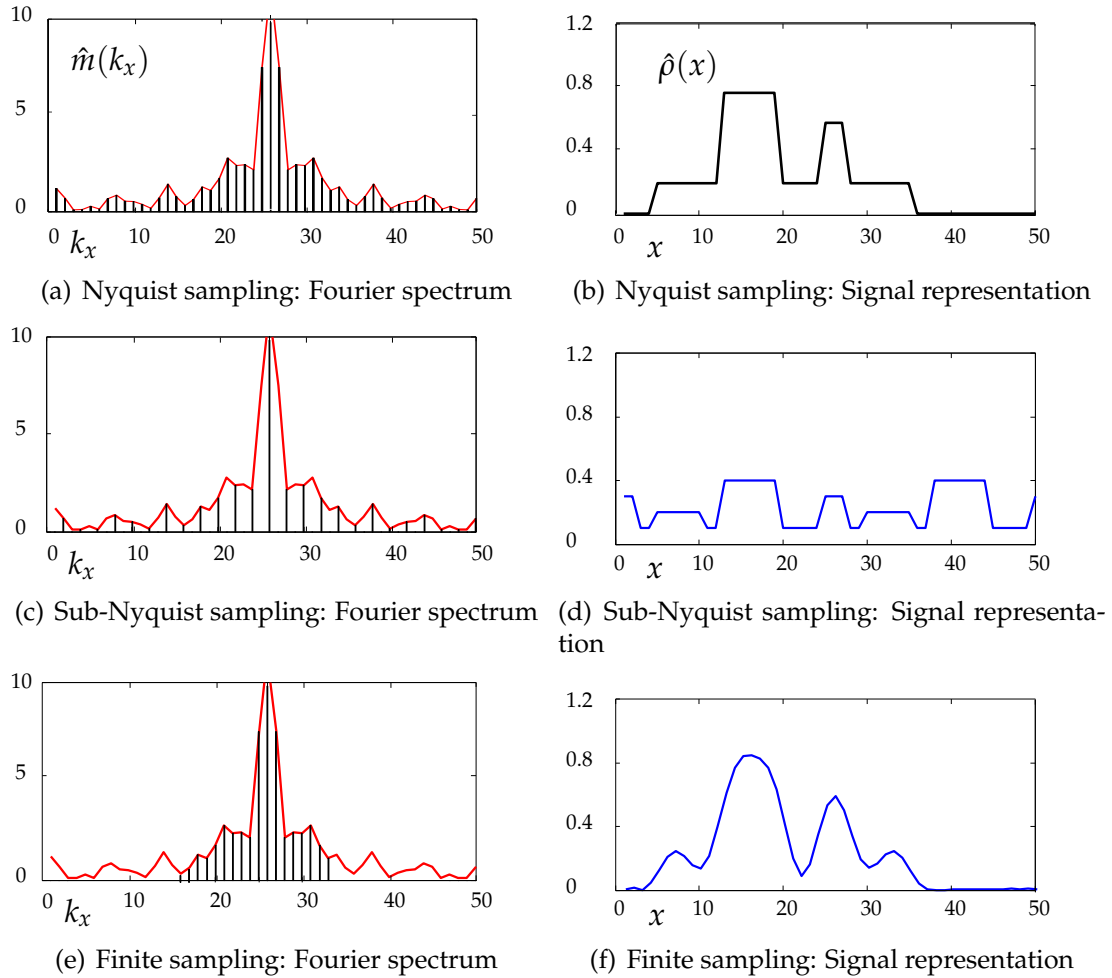


Figure 3.2: The concepts of aliasing and resolution are illustrated on a line through a simulated 2-D phantom. The Fourier Spectrum and the corresponding image domain representation is shown for three cases: (a-b) Nyquist sampling, (c-d) sub-Nyquist sampling and (d-e) finite sampling.

This illustrates the periodicity resulting from the convolution in Eq. (3.16). The infinite spin density equals an infinite series with a displacement of $\frac{1}{\Delta k_x}$, referred to as the Field of View (FOV).

An important derivation connecting the sampling frequency and the FOV is obtained from Eq. (3.17): An unique representation of the signal may only be chosen if adjacent copies of size $\frac{1}{\Delta k_x}$ do not overlap, as overlapping would lead to aliasing artefacts. Be A_x the extent of the object in x -direction, the condition can thus be formulated as

$$\frac{1}{\Delta k_x} > A_x \Leftrightarrow \Delta k_x < \frac{1}{A_x}, \quad (3.18)$$

meaning that the k -space must be sampled denser than the inverse of the object size. This relation is called the Nyquist sampling criteria. A k -space sampling that fulfils relation Eq. (3.18) is referred to as Nyquist sampling. If the Nyquist criteria is violated using sub-Nyquist sampling, the adjacent copies overlap and aliasing occurs. This effect is demonstrated in Figure 3.2(c)-3.2(d). The spacing between

adjacent samples is increased to $3\Delta k$ in the Fourier domain as illustrated on the left side, which results in overlapping aliased copies of the object in the image space on the right side. This effect is further illustrated for a PCI image in Figure 3.3(b).

3.1.3 Finite Sampling and Resolution

Since infinite sampling is not feasible given the temporal restrictions, the number of sampled k -space points in k_x direction is limited to N_{k_x} . This is modelled by multiplying the sampling function with a windowing function [Haac 99]

$$w(k_x) = \text{rect}\left(\frac{k_x + 1/2\Delta k_x}{W_x}\right) \text{ of width } W_x = N_{k_x}\Delta k_x. \quad (3.19)$$

This leads to the relation

$$\hat{m}(k_x) = \hat{m}_\infty \cdot w(k_x) = \Delta k_x \sum_{\kappa=-N_{k_x}/2}^{N_{k_x}/2} m(\kappa\Delta k_x)\delta(k_x - \kappa\Delta k_x). \quad (3.20)$$

Finally, the reconstructed spin density equals

$$\hat{\rho}(x) = \int_{-\infty}^{\infty} \hat{m}(k_x)e^{i2\pi(k_x x)} dk_x \quad (3.21)$$

$$= \int_{-\infty}^{\infty} \Delta k_x \sum_{\kappa=-N_{k_x}/2}^{N_{k_x}/2} \hat{m}(\kappa\Delta k_x)\delta(k_x - \kappa\Delta k_x)e^{i2\pi(k_x x)} dk_x \quad (3.22)$$

$$= \Delta k_x \sum_{\kappa=-N_{k_x}/2}^{N_{k_x}/2} \hat{m}(\kappa\Delta k_x)e^{i2\pi(\kappa\Delta k_x x)}. \quad (3.23)$$

The multiplication of the data with the windowing function means that higher frequencies are omitted, and results in a low-pass filtering of the image. The resolution of the image is thus influenced by the width of the windowing function. An example for the resolution loss is illustrated in Figure 3.2(e)-3.2(f). The Fourier spectrum sampled with spacing Δk_x but half the sampling width $W/2$ is shown on the left side, resulting in a lower resolution in the image domain on the right side. Using the convolution theorem, yields

$$\hat{\rho}(x) = \mathcal{F}^{-1}(m(k_x) \cdot u_\infty(k_x) \cdot w(k_x)) \quad (3.24)$$

$$= \mathcal{F}^{-1}(m(k_x)) * \mathcal{F}^{-1}(u_\infty(k_x)) * \mathcal{F}^{-1}(w(k_x)) \quad (3.25)$$

$$= \rho(x) * U(x) * W(x), \quad (3.26)$$

where $W(x)$ is the inverse Fourier transform of the windowing function $w(k_x)$. It equals

$$W(x) = (N_{k_x}\Delta k_x \text{sinc}(\pi N_{k_x}\Delta k_x x)e^{i2\pi(x\Delta k_x)}) \quad (3.27)$$

and is also used in the calculation of the spatial point spread function (PSF), which describes the blurring introduced by the finite sampling.

Not only the sampling of $\hat{m}(k_x)$ is finite and discrete, but also the resulting spin density $\rho(x)$. It is discretized with spacing Δx and the spatial width corresponding to the FOV. The discrete coordinates equal $x = \iota_x \Delta x$ for $\iota_x = [-N_x/2, +N_x/2]$. Finally, this leads to the following representation for the reconstructed spin density:

$$\hat{\rho}(x) = \Delta x \sum_{\iota_x = -N_x/2}^{N_x/2} \hat{\rho}(\iota_x \Delta x) \delta(x - \iota_x \Delta x). \quad (3.28)$$

The spacing Δx equals $\frac{FOV}{N_x}$ and is called the voxel size. It can be shown that $\hat{m}(\kappa_x \Delta k_x)$ and $\hat{\rho}(\iota_x \Delta x)$ form a discrete Fourier pair if the assumption that $N_{k_x} = N_x$ holds [Haac 99]:

$$\hat{\rho}(x) = \Delta k_x \sum_{\kappa_x = -N_{k_x}/2}^{N_{k_x}/2} \hat{m}(\kappa_x \Delta k_x) e^{i2\pi(\kappa_x \Delta k_x \iota_x \Delta x)} \quad \text{and} \quad (3.29)$$

$$\hat{m}(k_x) = \Delta x \sum_{\iota_x = -N_x/2}^{N_x/2} \hat{\rho}(\iota_x \Delta x) e^{-i2\pi(\kappa_x \Delta k_x \iota_x \Delta x)}. \quad (3.30)$$

$$(3.31)$$

This principle can be applied analogously for the other dimensions k_y/y and k_z/z . Both discrete and finite sampling, and their effects, aliasing and limited resolution are illustrated for the 2-D case in Figure 3.3.

3.2 Parallel MRI and Extensions to Spatio-Temporal Correlations

For parallel MRI (pMRI), k -space data is acquired simultaneously using multiple receiver coils placed around the object of interest. Started with Four-element phase arrays [Roem 90], modern coil setups can include 64 channels and more [Keil 13]. Every coil receives the signal with its own spatial sensitivity and thus generates additional encoding information. An example of an aortic PCI scan using nine coils is illustrated in Figure 3.4. This additional information can be used in two ways, either to enhance the image quality for a fully sampled acquisition or to replace time intensive phase-encoding gradient steps by utilizing the spatial information provided through the coil sensitivities.

3.2.1 Spatial sensitivity information

For pMRI, the signal equation in Eq. (3.1) is formulated for each coil $\gamma \in \{1, \dots, N_\gamma\}$ and models the spatial coil influence by multiplying the spin density ρ with the sensitivity information $s_\gamma(\mathbf{r})$:

$$m_\gamma(\mathbf{k}) = \int \rho(\mathbf{r}) s_\gamma(\mathbf{r}) e^{i2\pi(\mathbf{k}\mathbf{r})} d\mathbf{r}. \quad (3.32)$$

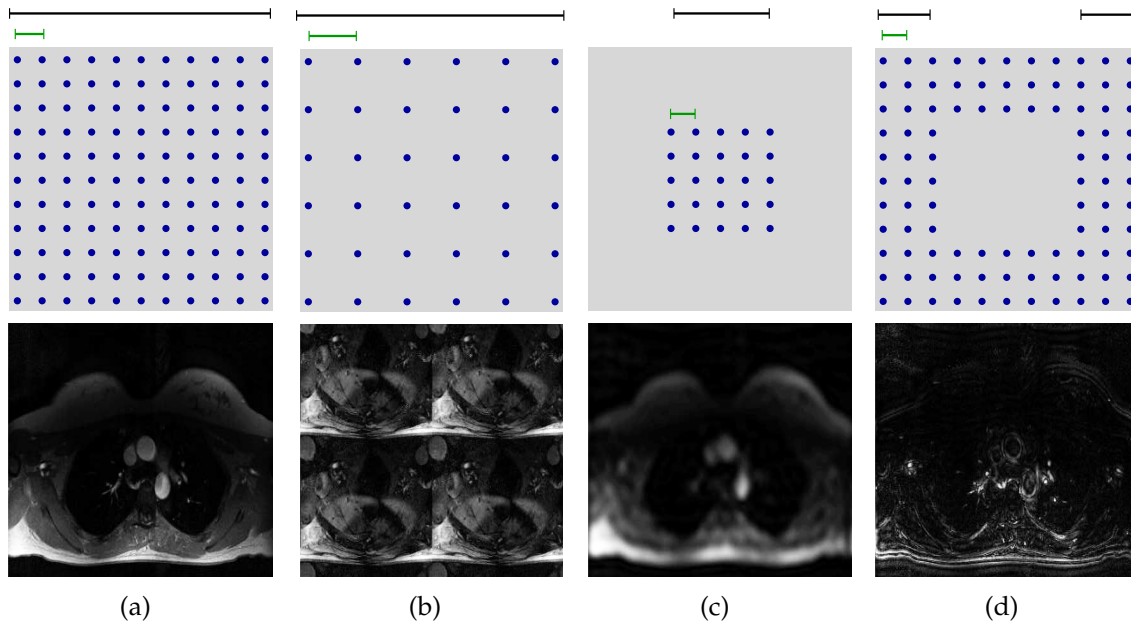


Figure 3.3: The influence of the sampling width $[W_x, W_y]$ and the sampling spacing $\Delta k = [\Delta k_x, \Delta k_y]$ is illustrated in an aortic PCI image. (a) Both the sampling width and the spacing were chosen adapted for the FOV. The resulting image is free of aliasing effects and resolution losses. (b) The sampling spacing was increased by two in both directions to $\Delta k = [2\Delta k_x, 2\Delta k_y]$, keeping the sampling width constant. Significant aliasing is visible in the image space. (c) The original spacing $\Delta k = [\Delta k_x, \Delta k_y]$ was applied, but the sampling width reduced to $[\frac{W_x}{2}, \frac{W_y}{2}]$. A clear loss in resolution becomes visible and the smaller vascular structures are not separable any more. (d) Here, the outer part of k -space was sampled. The result is an image with high contrast at the edges, for example the vessels walls and the back of the patient. The lines above the images indicate the FOV and the spacing in LR direction.

Here, $e_\gamma(\mathbf{k}, \mathbf{r}) = s_\gamma(\mathbf{r})e^{i2\pi(\mathbf{k}^T \mathbf{r})}$ is referred to as the net encoding function, or hybrid encoding [Prue06], containing both coil and gradient encoding.

Reconstruction of multi-coil data is possible by summing up the individual coil images $\rho_\gamma(\mathbf{r})$. Thereby, the Sum of Squares (SoS) technique is superior to linear summation over the coils due to phase cancellation effects with the latter [Roem90]. The final SOS reconstructed image is obtained by

$$\rho(\mathbf{r}) = \mathcal{S}(\mathbf{r}) = \sum_{\gamma=1}^{N_\gamma} (\rho_\gamma(\mathbf{r}))^2. \quad (3.33)$$

More advanced techniques further exploit the spatial sensitivities to compensate for fold over artefacts on account of sub-sampling. Among the first proposed methods was Simultaneous Acquisition of Spatial Harmonics (SMASH) [Sodi97] and derived techniques including AUTO-SMASH and VD-AUTO-SMASH, which generate non-acquired phase-encoding steps directly from combinations of coil-sensitivities. Later, Partially Parallel Imaging With Localized Sensitivities (PILS) was proposed, which assumes basically distinct sensitivities for each coil and combines the image directly using sub-images from each coil based on the idealized

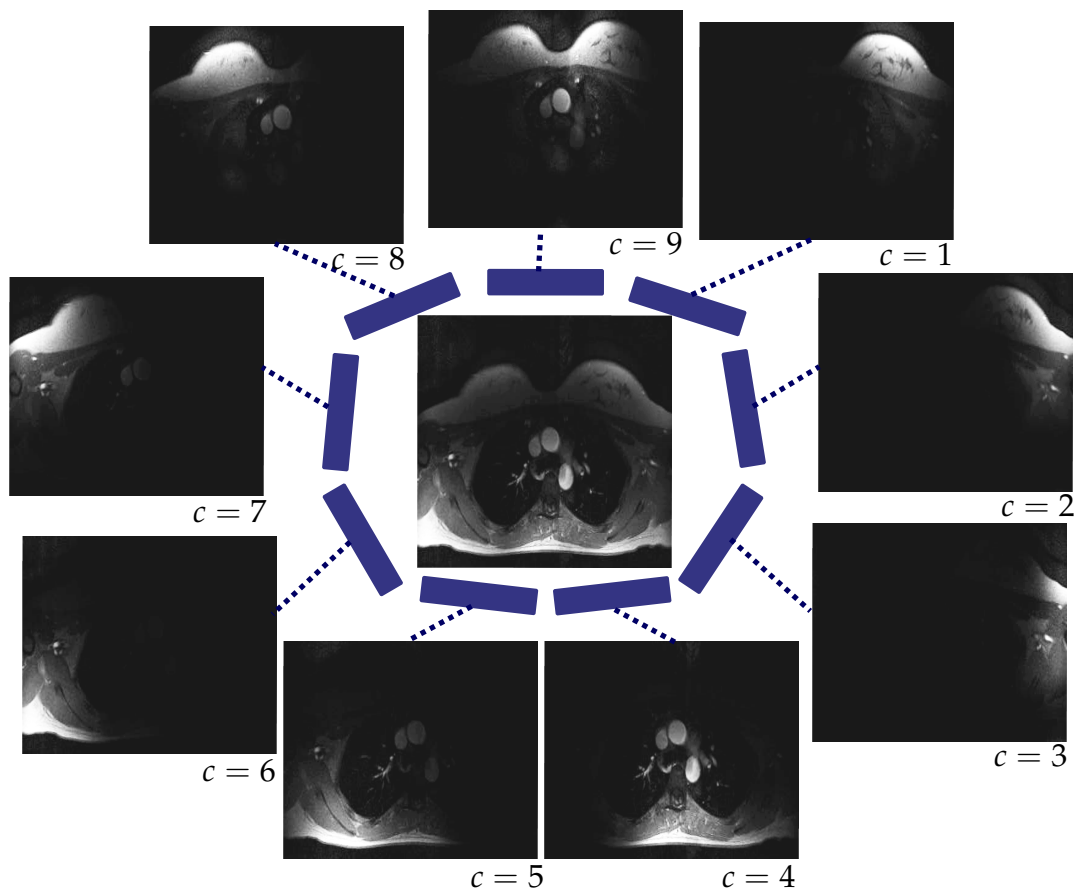


Figure 3.4: A multi-coil setup using 9 channels is illustrated for a 2-D aortic PCI acquisition. Images 1-9 show the single coil images sensitivities of the individual coil elements.

coil setup [Blai 04]. Another image space-based method is Sensitivity Encoding (SENSE) [Prue 99], formulating the signal at each pixel as a linear combination of the individual coil contributions, consisting of the sensitivities and the obtained signal. The final image is obtained by ‘unfolding’ in the image domain. Finally, GeneRALized Autocalibrating Partially Parallel Acquisitions (GRAPPA) [Gris 02] is a k -space based technique, using auto-calibrating signal and weights to interpolate missing k -space samples. The technique underlying SENSE will be further explained in detail, as it was included in the reconstruction developments of this thesis. See the reviews [Blai 04, Hoge 05] for more details about further pMRI techniques.

In addition to acceleration techniques that exploit spatial correlations, the inclusion of spatio-temporal correlations has been investigated for dynamic MRI applications, such as cardiac, blood flow or respiratory phase imaging. Those proposed include methods for single coil imaging [Vaal 93, Doyl 95] and techniques for multiple coils such as kt-BLAST and kt-SENSE [Tsao 05], UNFOLD [Mado 04], PEAK-GRAPPA [Jung 08b] and TSENSE [Kell 01].

While k -space-based methods such as GRAPPA and SMASH do not require explicit knowledge of the coil sensitivities, SENSE and further image-based methods need maps representing the sensitivities of each coil for the reconstruction. The maps are acquired separately for each acquisition as the coil setup and the exact localization of the coils can vary over time. This is commonly done based on a filtered low-frequency reconstruction from the innermost part of k -space. This allows for the estimation of the sensitivities by minimizing the effects of the objects. If these samples are acquired before the actual acquisition, this is referred to as ‘external coil sensitivities’ - if imaging samples are used the term, ‘internal coil sensitivities’ is employed.

3.2.2 SENSE reconstruction as a linear problem

Formulating the encoding 3.32 explicitly as a combination of Fourier coefficients and spatial coil information and using $e_\gamma(\mathbf{k}, \mathbf{r}) = \mathbf{s}_\gamma \mathbf{r} e^{i\pi \mathbf{k} \mathbf{r}}$ yields

$$m_\gamma(\mathbf{k}) = \int \rho(\mathbf{r}) e_\gamma(\mathbf{k}, \mathbf{r}) d\mathbf{r}. \quad (3.34)$$

Formulated for discrete k -space points, the measurement for coil γ at k -space position κ equals $m_{(\gamma, \kappa)}$, the k -space object for coil γ and all voxels is denoted by \mathbf{m}_γ . The entire acquired k -space samples from all coils are written in vector form using \mathbf{m} with

$$\mathbf{m} = \begin{pmatrix} \mathbf{m}_1 \\ \vdots \\ \mathbf{m}_{N_\gamma} \end{pmatrix}. \quad (3.35)$$

Using the discrete encoding $e_{(\gamma, \kappa)}(\mathbf{r}) = e^{i2\pi \mathbf{k}_\kappa \mathbf{r}} s_\gamma(\mathbf{r})$, Eq. (3.34) equals

$$m_{(\gamma, \kappa)} = \int \rho(\mathbf{r}) e_{(\gamma, \kappa)}(\mathbf{r}) d\mathbf{r}. \quad (3.36)$$

Corresponding to this, the reconstruction can be formulated as a linear problem, by expressing each voxel of the image as the linear combination of the measurements using the reconstruction matrix $\mathbf{F}_{l,(\gamma,\kappa)}$ of size $N \times N_\gamma N_k$:

$$\rho_l = \sum_{\gamma,\kappa}^{N_\gamma, N_k} \mathbf{F}_{l,(\gamma,\kappa)} m_{(\gamma,\kappa)}. \quad (3.37)$$

Combining Eqs. (3.32) and (3.37) highlights the relation between encoding and reconstruction:

$$\rho_l = \int \rho(\mathbf{r}) \left(\sum_{\gamma,\kappa}^{N_\gamma, N_k} \mathbf{F}_{l,(\gamma,\kappa)} e_{(\gamma,\kappa)}(\mathbf{r}) \right) d\mathbf{r}. \quad (3.38)$$

The product

$$\sum_{\gamma=1, \kappa=1} \mathbf{F}_{l,(\gamma,\kappa)} e_{(\gamma,\kappa)}(\mathbf{r}_l) \quad (3.39)$$

is referred to as voxel function, as it contains a description of the spatial weighting of the signal for each voxel l . The condition for spatially ideally separated voxels is formulated as a Dirac function centred at \mathbf{r}_l , decreasing the influence of neighbouring voxels:

$$\sum_{\gamma=1, \kappa=1} \mathbf{F}_{l,(\gamma,\kappa)} e_{(\gamma,\kappa)}(\mathbf{r}_l) = \delta_l(\mathbf{r} - \mathbf{r}_l). \quad (3.40)$$

This equation is also known as 'strong reconstruction' [Prue 99]. The encoding matrix $\mathbf{E}_{(\gamma,\kappa),l} \in \mathbb{C}^{N_\gamma N_k \times N}$ is obtained from the encoding function by evaluating $e_{(\gamma,\kappa)}(\mathbf{r})$ on the grid value positions \mathbf{r}_l :

$$\mathbf{E}_{(\gamma,\kappa),l} = e_{(\gamma,\kappa),l} = e_{(\gamma,\kappa)}(\mathbf{r}_l) = e^{i2\pi(\mathbf{k}_\kappa^T \mathbf{r}_l)} s_\gamma(\mathbf{r}_l). \quad (3.41)$$

The entries of the encoding matrix will be referred to as $e_{(\gamma,\kappa),l}$. The relation between the acquired k -space measurements $\mathbf{m} \in \mathbb{C}^{N_\gamma N_k}$ and the reconstructed object $\rho \in \mathbb{C}^N$ for N_γ coils is captured by the linear equation $\mathbf{E}\rho = \mathbf{m}$, formulated as

$$\begin{array}{l} \text{Coil } \gamma = 1 \\ \vdots \\ \text{Coil } \gamma = 2 \\ \vdots \\ \text{Coil } \gamma = N_\gamma \end{array} \left\{ \begin{array}{l} \left(\begin{array}{ccc} e_{(1,1),1} & \cdots & e_{(1,1),N} \\ \vdots & \ddots & \vdots \\ e_{(1,N_k),1} & \cdots & e_{(1,N_k),N} \\ e_{(2,1),1} & \cdots & e_{(2,1),N} \\ \vdots & \ddots & \vdots \\ e_{(2,N_k),1} & \cdots & e_{(2,N_k),N} \\ \vdots & \vdots & \vdots \\ e_{(N_\gamma,1),1} & \cdots & e_{(N_\gamma,1),N} \\ \vdots & \ddots & \vdots \\ e_{(N_\gamma,N_k),1} & \cdots & e_{(N_\gamma,N_k),N} \end{array} \right) \cdot \begin{pmatrix} \rho_1 \\ \vdots \\ \rho_N \end{pmatrix} = \begin{pmatrix} m_{(1,1)} \\ \vdots \\ m_{(1,N_k)} \\ m_{(2,1)} \\ \vdots \\ m_{(2,N_k)} \\ \vdots \\ m_{(N_\gamma,1)} \\ \vdots \\ m_{(N_\gamma,N_k)} \end{pmatrix} \end{array} \right. \begin{array}{l} \left. \begin{array}{l} \gamma = 1 \\ \vdots \\ \gamma = 2 \\ \vdots \\ \gamma = N_\gamma \end{array} \right\} \end{array} \quad (3.42)$$

As a result of Eq. (3.40), the condition for the reconstruction matrix \mathbf{F} for fully spatial unwrapping, termed 'weak reconstruction' equals $\mathbf{F}\mathbf{E} = \mathbf{Id}$.

The solution to the problem depends on the dimensions: If the number of rows in \mathbf{E} , $N_\gamma N_k$, equal the number of columns N , it signifies that the used parallel coils equal the k -space sub sampling factor $\xi = N_k/N$. In this case the equation is invertible, and the Moore-Penrose inverse yields the optimal solution:

$$\rho = \mathbf{F}\mathbf{m} = (\mathbf{E}^H\mathbf{E})^{-1}\mathbf{E}^H\mathbf{m}. \quad (3.43)$$

In the case $N_\gamma N_k < N$, more unknowns than data points are given. Further restrictions, such as noise minimization and SNR optimization can thus be included [Prue 99]. The basic case of full k -space sampling with a single coil ($N_\gamma = 1, N_k = N$) lead to the expected relation $\mathbf{F} = \mathbf{E}^{-1}$.

The reduction of scan time by a factor of ξ comes at the cost of Signal-to-noise-Ratio (SNR). The relation between the SNR of a fully sampled scan (SNR^f) and the SNR of a reduced scan (SNR^r) is indicated by [Prue 99]:

$$\text{SNR}_i^r = \frac{\text{SNR}_i^f}{\sqrt{\xi}g_i} \quad (3.44)$$

. Two sources of SNR loss are identified, the signal reduction which reduces SNR by a factor of $\sqrt{\xi}$ and a reduction by an insufficiently spatially independent coil setup. This geometrical noise amplification is measured by the geometric factor, called g -factor [Prue 99].

3.3 Compressed Sensing in MRI

The theory of *Compressed Sensing* (CS), proposed in the last decade by Candès and Donoho [Cand 08, Dono 06], has been employed in multiple fields and has caused a stir in the field of MRI. Based on the observation that a wide range of signals are compressible, i.e. that they have a sparse representation in a transfer domain, CS suggests that signals can be reconstructed from sub-sampled data. The huge impact in MRI originates from the acceleration possibilities due to long acquisition times, the flexibility of the sampling and the huge range of possible sparsity transforms.

3.3.1 Compressed Sensing

The information content of a signal can often be represented by far less samples than acquired in accordance with the Nyquist criteria. This principle forms the basis of all sorts of compression routines, used for example to reduce the memory footprint of image or video data. A prominent example is the use of the wavelet transform in the JPEG2000 standard. Typically, the data is first acquired at the Nyquist sampling rate and then compressed using sparse representations. The compressed signal is obtained by using only the compressed coefficients in the signal reconstruction. CS aims to sample data at sub-Nyquist rate right from the beginning and to decompress the data into a good object representation afterwards. This inverse approach is illustrated in Figure 3.5.

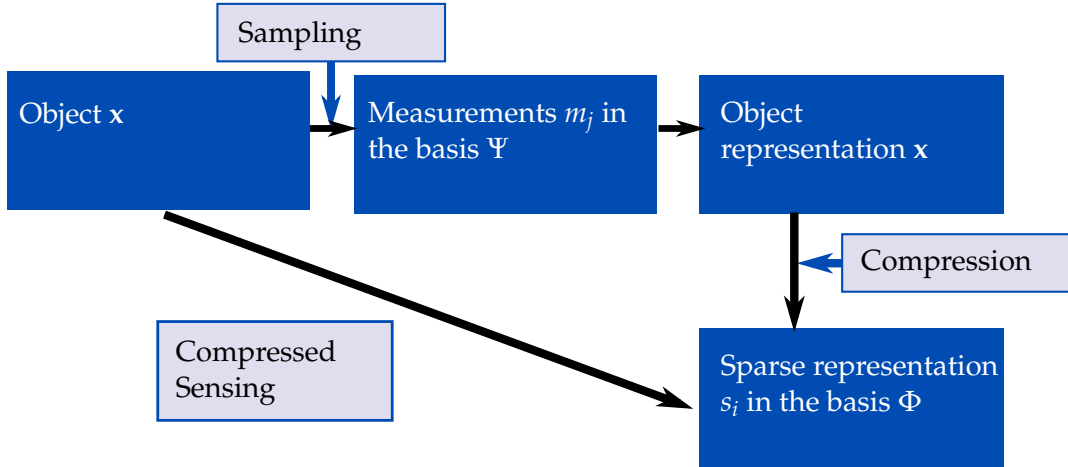


Figure 3.5: Compressed Sensing: Reduced sampling of the object instead of compressing the fully acquired signal

Let $\mathbf{x} \in \mathbf{C}^N$ be the signal of interest, and $\mathbf{m} \in \mathbf{C}^M$ a series of measurements conducted to obtain \mathbf{x} . Here $\Psi = [\psi_1, \dots, \psi_M]$ is an orthogonal basis for the sampling, resulting in $m_j = \langle \mathbf{x}, \psi_j \rangle$. Recovering \mathbf{x} from \mathbf{m} for $M \ll N$ involves mapping the data into a transform domain Φ , where the signal is assumed to have a simpler structure with only few non-zero entries. The orthogonal basis of the transform domain Φ given by $\Phi = [\phi_1, \dots, \phi_N]$ and the signal $\mathbf{x} \in \mathbf{C}^N$ can be written with the coefficients s_i as $\mathbf{x} = \sum_{i=1}^N s_i \phi_i$ for $i \in \{1, \dots, N\}$. If \mathbf{x} can be represented using only S non-zero coefficients out of N , it is called S -sparse in the transform domain Φ . The sparse signal is referred to by \mathbf{x}_S . For real signals, due to noise the coefficients are rather insignificantly small than exactly zero, resulting in $\|\mathbf{x} - \mathbf{x}_S\|_{L_2}^2$ being small as well. Knowledge about the transform Φ facilitates storage of the meaningful information of the signal in a lower number of coefficients. Crucial for the success of the reconstruction is the choice of the sampling basis Ψ . Samples only add information to the reconstruction problem, if they contain measurements from the entire linear space of Φ . An important theorem in this context is the Restricted Isometry Property (RIP) [Sche 11], which helps to formulate a sufficient condition for signal recovery from a sparse signal obtained with a sampling scheme below the Nyquist rate. The isometry constant δ_S of a matrix Φ is defined as the smallest number such that

$$(1 - \delta_S) \|\mathbf{x}\|_{L_2}^2 \leq \|\Phi \mathbf{x}\|_{L_2}^2 \leq (1 + \delta_S) \|\mathbf{x}\|_{L_2}^2. \quad (3.45)$$

One of the central theorems derived from this is the exact recovery of the S -sparse signal \mathbf{x} if the isometry constant can be shown to be smaller than $\sqrt{2} - 1$ [Cand 08]. The mutual coherence $\mu(\Phi, \Psi)$ between the sampling basis Ψ and the sparsity transform basis Φ is calculated as

$$\mu(\Phi, \Psi) = \sqrt{N} \max_{1 \leq i, j \leq N} |\langle \phi_i, \psi_j \rangle| \quad \text{with } \mu(\Phi, \Psi) \in [1, \sqrt{N}]. \quad (3.46)$$

The relation between coherence, sparsity S and the number of required samples M [Cand 08] is given by

$$M \geq C \cdot \mu(\Phi, \Psi)^2 \cdot S \cdot \log(N) \quad (3.47)$$

with a constant C . This illustrates the relation: The higher the incoherence between Φ and Ψ , the lower the number of samples M can be for a given sparsity S . Frequent choices for Ψ are random bases, as they have been shown to be incoherent to other bases.

In addition to the principles of sparsity and incoherence introduced, the third fundamental principle of CS is the choice of the reconstruction algorithm $\mathbf{A} : \mathbf{C}^M \mapsto \mathbf{C}^N$. The recovery problem for \mathbf{x} , sampled with an incoherent measurement system Ψ is under-determined with $N \gg M$:

$$\mathbf{m} = \Psi\mathbf{x}. \quad (3.48)$$

Inclusion of the sparsity transform Φ into the reconstruction problem allows to identify the best solution in terms of sparsity from the infinite number of possible solutions for \mathbf{x} suggested from Eq. (3.48):

$$\min_{\mathbf{x}} \|\Phi\mathbf{x}\|_{L_0}, \text{ subject to } \Psi\mathbf{x} = \mathbf{m}, \quad (3.49)$$

In general, imperfections in the acquisition do not allow $\Psi\mathbf{x} = \mathbf{m}$. Instead, the least squares approximation $\|\mathbf{m} - \Psi\mathbf{x}\|_{L_2}^2$ referred to as data fidelity term, is employed:

$$\min \|\Phi\mathbf{x}\|_{L_0}, \text{ subject to } \|\mathbf{m} - \Psi\mathbf{x}\|_{L_2}^2 < \epsilon \text{ with } \epsilon > 0. \quad (3.50)$$

3.3.2 Sparsity and Incoherence in MRI

MRI was one of the first technologies to adapt the Compressed Sensing theory early after its emergence around the year 2007. Lustig et al. discussed main features and forms of sparsity as well as incoherence for MRI [Lust10] with the *Sparse-MRI* and *L₁-Spirit* algorithms. Gamper et al. proposed Compressed Sensing for dynamic MRI in 2008 [Gamp08]. Ever since, CS has been an area of active research in MRI with an increasing number of innovations such as adapted sparsity transforms, reconstruction algorithms and new ways of sampling below the Nyquist criteria.

Intuitively, the highest compression factors are possible in data which can be represented by very few coefficients in the transform domain, thus showing the highest degree of correlation. Examples for applications include dynamic applications with high spatio-temporal correlation, parameter mapping with a substantial amount of correlation across the different parameters or naturally sparse angiographic exams. Lower acceleration factors should be expected for static high-resolution applications.

Although MRI sampling in the Fourier space, or k -space, is relatively flexible, the theoretical proposed randomness of sampling points is not practicable due to several reasons: Trajectories in k -space need to be chosen as smoothly as possible due to the effects of hardware imperfections, gradient delays, eddy currents and phase offsets. Furthermore, since the energy is concentrated in the center of k -space representing the low frequencies and should be sampled densely. Therefore, a well-suited sampling pattern for CS MRI needs to comply to these side constraints while maximizing the incoherence [Lust08]. Two measures to analyse

the degree of incoherence for various MRI sampling options are the Point Spread Function (PSF) and, assuming sparsity in a transform domain rather than the image domain, the Transform Point Spread Function (TPSF). Both have been introduced [Lust 10] as:

$$PSF(i, j) = \mathbf{e}_j^H \Phi^H \Phi \mathbf{e}_i \text{ and } TPSF(i, j) = \mathbf{e}_j^H \Psi \Phi^H \Phi \Psi^H \mathbf{e}_i. \quad (3.51)$$

Sparsity While some images provide sparsity in the image domain with $\Phi = \mathbb{1}$ including for example contrast-enhanced angiographic images with a good background suppression, most MRI images are sparse in a transform domain rather than the image domain. The choice of the transformation Φ is either influenced by general assumptions about medical images or derived by the specific application and with respect to the employed acquisition technique. Another aspect that can be used to differentiate sparsity transforms is their operation range. They are either intra-volume or inter-volume based.

Total variation and wavelet decomposition are given as examples along with their coefficients in Figure 3.6 for a PCI volume of the aorta. The wavelet decomposition using Daubechies 4 wavelets is shown in Figure 3.6(a), the TV decomposition in Figure 3.6(c). The coefficient plot, containing all entries of $\Phi(\mathbf{x})$ sorted by magnitude, illustrates well, that the information is contained within few large entries.

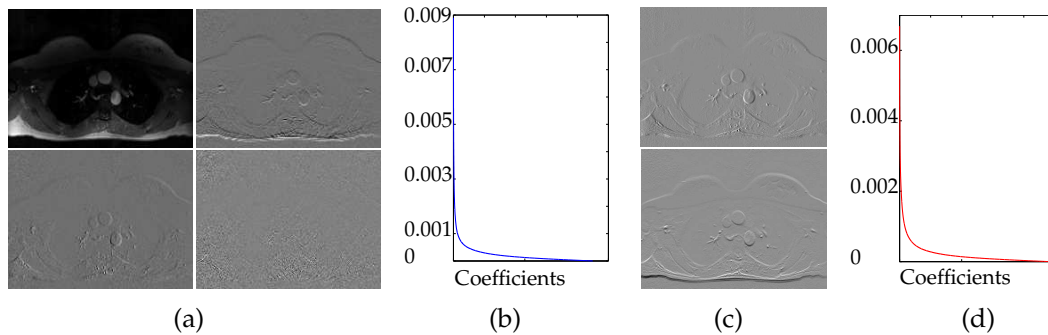


Figure 3.6: Illustration of the wavelet transform and total variation as two widely used sparsity transforms. (a) Wavelet transform for level 1 with (b) the coefficients sorted by magnitude. (c) Illustration of the 2-D total variation along with (d) the coefficients sorted by magnitude.

3.4 Parallel MRI Reconstruction in Compressed Sensing

For this thesis, the pMRI algorithm SENSE was included into CS. The basic equation of the considered reconstruction problem is derived in the following.

3.4.1 Problem Formulation

The non-linear reconstruction algorithm used for recovery of a sparse signal with CS must accomplish two goals simultaneously: achieve a fit to the measured data and enforce the sparsity assumption as shown in Eq. (3.50).

For MRI, the number of measurements M equals the number of acquired samples across all coils $N_\gamma N_k$. The measurement vector \mathbf{m} include the combined raw data vector $\mathbf{m} \in \mathbb{C}^{N_\gamma N_k}$ and the sampling basis $\Psi \in \mathbb{C}^{M \times N}$ is substituted by the encoding matrix $\mathbf{E} \in \mathbb{C}^{N_\gamma N_k \times N}$. The entries equal $e_{(\gamma,\kappa),\iota} = u_\kappa e^{i\mathbf{k}_\kappa \mathbf{r}_\iota} c_\gamma^\iota$, with \mathbf{r}_ι being the position of voxel ι , \mathbf{k}_κ the κ th frequency, u_κ the chosen sampling pattern for k -space point κ and c_γ^ι the coil sensitivity value for coil γ and voxel ι . The sampling u_κ equals 1 for sampled and 0 for zero filled k -space positions. The sparsity transform, previously formulated as $\Phi \mathbf{x}$, is extended to $\Phi(\mathbf{x})$ to include a wide range of possible regularization terms within the operator Φ . The entire problem including the sparsity assumption is

$$\min \|\Phi(\mathbf{x})\|_{L_0}, \text{ subject to } \|\mathbf{E}\mathbf{x} - \mathbf{m}\|_{L_2} < \epsilon \text{ with } \epsilon > 0. \quad (3.52)$$

The problem of Eq. (3.52) has been proven to be NP-hard [Nata 95], therefore dedicated optimization strategies are required. As a consequence, a common direction is the relaxation of the L_0 norm to the L_1 norm:

$$\min \|\Phi(\mathbf{x})\|_{L_1}, \text{ subject to } \|\mathbf{E}\mathbf{x} - \mathbf{m}\|_{L_2} < \epsilon \text{ with } \epsilon > 0. \quad (3.53)$$

The problem is frequently formulated in its unconstrained form or Lagrange formulation by introducing the parameter $\lambda > 0$ to control the influence of the sparsity term. The objective function equals

$$\mathcal{L}(\mathbf{x}) = \|\mathbf{E}\mathbf{x} - \mathbf{m}\|_{L_2} + \lambda \|\Phi(\mathbf{x})\|_{L_1}. \quad (3.54)$$

For N_r sparsity transforms, the formulation corresponds to

$$\mathcal{L}(\mathbf{x}) = \|\mathbf{E}\mathbf{x} - \mathbf{m}\|_{L_2} + \sum_{r=1}^{N_r} \lambda_r \|\Phi_r(\mathbf{x})\|_{L_1}. \quad (3.55)$$

The minimization problem is formulated as

$$\hat{\mathbf{x}} = \underset{\mathbf{x}}{\operatorname{argmin}} \mathcal{L}(\mathbf{x}). \quad (3.56)$$

This can be solved iteratively, defining a starting value \mathbf{x}^0 using N_i iterations. The intermediate result of iteration $i + 1$ is obtained as

$$\mathbf{x}^{i+1} = \underset{\mathbf{x}^i}{\operatorname{argmin}} \mathcal{L}(\mathbf{x}^i). \quad (3.57)$$

3.4.2 State of the Art

In the following, state of the art for the three mentioned pillars of CS in MRI, the sampling, the regularization and the optimization algorithm, will be given.

Sampling strategies for MRI vary from the originally for CS proposed random pattern, as these are not practical for MRI. Therefore, a range of adapted sampling trajectories was proposed accounting for the non-linear distribution of energy from k -space centre to periphery. Aside the most straight forward adaption, a fully sampled centre combined with a randomly sampled periphery, pseudo random sampling schemes were proposed. These include a sequence and gradient switch-based technique by Wang et al. [Wang 09], variable density sampling using probability density functions proposed by Lustig et al. [Lust 07] or Poisson disc approximations initially formulated by Yellott et al. and Nayak et al. [Yell 83, KNNa 89]. IN principle, previously developed ideas for under sampling were adapted and used for CS, such as accelerated radial acquisition schemes as proposed by Glover et al. and Berger et al. [Glov 92, Barg 02], or variable density acquisition techniques as shown by Greiser et al. [Grei 03] were adapted for CS. Further used patterns include the phyllotaxis pattern as proposed for cardiac MRI by Piccini et al. [Picc 11].

Sparsity assumptions can be divided in intra-volume and inter-volume approaches. Intra-volume based sparsity transforms include the very generic wavelet as included by Lustig et al. [Lust 10] and total variation (TV) transforms formulated by Block et al. and for different complex versions by Chen et al. [Bloc 07, Chen 10]. TV is based on the assumption, that medical images are piecewise smooth, resulting in a low value for the integral over the image gradient. Noise pixels, in contrast, show high gradient variations. For wavelets, the level may vary as well as the used Wavelet family. Furthermore, the wavelet concept has been extended to incorporate curvilinear and anisotropic structures using curvelets such as used by Holland et al. [Holl 10] or ridgelets as was shown by Al Zubi et al. [AlZu 11].

The second category, inter-volume sparsity transforms assume sparsity in transform domains spanning over multiple acquisitions, for example temporal frames, different flip angles, multiple slices or multi-contrast settings. These include temporal wavelets and Fourier transform in time direction, used for example in the kt-SPARSE algorithm by Lustig et al. [Lust 06] and extensions of kt-BLAST by Gamper et al. [Gamp 08]. Furthermore, the TV norm was also applied in time domain as proposed in the GRASP algorithm by Feng et al. [Feng 13]. Multiple dimensions are involved in group sparsity algorithms, originally formulated by Huang et al. [Huan 09] and used either for dynamic or multi-contrast settings by Usman et al., [Usma 11] Majumdar et al. and Huang et al. [Maju 11, Huan 12].

Another possible division among sparsity techniques focuses on the adaptivity. The so far discussed sparsity assumptions are formulated a priori as a mathematical model. But there are also techniques focusing on adapting the sparsity model to the data during the reconstruction process. A popular example is the kt-FOCUSS algorithm as proposed by Jung et al. [Jung 09], which uses low resolution images as a start guess and prunes this to a sparse representation which is refined over iterations. Several algorithms learn the sparsity assumptions in increasingly adapted dictionaries such as the methods by Ravishankar et al. and Rubinstein et

al. [Ravi 11, Rubi 10] and the recent adaptation to cardiac MRI by Caballero et al. [Caba 12].

Optimization algorithms efficiently solving the unconstrained problem in Eq. (3.52) are an active field of research since the emergence of CS techniques.

Two general classes can be distinguished: greedy algorithms operating on the unrelaxed problem such as Matching Pursuit (MP) algorithms formulated by Mallat et al. [Mall 93] and algorithms focusing on the relaxed form in Eq. (3.53). These latter include non-linear variants of the conjugate gradients (CG) algorithm used by Block et al. and Lustig et al. [Bloc 07], [Lust 07], which were among the first methods proposed. In a first step, the gradient of the actual x in combination with the prior search direction is used to identify the direction, the second step performs a line search, minimizing the functional in the defined direction. A wide range of non-linear variants were also proposed and are discussed in Hager et al. [Hage 06]. Further algorithms include interior point methods as proposed by Chen et al. [Chen 01], iterative thresholding algorithms introduced by Blumensath et al. [Blum 08] and Daubechies et al. [Daub 04], iteratively re-weighted least squares by Ye et al. [Ye 07] and iterative regularized Gauss-Newton algorithms such as proposed by Uecker et al. and Knoll et al. [Ueck 08, Knol 12].

3.5 Summary and Conclusions

This chapter provided the basis of the developed reconstruction algorithms. Relevant concepts in MRI reconstruction, parallel MRI and Compressed Sensing were introduced and combined to form the basis of the reconstruction problem formulation used throughout this thesis. The application of this formulation to nceMRA and PCI - both techniques that can benefit significantly from sub Nyquist-sampling and scan time reduction - will be the subject of the following chapters.

Part II

**Compressed Sensing in MR
Angiography**

Highly Accelerated Static NceMRA

4.1 Motivation	47
4.2 State of the Art	48
4.3 Regularization and Sampling Strategy	49
4.4 Reconstruction Algorithms	54
4.5 Implementation	61
4.6 Summary and Conclusion	65

This Chapter presents a reconstruction algorithm developed for static nceMRA methods, in particular 2-D peripheral TOF and 3-D free-breathing renal visualization. The main algorithmic contents are the novel adapted analytical sampling strategy combining elements of pMRI and CS, called Multi-Coil Compressed Sensing (MICCS) pattern, and a dedicated Split Bregman minimization algorithm. Parts of these results were presented in [Hutt 14b, Hutt 11b, Hutt 11a, Hutt 12a, Hutt 12b] and [Hutt 14a].

The algorithmic contents will be presented in this chapter and evaluated in both applications in the following chapter. The evaluation thereby focuses both on the image quality and organ specific measures showing the diagnostic usability of the novel method.

4.1 Motivation

Two frequent angiographic examinations are the visualization of the lower extremity vasculature and the acquisition of the renal vasculature. While for both applications, nceMRA techniques are not the method of choice in the clinical routine, the concerned patient population would highly benefit from the availability of non-invasive methods. The common diagnostic examinations, including DSA, US and ceMRA present severe problems, ionizing radiation and iodinated contrast material for DSA, user dependent results for US and the administration of gadolinium-based contrast agent for ceMRA, which is especially contraindicated for patients with renal diseases [Gloc 10]. The specific problems for both applications differ, but both are currently hampered by their long acquisition time, espe-

cially if a good resolution is yielded to visualize and quantize stenosis and smaller arteries. The emerging common goal is a highly accelerated acquisition technique which enables their wider clinical usage. Both being based on contrast mechanisms that highlight vessels while suppressing static tissue, they share the possibilities for data compression using sparsity constraints. Especially if high acceleration factors are desired, two challenges have to be addressed: the choice of the optimal sampling pattern and an adapted regularization and minimization strategy to overcome noise problems. The choice of the sampled lines becomes increasingly important with growing acceleration factors and should therefore not be left to chance. An iterative reconstruction algorithm designed to address these challenges is proposed in the following.

4.2 State of the Art

CeMRA has been among the first applications for CS in MRI and as already mentioned by Lustig et al. in 2007 [Lust07]. It has been identified as a well suited application due to the typically long acquisition times, the required high spatial, and for dynamic ceMRA, temporal resolution and the natural sparsity in the image domain. The long acquisition time apply even more for nceMRA. Reducing the imaging time furthermore helps to reduce motion artefacts or blurring effects. A wide range of methods was proposed, differing in the sampling, the used reconstruction algorithm as well as the sparsity assumption. A subset is given below, focusing on methods applied either to peripheral and renal angiography or specifically proposed for nceMRA techniques.

For peripheral arteries, specific regularization was proposed by Stinson et al. [Stin13] with vascular masking in combination with CG-SENSE. Cukur et al. [Cuku09] accelerated mp-bSSFP peripheral angiography using pseudo-random sampling in combination with both coefficient sparsity and total variation. Specific techniques developed for renal MRA include sampling strategies such as non-contrast enhanced outer radial inner square k -space scheme, as proposed by Worters et al. [Wort12] or variable density tiled random k -space sampling, applied to nceMRA by Lai et al. [Lai11]. Techniques focusing on applying pMRI methods to renal acquisitions were proposed by Riffel et al. [Riff13] comparing the Caipirinha method with GRAPPA, Wright et al. [Wrig14] introduced GRAPPA with stack of stars sampling on time resolved contrast-enhanced renal angiography and Michaely et al. [Mich06] studied pMRI reconstructions of contrast-enhanced renal MRA with different accelerations factors regarding vessel depiction and SNR.

Further methods, applied not specifically to peripheral or renal MRA, but invented for nceMRA techniques include the method by Akcakaya et al. [Akca11], exploiting joint sparsity of the individual coil images for nceMRA of the pulmonary arteries. Storey et al. [Stor12] investigated the combination of GRAPPA with sparsity assumptions of nceMRA subtraction images. The method of Chang et al. [Chan13] focused also on ECG triggered mp-bSSFP acquisitions and used images subtraction in combination with the Karhunen Loeve transform as regularization. Finally, Otazo et al. [Otaz11] proposed to use principal component analysis along flip angles for a randomly sampled 3-D ECG gated acquisition with variable flip angles.

4.3 Regularization and Sampling Strategy

A common formulation is used for both, formulating the entire volume, respectively the entire stack of 2-D slices as a column vector. Therefore, the k -space data from one slice l is combined for all coils $\gamma \in \{1, \dots, N_\gamma\}$ to the vector $\mathbf{m}^l \in \mathbb{C}^{N_{k_x} N_{k_y} N_\gamma}$. Then, all slices are arranged in a column vector $\mathbf{m} \in \mathbb{C}^{N_k N_\gamma}$ with $N_k = N_{k_x} N_{k_y} N_{k_z}$:

$$\mathbf{m}^l = \begin{pmatrix} \mathbf{m}_1^l \\ \vdots \\ \mathbf{m}_{N_\gamma}^l \end{pmatrix} \text{ and } \mathbf{m} = \begin{pmatrix} \mathbf{m}^1 \\ \vdots \\ \mathbf{m}^{N_l} \end{pmatrix}. \quad (4.1)$$

The 2-D slice images, written as column vectors $\mathbf{x}^l \in \mathbb{C}^{N_x N_y}$ and $l \in \{1, \dots, N_z\}$, are likewise arranged in a common vector $\mathbf{x} \in \mathbb{C}^N$ with $N = N_x N_y N_z$:

$$\mathbf{x} = \begin{pmatrix} \mathbf{x}^1 \\ \vdots \\ \mathbf{x}^{N_l} \end{pmatrix}. \quad (4.2)$$

The reconstruction problem is formulated using the encoding matrices $\mathbf{E} \in \mathbb{C}^{N_\gamma N_k \times N}$ with

$$e_{(\gamma, \kappa), l} = u_\kappa e^{i \mathbf{k}_\kappa \mathbf{r}_l} c_{(\gamma, l)}. \quad (4.3)$$

Thereby \mathbf{r}_l is the position of voxel l , \mathbf{k}_κ the κ th frequency, u_κ the chosen sampling for k -space sample κ , $c_{(\gamma, l)}$ the coil sensitivity value for coil γ and image space voxel l . The data fidelity term is

$$H(\mathbf{x}) = \frac{1}{2} \|\mathbf{E}\mathbf{x} - \mathbf{m}\|_{L_2}^2. \quad (4.4)$$

4.3.1 Regularization

The pMRI problem, formulated in the developed algorithms in its least squares form using the encoding matrix \mathbf{E} , is in general ill-conditioned [Ueck 09]. Therefore, noise amplification is a known problem in SENSE reconstructions [Prue 99, Qu 07, Liu 09a, Hoge 05]. Its origin is traced back to non fully linear independent coil setups leading to ill-conditioned reconstruction matrices [Lin 04, Hoge 04]. As a result, the problem is vulnerable to small errors in the input data, as they occur for example in the approximated coil profiles. High under sampling factors as desired for the stated applications deteriorate this problem. Therefore, adapted regularization is required. Total variation (TV) and wavelet transform sparsity were used as regularizers in the present cases. TV is based on the observation that medical images are piecewise constant and smooth.

Let

$$\nabla \mathbf{x} = (\nabla_x^T \mathbf{x}, \nabla_y^T \mathbf{x}, \nabla_z^T \mathbf{x})^T \quad (4.5)$$

be the gradient of \mathbf{x} , calculated numerically as

$$(\nabla_x \mathbf{x})_i = (\nabla_x \mathbf{x})_{(t_x, t_y, t_z)} = x_{(t_x, t_y, t_z)} - x_{(t_x - 1, t_y, t_z)} \quad (4.6)$$

$$(\nabla_y \mathbf{x})_i = (\nabla_y \mathbf{x})_{(t_x, t_y, t_z)} = x_{(t_x, t_y, t_z)} - x_{(t_x, t_y - 1, t_z)} \quad (4.7)$$

$$(\nabla_z \mathbf{x})_i = (\nabla_z \mathbf{x})_{(t_x, t_y, t_z)} = x_{(t_x, t_y, t_z)} - x_{(t_x, t_y, t_z - 1)}. \quad (4.8)$$

The total variation in its original isotropic version [Oshe 92] equals

$$TV_i(\mathbf{x}) = \|\nabla \mathbf{x}\|_{L_{2,1}} = \sum_{i=1}^N \sqrt{|(\nabla_x \mathbf{x})_i|^2 + |(\nabla_y \mathbf{x})_i|^2 + |(\nabla_z \mathbf{x})_i|^2}. \quad (4.9)$$

The second, anisotropic, version is calculated as

$$TV_a(\mathbf{x}) = \|\nabla \mathbf{x}\|_{L_1} = \sum_{i=1}^N |(\nabla_x \mathbf{x})_i| + |(\nabla_y \mathbf{x})_i| + |(\nabla_z \mathbf{x})_i|. \quad (4.10)$$

Wavelet decomposition has been successfully applied to image denoising in multiple domains [Jin 05] including MRI [Pivz 06]. The discrete wavelet transforms (DWT) considered here represent a given function by discretely sampled wavelets. It differs from further transforms such as the Fourier transform by including local frequency information. A wide range of different wavelets exist, among these are the orthogonal *Daubechies wavelets*, defined by a high pass filter \mathbf{f}_h and a low pass filter \mathbf{f}_l available with different coefficient numbers. In the following the *Daubechies 4 wavelets* (D4) are used, which are defined by the coefficients

$$h_{-2} = \frac{1 + \sqrt{3}}{4\sqrt{2}}, \quad h_{-1} = \frac{3 + \sqrt{3}}{4\sqrt{2}}, \quad h_0 = \frac{3 - \sqrt{3}}{4\sqrt{2}} \quad \text{and} \quad h_1 = \frac{1 - \sqrt{3}}{4\sqrt{2}}, \quad (4.11)$$

resulting in the filter specifications

$$f_h(z) = h_{-2}z^{-2} + h_{-1}z^{-1} + h_0 + h_1z \quad \text{and} \quad (4.12)$$

$$f_l(z) = -h_1z^{-2} + h_0z^{-1} + h_{-1} + h_{-2}z. \quad (4.13)$$

The analysis operation consists of filtering the signal of interest $\mathbf{a} \in \mathbb{C}^N$ with both filters, followed by successive down sampling. This results in both approximation and detail coefficients. A multi-scale approach is employed, where the results of level α are obtained by:

$$a_k^\alpha = \sum_{i=1}^N f_h(i - 2k) a_i^{\alpha-1} \quad \text{and} \quad (4.14)$$

$$d_k^\alpha = \sum_{i=1}^N f_l(i - 2k) a_i^{\alpha-1}, \quad (4.15)$$

where $\mathbf{a}^0 = \mathbf{a}$. The application of the DWT to images is done sequentially on the columns and the rows of the image, resulting in four sets of coefficients: $\mathbf{a}^\alpha, \mathbf{d}^{\alpha,h}, \mathbf{d}^{\alpha,v}, \mathbf{d}^{\alpha,d}$ of size $N/(2^\alpha 2^\alpha)$ each. In the following, the second level wavelet

transform using the above stated filters will be described by the transform $W : \mathbb{C}^N \mapsto \mathbb{C}^N$ with

$$W(\mathbf{x}) = \begin{pmatrix} \mathbf{a}^2 \\ \mathbf{d}^{2,h} \\ \mathbf{d}^{2,v} \\ \mathbf{d}^{2,d} \\ \mathbf{d}^{1,h} \\ \mathbf{d}^{1,v} \\ \mathbf{d}^{1,d} \end{pmatrix}. \quad (4.16)$$

The wavelet transform is typically used as regularization in combination with the L_1 norm, resulting in

$$WV(\mathbf{x}) = \|W(\mathbf{x})\|_{L_1}. \quad (4.17)$$

Further regularization involving multiple adjacent slices that exploits for example the continuity of vessels has been proposed as *Vessel Prior Knowledge* in [Hutt 11b] and [Hutt 12b], but is not part of this thesis. For the multi-slice case, the sparsity transforms are calculated slice wise and added over the entire stack of slices.

The unconstrained objective function $\mathcal{L}_{UC}(\mathbf{x})$ including the data fidelity term and the regularization terms equals

$$\begin{aligned} \mathcal{L}_{UC}(\mathbf{x}) &= H(\mathbf{x}) + \lambda_t \text{TV}_i(\mathbf{x}) + \lambda_w WV(\mathbf{x}) \\ &= \underbrace{\frac{1}{2} \|\mathbf{E}\mathbf{x} - \mathbf{m}\|_{L_2}^2}_{\text{Data fidelity term}} + \underbrace{\lambda_t \|\nabla \mathbf{x}\|_{L_{2,1}}}_{\text{Total variation}} + \underbrace{\lambda_w \|W(\mathbf{x})\|_{L_1}}_{\text{Wavelet transform}}, \end{aligned} \quad (4.18)$$

where $\lambda_t, \lambda_w \in \mathbb{R}$ with $\lambda_t, \lambda_w \geq 0$ are the regularization weights.

The minimization problem to be solved is

$$\hat{\mathbf{x}} = \underset{\mathbf{x}}{\text{argmin}} \mathcal{L}_{UC}(\mathbf{x}). \quad (4.19)$$

4.3.2 MICCS Sampling Strategy

The developed acquisition pattern combines aspects of well-known parallel MRI (pMRI) reconstruction techniques such as SENSE with Compressed Sensing (CS) ideas. The proposed pattern, called Multi-Coil Compressed Sensing (MICCS) sampling strategy, is described by the mask vector $\mathbf{u} \in \{0, 1\}^N$ where u_κ stands for the sampling at k -space voxel $\kappa = \mathcal{M}(\kappa_x, \kappa_y, \kappa_z)$.

Thereby u_κ equals

$$u_{(\kappa_x, \kappa_y)} = u_\kappa \begin{cases} 1, & \text{for a sampled voxel and} \\ 0, & \text{for a non-sampled voxel.} \end{cases} \quad (4.20)$$

The pattern will be detailed in its 2-D version for individual slices for illustration purposes. The proposed pattern consists of a central region with size $N_{\kappa_{cy}}$ around the middle point $\kappa_{my} = \left\lfloor \frac{N_{\kappa_y}}{2} \right\rfloor$ and an outer region. The respective start and end

points of the central region equal $\kappa_{msy} = \kappa_{my} - \left\lfloor \frac{N_{\kappa_{cy}}}{2} \right\rfloor$ and $\kappa_{mey} = \kappa_{my} + \left\lfloor \frac{N_{\kappa_{cy}}}{2} \right\rfloor$. The central region is defined as the index set \mathcal{C} , the peripheral region by \mathcal{P} , where

$$\mathcal{C} = \{(\kappa_x, \kappa_y) \mid (\kappa_{msy} \leq \kappa_y \leq \kappa_{mey}) \wedge (1 \leq \kappa_x \leq N_{k_x})\} \text{ and} \quad (4.21)$$

$$\mathcal{P} = \{(\kappa_x, \kappa_y) \mid (1 \leq \kappa_y < \kappa_{msy} \vee \kappa_{mey} < \kappa_y \leq N_{k_y}) \wedge (1 \leq \kappa_x \leq N_{k_x})\}, \quad (4.22)$$

with $\kappa = \mathcal{M}(\kappa_x, \kappa_y)$. This division is illustrated symbolically in Figure 4.1.

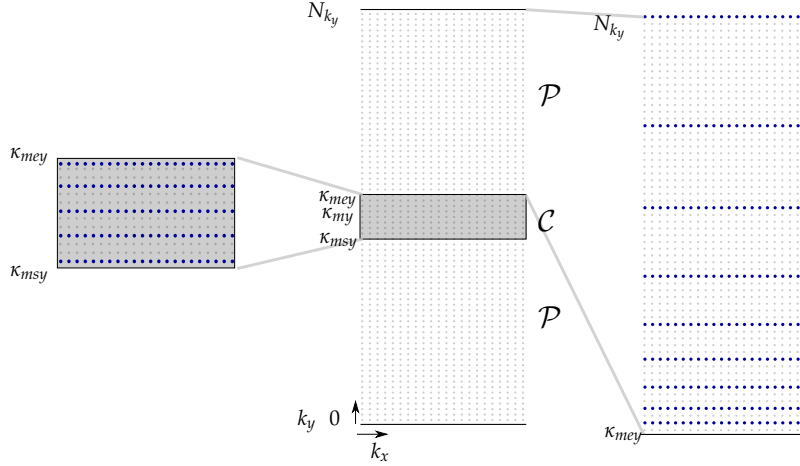


Figure 4.1: Illustration of the MICCS pattern. The k -space is divided into a central region \mathcal{C} and a peripheral region \mathcal{P} . The sampling of the peripheral region is illustrated using an exemplary parameter set. The regular sampling of the central region is shown with $d_{cy} = 3$.

The central region is regularly under sampled with distance $d_{cy} \in \mathbb{Z}$, adapted to the number of coils located in the under sampling direction, which is beneficial for the pMRI reconstruction aspect. Neighbouring slices are sampled such that their central lines are interleaved with offset $o_{cy}(l) \in \mathbb{Z}$:

$$u_{(\kappa_x, \kappa_y)}^l = \begin{cases} 1, & \text{for } \kappa_y = \kappa_{msy} + o_{cy}(l) + i \cdot d_{cy} \text{ and } 1 \leq \kappa_x \leq N_{k_x} \\ & \text{where } i \in \mathbb{N} \text{ subject to } \mathcal{M}(\kappa_x, \kappa_y) \in \mathcal{C} \text{ and} \\ 0, & \text{otherwise.} \end{cases} \quad (4.23)$$

The peripheral region is sampled with density decreasing towards the k -space borders, the distances between succeeding sampling points are calculated using the distance function $d(\chi, (a, b))$, where $\chi \in \mathbb{Z}$ is the distance index and $a, b \in \mathbb{R}$ are the pattern parameters:

$$d : \mathbb{N} \times \mathbb{R}^2 \rightarrow \mathbb{N} \text{ with } d(\chi, (a, b)) = \lceil (a \cdot \chi)^b \rceil. \quad (4.24)$$

The location of the i th sampling point results from the derived cumulative function $s(i, (a, b))$:

$$s : \mathbb{N} \times \mathbb{R}^2 \rightarrow \mathbb{N} \text{ with } s(i, (a, b)) = \sum_{\chi=1}^i d(\chi, (a, b)). \quad (4.25)$$

These functions, as well as the peripheral offset $o_{py} \in \mathbb{N}$, are included in the sampling pattern calculation as follows:

$$u_{(\kappa_x, \kappa_y)}^l = \begin{cases} 1, & \text{for } (\kappa_y = \kappa_{msy} - (o_{py}(l) + s(i, (a, b)))) \wedge 1 \leq \kappa_x \leq N_{k_x} \\ & \text{where } i \in \mathbb{N} \text{ subject to } \mathcal{M}(\kappa_x, \kappa_y) \in \mathcal{P}, \\ 1, & \text{for } (\kappa_y = \kappa_{mey} + (o_{py}(l) + s(i, (a, b)))) \wedge 1 \leq \kappa_x \leq N_{k_x} \\ & \text{where } i \in \mathbb{N} \text{ subject to } \mathcal{M}(\kappa_x, \kappa_y) \in \mathcal{P} \text{ and} \\ 0, & \text{otherwise.} \end{cases} \quad (4.26)$$

Thereby, the peripheral offset is typically chosen identical to the central offset $o_{py} = o_{cy}$.

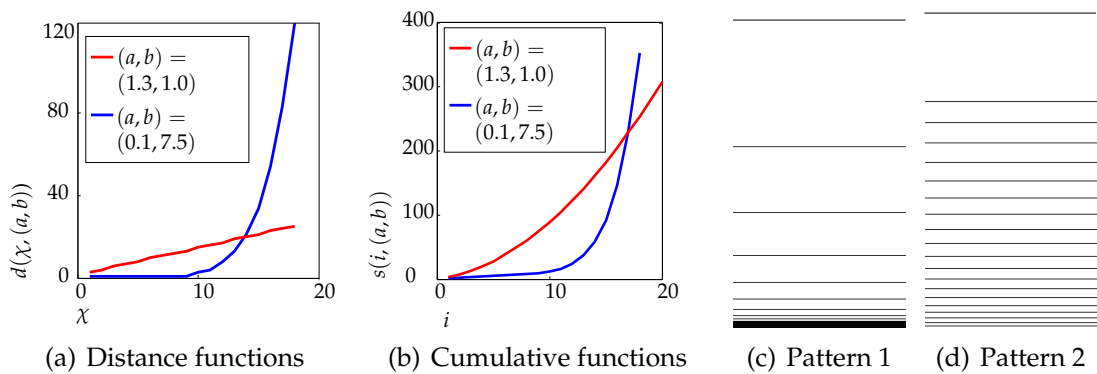


Figure 4.2: Illustration of the peripheral pattern construction for two parameter settings $(a, b) = (1.3, 1.0)$ and $(a, b) = (0.1, 7.5)$. (a) Distance and (b) cumulative function. (c)-(d) Final patterns for both parameter choices.

Examples for the central and peripheral region are shown in Figure 4.1. The obtained total number of sampled lines depends on the k -space size N_{k_y} and on the parameters (a, b) . Figure 4.2 illustrates the distance function $d(\chi, (a, b))$, the cumulative function $s(i, (a, b))$ and the resulting peripheral pattern for two specific parameter settings to demonstrate the high flexibility of the proposed pattern. These, specified by $(a, b) = (1.3, 1.0)$ and $(a, b) = (0.1, 7.5)$, result in the same number of 36×2 sampled lines in the periphery for $N_{k_y} = 600$.

Internal, Interleaved and Interpolated Coil Calculation

The complex spatial coil profiles, required for SENSE based algorithms, are described by $\mathbf{c}_\gamma^l \in \mathbb{R}^N$ for slice l and coil γ , are calculated based on k -space data. Two different ways to obtain them are common, either by a separate external scan, or internally from the image data. Based on the k -space data, filtering strategies are employed to obtain smooth profiles. The spatial closeness of neighbouring slices is exploited twofold. The central k -space data is obtained fully internally by using an interleaved approach, the resulting coil profiles are filtered in slice direction.

The parameters for the regular k -space center under sampling $o_{cy}(l)$ and d_{cy} are chosen as $o_{cy}(l) = \text{mod}(l, 3)$ and $d_{cy} = 3$ to ensure full k -space coverage over three adjacent slices. The interleaving strategy is illustrated in Figure 4.3(a)

through (c), showing the central sampling of three adjacent slices. The combined fully sampled central sampling, used as basis for the coil sensitivity calculation, is depicted in 4.3(d).

Spatial filtering in slice direction smooths the obtained coil profiles

$$\tilde{c}_{(\gamma,t)}^l = \frac{1}{4}c_{(\gamma,t)}^{l-1} + \frac{1}{2}c_{(\gamma,t)}^l + \frac{1}{4}c_{(\gamma,t)}^{l+1}. \quad (4.27)$$

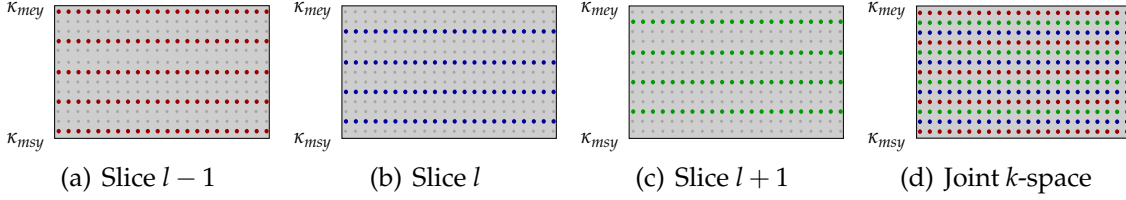


Figure 4.3: Scheme of the central sampling required for internal interleaved coil sensitivity calculation for three adjacent slices (a-c). Combined, a fully sampled k -space central region is obtained (d).

4.4 Reconstruction Algorithms

The unconstrained problem in Eq. (4.19) can be solved using a wide variety of methods, some of which were stated in Section 3.4.2. Two different methods will be detailed in the following, a Quasi Newton method belonging to the group of gradient based methods and the unconstrained Split Bregman method.

4.4.1 Gradient Based Optimization

Gradient based optimization methods minimize the objective function $\mathcal{L}(\mathbf{x})$ using its gradient $\nabla \mathcal{L}(\mathbf{x})$ in multiple iterations. The value for \mathbf{x}^{i+1} in the $i+1$ th iteration is obtained using the step size $t^{i+1} \in \mathbb{R}$ and the direction $\mathbf{p}^{i+1} \in \mathbb{C}^N$:

$$\mathbf{x}^{i+1} = \mathbf{x}^i + t^{i+1} \mathbf{p}^{i+1}. \quad (4.28)$$

They differ in the calculation of the step size and the direction.

The considered objective function $\mathcal{L}(\mathbf{x})$ for the given pMRI-CS reconstruction problem is, as a sum of convex functions, convex. It is furthermore differentiable and thus allows for the use of gradient based optimization methods such as Conjugate Gradient (CG) [Hest 52] or Quasi Newton methods [Noce 80]. These require the evaluation of the objective function $\mathcal{L}(\mathbf{x})$ as well as its gradient

$$\nabla \mathcal{L}(\mathbf{x}) = \nabla H(\mathbf{x}) + \lambda_t \nabla TV_i(\mathbf{x}) + \lambda_w \nabla WV(\mathbf{x}). \quad (4.29)$$

Be \mathbf{E}^* the Hermitian conjugate of the encoding matrix \mathbf{E} , the derivative of the data fidelity term equals

$$\nabla H(\mathbf{x}) = \mathbf{E}^*(\mathbf{E}\mathbf{x} - \mathbf{m}). \quad (4.30)$$

Algorithm 4.1 Calculation of the MICCS pattern

Require: $N_{k_x}, N_{k_y}, N_{k_{cy}}, o_{cy}, d_{cy}, a, b$

```

1: for all  $l$  do
2:   for all  $\kappa$  do
3:      $u_{\kappa}^l = 0$ 
4:   end for
5:    $i = 0$ 
6:   while  $\mathcal{M}(\kappa_x, \kappa_y) \in \mathcal{C}$  do
7:      $\kappa_y = \kappa_{msy} + o_{cy}(l) + id_{cy}, i = i + 1$ 
8:     for all  $\kappa$  do
9:        $u_{\kappa}^l = 1$ 
10:    end for
11:  end while
12:   $i = 0$ 
13:  while  $\mathcal{M}(\kappa_x, \kappa_y) \in \mathcal{P}$  do
14:     $\kappa_y = \kappa_{msy} + (o_{py}(l) + s(i, (a, b))), i = i + 1$ 
15:    for all  $\kappa$  do
16:       $u_{\kappa}^l = 1$ 
17:    end for
18:  end while
19:   $i = 0$ 
20:  while  $\mathcal{M}(\kappa_x, \kappa_y) \in \mathcal{P}$  do
21:     $\kappa_y = \kappa_{msy} - (o_{py}(l) + s(i, (a, b))), i = i + 1$ 
22:    for all  $\kappa$  do
23:       $u_{\kappa}^l = 1$ 
24:    end for
25:  end while
26: end for
27: return  $u_{\kappa}^l \forall l, \kappa$ 

```

The encoding matrix \mathbf{E} is not calculated explicitly in the algorithm, but evaluated as an operator. Therefore, the operator $E : \mathbb{C}^N \mapsto \mathbb{C}^{N_k N_\gamma}$ is formulated as

$$E(\mathbf{x}) = \begin{pmatrix} \mathbf{u} \cdot \mathcal{F}(\mathbf{c}_1 \cdot \mathbf{x}) \\ \vdots \\ \mathbf{u} \cdot \mathcal{F}(\mathbf{c}_{N_\gamma} \cdot \mathbf{x}) \end{pmatrix}, \quad (4.31)$$

where $\mathbf{u} \in \mathbb{R}^N$ and $\mathcal{F}^* = \mathcal{F}^{-1}$, the adjoint operator $E^* : \mathbb{C}^{N_k N_\gamma} \mapsto \mathbb{C}^N$ equals

$$E^* \begin{pmatrix} \mathbf{m}_1 \\ \vdots \\ \mathbf{m}_{N_\gamma} \end{pmatrix} = \sum_{\gamma=1}^{N_\gamma} \mathbf{c}_\gamma^* \cdot \mathcal{F}^{-1}(\mathbf{u} \cdot \mathbf{m}_\gamma). \quad (4.32)$$

Here, \cdot stands for the element wise multiplication of two vectors. Both operators are illustrated schematically in Figure 4.4.

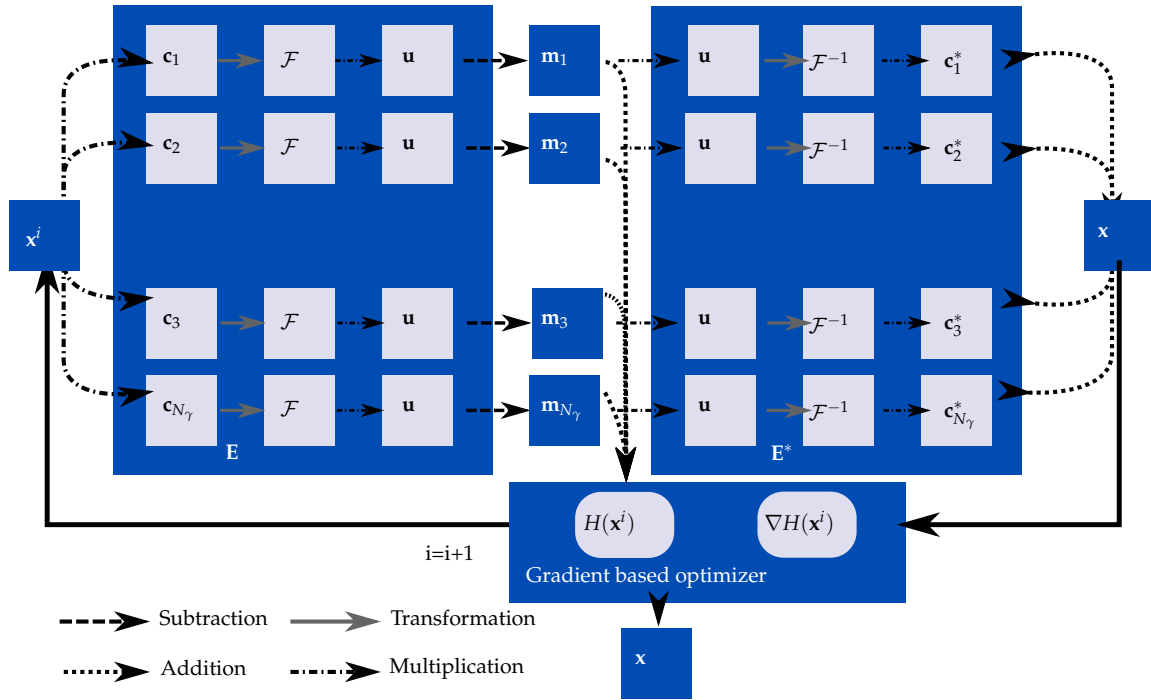


Figure 4.4: Illustration of the encoding operator and its inverse for the SENSE algorithm.

To avoid singularities in the derivative, the TV term is approximated [Acar 94, Lust 07] using

$$|\mathbf{x}|_l = \sqrt{\mathbf{x}^2 + \tau} \quad (4.33)$$

where $\tau \in \mathbb{R} > 0$ is a constant, referred to as corner rounding parameter. This results in

$$\nabla TV_i(\mathbf{x}) = \frac{(\nabla_x^2 \mathbf{x}) + (\nabla_y^2 \mathbf{x}) + (\nabla_z^2 \mathbf{x})}{\sqrt{|\nabla_x \mathbf{x}|^2 + |\nabla_y \mathbf{x}|^2 + |\nabla_z \mathbf{x}|^2 + \tau}} \quad (4.34)$$

Finally, for the derivation of the wavelet L_1 term, the inverse wavelet operation $W^H : \mathbb{C}^N \mapsto \mathbb{C}^N$, called wavelet synthesis is used. This is, using the filter operators stated above, described by

$$a_l^{\alpha-1} = \sum_{n=1}^{N/(2^\alpha)} \tilde{f}_h(l-2n)a_n^\alpha + \sum_{n=1}^{N/(2^\alpha)} \tilde{f}_l(l-2n)d_n^\alpha, \quad (4.35)$$

for the signal \mathbf{a} .

Combined with the product rule and the differentiation for the absolute value in the L_1 norm it results for the derivative

$$\nabla W V(\mathbf{x}) = W^H(\text{sgn}(W(\mathbf{x}))). \quad (4.36)$$

The limited-memory Broyden Fletcher Goldfarb Shanno (IBFGS), a Quasi Newton algorithm with limited memory requirements, was chosen as gradient based optimizer. It was proposed for large-scale optimization problems such as the considered regularized reconstruction. Its equivalence to the CG solver under certain assumptions was proven by Nazareth et al. [Naza 79].

In contrast to Newton methods, Quasi Newton method do not require explicit calculation of the Hessian matrix $\Delta^2(\mathcal{L})$, but use the numerical approximation \mathbf{H} for the inverse Hessian. This approximation is based on the secant condition, the Taylor extension of the gradient of the objective function

$$\mathbf{H}^{i+1}(\nabla \mathcal{L}(\mathbf{x}^{i+1}) - \nabla \mathcal{L}(\mathbf{x}^i)) = -t^i \mathbf{H}^i \nabla \mathcal{L}(\mathbf{x}^i). \quad (4.37)$$

The Quasi Newton variants vary with the used update formula for \mathbf{H} , for the used Broyden Fletcher Goldfarb Shanno (BFGS), the update equals

$$\mathbf{H}^{i+1} = \mathbf{V}^i \mathbf{H}^k + t^i (\mathbf{p}^{iT} \mathbf{y}^i)^{-1} \mathbf{p}^i \mathbf{p}^{iT} \text{ where } \mathbf{V}^i = \mathbf{I} - (\mathbf{p}^{iT} \mathbf{y}^i)^{-1} \mathbf{p}^i \mathbf{y}^{iT}. \quad (4.38)$$

The direction is obtained by

$$\mathbf{p}^i = -\mathbf{H}^i \nabla \mathcal{L}(\mathbf{x}^i) \text{ and } \mathbf{y}^i = \nabla \mathcal{L}(\mathbf{x}^{i+1}) - \nabla \mathcal{L}(\mathbf{x}^i). \quad (4.39)$$

A further development is the limited memory BFGS algorithm, storing not the entire Hessian approximation \mathbf{H}^i , but only the vectors \mathbf{p}^i and \mathbf{y}^i for the subsequent update to \mathbf{H}^{i+1} [Noce 80]. The BFGS algorithm is given in Algorithm 4.2, with a total of N_i iterations. The step size was determined using the backtracking line search with the Wolfe conditions.

4.4.2 Split Bregman Algorithm

The Split Bregman approach offers multiple advantages over the previously discussed gradient based optimization methods. It allows better incorporation of the constraints into the minimization by formulating the concept in a two-step approach and it splits the regularization constraints by introducing auxiliary variables. The resulting sub problems can thus be solved using shrinkage techniques. Furthermore, its faster convergence was shown [Gold 09, Nien 14].

Algorithm 4.2 Broyden Fletcher Goldfarb Shanno algorithm

Require: $\mathcal{L}, \mathbf{H}^0$ **INPUT:** \mathbf{x}^0 **for all** $i = 1$ to N_i **do** Calculate the step size t^i using the backtracking line search Calculate the direction $\mathbf{p}^i = -\mathbf{H}^{i-1} \nabla \mathcal{L}(\mathbf{x}^{i-1})$ Update $\mathbf{x}^i = \mathbf{x}^{i-1} + t^i \mathbf{p}^i$ Calculate $\mathbf{y}^i = \nabla \mathcal{L}(\mathbf{x}^i) - \nabla \mathcal{L}(\mathbf{x}^{i-1})$ Hessian approximation \mathbf{H}^i from the BFGS update rule in Eq. (4.38)**end for****OUTPUT:** \mathbf{x}^{N_i}

Development of the Split Bregman Algorithm

A constrained reconstruction problem with convex functionals H and J and any norm $\|J(\mathbf{x})\|$ is considered with

$$\hat{\mathbf{x}} = \underset{\mathbf{x}}{\operatorname{argmin}} \|J(\mathbf{x})\|, \quad (4.40)$$

$$\text{subject to } H(\mathbf{x}) < \epsilon, \quad (4.41)$$

with $\epsilon \in \mathbb{R}$, $\epsilon > 0$.

Converted into an unconstrained problem it reads

$$\hat{\mathbf{x}} = \underset{\mathbf{x}}{\operatorname{argmin}} \|J(\mathbf{x})\| + \mu H(\mathbf{x}). \quad (4.42)$$

While classically, a sequence of μ^k with $\mu^{k-1} < \mu^k$ is used over iterations to enforce data consistency, Bregman iterations use the concept of the Bregman distance to formulate the problem as a sequence of unconstrained problems. The Bregman distance is calculated as

$$D_j^{\mathbf{p}}(\mathbf{x}, \mathbf{v}) = J(\mathbf{x}) - J(\mathbf{v}) - \langle \mathbf{p}, \mathbf{x} - \mathbf{v} \rangle, \quad (4.43)$$

where $\mathbf{p} \in \mathbf{C}^N$ is the sub-gradient of J at \mathbf{v} . The unconstrained problem of Eq. (4.42) [Breg 67], is formulated using the Bregman distance [Gold 09]. For differentiable H it holds for the sub-gradients that

$$0 \in \partial(D_j^{\mathbf{p}}(\mathbf{x}, \mathbf{x}^k) + \mu H(\mathbf{x})) \quad \text{at} \quad \mathbf{x}^{k+1} \quad \text{and} \quad \mathbf{p}^{k+1} \in \partial J(\mathbf{x}^{k+1}). \quad (4.44)$$

This results in

$$\begin{aligned} \mathbf{x}^{k+1} &= \underset{\mathbf{x}}{\operatorname{argmin}} D_j^{\mathbf{p}}(\mathbf{x}, \mathbf{x}^k) + \mu H(\mathbf{x}) \\ &= \underset{\mathbf{x}}{\operatorname{argmin}} J(\mathbf{x}) - \langle \mathbf{p}^k, \mathbf{x} - \mathbf{x}^k \rangle + \mu H(\mathbf{x}), \end{aligned} \quad (4.45)$$

where $J(\mathbf{x}^k)$ is omitted because of its independence from \mathbf{x} , and

$$\mathbf{p}^{k+1} = \mathbf{p}^k - \mu \nabla H(\mathbf{x}^{k+1}). \quad (4.46)$$

Connection to Augmented Lagrangian and Penalty Methods

The presented Split Bregman method is closely related to the Augmented Lagrangian formulation, resulting for the stated problem in the function

$$\mathcal{L}(\mathbf{x}, \mathbf{a}, \mu) = J(\mathbf{x}) + \mathbf{a}^T H(\mathbf{x}) + \mu \|H(\mathbf{x})\|_{L_2}^2, \quad (4.47)$$

where $\mathbf{a} \in \mathbb{R}^N$ equals the Lagrangian multiplier and $\mu > 0$ the penalty parameter. This is solved in a two step method

$$\mathbf{x}^{k+1} = \underset{\mathbf{x}^k}{\operatorname{argmin}} \mathcal{L}(\mathbf{x}^k, \mathbf{a}^k, \mu) \quad (4.48)$$

$$\mathbf{a}^{k+1} = \mathbf{a}^k + \mu H(\mathbf{x}^{k+1}). \quad (4.49)$$

The penalty methods fits into this formulation with $\mathbf{a} = \mathbf{0}$, the SB method in Eqs. (4.45-4.46) is obtained by $\mathbf{a} = \mathbf{E}\mathbf{p}$ [Rama 11]. Both, the Augmented Lagrangian and the Split Bregman method have in common, that they do not require $\mu \rightarrow \infty$.

Variable Splitting

The unconstrained problem in Eq. (4.42) can be converted into a series of unconstrained problems by introducing additional auxiliary variables [Afon 11, Gold 09]. The obtained decoupling of the minimization problem and its regularization terms allows specific optimization techniques for each sub problem. The actual values of the remaining components are fixed and included into the objective function. This mechanism is illustrated in the following section with the concrete pMRI CS problem.

4.4.3 Formulation of Split Bregman for the pMRI CS Problem

The data fidelity term and the energy function of Eq. (4.42) fit into the given Split Bregman formulation with

$$H(\mathbf{x}) = \frac{1}{2} \|\mathbf{E}\mathbf{x} - \mathbf{m}\|_{L_2}^2 \quad \text{and} \quad (4.50)$$

$$J(\mathbf{x}) = \lambda_t \|\nabla \mathbf{x}\|_{L_{2,1}} + \lambda_w \|W(\mathbf{x})\|_{L_1}. \quad (4.51)$$

This formulation corresponds to an extension of Eq. (3.53) to a more general regularization form. The introduction of the additional variables $\mathbf{d}_w, \mathbf{d}_x$ and $\mathbf{d}_y \in \mathbb{C}^N$ yields the formulation with penalty terms

$$\begin{aligned} (\hat{\mathbf{x}}, \hat{\mathbf{d}}_x, \hat{\mathbf{d}}_y, \hat{\mathbf{d}}_w) = & \\ & \operatorname{argmin}_{\mathbf{x}, \mathbf{d}_x, \mathbf{d}_y, \mathbf{d}_w} \frac{\mu}{2} \|\mathbf{E}\mathbf{x} - \mathbf{m}\|_{L_2}^2 + \lambda_t \|(\mathbf{d}_x, \mathbf{d}_y)\|_{L_2} + \lambda_w \|\mathbf{d}_w\|_{L_1} \\ & + \frac{\alpha \lambda_t}{2} \left(\|\mathbf{d}_x - \nabla_x \mathbf{x}\|_{L_2}^2 + \|\mathbf{d}_y - \nabla_y \mathbf{x}\|_{L_2}^2 \right) \\ & + \frac{\alpha \lambda_w}{2} \|\mathbf{d}_w - W(\mathbf{x})\|_{L_2}^2, \end{aligned} \quad (4.52)$$

where $\mu, \alpha \in \mathbb{R}$ with $\mu, \alpha > 0$ and $\|(\mathbf{d}_x, \mathbf{d}_y)\|_{L_2} = \sum_{i=1}^N \sqrt{(\mathbf{d}_x)_i^2 + (\mathbf{d}_y)_i^2}$. Thereby, the isotropic TV does not allow decoupling the variables \mathbf{d}_x and \mathbf{d}_y [Plon 11]. With linear H , as given for the data fidelity term specified in Eq. (4.50), the simplifications proposed by Goldstein [Gold 09] can be applied. Then, Eq. (4.45) equals

$$\begin{aligned} (\hat{\mathbf{x}}, \hat{\mathbf{d}}_x, \hat{\mathbf{d}}_y, \hat{\mathbf{d}}_w) = & \\ \operatorname{argmin}_{\mathbf{x}, \mathbf{d}_w, \mathbf{d}_x, \mathbf{d}_y} \frac{\mu}{2} \|\mathbf{E}\mathbf{x} - \mathbf{m}\|_{L_2}^2 + \lambda_t \|(\mathbf{d}_x, \mathbf{d}_y)\|_{L_2} + \lambda_w \|\mathbf{d}_w\|_{L_1} & \\ + \frac{\alpha\lambda_t}{2} \left(\|\mathbf{d}_x - \nabla_x \mathbf{x} - \mathbf{b}_x^j\|_{L_2}^2 + \|\mathbf{d}_y - \nabla_y \mathbf{x} - \mathbf{b}_y^j\|_{L_2}^2 \right) & \\ + \frac{\alpha\lambda_w}{2} \|\mathbf{d}_w - W(\mathbf{x}) - \mathbf{b}_w^j\|_{L_2}^2 & \end{aligned} \quad (4.53)$$

for the stated problem. Eq. (4.46) is formulated for the concrete problem with three equations as

$$\mathbf{b}_x^{j+1} = \mathbf{b}_x^j + \nabla_x \mathbf{x}^{j+1} - \mathbf{d}_x^{j+1}, \quad (4.54)$$

$$\mathbf{b}_y^{j+1} = \mathbf{b}_y^j + \nabla_y \mathbf{x}^{j+1} - \mathbf{d}_y^{j+1}, \text{ and} \quad (4.55)$$

$$\mathbf{b}_w^{j+1} = \mathbf{b}_w^j + W(\mathbf{x}^{j+1}) - \mathbf{d}_w^{j+1}. \quad (4.56)$$

where $\mathbf{b}_x, \mathbf{b}_y, \mathbf{b}_w \in \mathbb{C}^N$ are the residual errors.

The minimization in Eq. (4.53) can now be split into sub-problems allowing to de-couple the L_1 and L_2 parts. The minimization problem for the L_2 component equals

$$(\mathbf{x}^{j+1}) = \operatorname{argmin}_{\mathbf{x}} \mathcal{L}_{L_2}(\mathbf{x}, \mathbf{d}_x^j, \mathbf{d}_y^j, \mathbf{d}_w^j, \mathbf{b}_x^j, \mathbf{b}_y^j, \mathbf{b}_w^j) \quad (4.57)$$

where the objective function for the L_2 problem $\mathcal{L}_{L_2}(\mathbf{x})$ is formulated as

$$\begin{aligned} \mathcal{L}_{L_2}(\mathbf{x}, \mathbf{d}_x^j, \mathbf{d}_y^j, \mathbf{d}_w^j, \mathbf{b}_x^j, \mathbf{b}_y^j, \mathbf{b}_w^j) = \frac{\mu}{2} \|\mathbf{E}\mathbf{x} - \mathbf{m}\|_{L_2}^2 & \\ + \frac{\alpha\lambda_t}{2} \left(\|\mathbf{d}_x^j - \nabla_x(\mathbf{x}) - \mathbf{b}_x^j\|_{L_2}^2 + \|\mathbf{d}_y^j - \nabla_y(\mathbf{x}) - \mathbf{b}_y^j\|_{L_2}^2 \right) & \\ + \frac{\alpha\lambda_w}{2} \|\mathbf{d}_w^j - W(\mathbf{x}) - \mathbf{b}_w^j\|_{L_2}^2 & \end{aligned} \quad (4.58)$$

The sub problems for the wavelet and TV terms are formulated as

$$\begin{aligned} (\mathbf{d}_x^{j+1}, \mathbf{d}_y^{j+1}) = \operatorname{argmin}_{\mathbf{d}_x, \mathbf{d}_y} \frac{\alpha\lambda_t}{2} \|\mathbf{d}_x - \nabla_x(\mathbf{x}^{j+1}) - \mathbf{b}_x^j\|_{L_2}^2 + \frac{\alpha\lambda_t}{2} \|\mathbf{d}_y - \nabla_y(\mathbf{x}^{j+1}) - \mathbf{b}_y^j\|_{L_2}^2 & \\ + \lambda_t \|(\mathbf{d}_x, \mathbf{d}_y)\|_{L_2} \text{ and} & \end{aligned} \quad (4.59)$$

$$(\mathbf{d}_w^{j+1}) = \operatorname{argmin}_{\mathbf{d}_w} \frac{\alpha\lambda_w}{2} \|\mathbf{d}_w - W(\mathbf{x}^{j+1}) - \mathbf{b}_w^j\|_{L_2}^2 + \lambda_w \|\mathbf{d}_w\|_{L_1}. \quad (4.60)$$

The L_2 problem is solved using an IBFGS algorithm with N_i steps. The isotropic TV in equation (4.59) is minimized using the generalized shrinkage formula [Gold 09]:

$$(\mathbf{d}_x^{j+1}, \mathbf{d}_y^{j+1}) = s_1(\mathbf{x}^{j+1}, \mathbf{b}_x^j, \mathbf{b}_y^j, 1/\alpha), \quad (4.61)$$

with

$$(\mathbf{d}_x^{j+1})_l = \frac{(\nabla_x(\mathbf{x}^j))_l + (\mathbf{b}_x^j)_l}{(\mathbf{z}^j)_l} ((\mathbf{z}^j)_l - 1/\alpha)_+ \text{ and} \quad (4.62)$$

$$(\mathbf{d}_y^{j+1})_l = \frac{(\nabla_y(\mathbf{x}^j))_l + (\mathbf{b}_y^j)_l}{(\mathbf{z}^j)_l} ((\mathbf{z}^j)_l - 1/\alpha)_+, \quad (4.63)$$

where

$$(\mathbf{z}^j)_l = \sqrt{(\nabla_x(\mathbf{x}^j)_l + \mathbf{b}_x)_l^2 + (\nabla_y(\mathbf{x}^j)_l + \mathbf{b}_y)_l^2} \quad (4.64)$$

and where $(t)_+$ represents the positive part of t : $(t)_+ = \max(t, 0)$. In contrast to the gradient based optimization numerical calculation of the gradient of the total variation norm, the wavelet L_1 norm as well as the corner smoothing parameter τ are not required. This is a benefit, as the choice of adapted τ constitutes a trade-off between convergence speed and the quality of the obtained solution [Rama 11, Lust 07].

The wavelet term minimization is done with soft thresholding

$$(\mathbf{d}_w^{j+1}) = s_2(\mathbf{x}^{j+1}, \mathbf{b}_w^j, 1/\alpha), \quad (4.65)$$

where

$$(\mathbf{d}_w^{j+1})_l = \frac{(W(\mathbf{x}^{j+1}))_l}{|(W(\mathbf{x}^{j+1}))_l|} \left(|(W(\mathbf{x}^{j+1}))_l| - 1/\alpha \right)_+. \quad (4.66)$$

The stated steps, minimization of the L_2 term, generalized TV thresholding and wavelet soft thresholding is repeated in each iteration j for $j \in \{1, \dots, N_j\}$.

4.5 Implementation

All following algorithms are implemented for this thesis in a C++ framework, shown as an overview in Figure 4.5. It offers both the connection to the manufacturer's scanner and can operate as a standalone platform. It consists of a basic layer including mathematical libraries, image processing libraries and the data container, used for both the 2-D and 3-D static data as well as for the 6-D PCI data. The necessary steps for the CS based reconstruction pipeline, as depicted in Figure 1.2 of Chapter 1, can be retrieved in the framework:

- Sampling and coil sensitivities,
- objective function and regularization terms and
- reconstruction algorithms.

A wide range of sampling options, including the proposed MICCS sampling strategy and the coil sensitivity combinations are implemented within the framework. Different regularization terms are realized, either described or developed within this thesis, which are combined to objective functions. The next layer are the reconstruction algorithms, used to solve the emerging optimization problems. As for the regularizers, both state of the art methods and novel proposed algorithms are implemented.

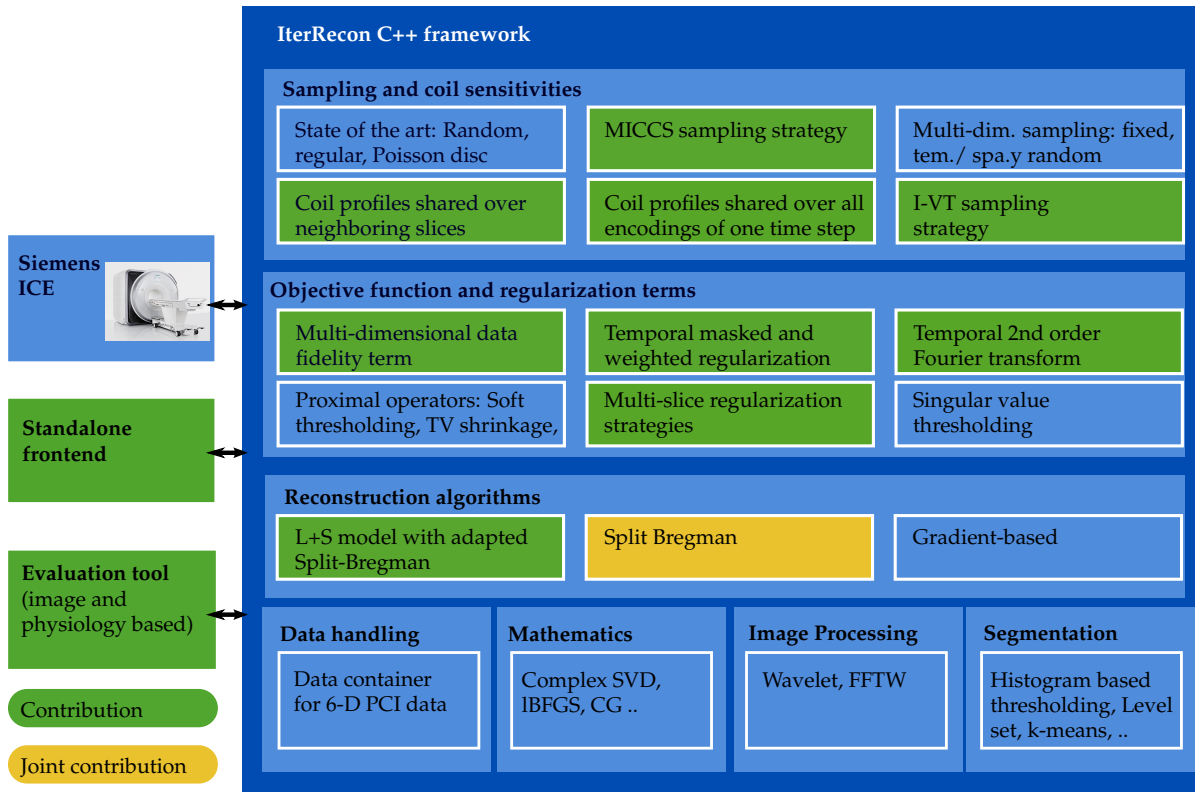


Figure 4.5: Illustration of the IterRecon framework. The joint contributions are marked in yellow, the contributions of this thesis in green.

4.5.1 Complexity Analysis

The gradient based and Split Bregman based algorithms are shown in flow charts in Figure 4.6 and in the Algorithms 4.3 and 4.4. The complexity of both will be analysed in the following. Let N be, as previously stated, the number of considered image voxels, N_γ the number of coils, N_i the number of performed IBFGS iterations for the GB algorithm, N_j the number of Bregman iterations and N_k the number of the IBFGS iterations used to minimize the L_1 term.

The evaluation of the data fidelity term is not performed as a matrix multiplication as in the theoretical formulation in Eq. (4.3) but operator wise as described in Section 4.4.1 and illustrated in Figure 4.4. It requires fast Fourier transforms (FFT) for each of the N_γ coils with, in the worst case for a fully 3-D Fourier transform, complexity $O(N \log N)$ for each coil. Furthermore, $2N$ additional multiplications and N subtractions, and for the L_2 norm, N multiplications and subtractions are performed, resulting in a total complexity of $O(N_\gamma N \log N)$. The gradient requires in addition a further Fourier transform and for each voxel 2 multiplications and one addition, resulting in $O(N_\gamma N \log N)$. The evaluation of the regularizers total variation and wavelet transform with a complexity of $O(N)$ each complete the objective function evaluation. In total, for N_i iterations and a maximum of 20 evaluations of the objective function, with the IBFGS being linear in the complexity, the effort of the gradient based algorithm lays within $O(N_i N_\gamma N \log N)$.

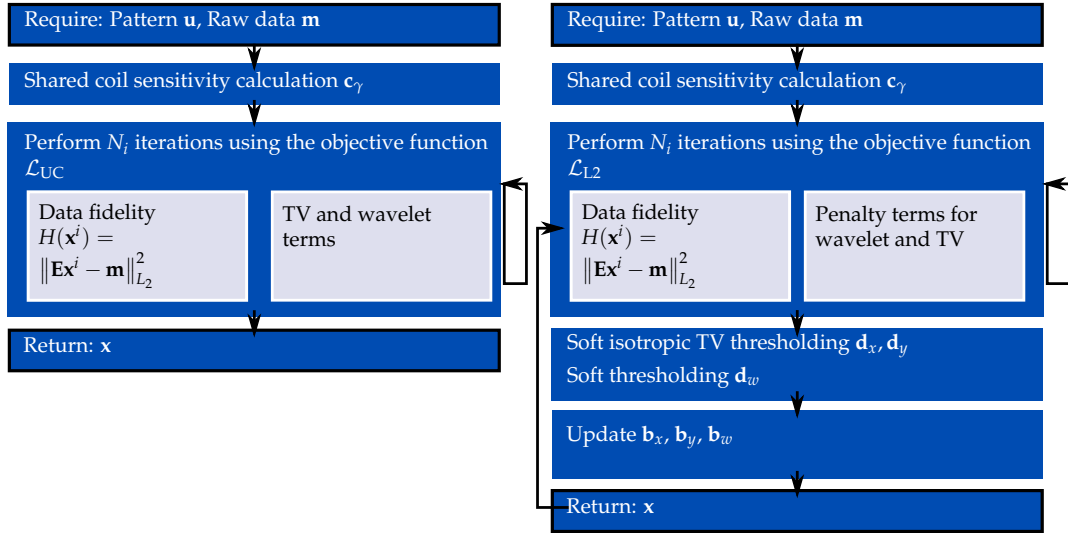


Figure 4.6: Schematic representation of the gradient based and Split Bregman based algorithm.

Application	Algorithm	$N_x \times N_y$	N_z	N_γ	$N_i/N_j/N_i$	Run time [sec]
Peripheral	SB	448×184	32	26	-/5/3	9517.2
Peripheral	GB	448×184	32	26	8/-/-	9250.9
Renal	SB	192×68	156	10	-/5/3	1160.4
Renal	GB	192×68	156	10	5/-/-	693.8

Table 4.1: The run times for the considered GB and SB for the peripheral and renal acquisitions are given with the corresponding parameters.

The complexity of the Split Bregman algorithm is evaluated separately for the three innermost steps, the minimization of the L_2 function using the objective function \mathcal{L}_{L2} , the shrinkage steps and the update of the residual errors. The effort for the objective function \mathcal{L}_{L2} thereby equals to the previously calculated of \mathcal{L} as it is governed again by the Fourier transform. The evaluation of the penalty terms requires uniquely additional additions, wavelet and TV evaluations. The minimization of the L_2 minimization step thus lies within $O(N_i N_\gamma N \log N)$. Both shrinkage and soft thresholding have complexity $O(N)$. The same applies for the update of the residual errors. The total complexity thus equals $O(N_j(N_i N_\gamma N \log N + 2N + N)) = O(N_j N_i N_\gamma N \log N)$.

The run times for the current implementation on a standard notebook with 8.0 GB RAM using a i3-2328M CPU with 2.2GHz are given in Table 4.1. These are measured for the entire reconstruction, but without taking the data I/O and the calculation of the coil sensitivities into account. The Split Bregman algorithm requires for example for a renal 3-D volume with matrix size $N = 192 \times 68 \times 156$ with $N_\gamma = 10$ coils, using TV regularization and performing $N_i = 3$ inner and $N_j = 5$ outer iterations around 19 minutes.

Algorithm 4.3 Gradient based algorithm

Require: $\mathbf{u}, \mathbf{m}, \lambda_t, \lambda_w, \mathcal{L}_{UC}, N_i$ **INPUT:** \mathbf{x}^0

- 1: Calculate combined coil profiles $c_{(\gamma,t)}$
 - 2: **for all** $i = 1$ to N_i **do**
 - 3: Perform optimizer step with the objective function $\mathcal{L}_{UC}(\mathbf{x}^{i-1})$ and its gradient $\nabla \mathcal{L}_{UC}(\mathbf{x}^{i-1})$
 - 4: Calculate the data fidelity term $H(\mathbf{x}^{i-1})$ as illustrated in Figure 4.4
 - 5: Calculate finite differences and evaluate the TV term $TVi(\mathbf{x}^{i-1})$
 - 6: Perform 2nd level wavelet decomposition $W(\mathbf{x}^{i-1})$
 - 7: Evaluate $WV(\mathbf{x}^{i-1})$
 - 8: Update \mathbf{x}^i
 - 9: **end for**
- OUTPUT:** \mathbf{x}^{N_i}
-

Algorithm 4.4 Split Bregman algorithm

Require: $\mathbf{u}, \mathbf{m}, \lambda_t, \lambda_w, \mathcal{L}_{L2}, N_j, N_i$ **INPUT:** \mathbf{x}^0

- 1: **for all** $j = 1$ to N_j **do**
 - 2: $\mathbf{x}^0 = \mathbf{x}^{j-1}$
 - 3: **for all** $i = 1$ to N_i **do**
 - 4: Perform optimizer step with the objective function $\mathcal{L}_{L2}(\mathbf{x}^{i-1})$ and its gradient
 - 5: Calculate the data fidelity term $H(\mathbf{x}^{i-1})$ as illustrated in Figure 4.4
 - 6: Calculate finite differences and evaluate the TV penalty term $TVi(\mathbf{x}^{i-1})$
 - 7: Perform wavelet 2nd level decomposition $W(\mathbf{x}^{i-1})$
 - 8: Evaluate $WV(\mathbf{x}^{i-1})$
 - 9: Update \mathbf{x}^i
 - 10: **end for**
 - 11: Set $\mathbf{x}^j = \mathbf{x}^{N_i}$
 - 12: Perform the shrinkage operations
 - 13: $(\mathbf{d}_x^j, \mathbf{d}_y^j) = s_1(\mathbf{x}^j, \mathbf{b}_x^{j-1}, \mathbf{b}_y^{j-1}, 1/\alpha)$
 - 14: $\mathbf{d}_w^j = s_2(\mathbf{x}^j, \mathbf{b}_w^{j-1}, 1/\alpha)$
 - 15: Update the residual errors
 - 16: $\mathbf{b}_x^j = \mathbf{b}_x^{j-1} + \nabla_x \mathbf{x}^j - \mathbf{d}_x^j$
 - 17: $\mathbf{b}_y^j = \mathbf{b}_y^{j-1} + \nabla_y \mathbf{x}^j - \mathbf{d}_y^j$
 - 18: $\mathbf{b}_w^j = \mathbf{b}_w^{j-1} + W(\mathbf{x}^j) - \mathbf{d}_w^j$
 - 19: **end for**
- OUTPUT:** \mathbf{x}^{N_j}
-

4.5.2 Parameter Choices

The convergence analysis for the proposed optimization methods for the specific pMRI CS reconstruction is hampered by the problem of noise amplification for pMRI. Taking this into account, a solution found as optimal for the stated problem, may not correspond to the desired image result, as the L_2 data fidelity term is not a suitable measure for optimality. A fixed number of iterations for all processed data sets of the same application is chosen in this thesis. The identification of a suitable stopping criteria would be beneficial, but is beyond the scope of this thesis. The same holds true for the chosen regularization parameters λ . While they are optimized for the presented cases, and fixed over all data sets, they may need to be chosen differently for data from further manufacturers, different protocols or further setup modifications.

In the experiments in Chapter 5 and Chapter 6, the gradient based (GB) and Split Bregman (SB) reconstruction will be applied to accelerate peripheral and renal data sets. In this purpose, the parameters given for the GB methods will all be based on the objective function in Eq. (4.18) and the minimization problem formulated in Eq. (4.19). The parameter thus include N_i , λ_t and λ_w .

For SB, the minimization problem of interest is formulated in Eq. (4.52). The relevant parameters are the number of Split Bregman iterations N_j , the number of quasi newton iterations used to solve the L_2 problem N_i and the regularization weights. Thereby, to limit redundancy and without any loss of freedom, the weights μ, α are chosen as $\mu = 1.0$ and $\alpha = 2.0$ and the TV and wavelet weights are referred to by λ_t^{SB} and λ_w^{SB} .

4.6 Summary and Conclusion

The algorithmic elements for a novel iterative algorithm for static nceMRA techniques, focusing explicitly on high acceleration factors, were presented in this section. These include an parametrizable analytical sampling strategy, called MICCS pattern combining elements of multi-coil pMRI methods with the requirements of Compressed Sensing. Furthermore, the Split Bregman for the pMRI-CS problem, regularized with isotropic TV and wavelets, was formulated. The following chapters present the data and the evaluation techniques used for the comparison of the proposed algorithmic elements as well as the results for both peripheral and renal acquisitions.

Accelerated 2-D Peripheral NceMRA

5.1 Motivation	67
5.2 Data and Evaluation	68
5.3 Evaluation of the MICCS Sampling Strategy	70
5.4 Highly Accelerated NceMRA of the Peripheral Arteries	72
5.5 Summary and Conclusions	74

The proposed MICCS pattern in combination with the Split Bregman algorithm is applied in this Chapter to 2-D peripheral TOF data from 10 volunteers. The pattern is compared to further sampling strategies and the influence of the algorithm is evaluated. Finally, the clinical usability is shown with accelerated acquisitions of the entire lower vasculature.

5.1 Motivation

Peripheral arterial occlusive disease is a cardiovascular disease with high prevalence [Juer 63]. Comprehensive visualization, typically covering the abdominal aorta and iliac arteries, the femoral and popliteal arteries down to the tibial and fibular arteries, is required for its diagnosis and management.

An electrocardiography (ECG) triggered 2-D TOF sequence provides a non-invasive alternative to commonly used invasive techniques. It offers both high resolution and excellent vascular contrast. The reasons for a 2-D rather than a 3-D acquisition scheme are physiologically motivated. As explained in section 2, the TOF contrast depends on the inflow of unsaturated spins, resulting in a need for an inflow of blood into the imaging slice during the acquisition. Another important parameter is the thickness of the imaging area. Thicker slices yield to a more significant saturation, observed even for flowing spins that experience pulses while travelling within the volume. These two constraints apply especially in the periphery due to the highly pulsatile arterial inflow profile. Furthermore, studies in patients with stenosis in the peripheral vasculature showed damped arterial flow profiles in the femoral arteries with a significantly reduced systolic peak [Wiks 07], contributing to further saturated vascular signal in thick slices.

5.2 Data and Evaluation

Data sets from the peripheral arteries were acquired on clinical 3T MR Scanners (MAGNETOM Trio A Tim System, MAGNETOM Skyra, Siemens Healthcare Sector, Erlangen) in 10 healthy volunteers.

5.2.1 Peripheral TOF Data Acquisition

Peripheral data sets were acquired in 10 volunteers using an ECG-triggered 2-D sequence and a 36-channel peripheral coil. To evaluate the image quality achieved with the presented algorithms, the data sets were fully sampled so that they can be used as a reference. Two different types of data sets were acquired, specified by protocols Peri I and Peri II. Protocol Peri I acquires data sets from 4 slices from the region below the bifurcation of the popliteal artery into arterial and posterior tibial and the origin of the peroneal artery as shown in Figure 5.1(a). Used parameters were an in-plane FOV of $448 \text{ mm} \times 448 \text{ mm}$ and a matrix size of 460×460 leading to a resolution of $0.97 \text{ mm} \times 0.97 \text{ mm}$. With the second protocol Peri II, data from the entire upper and lower peripheral vasculature is acquired in 3 steps with 128 slices each as depicted in Figure 5.1(a). Using this protocol, data sets were acquired in 5 volunteers. The FOV was chosen as small as possible as $448 \text{ mm} \times 168 \text{ mm}$ which is sufficient for covering the volunteer anatomy. Together with a matrix size of 448×184 the in-plane resolution equals $1 \text{ mm} \times 0.9 \text{ mm}$. Further imaging parameters for both data sets were $TE / TR = 5 \text{ ms} / 34.7 \text{ ms}$ and a slice thickness of 2 mm . In total 384 slices were acquired for these data sets in three table positions with 128 slices each.

5.2.2 Volume Based Evaluation

The obtained result vectors \mathbf{x} were quantitatively analysed and compared to the reference \mathbf{r} both using quantitative volume based measures as well as specific organ based evaluations. The image quality was compared to the fully sampled reference using the Normalized Root Mean Squared Error (NRMSE) and the Structured Similarity (SSIM). The measures were calculated as

$$\begin{aligned} \text{NRMSE}(\mathbf{r}, \mathbf{x}) &= \frac{1}{N} \|\mathbf{r} - \mathbf{x}\|_{L_2} \text{ and} \\ \text{SSIM}(\mathbf{r}, \mathbf{x}) &= \left(\frac{2\mu(\mathbf{r})\mu(\mathbf{x}) + c_1}{\mu(\mathbf{x})^2 + \mu(\mathbf{r})^2 + c_1} + \frac{\text{cov}(\mathbf{x}, \mathbf{r}) + c_2}{\sigma(\mathbf{r})^2 + \sigma(\mathbf{x})^2 + c_2} \right), \end{aligned}$$

where $\mu(\mathbf{x}) \in \mathbb{R}$ is the mean value of \mathbf{x} , $\sigma(\mathbf{x}) \in \mathbb{R}$ the standard deviation of \mathbf{x} and $\text{cov}(\mathbf{x}, \mathbf{r}) \in \mathbb{R}$ the covariance between \mathbf{x} and \mathbf{r} .

Furthermore, more specific angiographic evaluation was employed using Contrast to Noise Ratios (CNR). For the CNR, a background region (\mathbf{x}_b) outside the object was chosen as well as a tissue (\mathbf{x}_t) and a vascular region of interest (\mathbf{x}_v). The tissue region in the peripheral data sets was a quadratic region within the soleus muscle and the femoral artery was chosen to provide vascular contrast as

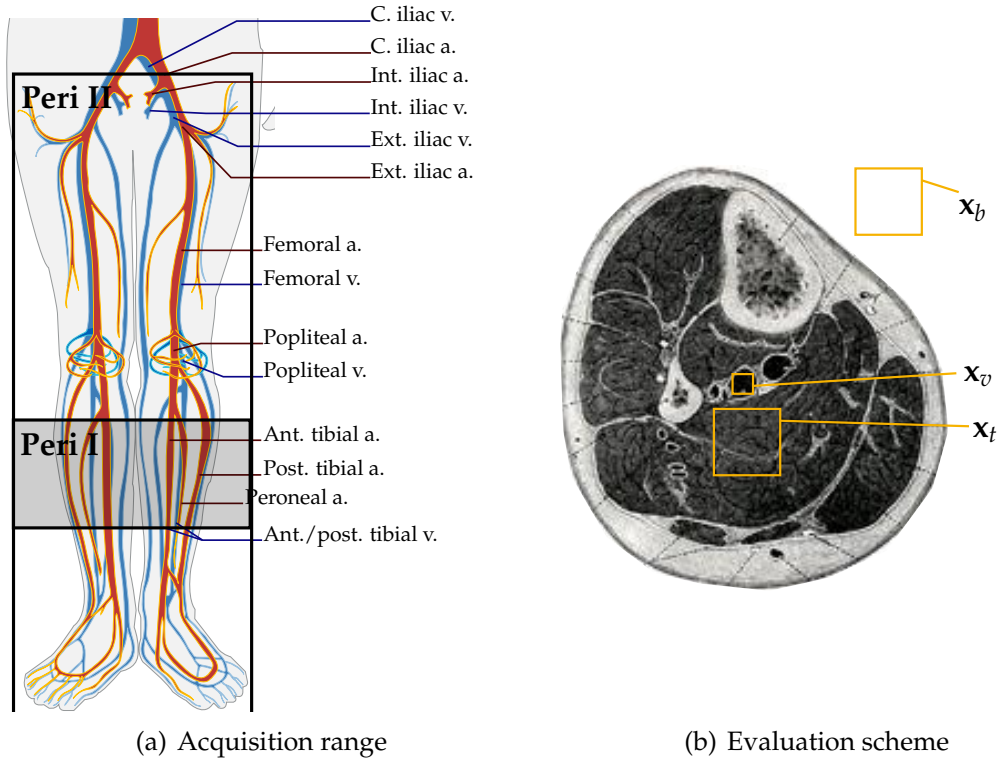


Figure 5.1: Vascular system of the lower extremities. (a) Covered range in head-foot direction for the protocols Peri I and Peri II. (b) Schematic evaluation scheme. Images adapted from [Gray 01].

depicted in Figure 5.1(b). The CNR values for vessel-tissue (CNRVT) and vessel-background (CNRVB) equal

$$\text{CNRVT}(\mathbf{x}_v, \mathbf{x}_t) = \left(\frac{\mu(\mathbf{x}_v) - \mu(\mathbf{x}_t)}{\sqrt{0.5(\sigma(\mathbf{x}_v)^2 + \sigma(\mathbf{x}_t)^2)}} \right) \text{ and}$$

$$\text{CNRVB}(\mathbf{x}_v, \mathbf{x}_b) = \left(\frac{\mu(\mathbf{x}_v) - \mu(\mathbf{x}_b)}{\sqrt{0.5(\sigma(\mathbf{x}_v)^2 + \sigma(\mathbf{x}_b)^2)}} \right).$$

5.2.3 Organ Based Evaluation

In addition to the described image based evaluation, additional organ based measures were evaluated. This organ- rather than volume - based approach analyses the depiction of the peripheral arteries. Therefore, the Vessel Sharpness Index (VSI) was evaluated. The VSI calculation is based on the method proposed by Li. et al. for the coronar arteries [Li 01], by analyzing the signal intensity projection across the diameter of the vessel.

5.3 Evaluation of the MICCS Sampling Strategy

The reconstruction experiments conducted with both the peripheral and renal data described above had the purpose to investigate both the proposed sampling strategy and the choice of the reconstruction algorithm. In a first step, the proposed MICCS sampling strategy is evaluated broadly compared to further patterns providing the same acceleration. In the next experiment, the pattern was applied in combination with the GB and SB algorithms to the presented application of interest. Reference volumes $\mathbf{r} \in \mathbb{C}^N$, obtained by direct reconstruction of the fully sampled datasets with SoS were used for all experiments. Finally, the clinical usability and applicability is shown with full leg acquisitions as they are performed for example for the diagnosis and treatment decision for peripheral occlusive disease.

5.3.1 Experimental Setup

The proposed sampling pattern is evaluated by reconstructing all Peri I data sets with six different patterns, all corresponding to the same acceleration factor of 6, corresponding to 76 phase encoding lines of 460. The analysed patterns are schematically illustrated in Figure 5.2. Beside the full sampling Full (Figure 5.2(a)) the proposed MICCS pattern (Figure 5.2(b)) with a center with size $N_{k_{cy}} = \lfloor 0.1 \cdot N_{k_y} \rfloor$ and under sampling $d_{cy} = 2$, two patterns with a regularly sampled periphery Reg1 and Reg2 (Figure 5.2(c)-5.2(d)) and two with randomly sampled periphery Ran1 and Ran2 (Figure 5.2(e)-5.2(f)) were included. Thereby, the center of the Reg1 and Ran1 was fully sampled, while Reg2 and Ran2 were constructed with the same central under sampling as MICCS. The used reconstruction algorithm was the iterative unregularized SENSE algorithm (ISENSE) with $N_i = 8$.

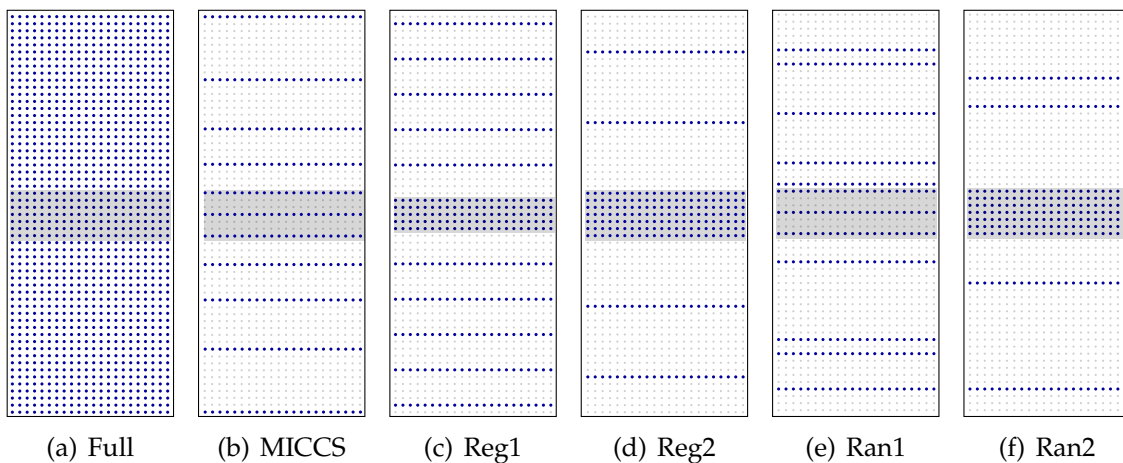


Figure 5.2: Schematic illustration of the different patterns with the under sampling factor of 6. Besides the full sampling Full in (a) and the proposed MICCS pattern in (b), two regular under sampled patterns Reg1 and Reg2 are shown in (c) and (d) as well as two randomly under sampled patterns Ran1 and Ran2 in (e) and (f).

5.3.2 Results

The quantitative results for the different pattern choices are given in Tables 5.1 and 5.2 and representative image results for one slice are illustrated in Figure 5.3.

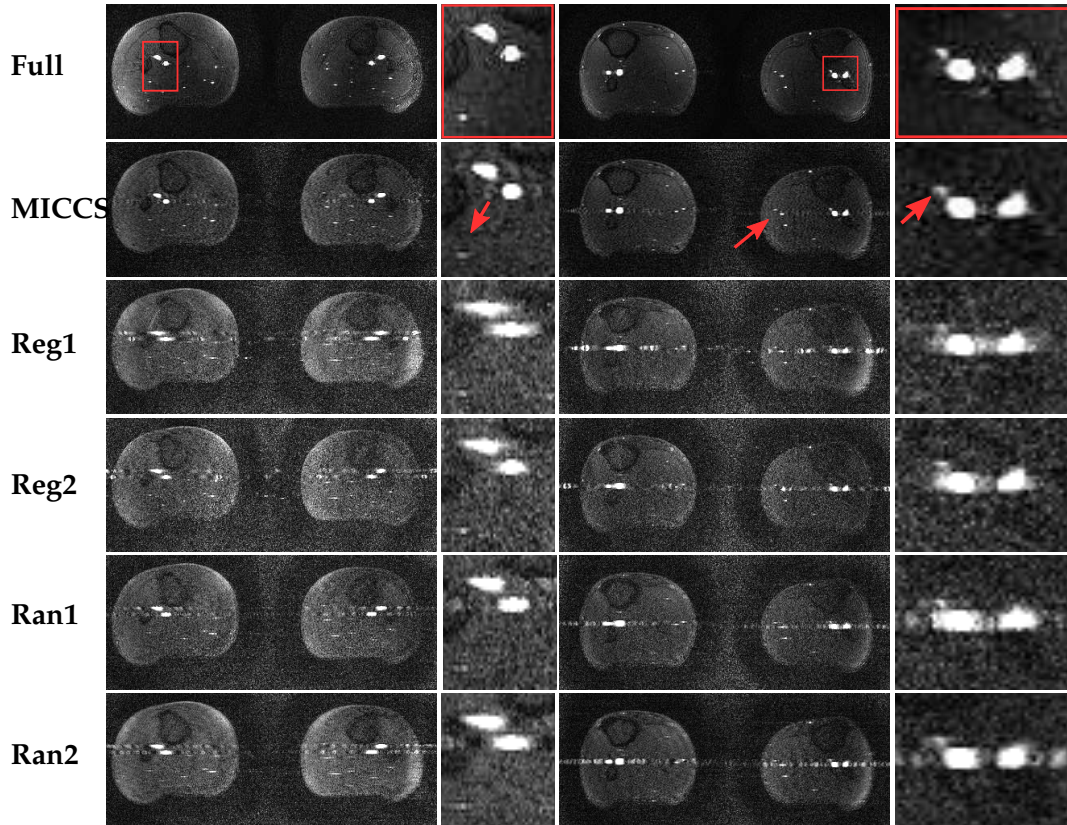


Figure 5.3: Representative image results for the in-vivo study for the reference and six different under sampling patterns with an acceleration of 6. The first column shows results for volunteer 1 along with a zoom to the left leg in the middle column. The right column illustrates results for volunteer 2 along with a zoom to the right leg.

The image results in Figure 5.3 show the increased vessel sharpness and general enhanced image quality of the proposed MICCS pattern in comparison to the further patterns. The red arrows indicate small vascular structures, well depicted with the MICCS, but barely visible using the regular or random under sampling patterns. Furthermore, the noise and aliasing artefacts are visibly reduced for MICCS, and the image impression manages well to recover the fully sampled reference in the first row of Figure 5.3. The visual result of a better image impression corresponds well with the quantitative results in Table 5.1. The NRMSE of the MICCS pattern of 0.029 ± 0.003 was decreased by 42% compared to the next best comparison method regarding NRMSE, Ran1, with 0.050 ± 0.006 , the SSIM increased from 0.056 ± 0.008 for Ran2 to 0.959 ± 0.013 by 8.7%. The CNR values reached values of 32.401 ± 18.225 and 31.707 ± 14.910 , which corresponds to an increase of 22% respectively 26% in the mean compared to Ran1. The CNR values, however, vary significantly over the data sets. Furthermore, the sharpness value for VSI amounted to 0.239 ± 0.039 , nearly reaching the reference with 0.279 ± 0.046 .

Method	NRMSE	SSIM
Ref	0.000 ± 0.000	1.000 ± 0.000
MICCS	0.029 ± 0.003	0.959 ± 0.013
Reg1	0.070 ± 0.012	0.793 ± 0.047
Reg2	0.061 ± 0.012	0.830 ± 0.048
Ran1	0.050 ± 0.006	0.854 ± 0.039
Ran2	0.056 ± 0.008	0.882 ± 0.024

Table 5.1: Quantitative image and vessel sharpness index evaluation for the in-vivo study. The reference was used to calculate the normalized root mean square error and the structural similarity for all patterns.

Method	CNRVT	CNRVB	VSI
Ref	30.190 ± 15.942	34.714 ± 19.416	0.279 ± 0.046
MICCS	32.401 ± 18.225	31.707 ± 14.910	0.239 ± 0.039
Reg1	24.301 ± 12.417	19.881 ± 6.885	0.173 ± 0.046
Reg2	23.837 ± 13.153	21.674 ± 8.461	0.198 ± 0.050
Ran1	26.486 ± 13.941	25.112 ± 9.832	0.177 ± 0.044
Ran2	23.791 ± 10.920	22.378 ± 7.422	0.171 ± 0.041

Table 5.2: Quantitative image and vessel sharpness index evaluation for the in-vivo study. The contrast-to-noise ratio between vessel and background and vessel and tissue as well as the vessel sharpness index were evaluated for all six pattern reconstruction results.

This corresponds to an increase of 20% in reference to the best comparison method regarding sharpness, Reg2, with 0.198 ± 0.050 .

In summary, the study of different under sampling patterns showed significant benefits for the proposed MICCS pattern. Its major advantages are its analytical and flexible generation as well as the excellent results regarding sharpness, NRMSE and SSIM.

5.4 Highly Accelerated NceMRA of the Peripheral Arteries

After the evaluation of the pattern in the previous section, the entire proposed method, consisting of the MICCS pattern and the Split Bregman algorithm, will be in the focus of this section.

Parameters	Full	ISENSE	SB _{TV}	SB _W	SB _{TV-W}	GB _{TV}	GB _W	GB _{TV-W}
$\lambda_t / \lambda_t^{SB}$	n.a.	0.0	0.002	0.0	0.002	0.002	0.0	0.002
$\lambda_w / \lambda_w^{SB}$	n.a.	0.0	0.0	0.001	0.001	0.0	0.001	0.001
N_i	n.a.	5	n.a.	n.a.	n.a.	8	8	8
N_j / N'_i	n.a.	n.a.	5/3	5/3	5/3	n.a.	n.a.	n.a.

Table 5.3: Weighting parameters for the reconstructions.

5.4.1 Experimental Setup

The comparison of the SB and GB algorithm for high acceleration factors of 12 is in the focus for the following reconstruction. The data sets acquired with protocol Peri I were used in combination with the MICCS sampling scheme. The result of the fully sampled reference reconstruction is compared to different reconstruction results based MICCS pattern. The reconstruction problems are formulated as discussed in Section 4.5.2. The raw data is reconstructed first using an unregularized iterative SENSE algorithm (ISENSE). Then, two different ways are applied: using a gradient-based (GB) solver operating on the unconstrained function (Algorithm 4.3) with $N_i = 8$ and the proposed split formulation with the Split Bregman algorithm (SB) (Algorithm 4.4) with $N'_i = 3$ and $N_j = 5$.

Both reconstruction pathways were combined with total variation regularization (GB_{TV}, SB_{TV}), with wavelet regularization (GB_W, SB_W) and with the combination of both (GB_{TV-W}, SB_{TV-W}). The regularization weights λ_t and λ_w , respectively λ_t^{SL} and λ_w^{SL} and the iteration numbers were optimized to low NRMSE for each of the combinations and kept fixed over all data sets. The chosen settings are given in Table 5.3.

To demonstrate the diagnostic usability, the data sets acquired with protocol Peri II, including the data from the entire lower peripheral vasculature are reconstructed. Maximum intensity projections (MIP) are generated in axial direction to evaluate the visualization of the vessels along the entire leg.

5.4.2 Results

Tables 5.4 and 5.5 state the calculated quantitative results for the algorithm study. Comparisons are possible both between SB and GB as well as between the different regularization terms. The best result was obtained using the SB algorithm with both wavelet and TV regularization (SB_{TV-W}). The NRMSE was reduced by 76% compared to ISENSE and by 40.5 % compared to the GB method using the same regularizations. The CNR increased for SB in the mean by roughly 30% and the VSI by 64% compared to (GB_{TV-W}). These values are very similar to those obtained by (SB_{TV}). The errors for the SB_W results are higher, the CNR and SSIM lower even compared to the GB_W results. The discrepancies between different regularizers are less prominent in the GB results. There is, however, a difference observable in favour of the TV-based variants. Those results correspond well to the image based findings of two representative volunteers in Figure 5.4, depicting an axial

Method	NRMSE	SSIM
Ref	0.000 ± 0.000	1.000 ± 0.000
ISENSE	0.0652 ± 0.102	0.817 ± 0.036
SB_{TV}	0.0153 ± 0.004	0.991 ± 0.003
SB_W	0.0715 ± 0.020	0.788 ± 0.002
SB_{TV-W}	0.0152 ± 0.004	0.991 ± 0.003
GB_{TV}	0.0400 ± 0.008	0.931 ± 0.020
GB_W	0.051 ± 0.009	0.885 ± 0.028
GB_{TV-W}	0.0405 ± 0.008	0.929 ± 0.001

Table 5.4: Quantitative image and vessel sharpness index evaluation for the in-vivo study. The reference was used to calculate the normalized root mean square error and the structural similarity for all patterns.

slice for all eight discussed reconstruction techniques. The SB_{TV} and SB_{TV-W} show a suppressed background noise, nice delineation of the vascular structures and sharp vessel borders.

Finally, the maximum intensity projection results obtained with SB_{TV-W} for the protocol Peri II in Figure 5.5 illustrate the diagnostic usability of the proposed method. The results for the entire lower vasculature are shown for volunteers 2 and 3 in Figures 5.5(a) and 5.5(b). The smaller vessels are accurately depicted, as can be well observed with the arrows indicating the perforating branches of the femoral artery. Furthermore, the vessels of the lower leg, the anterior, posterior and peroneal artery are indicated equivalently with red arrows. The results from the region around the trifurcation are depicted for volunteers 1 and 4 in Figures 5.5(c) and 5.5(d).

5.5 Summary and Conclusions

Several algorithmic elements were proposed in this chapter, including a fully analytical k -space sampling pattern. Combined from a regularly under sampled k -space center and a periphery with density decreasing towards higher k -space values. It showed to produce results with high sharpness, SSIM and low NRMSE values. The formulation of the pattern offers a wide range of possible sampling schemes with decreasing density. Furthermore, the Split Bregman algorithm was introduced for combined CS-pMRI algorithms with TV and wavelet-based regularization. Experiments involving 10 data sets showed the decrease of the imaging time by a factor of 12 using the proposed strategy. The reconstructions done with the entire lower leg vasculature showed its clinical usability, as it depicted very well both the main peripheral arteries and the perforating branches by accelerating the imaging time significantly.

Method	CNRVT	CNRVB	VSI
Ref	37.540 ± 20.267	43.557 ± 27.601	0.292 ± 0.025
ISENSE	30.775 ± 10.824	26.304 ± 06.527	0.178 ± 0.034
SB _{TV}	43.218 ± 24.753	46.140 ± 23.372	0.296 ± 0.067
SB _W	25.934 ± 07.884	24.326 ± 05.253	0.186 ± 0.034
SB _{TV-W}	43.184 ± 24.374	45.950 ± 22.714	0.300 ± 0.072
GB _{TV}	33.987 ± 14.134	33.619 ± 10.502	0.182 ± 0.040
GB _W	28.509 ± 15.000	28.630 ± 13.286	0.164 ± 0.056
GB _{TV-W}	33.180 ± 12.524	33.396 ± 10.278	0.182 ± 0.039

Table 5.5: Quantitative image and vessel sharpness index evaluation for the in-vivo study. The CNR between vessel and background and vessel and tissue as well as the VSI were evaluated for all seven reconstruction results.

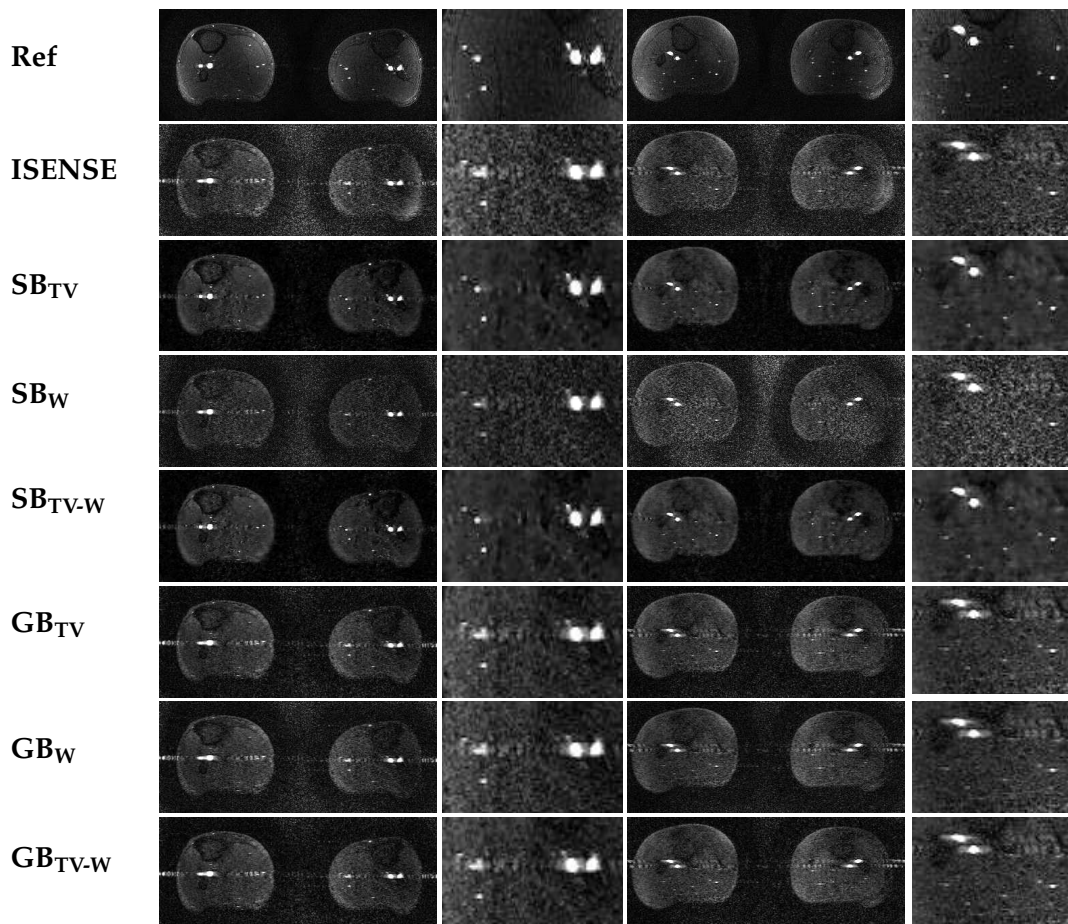


Figure 5.4: Representative image results for the in-vivo study for the reference and six different reconstruction methods with an acceleration of 12. The first columns shows results for volunteer 1, column 3 and 4 results for volunteer 2.

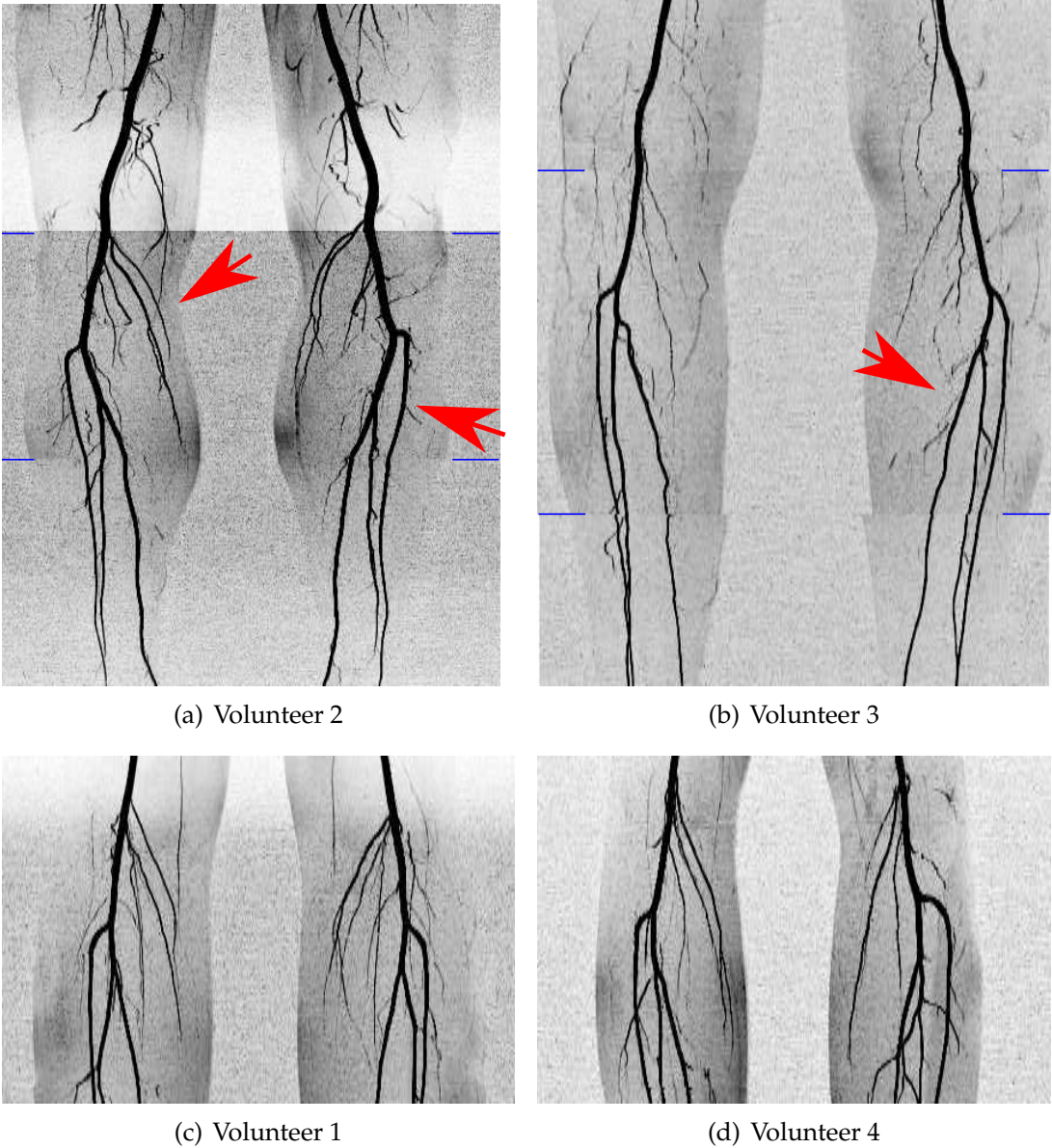


Figure 5.5: Exemplary image results for the Peri II data set for volunteers 1-4.

Accelerated 3-D Renal NceMRA

6.1 Motivation	77
6.2 Data and Evaluation	78
6.3 Acceleration Study	79
6.4 Highly Accelerated NceMRA of the Renal Arteries	80
6.5 Comparison With Clinical State of the Art	81
6.6 Discussion	83
6.7 Summary and Conclusion	83

In this chapter, the method proposed in Chapter 4, which combines a highly under sampled analytical pattern and an iterative Split Bregman-based reconstruction, is applied to 3-D free-breathing renal acquisitions. The purpose of this study is threefold: (i) Feasible acceleration factors using the novel MICCS pattern are determined for this application, (ii) TV regularization in combination with the gradient based and Split Bregman algorithms is evaluated and (iii) the proposed iterative method is compared with clinically used SENSE and GRAPPA methods. These experiments are extensively evaluated using a quantitative volume- and organ-based approach, focusing on the diagnostic value of the obtained results.

6.1 Motivation

Cardiovascular renal diseases such as renal artery stenosis or others are major causes for severe renal insufficiency or malfunction. In the worst case, failure in identifying them early enough may result in the need for extracorporeal dialysis or even kidney transplantation [Herb 06]. Angiographic examinations of the renal arteries, from the aorta, the ostium, the main trunk until the peripheral second and third order branches, therefore play a major role for accurate diagnosis and treatment planning at an early stage.

High resolution balanced Steady State Free Precession (bSSFP) techniques combined with respiratory gating have been described for a non-invasive patient-friendly renal angiography. As shown in multiple studies in the past years, its results are comparable to DSA and ceMRA [Maki 07, Wytt 07, Mohr 10, Liu 09a,

Lanz 09]. The method does not require breath holds and is therefore well adapted for non-cooperative patients such as children or patients in pain.

6.2 Data and Evaluation

The used renal data sets obtained in a total of 10 volunteers and the organ-based evaluation strategy are presented in this section.

6.2.1 Renal mp-bSSFP Data Acquisition

Non-contrast-enhanced renal angiography data sets were acquired with an IR-prepared 3-D bSSFP technique [Wytt 07, Kato 04] using the standard body and spine matrix coils of the system (six elements with two rings each) on clinical 3T MR Scanners (MAGNETOM Trio A Tim System, MAGNETOM Skyra, Siemens Healthcare Sector, Erlangen, Germany) in ten healthy volunteers. The acquisition was free-breathing and respiratory-triggered with a respiration belt. The readout direction was chosen from left to right. An inversion slab was applied to suppress both venous blood originating from the vena cava and stationary background tissue. The thickness of the 3-D slab in z-direction was chosen depending on the individual position and size of the kidneys and the tipping between right and left kidney, as illustrated in Figure 6.1(a). Therefore for this parameter a range is given.

High resolution data (protocol Renal I) was acquired in four volunteers. The imaging parameters included an imaging matrix of $480 \times 480 \times [60,90]$, a FOV of $256 \text{ mm} \times 256 \text{ mm} \times [120 \text{ mm}, 180 \text{ mm}]$, TI of 1300 ms, TE / TR = 1.640 ms / 1451 ms and a flip angle of 90° . Furthermore, for the comparison with clinically available acceleration techniques SENSE and GRAPPA three datasets were acquired in each of the remaining six volunteers with the Renal II protocol: A fully sampled reference dataset, a GRAPPA dataset using an under sampling factor of $\xi = 6$ and a SENSE dataset, equivalently accelerated by a factor of $\xi = 6$. For these datasets, imaging parameters included an imaging matrix of $192 \times 265 \times [60,90]$, a FOV of $256 \text{ mm} \times 256 \text{ mm} \times [120 \text{ mm}, 180 \text{ mm}]$, TI of 1300 ms, TE / TR = 1.570ms / 2200ms and a flip angle of 90° .

6.2.2 Evaluation Strategy

The obtained vectors, written as previously as result vectors $\mathbf{x} \in \mathbb{C}^N$, were quantitatively analysed and compared to the reference $\mathbf{r} \in \mathbb{C}^N$ using both quantitative volume based measures and specific organ based evaluations. The image quality was compared to the fully sampled reference using the Normalized Root Mean Squared Error (NRMSE) and the Structured Similarity (SSIM) as presented in Section 5.2.2 for the entire 3-D volume. The vessel sharpness index (VSI) was evaluated in two axial cross sections of the aorta, pre- and post-bifurcation ($\mathbf{a}_{pr}, \mathbf{a}_{po}$), and two sagittal cross sections of the main right and left renal arteries (RRA, LRA) ($\mathbf{ra}_r, \mathbf{ra}_l$), as illustrated in Figure 6.1(b). The sharpness values at these locations were added to obtain cumulative sharpness results for the aorta $VSI_a \in \mathbb{R}$ and the renal arteries $VSI_{ra} \in \mathbb{R}$.

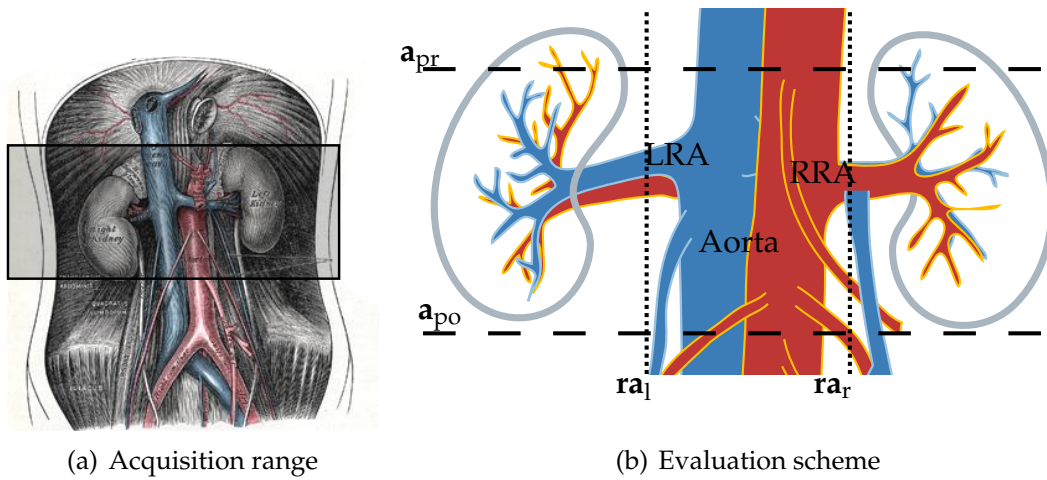


Figure 6.1: (a) The 3-D imaging slab is presented and (b) the organ-based evaluation including the sharpness and contrast at four chosen localizations are illustrated in the schematical illustration of the renal vasculature. Images adapted from [Gray 01].

Acceleration	$\zeta = 1$	$\zeta = 3$	$\zeta = 6$	$\zeta = 9$	$\zeta = 12$
Encoding lines	28800	9412	4800	3179	2382
Time volunteer 1	8:45	2:55	1:28	0:58	0:44

Table 6.1: Encoding steps and re-calculated acquisition times for the renal acquisitions.

$$VSI_a = VSI_{a_{pr}} + VSI_{a_{po}} \quad \text{and} \quad (6.1)$$

$$VSI_{ra} = VSI_{ra_l} + VSI_{ra_r}. \quad (6.2)$$

6.3 Acceleration Study

The influence of the acceleration factor on the image and diagnostic quality of the results was evaluated with the high-resolution datasets acquired with protocol Renal I. The fully sampled data was reconstructed using SoS. Then, the fully sampled data was under sampled with factors $\zeta = 3, 6, 9,$ and 12 using the novel MICCS pattern. These accelerated data sets were reconstructed using the iterative unregularized SENSE reconstruction (ISENSE). Results for volunteer 1 are shown in Figure 6.2. The two top rows illustrate the results for two axial slices within the kidney and perpendicular to the main left renal artery. Following in the 3rd and 4th row are the axial and coronal MIPs. The last row shows details of the fine peripheral renal vasculature as well as the main left renal arteries. Even if a loss in image quality is observable for higher accelerations, the image results even for higher factors such as $\zeta = 9$ and $\zeta = 12$ depict the aorta, main trunks and peripheral renal arteries.

Acceleration	NRMSE	SSIM	VSI _a	VSI _{ra}
Reference	0.000 ± 0.000	1.000 ± 0.000	0.252 ± 0.060	0.267 ± 0.025
$\xi = 3$	0.087 ± 0.017	0.871 ± 0.041	0.189 ± 0.027	0.241 ± 0.016
$\xi = 6$	0.101 ± 0.019	0.867 ± 0.042	0.158 ± 0.007	0.189 ± 0.033
$\xi = 9$	0.106 ± 0.018	0.865 ± 0.043	0.165 ± 0.020	0.156 ± 0.032
$\xi = 12$	0.123 ± 0.021	0.861 ± 0.046	0.130 ± 0.031	0.091 ± 0.013

Table 6.2: Quantitative evaluation for the renal acceleration study.

The correlating acceleration factors and the resulting acquisition times are given in Table 6.1 for volunteer 1 both in absolute number of phase encoding lines as well as with the acquisition times. The times depend on the breathing pattern of the patient, therefore the relative acceleration should be regarded.

The quantitative values in Table 6.2 show the increase of NRMSE, the loss of SSIM and the decrease in VSI with growing acceleration factor. The sharpness is illustrated furthermore in Figure 6.3 with zoomed visualizations of the positions where the sharpness was evaluated, thus the upper and lower aorta and the right and left renal artery. Both the preserved sharpness even for higher factors, as well as the influence of the iterative reconstruction on the quality of the data sets are visible.

6.4 Highly Accelerated NceMRA of the Renal Arteries

After the acceleration study performed in the previous section, the reconstruction algorithm is in the focus of this section.

6.4.1 Experimental Setup

The high-resolution data sets were reconstructed directly using SoS and under sampled with a factor of $\xi = 9$ and reconstructed with the iterative unregularized SENSE method (ISENSE). Then, both the gradient based iterative SENSE algorithm (GB_{TV}) and the proposed Split Bregman reconstruction (SB_{TV}) with total variation regularization were applied as formulated in Section 4.5.2. The regularization weights were optimized to the lowest NRMSE for each algorithm to ensure fair comparison. The TV weights for the GB_{TV} were optimized in the range of $\lambda_t \in [0.0, 0.01]$ and the optimal weight was found to be $\lambda_t = 0.001$. For SB_{TV}, the range was $\lambda_t^{SL} \in [0.0, 0.1]$, with the chosen best value at $\lambda_t^{SL} = 0.005$. Only TV regularization was chosen as a result of the obtained results for peripheral data in Section 5.4.2.

6.4.2 Results

The axial and coronal MIPs obtained from all four algorithms are shown in Figure 6.4 with detail views of the interesting regions in the last row. They illustrate the advantages of the SB_{TV} algorithm in combination with the MICCS pattern. The general image quality is good in the nine-fold accelerated ISENSE reconstruction, but losses in the vessel sharpness can be identified both in the main renal arteries as well as in the small peripheral renal arteries as indicated by red arrows. In addition, the contrast between the vascular structures and the background is corrupted by the reconstruction, resulting in a loss of details. The GB_{TV} algorithm does not manage to recover these issues. The smoother image impression is counteracted by an additional loss of small structures, indicated again by the red arrows. The improvement of the SB_{TV} algorithm is noticeable both in the recovery of small peripheral vessels as well as in the improved sharpness of the main renal branches. These improvements correspond well to the reported quantitative values given in Table 6.3. The NRMSE improved slightly for GB_{TV} compared to ISENSE from 0.106 to 0.105, the SSIM improved from 0.865 to 0.878. However, the sharpness values confirmed the visual image impressions as they decreased from 0.165, respectively 0.156 to 0.140 and 0.125. The proposed SB_{TV} algorithm improved both the image quality measures NRMSE by about 25% and the structured similarity of around 10%. The most significant results regard the sharpness measures, which were improved compared to the ISENSE method by 56 % and 95% and relative to the GB_{TV} reconstruction even by 32 % and 60%. The reported acceleration factor of 9, corresponds to a reduction in the imaging time from 8 minutes and 45 seconds to 58 seconds.

Method	NRMSE	SSIM	VSI_a	VSI_{ra}
Reference	0.000 ± 0.000	1.000 ± 0.000	0.252 ± 0.060	0.267 ± 0.024
ISENSE	0.106 ± 0.018	0.865 ± 0.043	0.165 ± 0.020	0.156 ± 0.032
GB_{TV}	0.105 ± 0.018	0.870 ± 0.042	0.140 ± 0.027	0.125 ± 0.030
SB_{TV}	0.075 ± 0.004	0.949 ± 0.021	0.219 ± 0.058	0.250 ± 0.088

Table 6.3: Quantitative evaluation for the algorithm study using renal datasets.

6.5 Comparison With Clinical State of the Art

In this section, the proposed algorithm is evaluated in data sets from volunteers, where a fully sampled scan, as well as clinical GRAPPA and SENSE acquisitions were performed.

6.5.1 Experimental Setup

The additional GRAPPA and SENSE datasets acquired with acceleration factor 6 were reconstructed using clinically available internal reconstruction. The fully

Method	NRMSE	SSIM	VSI _a	VSI _{ra}
Reference	0.000 ± 0.000	1.000 ± 0.000	0.270	0.316
ISENSE	0.125 ± 0.012	0.43 ± 0.086	0.232	0.234
SB_{TV}	0.117 ± 0.014	0.744 ± 0.090	0.247	0.254
GRAPPA	–	–	0.190	0.132
SENSE	–	–	0.088*	0.014*

Table 6.4: Quantitative evaluation for the study comparing the proposed algorithm with the reference and clinically used SENSE and GRAPPA algorithms. The stars for the SENSE sharpness results indicate, that the quality of two datasets reconstructed with SENSE did not allow to calculate the sharpness indices.

sampled datasets were retrospectively under sampled using the dedicated pattern with acceleration factor 6. This results in sampling 1920 instead of 11520 phase encoding lines for the dataset with matrix size $192 \times 265 \times 60$. Finally, the under sampled data was reconstructed with ISENSE where $N_i = 5$ and with SB_{TV} where $N'_i = 3, N_j = 5$ and $\lambda_t^{SL} = 0.001$.

6.5.2 Results

Quantitative results for the comparison are given in Table 6.4. The NRMSE and SSIM are reported for the iteratively reconstructed algorithms.

The physiologically motivated sharpness values were evaluated at the previously described locations for all five algorithms. Thereby, two of the SENSE results did not allow vessel sharpness evaluation due to the poor image quality. The resulting sharpness values for SB_{TV} were close to the reported reference values, but were significantly lower for the GRAPPA and SENSE method. The aortic sharpness values decreased from 0.247 for SB_{TV} over 0.190 for GRAPPA to 0.088 for SENSE. These performances are also observable in the reconstructed results for all four vessel sharpness locations shown in Figure 6.5. These figures were done in colour to better illustrate the differences. While the SB_{TV} results provide a very clear depiction of the arteries, the GRAPPA results are corrupted by noise especially in the aorta and the SENSE results do not allow any depiction of the vessels. Finally, axial slices for all five discussed methods are illustrated in Figure 6.6 with a zoom to the left kidney. The SB_{TV} results depict nicely the aorta and main renal artery as well as peripheral smaller branches. The increased sharpness compared to ISENSE is as well visible, While the GRAPPA results visualized the aorta and the main branch, significant noise enhancement is observable and the peripheral branches are lost. The SENSE result does not provide visualization of the renal arteries when performed with the used acceleration factor of $\xi = 6$.

6.6 Discussion

The shown results illustrate the performance of the proposed combination of the novel MICCS pattern and the SB_{TV} algorithm. The acceleration study showed its capacity to produce very good results for high acceleration factors. The evaluation of the GB_{TV} and the SB_{TV} algorithms underlined the ability of the Split Bregman based algorithm to preserve and recover vascular structures for nine fold accelerated raw data. Small structures, such as the peripheral renal arteries not visible in the non-regularized method, could be clearly depicted. This study included only TV regularization. Evaluation of further sparsity assumptions would be beneficial. The evolution of the NRMSE over the y-coordinate, depicted in Figure 6.7 for the ISENSE and the SB_{TV} algorithm further reveals that the obtained improvement is higher in the regions corresponding to kidneys and thus containing the peripheral renal arteries. As a consequence, it could be thought of specific regularizations or weights to incorporate the different tissue distribution known a priori in this acquisition. Finally, the comparison to clinically implemented and available GRAPPA and SENSE algorithm showed the performance of the proposed iterative algorithm to deliver diagnostic results where these methods fail. It should be noted, however, that these methods would not be used with acceleration factors of 6 in a clinical application. The use of iterative reconstruction with adapted sampling, regularization and minimization strategies allows for the reported higher acceleration factors. So far, the method was applied to ten data sets. Both the excellent visual and quantitative sharpness results as well as the low NRMSE show its ability to produce accurate diagnostically useful visualisation of the renal arteries. Next steps should include the validation in patients with pathologies and comparison with results achieved with standard clinical methods such as ceMRA.

6.7 Summary and Conclusion

The proposed combination of the novel MICCS pattern and the Split Bregman based SB_{TV} algorithm was able to accelerate the free-breathing 3-D renal acquisition by a factor of 9, corresponding to a reduction in the imaging time from 8 minutes and 45 seconds to 58 seconds, while maintaining excellent sharpness and depiction of the entire renal vasculature. The reduction of the imaging time could be invested in higher spatial resolution which could in return allow for even better depiction of the smallest renal arteries.

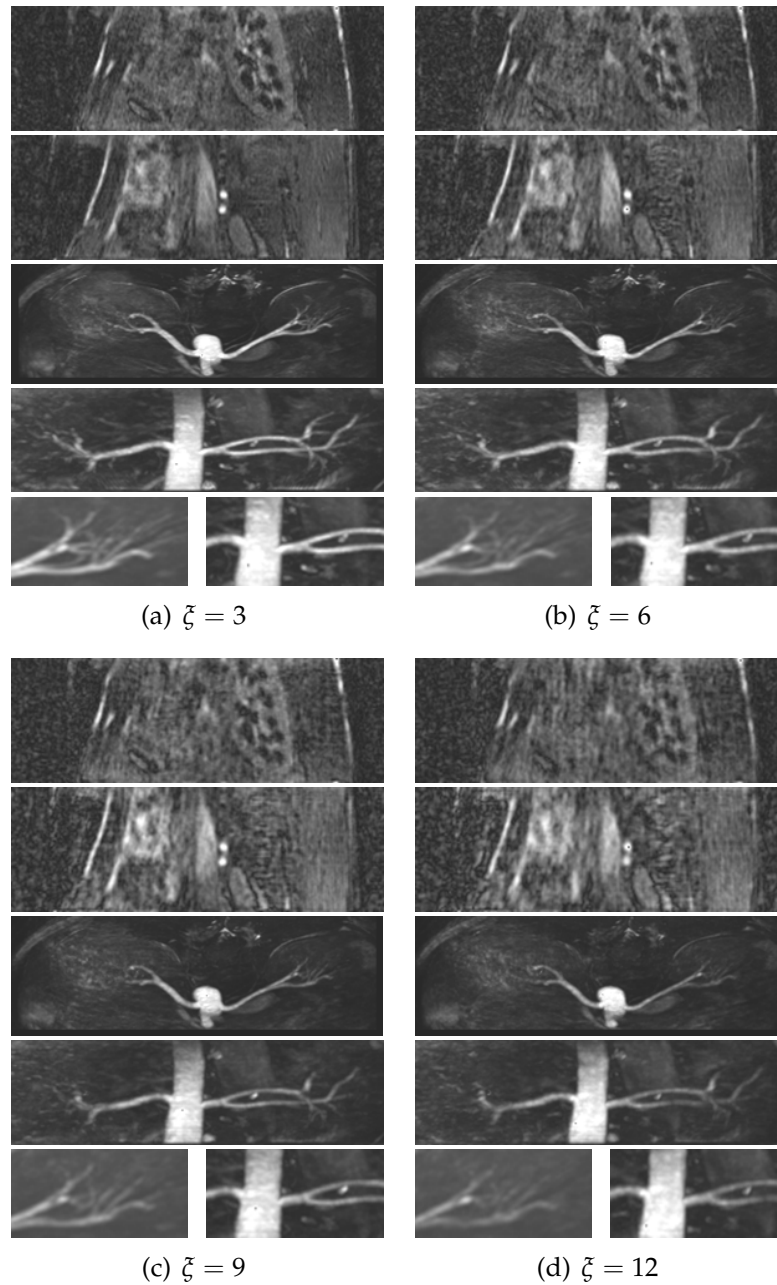


Figure 6.2: The reconstruction results for the acceleration factors $\xi = 3$, $\xi = 6$, $\xi = 9$ and $\xi = 12$ are shown. In the first and second row axial slices within the kidney and perpendicular to the main left renal artery are depicted. Following in the middle rows are the axial and coronal mips and finally, the last row shows details of the fine peripheral renal vasculature and the main left renal arteries.

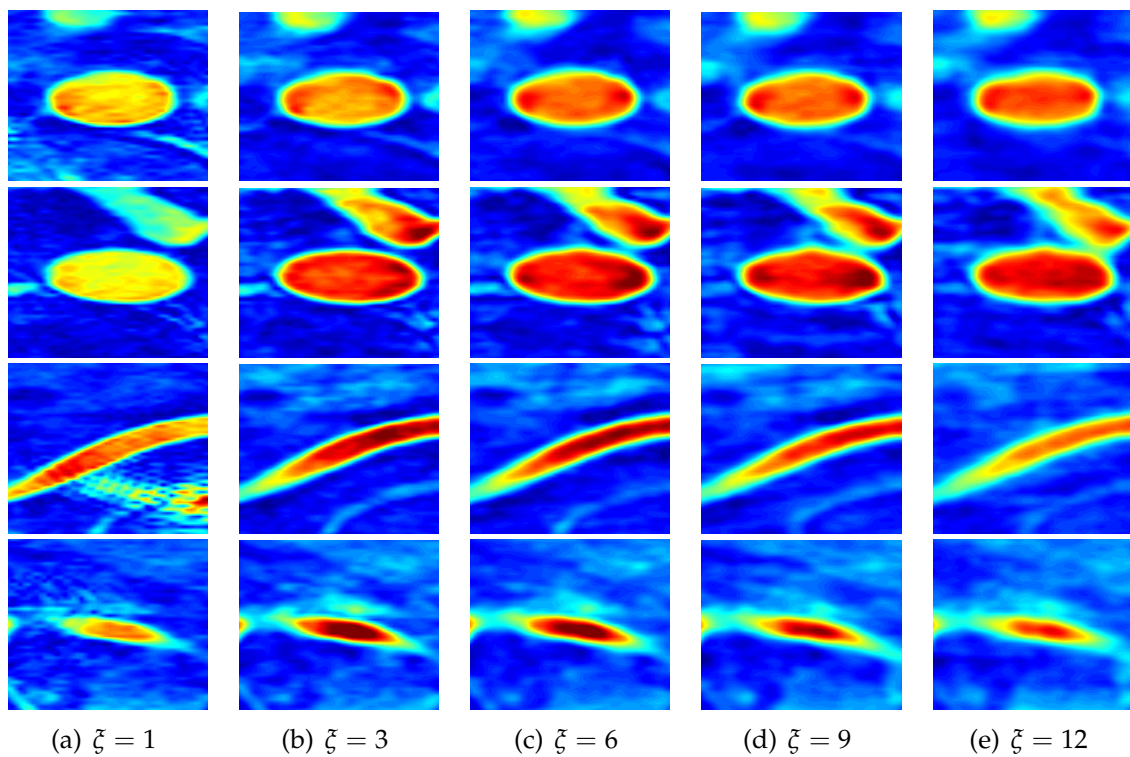


Figure 6.3: The four evaluated positions at the aorta before and after the renal bifurcation and at two positions in the right and left renal artery are shown for the reference and the reconstructions using acceleration factors of $\zeta = 3$, $\zeta = 6$, $\zeta = 9$ and $\zeta = 12$.

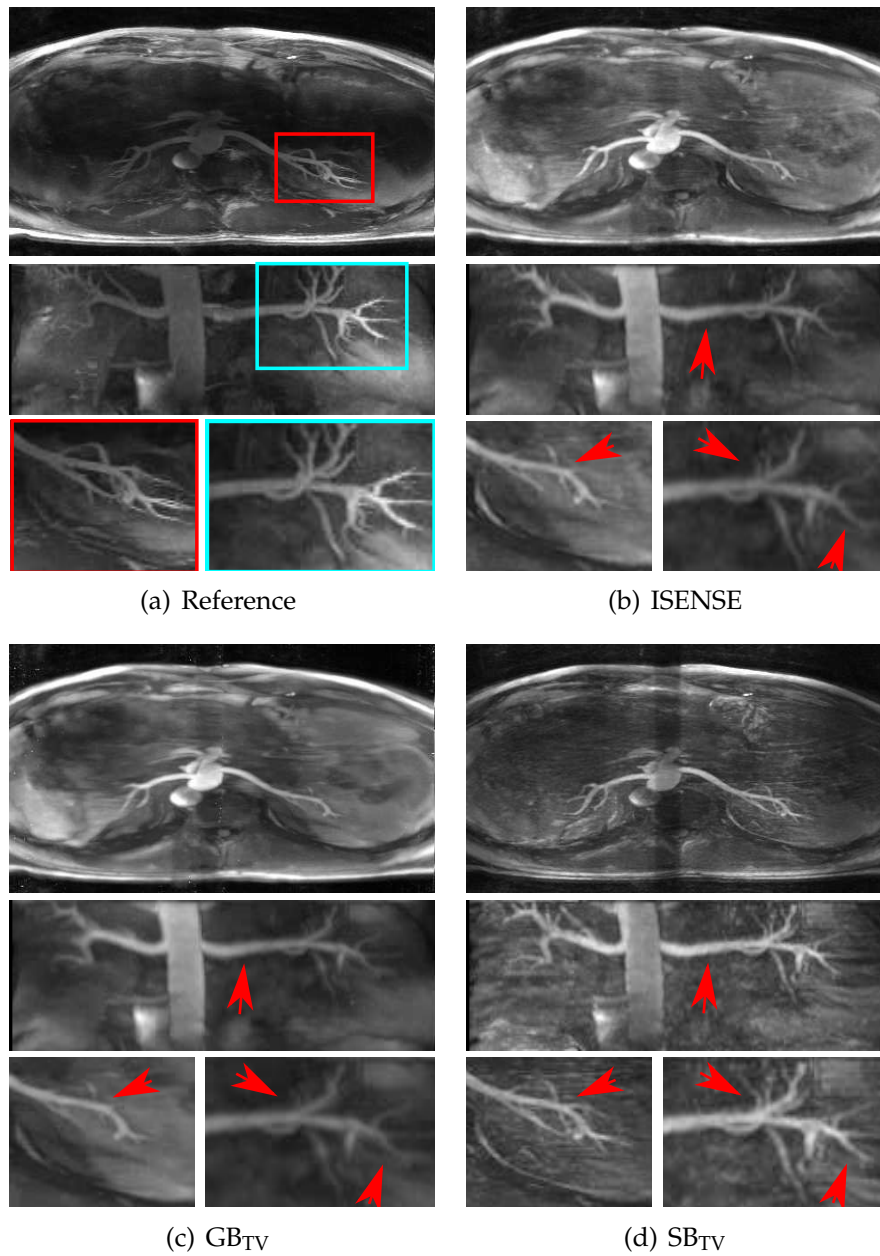


Figure 6.4: The axial and coronal MIPs are shown along with zooms to the peripheral renal arteries for the reference and the iterative algorithms using the MICCS pattern. The ISENSE, the GB_{TV} and the SB_{TV} algorithm were performed.

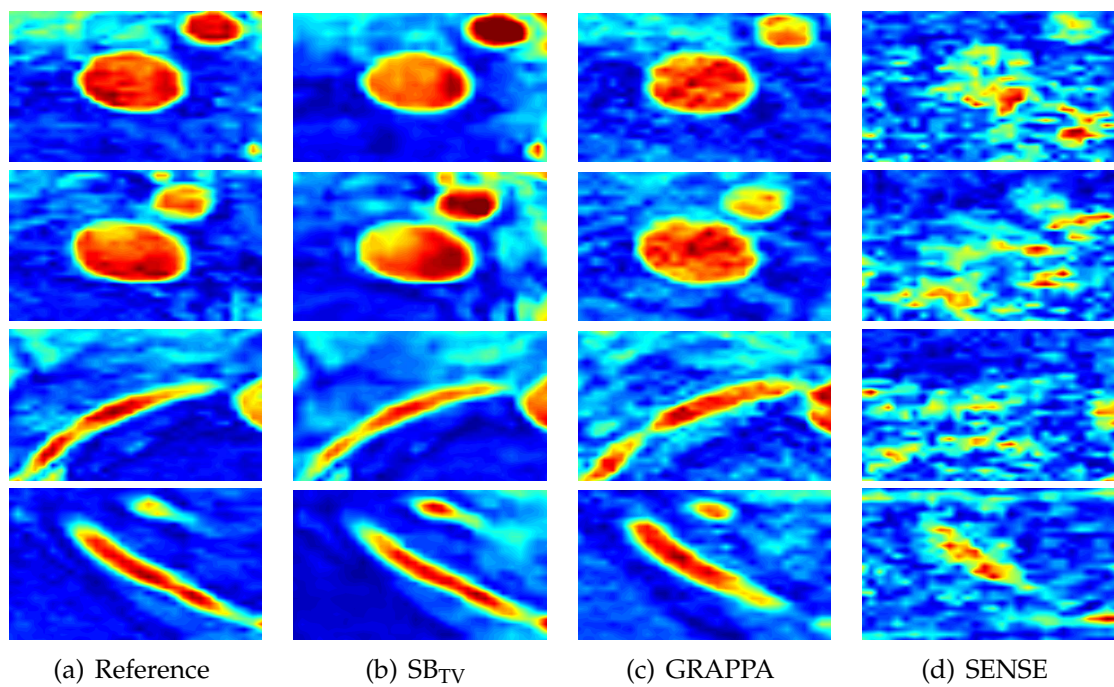


Figure 6.5: The four evaluated positions at the aorta before and after the renal bifurcation and at two positions in the right and left renal artery are shown for the reference, the proposed SB iterative reconstruction using the MICCS pattern, for the GRAPPA and the SENSE reconstruction.

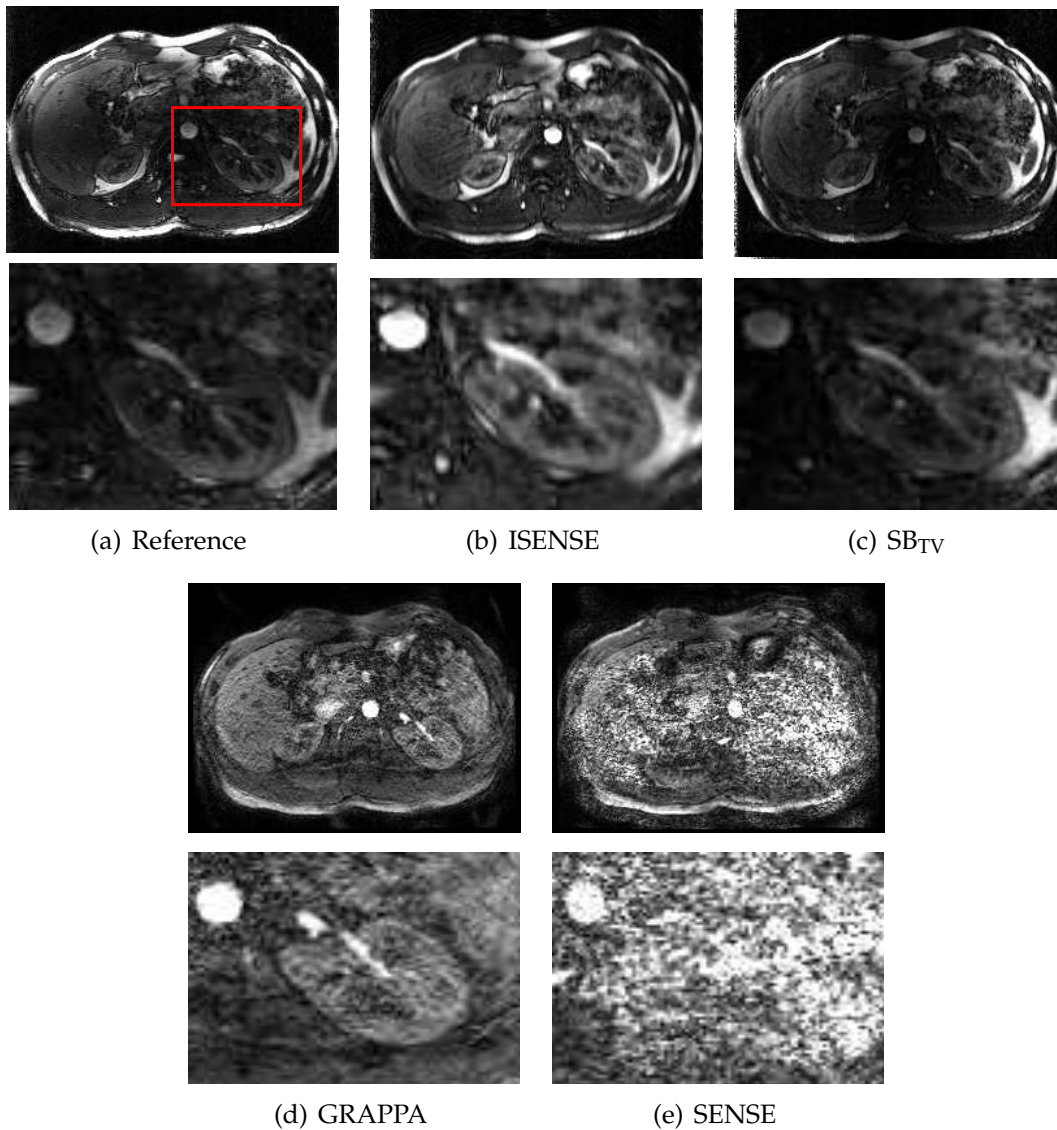


Figure 6.6: Axial slices from the reconstruction results for the comparison study against clinical methods using renal data are shown for the reference, ISENSE, the proposed SB method using the MICCS pattern, GRAPPA and SENSE.

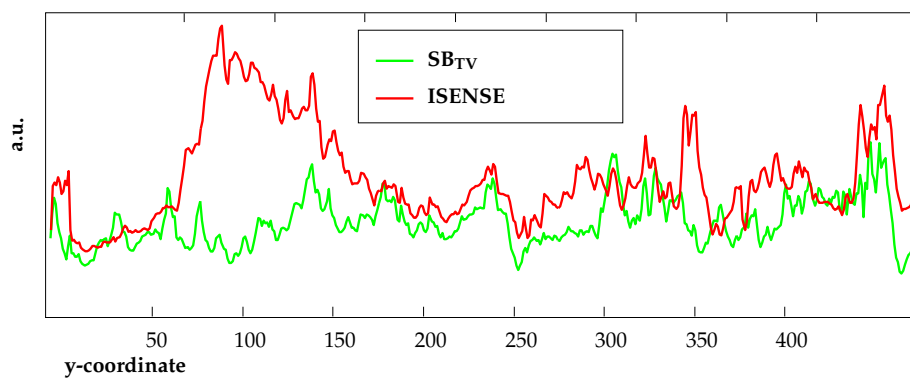


Figure 6.7: The evolution of the NRMSE across the region of interest is depicted for both the ISENSE and the proposed SBTV algorithm.

Part III

Compressed Sensing in MR Phase Contrast

Processing Pipeline and State of the Art in Phase Contrast MRI

7.1 Motivation	91
7.2 From Moving Magnetization to Physiological Values	92
7.3 State of the Art in Accelerated PCI Reconstruction	96
7.4 Summary and Conclusion	98

This chapter marks the beginning of Part III which presents algorithms developed specifically to accelerate PCI acquisitions. The special challenges of PCI data for the reconstruction are presented in this chapter.

7.1 Motivation

The reconstruction problem for PCI differs from the previously presented applications in the dimensionality and in the way the data is processed. In contrast to the so far presented static application considering up to 3 spatial dimensions, PCI data is characterized by its additional temporal and velocity encoding dimension. While most MRI techniques yield static volumes, obtained after acquisition and reconstruction, PCI examinations provide dynamic physiological information. There are various physiological parameters that can be measured with MRI like perfusion, diffusion and velocity. This work focuses on the physiological flow related parameters that can be determined with PCI. Additional processing of the data is required to extract the velocity and flow information. This chapter will present the processing pipeline for PCI data, along with the used notations and the discretization. Furthermore, relevant state of the art in accelerated PCI is reported.

7.2 From Moving Magnetization to Physiological Values

In the following section, the PCI pipeline, detailing the steps from moving magnetization to the calculation of physiological values will be presented. An illustration of the pipeline is given in Figure 7.1.

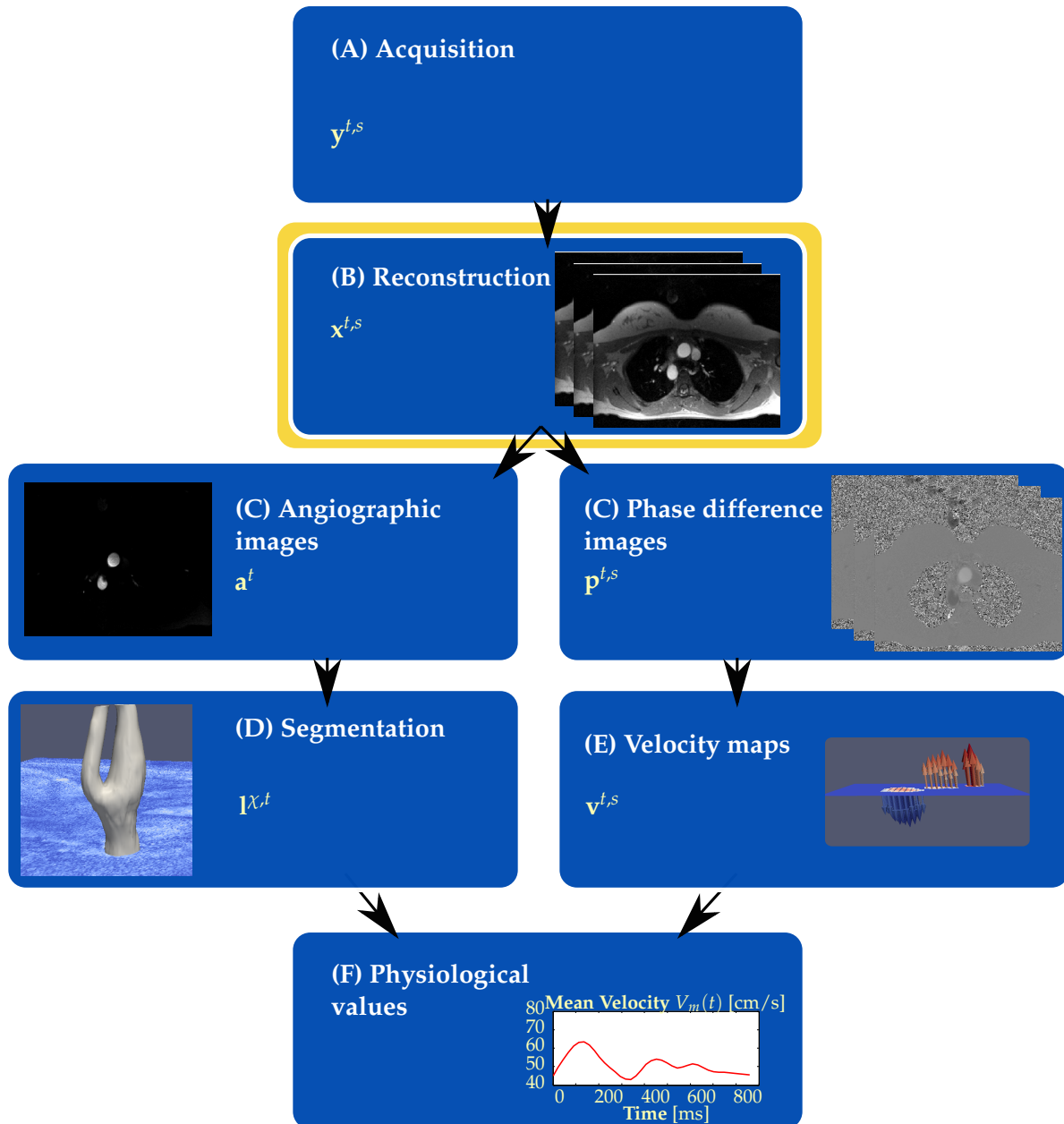


Figure 7.1: Pipeline for processing PCI data from acquisition to calculation of physiological values. The focus for this thesis lies on the reconstruction part, which is highlighted in yellow.

7.2.1 Acquisition and Reconstruction

The physical basis of PCI acquisition, corresponding to step (A), was given in Section 2.2.3. Results of this step are k -space volumes for every time step t with $t \in \{1, \dots, N_t\}$ and for every velocity encoding s with $s \in \{1, \dots, N_s\}$. The total number of volumes equals $N_p = N_t N_s$, where N_p is referred to as problem size. In the case of pMRI using N_γ coils, k -space raw data is acquired for each coil γ with $\gamma \in \{1, \dots, N_\gamma\}$. Using the same conventions as for the static applications, the volumes are represented by column vectors

$$\mathbf{m}_\gamma^{t,s} = \begin{pmatrix} m_{\gamma 1}^{t,s} \\ \vdots \\ m_{\gamma N_k}^{t,s} \end{pmatrix} \in \mathbb{C}^{N_k}, \quad (7.1)$$

where $N_k = N_{k_x} N_{k_y} N_{k_z}$ is the number of k -space points indexed by κ . The discrete coordinates of sampling point κ equal $(\kappa_x, \kappa_y, \kappa_z)$. The all channel vector $\mathbf{m}^{t,s} \in \mathbb{C}^{N_\gamma N_k}$ is obtained by concatenating the data of all coils. The multi-dimensionality of PCI data with up to 3 spatial dimensions, the temporal dimension as well as the encoding dimension offers multiple choices for the employed k -space sampling strategies during the acquisition. The k -space dimensions representing phase encoding directions, κ_y in the 2-D case and κ_y, κ_z in the 3-D case, will be referred to by intra-volume dimensions. The read-out direction is fixed as κ_x , but is not taken into account for under sampling. The remaining time and velocity encoding dimensions are called inter-volume dimensions. The set of all k -space volumes shall be referred to as

$$M = \{\mathbf{m}^{t,s} | t \in \{1, \dots, N_t\} \text{ and } s \in \{1, \dots, N_s\}\} \quad (7.2)$$

where $|M| = N_p$.

The reconstruction step (b) yields image space volumes for each time step t and encoding s

$$\mathbf{x}^{t,s} = \begin{pmatrix} x_1^{t,s} \\ \vdots \\ x_N^{t,s} \end{pmatrix} \in \mathbb{C}^N \quad (7.3)$$

from the given raw data. The same discretization in the spatial dimensions is chosen as detailed for the static data sets. The total number of the image volume voxels equals $N = N_x N_y N_z$, written as column vector with voxel index ι . The discrete coordinates of voxel ι equal $(\iota_x, \iota_y, \iota_z)$. The set of all image volumes is in the following referred to as

$$X = \{\mathbf{x}^{t,s} | t \in \{1, \dots, N_t\} \text{ and } s \in \{1, \dots, N_s\}\} \quad (7.4)$$

where $|X| = N_p$. The reconstruction of a PCI volume for multi coil data is formulated by the operator \mathcal{R} defined as

$$\mathcal{R} : \underbrace{\mathbb{C}^{N_k N_\gamma} \times \dots \times \mathbb{C}^{N_k N_\gamma}}_{N_p} \mapsto \underbrace{\mathbb{C}^N \times \dots \times \mathbb{C}^N}_{N_p} \quad (7.5)$$

with

$$\mathcal{R}(M) = X. \quad (7.6)$$

A subset of a reconstructed PCI data set for $N_t = 3$ and $N_s = 4$ is illustrated in Figure 7.2.

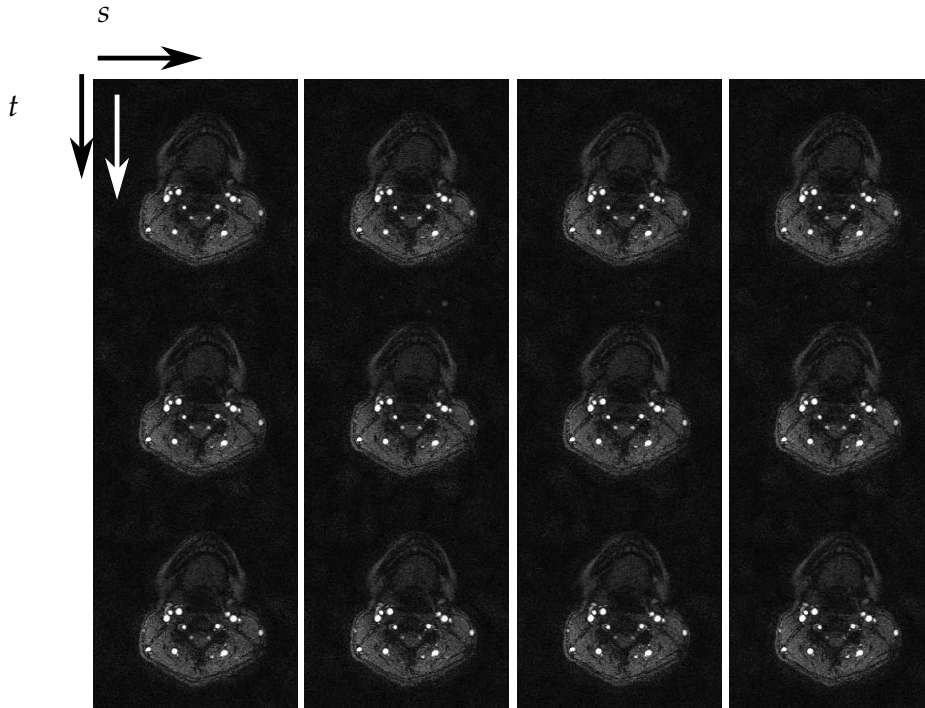


Figure 7.2: Subset of a representative PCI data set illustrating the temporal dimension t , the velocity-encoding dimension s with black arrows, as well as the spatial dimension indicated by the white arrow.

7.2.2 Postprocessing

The image space volumes are the input for step (C), where both angiographic and phase difference images are calculated. The angiographic images $\mathbf{a}^t \in \mathbb{R}^N$ are calculated as the voxel wise magnitude sum of the complex differences between velocity-compensated and velocity-encoded acquisitions:

$$a_i^t = \sum_{s_i=2}^{N_s} |x_i^{t,1} - x_i^{t,s_i}|. \quad (7.7)$$

These images highlight the regions with moving magnetization and provide high contrast for areas with flow irrespective of the direction. Static areas are suppressed due to the small magnitude.

The phase difference between velocity-compensated and velocity-encoded acquisition allows to quantify the velocities for each voxel $\mathbf{p}^{t,s} \in [-\pi/2, +\pi/2]^N$. Those are calculated voxel wise for each encoding $s \in \{2, \dots, N_s\}$, resulting thus in phase difference maps highlighting the velocities in the considered encoding direction:

$$p_i^{t,s-1} = \arg(x_i^{t,1}) - \arg(x_i^{t,s}), \quad (7.8)$$

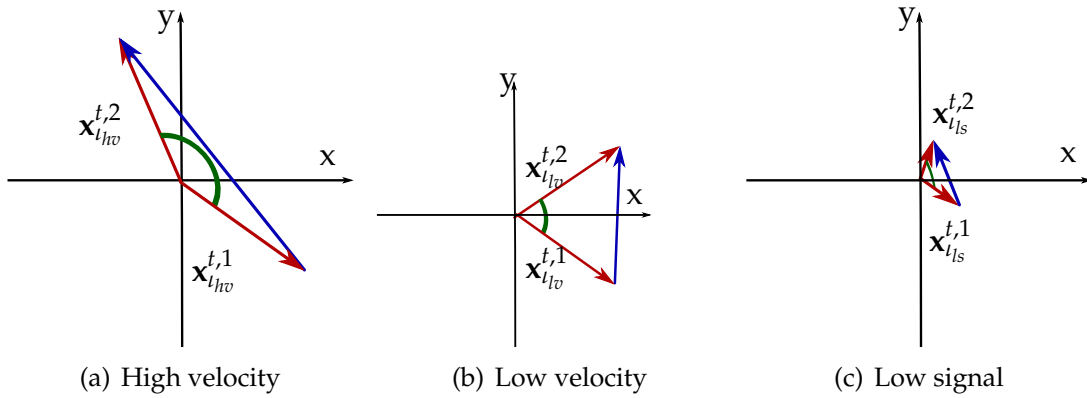


Figure 7.3: Illustration of the formation of the anatomical \mathbf{a}^t and phase difference images $\mathbf{p}^{t,s}$. The magnetization vectors for the flow-compensated and velocity-encoded acquisitions for three voxels representing spins with high velocity l_{hv} , (a) with low velocity l_{lv} (b) and within a region with low signal l_{ls} (c) for $N_s = 2$ are shown in the complex plane. The derived length of the difference vector, depicted in blue, is used to calculate \mathbf{a}^t , the phase difference, indicated by the green angle, for $\mathbf{p}^{t,1}$.

where $\arg(x)$ represents the phase of the complex number x . The calculation of angiographic and phase difference images is illustrated in Figure 7.3 depicting the magnetization for three voxels representing spins with high velocity l_{hv} , with low velocity l_{lv} and within areas with low signal l_{ls} for $N_s = 2$. The complex number $\mathbf{x}_i^{t,s} \in \mathbb{C}$ is identified with its vector representation

$$\mathbf{x}_i^{t,s} = \begin{pmatrix} \text{Re}\{\mathbf{x}_i^{t,s}\} \\ \text{Im}\{\mathbf{x}_i^{t,s}\} \end{pmatrix} \in \mathbb{R}^2. \quad (7.9)$$

The vector is illustrated in the xy plane, corresponding to the complex plane representation. The magnetization vector for the flow-compensated scan and the first velocity-encoded scan at time step t for pixel i is called $\mathbf{x}_i^{t,1}$ and $\mathbf{x}_i^{t,2}$, in accordance with the previously introduced notation. The complex difference vectors are shown in blue, the phase difference angle in green. The length of the difference vector, corresponding to a_i^t in Figure 7.3 illustrate the differentiation between spins moving at different velocities. The velocity difference translates in different values for the phase differences. The overall low signal intensity in areas with low signal, such as outside the object, translates in difference vectors with small magnitude as illustrated in Figure 7.3(c), leading to their suppression in the angiographic images. The arbitrary phase of the low signal results, however, in salt and pepper noise artefacts in the phase difference images.

The angiographic images are used to obtain segmentations for the vessels of interest in step (D). The lumen for vessel χ is represented discrete by $\mathbf{I}^{\chi,t} \in \{0,1\}^N$ where $I_i^{\chi,t}$ equals '1' within vessel χ and '0' outside.

The phase difference images are further processed in step (E). Three-dimensional velocity fields $\mathbf{v}^{t,s} \in \mathbb{R}^N$, containing absolute velocities are obtained by multiplying the velocity maps with the encoding velocity v :

$$\mathbf{v}^{t,s} = \frac{v}{\pi} \mathbf{p}^{t,s}. \quad (7.10)$$

Finally, step (F) combines vessel lumen and velocity maps to obtain physiological quantities. These include parameters such as volumetric flow $Q_v(t)$, the mean velocity $V_m(t)$ and the peak velocity $V_p(t)$ for individual vessels. Further derived quantities such as wall shear stress [Stal08], antegrade and retrograde flow volume across the heart valves, total stroke volume and regurgitation volume [Caw109], and eccentric systolic blood flow in the ascending aorta [Sigo11] are tailored for specific applications but all based on PCI data.

Besides flow measurements, further applications of PCI include velocity measurements in the cerebrospinal fluid, where parameters such as intra cranial compliance and local craniocervical hydrodynamic parameters such as cord displacement and systolic cerebrospinal fluid velocity are analysed [Alpe05].

7.3 State of the Art in Accelerated PCI Reconstruction

Time-consuming techniques such as PCI raise the biggest demand for acceleration techniques. Their clinical acceptance and their entrance to routine applications depend on the progress made towards a speed up of the acquisition time. Progress has been made in the last 20 years on different levels, from trajectory optimizations, pMRI techniques, specific temporal based methods up to CS based techniques.

7.3.1 Non-iterative Reconstruction

Parallel imaging techniques had a wide resonance in PCI. Multiple studies were proposed with both SENSE based [Thun03, Beer05] and GRAPPA based methods by various groups [Lew10, Peng10]. The dynamic character has been exploited by view sharing methods [Foo95, Mark01] as well as a high number of spatio-temporal methods. These include kt-BLAST [Thun12, Stad09, Ooij13] kt-BLAST-SENSE [Balt05], kt-GRAPPA [Baue13], kt-PCA [Gies12, Knob13], Turbo BRISK [Doyl99] and PEAK-GRAPPA [Jung08a]. An extension to these methods, but adapted specifically to PCI is the compartment-based temporal Principal Component Analysis (PCA) proposed by Giese et al. [Gies12].

7.3.2 Iterative Methods

Iterative methods based on CS have been emerging since the adaptation of CS to MRI. These vary widely along used trajectory, sparsity assumption, reconstruction type, acceleration and application. Recent methods include the study by Kim et al. [Kim12a], applying the kt-SPARSE-SENSE approach to phantom, liver and peripheral PCI data. Temporal regularization with principal component analysis and Fourier transform was combined with the conjugate gradient algorithm and applied in two steps. The reconstructions involved acceleration factors of 6 versus factor 3 pMRI (GRAPPA) reconstructions. Further regularization ideas include the sparsity of the complex difference image, applied in combination with TV to Cartesian randomly sampled aortic data and solved using alternating directions by Kwak et al. [Kwak12]. This method was applied with acceleration factors of

1 to 6 to pulmonary PCI. Second order temporal differences were used for cardiac MRA by Velikina et al. [Veli 10] in combination with iteratively reweighted least squares. Further algorithms relying on spatially varying temporal gradients include spatially temporal constrained reconstruction proposed by Hulet et al [Hule 13] for radially sampled aortic data using 16 views from 128. The CG algorithm was used to solve the emerging minimization problem. Specific phase regularization is also applied to random Cartesian aortic datasets involving different solvers such as iterative soft thresholding and the Newton-Raphson algorithm as used by Zhao et al. [Zhao 12]. Two algorithms based on 11-SPIRIT have been developed for radial golden-angle sampled PCI by Santelli et al. [Sant 13] using Tikhonov regularization in aortic arch data and for Poisson Disc sampled pediatric aortic patient data using Wavelet regularization proposed by Hsiao et al. [Hsia 12]. Holland et al. [Holl 10] applied Curvelet, Wavelet and TV regularization in combination with a CG solver to gas-phase velocity images. The only CS based method applied to in-vivo carotid PCI so far was the study by Tao et al. [Tao 13]. They propose L_1 minimization of the yf -space solved with the SPGL1 algorithm. The 3 fold accelerated results were compared to GRAPPA images.

7.3.3 Sampling

Proposed sampling strategies for non-iterative approaches include radial sampling such as shown by Thompson et al. [Thom04] and spiral trajectories as proposed by Pike et al. and Sigfridsson et al. [Pike 94, Sigf 12]. For the iterative methods, state of the art approaches typically employ intra-volume variation and partly as well variation in t -direction but the freedom in encoding direction s is rarely used.

Radial acquisition was used by Velikina et al. [Veli 10] with the stack of stars sampling scheme. The temporal dimension was included into the golden-angle radial acquisition by Santelli et al. [Sant 13] as well as by Hulet et al. [Hule 13] using a radial sampling scheme, selecting 16 views from 128 using offsets for neighbouring phases to enhance incoherence.

Besides radial strategies, Cartesian sampling patterns were employed in combination with CS techniques. Random sampling in the periphery, combined with a fully sampled central k -space region was used in the studies by Kwak et al. and Tao et al. [Kwak 12, Tao 13] and by Zhao et al. [Zhao 12], which does not include variation over encodings but includes different random distributions for the temporal dimension. Very similar is the Monte Carlo based sampling strategy employed by Holland et al. [Holl 10] and the Poisson disc strategy in the study of Hsiao et al. [Hsia 12]. The sampling strategy in Kim et al. [Kim 12a] is as well based on a Cartesian pattern, randomly sampled in t direction with a 8th order polynomial function. The variation in encoding direction was proposed, but the experiments used a fixed pattern 'due to computational ease'.

7.4 Summary and Conclusion

The special challenges of PCI data were presented in this Chapter focusing especially on their implications on the reconstruction. These include the multi-dimensionality, which leads to higher computational complexity of the reconstruction, but allows as well to develop dedicated sampling and regularization strategies exploiting all dimensions in the goal to further speed up acceleration. Furthermore, the PCI pipeline, detailing the way from moving blood particles to physiological values was introduced. The required post processing of the reconstructed volumes implies an increased need for both spatial and temporal accuracy in the complex reconstruction results.

Experimental Setup

8.1 Motivation for Carotid PCI	99
8.2 Data	100
8.3 Evaluation Strategy	103
8.4 Summary and Conclusion	104

This Chapter motivates PCI as a challenging application and presents the experimental setup for the developed acceleration algorithms for PCI data. The acquired data sets including phantom, volunteer and patient data as well as the used evaluation strategy for the experiments in the following chapters are detailed.

8.1 Motivation for Carotid PCI

The increasing importance of hemodynamic information in clinical diagnosis, the advantages of PCI in assessing blood flow information but also the long acquisition times can be well observed in the example of the carotid bifurcation region. The trade-off between clinically acceptable imaging time and high temporal and spatial resolution applies particularly to smaller and complex arterial systems such as the carotid bifurcation, where partial volume effects can influence the measurement of flow velocities and thus may lead to non-diagnostic results.

The carotid bifurcation region is of clinical relevance due to the high prevalence of calcifications, vessel narrowing and stenosis and the need for accurate planning of invasive procedures such as endarterectomy. Furthermore, it presents the challenges of relatively small anatomical structures, complex flow patterns in the bifurcation as well as high peak velocities as they would occur in stenosis. High spatial and temporal resolution is required, which increases the acquisition time and thus the need for acceleration. Two possible applications are the bilateral assessment of carotid flow to evaluate consequences of stroke or the diagnosis and evaluation of severe internal carotid artery (ICA) stenosis. The algorithms developed in the following chapters were applied to data from volunteers and two patient cases from the carotid artery bifurcation, including the common carotid artery (CCA) and distal to the bifurcation of the internal and external carotid artery (ECA).

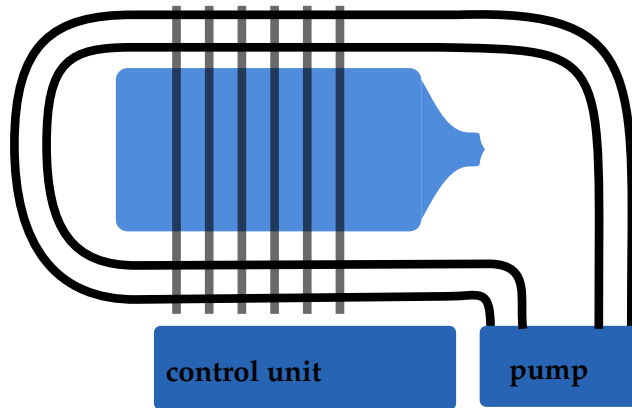


Figure 8.1: Illustration of the phantom experiment setup. The pump is controlled by the control unit in the operators room. The grey lines indicate the imaging planes.

8.2 Data

The evaluation of a reconstruction algorithm for PCI requires different studies. First, the obtained flow profiles need to be verified using physical laws, second, a bigger volunteer study is required to show its robustness and finally, third, its capability to produce useful data for patients with significant pathologies has to be demonstrated. The following sections present the data acquired in these purposes.

8.2.1 Phantom Experiment

Phantom data sets were acquired using an MR-compatible pump (CardioFlow 5000 MR, Shelley Medical, Toronto, Canada) connected to a control unit outside the scanner room and a tube system filled with blood mimicking fluid. An inflow-outflow setup was used for this study, consisting of two connected tubes with a diameter of 1.9 mm which are connected to the pump and placed around a phantom bottle to simulate tissue contrast. The imaging slice was chosen orthogonal to the tubes, such that each imaging plane contained a cross section of the bottle and both the in- and out-flow tube. See Figure 8.1 for a schematic representation of the setup. Fluid was pumped through the phantom with a regulated laminar flow of 150 ml/s and imaged on a 3T MR scanner (MAGNETOM Skyra, Siemens Healthcare Sector, Erlangen, Germany). The imaging parameters were FOV 190 mm \times 130 mm, matrix 256 \times 176 and a slice thickness of 3.1 mm, TE / TR = 3.4 ms / 6.2 ms, and flip angle 20 $^{\circ}$.

8.2.2 In-vivo Study

PCI data was acquired in 18 healthy volunteers (18-72 years) on a clinical 3T MR scanner (MAGNETOM Skyra, Siemens Healthcare Sector, Erlangen, Germany) using an ECG-triggered PC sequence. The region of interest (ROI) was chosen around the carotid artery bifurcation. Up to 16 transverse slices were acquired,

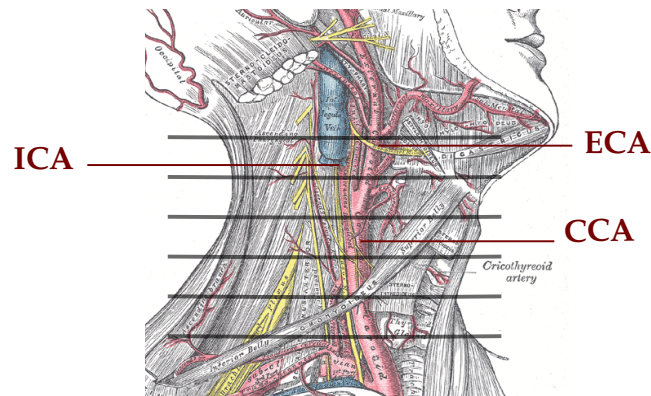


Figure 8.2: Illustration of the carotid volunteer experiment setup. The grey lines indicate the imaging planes. Image adapted from [Gray 01].

starting from the common carotid artery (CCA), about 40 mm below the bifurcation up to the internal and external carotid artery, approximately 20 mm above the bifurcation. This setup is illustrated in Figure 8.2. Imaging parameters were TE/TR = 3.5 / 49.76 ms, flip angle 20° , FOV $200 \text{ mm} \times 200 \text{ mm}$, slice thickness 2-4 mm, and imaging matrix 256×256 , with in-plane resolution of $0.78 \text{ mm} \times 0.78 \text{ mm}$. The encoding velocity v and the number of temporal phases were individually optimized. Between 11 and 20 temporal phases were acquired and v was chosen between 60 and 100 cm/s. The FOV was adapted if required.

8.2.3 Patient Cases

Two patients with severe high-grade stenosis in the ICA were examined on a clinical 3T MR scanner (MAGNETOM Verio, Siemens Healthcare Sector, Erlangen, Germany) using an ECG-triggered PC sequence. These data sets allow to evaluate the reconstruction algorithms in the presence of pathologies. Patient I was diagnosed with a severe high-grade stenosis of the left ICA (NASCET 80 %) and a low grade stenosis of the right ICA with ultrasound and Computed Tomography Angiography (CTA). The axial slices within the stenosis in Figure 8.3(a) and the coronal maximum intensity projection (MIP) from the CTA in Figure 8.3(a) illustrate the severity of the stenosis. Arrows indicate the location of the calcified plaque which causes the lumen narrowing. Patient II underwent nceMRA and ceMRA. Both showed a unilateral high-grade stenosis in the right ICA of over 80% as observable in Figure 8.4(a) and Figure 8.4(b). Both patients were examined prior to a scheduled endarterectomy. The velocity sensitivity ranges were optimized individually. Three slices were acquired, one in the CCA and two in the ICA at pre- and post-stenotic positions as indicated in Figure 8.3(b) and Figure 8.4(b).

The imaging parameters included TE/TR = 3.25 ms / 3.96 ms (3.96 ms / 6.51 ms for Patient II), echo spacing 26.04 ms, flip angle 20° , FOV $200 \times 200 \text{ mm}^2$, slice thickness 4 mm, imaging matrix 224×224 and in-plane resolution of $0.89 \text{ mm} \times 0.89 \text{ mm}$. The encoding velocity v was chosen as $v=180 \text{ cm/s}$ (150 cm/s) and the number of temporal phases as $N_t=26$ ($N_t=15$).

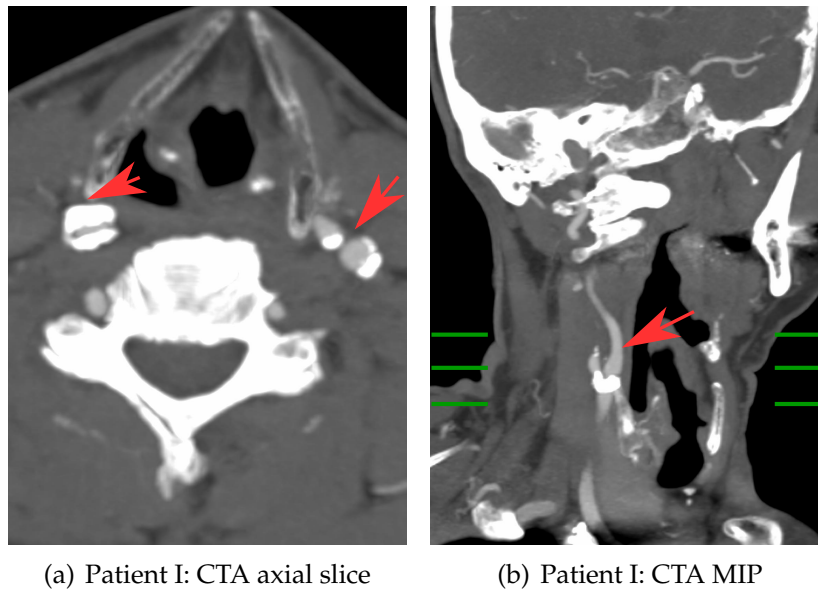


Figure 8.3: Presentation of the patient case I. Arrows indicate the location of the stenosis. (a) Axial slice through the stenosis and (b) coronal MIP from a CTA scan. The locations of the imaging planes are illustrated in green in (b).

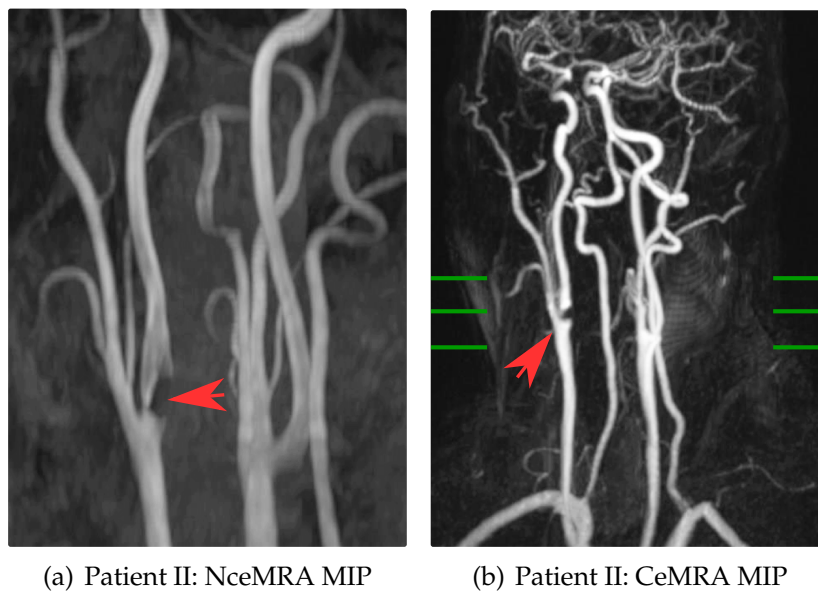


Figure 8.4: Presentation of the patient case II. Arrow indicate the location of the stenosis. Patient II: (a) MIP of a nceMRA (TOF) examination and (b) MIP of a ceMRA examination. The locations of the imaging planes are illustrated in green in (b).

8.3 Evaluation Strategy

The results obtained for PCI data are analysed quantitatively based on both the reconstructed volume set X after step (B) in the pipeline shown in Figure 7.1 and on the derived quantitative physiological values obtained after step (F).

8.3.1 Volume Based Evaluation

The volume-based quantitative measures were thereby always calculated for all velocity encodings and temporal steps, as the derived physiological values are based on the combination of different encodings. The accuracy of all components should thus be analysed. The measures are evaluated on the concatenated vectors for all encodings and temporal time steps as presented in Eq. (9.7) in Section 9.1.

The volume-based evaluation in comparison to the reference includes the normalized root mean square error (NRMSE) and the structural similarity measure (SSIM) [Wang 04]. The reference data set will be referred to by \mathbf{r} . The NRMSE and the SSIM, choosing the parameters c_1 and $c_2 \in \mathbb{R}$ as suggested by Wang et al. [Wang 04] are obtained as

$$\text{NRMSE}(\mathbf{r}, \mathbf{x}) = \frac{1}{N_p} \sum_{t=1}^{N_t} \sum_{s=1}^{N_s} \frac{1}{N} \|\mathbf{r}^{t,s} - \mathbf{x}^{t,s}\|_{L_2} \quad (8.1)$$

and

$$\text{SSIM}(\mathbf{r}, \mathbf{x}) = \frac{1}{N_p} \sum_{t=1}^{N_t} \sum_{s=1}^{N_s} \frac{2\mu(\mathbf{r}^{t,s})\mu(\mathbf{x}^{t,s}) + c_1}{\mu(\mathbf{x}^{t,s})^2 + \mu(\mathbf{r}^{t,s})^2 + c_1} + \frac{\text{cov}(\mathbf{x}^{t,s}, \mathbf{r}^{t,s}) + c_2}{\sigma(\mathbf{r}^{t,s})^2 + \sigma(\mathbf{x}^{t,s})^2 + c_2}. \quad (8.2)$$

More specifically for angiographic data, the Contrast to Noise Ratios involving the vessel background (CVRVB) and the vessel tissue contrast (CVRVT) were employed. Respective regions of interest were chosen manually in the vessel, tissue and background and are denoted by the index sets l_v, l_t and l_b . These measures were presented for static applications in Section 5, but are evaluated over the entire volume set for PCI with

$$\text{CNRVB}(\mathbf{x}, l_v, l_b) = \frac{1}{N_p} \sum_{t=1}^{N_t} \sum_{s=1}^{N_s} \frac{\mu(\mathbf{x}_{l_v}^{t,s}) - \mu(\mathbf{x}_{l_b}^{t,s})}{\sqrt{0.5(\sigma(\mathbf{x}_{l_v}^{t,s})^2 + \sigma(\mathbf{x}_{l_b}^{t,s})^2)}} \quad (8.3)$$

and

$$\text{CNRVT}(\mathbf{x}, l_v, l_t) = \frac{1}{N_p} \sum_{t=1}^{N_t} \sum_{s=1}^{N_s} \frac{\mu(\mathbf{x}_{l_v}^{t,s}) - \mu(\mathbf{x}_{l_t}^{t,s})}{\sqrt{0.5(\sigma(\mathbf{x}_{l_v}^{t,s})^2 + \sigma(\mathbf{x}_{l_t}^{t,s})^2)}}. \quad (8.4)$$

8.3.2 Physiology Based Evaluation

The obtained image results were further processed as explained in Figure 7.1 to obtain the volumetric flow $Q_v(t)$, the mean velocity $V_m(t)$ and the peak velocity $V_p(t)$. These parameters, evaluated for vessel χ , are calculated using the segmented dynamic vessel lumen IX^t and the 3-D velocity fields $\mathbf{v}^{t,s} \in \mathbb{R}^N$. The dynamic segmentation was done manually on the obtained image volumes.

The volumetric flow, mean and peak velocity are obtained by

$$Q_v(t) = \sum_{i=1}^N l_i^{\chi,t} \|v_i^t\|_{L_2}, \quad (8.5)$$

$$V_m(t) = \frac{Q_v(t)}{\sum_{i=1}^N l_i^{\chi,t}} \text{ and} \quad (8.6)$$

$$V_p(t) = \max_i l_i^{\chi,t} \|v_i^t\|_{L_2}. \quad (8.7)$$

The accuracy of those was analysed using the temporal normalized root mean square error (TNRMSE). The TNRMSE(p_r, p_t) for a dynamic parameter $p \in \mathbb{R}^{N_t}$, considering the reference $p_r \in \mathbb{R}_t^N$ and the test data result $p_t \in \mathbb{R}_t^N$ is calculated as

$$\text{TNRMSE}(p_r, p_t) = \frac{1}{N_t} \left\| \frac{p_r - p_t}{p_r} \right\|_{L_2}. \quad (8.8)$$

The quality of the TNRMSE of the mean velocity $V_m(t)$ and the volumetric flow $Q_v(t)$ follows from Eq. (8.5). The controlled phantom setup allows to verify the flow conservation law based on the total flow $Q \in \mathbb{R}$, calculated as

$$Q = \sum_{t=1}^{N_t} Q_v(t). \quad (8.9)$$

Two different conservation laws can be verified. First, the intra-slice flow conservation is measured calculating the deviation $\Delta Q_l \in \mathbb{R}$ between the inflow $Q_l^i \in \mathbb{R}$ and outflow $Q_l^o \in \mathbb{R}$ in and from slice l , which is obtained as

$$\Delta Q_l = \frac{|Q_l^i - Q_l^o|}{|Q_l^i|}. \quad (8.10)$$

Second, the inter-slice flow conservation, defined by the in- or outflow between adjacent slices l and $l - 1$, can be evaluated calculating the deviations ΔQ_l^i and ΔQ_l^o

$$\Delta Q_l^i = \frac{|Q_l^i - Q_{l-1}^i|}{|Q_l^i|} \quad \text{and} \quad (8.11)$$

$$\Delta Q_l^o = \frac{|Q_l^o - Q_{l-1}^o|}{|Q_l^o|}. \quad (8.12)$$

8.4 Summary and Conclusion

The assessment of the blood flow velocities in the carotid bifurcation region was presented as an application with both high clinical relevance as well as challenges regarding the required spatial and temporal resolution. The high blood flow velocities and the relative small vessel diameters of the CCA, ICA and ECA make this application especially prone for partial volume effects and thus raise the need for

techniques allowing both high acceleration factors and high accuracy. The gains in acquisition time could thus be invested in higher spatial and temporal resolution which is in turn of huge interest for its clinical usability. The presented phantom, in-vivo and patient data will be used in the following chapters, developing the iterative reconstruction for PCI and the algorithms MuFloCoS and LoSDeCoS. Special focus will be on the stability and robustness of the developed methods, evaluated by analysing a fixed algorithmic setup for the volunteers as well as the diagnostic output of the patient data.

Iterative Reconstruction for PCI

9.1 Joint Regularized Iterative Reconstruction 107
 9.2 Interleaved Velocity Encoding and Temporal Sampling 111
 9.3 Implementation 114
 9.4 Summary and Conclusion 114

The multi-dimensionality of PCI data offers challenges but also possibilities for the iterative reconstruction problem. This section will detail the joint iterative reconstruction along with the multi-dimensional regularizers as well as the novel interleaved velocity encoding and temporal sampling strategy, referred to by I-VT sampling.

9.1 Joint Regularized Iterative Reconstruction

The reconstruction of multi-coil PCI data was formulated in a general way in Eq. (7.5) as

$$\mathcal{R}(M) = X. \tag{9.1}$$

Conventional pMRI reconstruction approaches treat every volume as an individual reconstruction problem, which requires to change the operator application from \mathcal{R} into N_p applications of \mathcal{R}_i with

$$\mathcal{R}_i : \mathbb{C}^{N_k N_\gamma} \mapsto \mathbb{C}^N, \tag{9.2}$$

resulting in

$$\mathbf{x}^{t,s} = \mathcal{R}_i(\mathbf{m}^{t,s}) \quad \forall \quad t \in \{1, \dots, N_t\} \text{ and } \quad \forall \quad s \in \{1, \dots, N_s\}. \tag{9.3}$$

Thereby \mathcal{R}_i varies depending on the chosen reconstruction algorithm. Formulated iteratively as unconstrained minimization problem with data fidelity and regularization term, the operator \mathcal{R}_i equals

$$\mathcal{R}_i(\mathbf{m}^{t,s}) = \underset{\mathbf{x}^{t,s}}{\operatorname{argmin}} \mathcal{L}(\mathbf{x}^{t,s}), \tag{9.4}$$

where

$$\mathcal{L}(\mathbf{x}^{t,s}) = \underbrace{\frac{1}{2} \|\mathbf{E}^{t,s} \mathbf{x}^{t,s} - \mathbf{m}^{t,s}\|_{L_2}^2}_{\text{Data fidelity term}} + \underbrace{\lambda R(\mathbf{x}^{t,s})}_{\text{Regularization}}. \quad (9.5)$$

The data fidelity term comprises the under sampling pattern described by $\mathbf{u}^{t,s}$ for each time step t and velocity encoding s , the coil maps \mathbf{c}_γ^t describing the spatially varying sensitivity information of the N_γ coils and the Fourier coefficients. The encoding matrix $\mathbf{E}^{t,s} \in \mathbb{C}^{N_\gamma N_k \times N}$ is composed as

$$\mathbf{E}^{t,s} = e_{(\gamma\kappa,l)}^{t,s} = u_\kappa^{t,s} e^{i\mathbf{k}_\kappa \mathbf{r}_l} c_{(\gamma,l)}^t, \quad (9.6)$$

where \mathbf{r}_l is the position of voxel l and \mathbf{k}_κ the κ -th frequency in time step t and for encoding s . Depending on the degree of variations in the sampling, the same encoding matrix can be used for all encodings and all time steps.

9.1.1 Joint Iterative Reconstruction

Instead of the presented individual reconstruction, joint reconstruction of all volumes is beneficial to incorporate multi dimensional regularizers. In this approach, the sets M and X are written as column vectors. The volume for the entire parameter space is addressed by $\mathbf{x} \in \mathbb{C}^{N_p N}$:

$$\mathbf{x} = \begin{pmatrix} \mathbf{x}^{1,1} \\ \vdots \\ \mathbf{x}^{1,N_s} \\ \vdots \\ \mathbf{x}^{N_t,1} \\ \vdots \\ \mathbf{x}^{N_t,N_s} \end{pmatrix} \begin{matrix} \left. \begin{matrix} \} s = 1 \\ \vdots \\ \} s = N_s \end{matrix} \right\} t = 1 \\ \vdots \\ \left. \begin{matrix} \} s = 1 \\ \vdots \\ \} s = N_s \end{matrix} \right\} t = N_t \end{matrix} \quad (9.7)$$

Furthermore, representations for subsets of the entire vector are needed for certain reconstruction steps. The vector containing all velocity encoding information for time step t , shall be referred to by $\mathbf{x}^t \in \mathbb{C}^{N N_s}$. If all time steps for encoding s are considered, the respective vector equals $\mathbf{x}^s \in \mathbb{C}^{N N_t}$. The same subset conventions apply to the raw data vector \mathbf{m} . The vector containing all raw data points is referred to by $\mathbf{m} \in \mathbb{C}^{N_k N_\gamma N_p}$. To incorporate joint iterative PCI data, the encoding matrices $\mathbf{E}^{t,s}$ are combined to a joint encoding matrix $\mathbf{E} \in \mathbb{C}^{N_p N_\gamma N_k \times N_p N}$. It has a block structure and is composed of N_p matrices $\mathbf{E}^{t,s} \in \mathbb{C}^{N_\gamma N_k \times N}$:

$$\mathbf{E} = \begin{pmatrix} \mathbf{E}^1 & & 0 \\ & \ddots & \\ 0 & & \mathbf{E}^{N_t} \end{pmatrix} \quad \text{where} \quad \mathbf{E}^t = \begin{pmatrix} \mathbf{E}^{t,1} & & 0 \\ & \ddots & \\ 0 & & \mathbf{E}^{t,N_s} \end{pmatrix}. \quad (9.8)$$

Formulating the data fidelity term as presented in Section 4 as

$$H(\mathbf{x}) = \frac{1}{2} \|\mathbf{E}\mathbf{x} - \mathbf{m}\|_{L_2}^2, \quad (9.9)$$

the joint PCI objective function equals

$$\mathcal{L}_{\text{PCI}} = \underbrace{H(\mathbf{x})}_{\text{Data fidelity term}} + \underbrace{\lambda R(\mathbf{x})}_{\text{Regularization}} \quad (9.10)$$

This leads to the following minimization problem:

$$\hat{\mathbf{x}} = \underset{\mathbf{x}}{\operatorname{argmin}} \mathcal{L}_{\text{PCI}}. \quad (9.11)$$

The regularization $R(\mathbf{x})$ where $R : \mathbb{C}^N \mapsto \mathbb{R}$, will be detailed in the following.

9.1.2 Regularization Strategy

A wide range of possible constraints for the regularization term $R(\mathbf{x})$ exist. The additional dimensions time and velocity encoding enable further strategies beyond the known image based assumptions such as TV and Wavelet. Nevertheless, those are still valid assumptions and may be beneficial in combination. The dynamic character of PCI data allows for the use of temporal constraints such as temporal Fourier transform. Furthermore, the velocity encoding dimension can lead to either novel regularizers, or the advantageous combination of existing static or dynamic assumptions.

Previously introduced TV and Wavelet in Section 5 are applied for PCI data and are summed over time steps and encodings:

$$\begin{aligned} TV_i(\mathbf{x}) &= \sum_{t=1}^{N_t} \sum_{s=1}^{N_s} \sum_{l=1}^N \sqrt{|\nabla_x \mathbf{x}^{t,s}|^2 + |\nabla_y \mathbf{x}^{t,s}|^2 + |\nabla_z \mathbf{x}^{t,s}|^2} \\ &= \sum_{t=1}^{N_t} \sum_{s=1}^{N_s} \|\nabla \mathbf{x}\|_{L_{2,1}} \quad \text{and} \end{aligned} \quad (9.12)$$

$$WV(\mathbf{x}) = \sum_{t=1}^{N_t} \sum_{s=1}^{N_s} \|W(\mathbf{x}^{t,s})\|_{L_1}. \quad (9.13)$$

For the temporal Fourier transform $\mathcal{F}^{st}(\mathbf{x})$, different settings in combination with the velocity encoding dimension are possible.

The temporal Fourier transform for the individual encoding s is written as $\mathcal{F}_t(\mathbf{x}^s)$ where $\mathbf{x}^s \in \mathbb{C}^{NN_t}$. The temporal Fourier transform for all four encodings of a PCI dataset is illustrated next to the temporal evolution of all voxels in Figure 9.1(b).

Combinations of the temporal Fourier transform over the encodings are referred to by second order temporal-velocity Fourier transform in the following. The simplest version, direct summation of the individual Fourier components $\mathcal{F}_{t,s}^{\text{sum}}$ is illustrated in Figure 9.2(a) and calculated as

$$\mathcal{F}_{t,s}^{\text{sum}}(\mathbf{x}) = \sum_{s=1}^{N_s} \|\mathcal{F}_t(\mathbf{x}^s)\|_{L_1}. \quad (9.14)$$

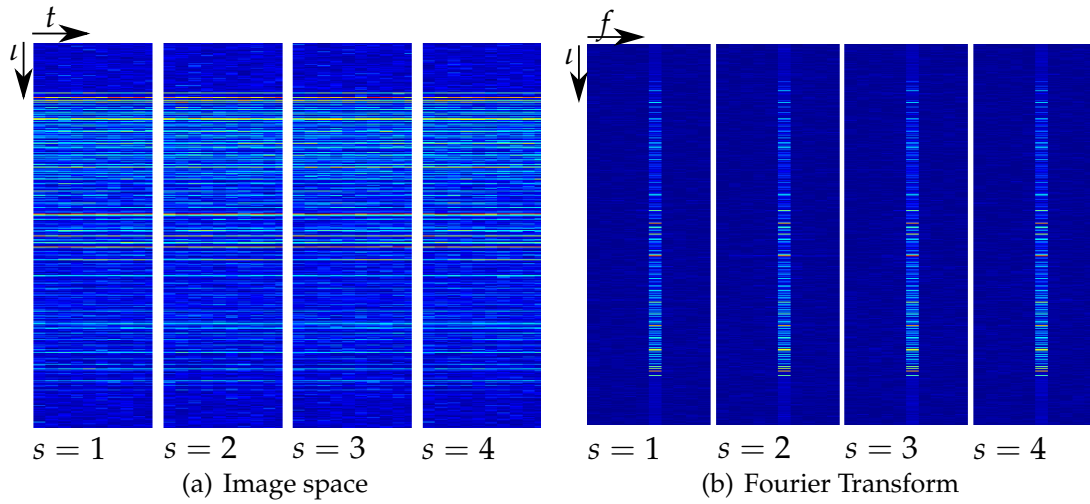


Figure 9.1: Temporal Fourier transform for the four encodings of a PCI dataset. The image results in the lt -space are shown in (a), the corresponding Fourier transform in the lf -space are depicted in (b) for all four velocity encodings.

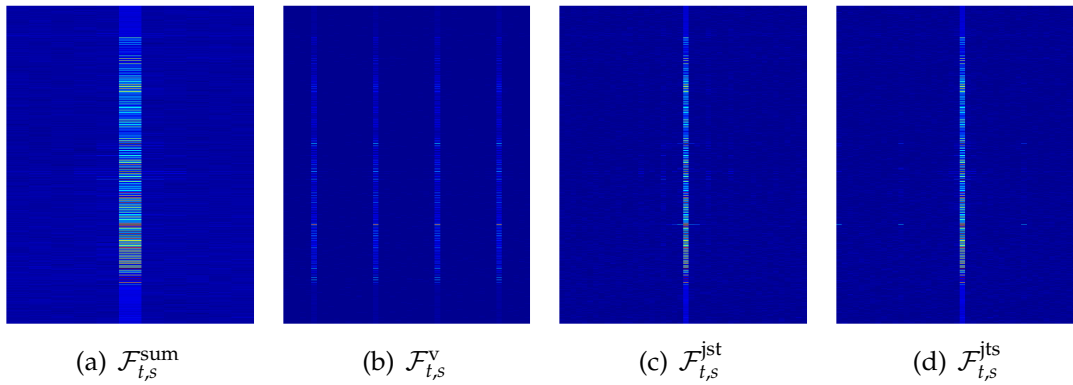


Figure 9.2: Different second order Fourier variants are shown: (a) $\mathcal{F}_{t,s}^{\text{sum}}$, (b) $\mathcal{F}_{t,s}^v$, (c) $\mathcal{F}_{t,s}^{\text{jst}}$ and (d) $\mathcal{F}_{t,s}^{\text{jts}}$

The resulting reduction of the dimensions is not beneficial, as the additional similarities over velocity encodings, visible in Figure 9.1(b) would not be exploited. Changing the sum and the L_1 norm leads to the vector wise L_1 norm calculation $\mathcal{F}_{t,s}^v$, shown in Figure 9.2(b) and obtained by

$$\mathcal{F}_{t,s}^v(\mathbf{x}) = \left\| \sum_{s=1}^{N_s} \mathcal{F}_t(\mathbf{x}^s) \right\|_{L_1}. \quad (9.15)$$

The Fourier information is used separately for each encoding, but the common information is not exploited.

Further ideas are the joint temporal and encoding Fourier transform either arranging the coefficients first by encoding and then by time step $\mathcal{F}_{t,s}^{\text{ist}}$ or vice versa $\mathcal{F}_{t,s}^{\text{its}}$:

$$\mathcal{F}_{t,s}^{\text{ist}}(\mathbf{x}) = \|\mathcal{F}_{t,s}(\mathbf{x})\|_{L_1} \quad \text{and} \quad \mathcal{F}_{t,s}^{\text{its}}(\mathbf{x}) = \|\mathcal{F}_{t,s}(\check{\mathbf{x}})\|_{L_1}. \quad (9.16)$$

These variants are illustrated in Figure 9.2(c) and Figure 9.2(d).

For this thesis, the vector wise version was used $\mathcal{F}_{t,s}^{\text{v}}(\mathbf{x})$ and is referred to by velocity encoding temporal Fourier transform (vtFT) in the following.

9.2 Interleaved Velocity Encoding and Temporal Sampling

This section presents an under sampling strategy for PCI data involving intra- and inter-volume variations. It is called interleaved velocity encoding and temporal sampling (I-VT). The proposed I-VT sampling strategy focuses on exploiting all degrees of freedom with two goals. The data shall be sampled such that the coherence is minimized while offering high acceleration factors and the degree of re-usability within the data set is maximized.

9.2.1 Pattern Formulation

The proposed sampling strategy is described by $\mathbf{u}^{t,s} \in \mathbb{C}^{N_k}$ where $u_{\kappa}^{t,s}$ stands for the sampling at k -space position κ with spatial indices $(\kappa_x, \kappa_y, \kappa_z)$, related by the mapping \mathcal{M} , in time step t and encoding s . Thereby

$$u_{\kappa}^{t,s} = u_{(\kappa_x, \kappa_y, \kappa_z)}^{t,s} = \begin{cases} 1, & \text{indicates a sampled voxel and} \\ 0, & \text{otherwise.} \end{cases} \quad (9.17)$$

The central region of the pattern is defined analogously to Section 4.3.2 around the middle point $\kappa_m = (\kappa_{my}, \kappa_{mz}) = (\lfloor \frac{N_{\kappa_y}}{2} \rfloor, \lfloor \frac{N_{\kappa_z}}{2} \rfloor)$ with size $(N_{\kappa_{cy}}, N_{\kappa_{cz}})$. The respective start and end points of the central region equal

$$\kappa_{ms} = (\kappa_{msy}, \kappa_{msz}) = (\kappa_{my} - \lfloor \frac{N_{\kappa_{cy}}}{2} \rfloor, \kappa_{mz} - \lfloor \frac{N_{\kappa_{cz}}}{2} \rfloor) \quad \text{and} \quad (9.18)$$

$$\kappa_{me} = (\kappa_{mey}, \kappa_{mez}) = (\kappa_{my} + \lfloor \frac{N_{\kappa_{cy}}}{2} \rfloor, \kappa_{mz} + \lfloor \frac{N_{\kappa_{cz}}}{2} \rfloor). \quad (9.19)$$

The central region is defined as index set \mathcal{C} , the peripheral region as \mathcal{P} , where

$$\mathcal{C} = \{\kappa \mid (\kappa_{msy} \leq \kappa_y \leq \kappa_{mey}) \wedge (\kappa_{msz} \leq \kappa_z \leq \kappa_{mez}) \wedge (1 \leq \kappa_x \leq N_{\kappa_x})\} \quad \text{and} \quad (9.20)$$

$$\mathcal{P} = \{\kappa \mid (1 \leq \kappa_y < \kappa_{msy} \vee \kappa_{mey} < \kappa_y \leq N_{\kappa_y}) \wedge (1 \leq \kappa_z < \kappa_{msz} \vee \kappa_{mez} < \kappa_z \leq N_{\kappa_z}) \wedge (1 \leq \kappa_x \leq N_{\kappa_x})\}. \quad (9.21)$$

9.2.2 Interleaved Central k-Space Sampling

The central sampling is based on a regularly under sampled template, parametrized by the distance

$$\mathbf{d}_c = [d_{cy}, d_{cz}]^T \quad (9.22)$$

and the offset

$$(j(t, s)) = [o_{cy}(j(t, s)), o_{cz}(j(t, s))]^T. \quad (9.23)$$

The offset depends on the time step t , the encoding s and the mapping $j : \mathbb{N}^2 \rightarrow \mathbb{N}$, referred to as shifting index in the following. Those are chosen for 2-D as

$$\mathbf{d}_c = \begin{bmatrix} N_s \\ 1 \end{bmatrix} \quad \text{and} \quad \mathbf{o}_c(j(t, s)) = \begin{bmatrix} (j-1) \\ 0 \end{bmatrix} \quad (9.24)$$

and for 3-D as

$$\mathbf{d}_c = \begin{bmatrix} \frac{N_s}{2} \\ \frac{N_s}{2} \\ \frac{N_s}{2} \end{bmatrix} \quad \text{and} \quad \mathbf{o}_c(j(t, s)) = \begin{bmatrix} \text{mod}(\lfloor (j-1)/2 \rfloor, \lfloor N_s/2 \rfloor) \\ \text{mod}(\lfloor j/2 \rfloor, \lfloor N_s/2 \rfloor) \end{bmatrix}. \quad (9.25)$$

The pattern is constructed with

$$u_{(\kappa_x, \kappa_y, \kappa_z)}^{t,s} = \begin{cases} 1, & \text{for } (\kappa_y, \kappa_z) = \kappa_{ms} + \mathbf{o}_c(j(t, s)) + i\mathbf{d}_c \text{ and} \\ & 1 \leq \kappa_x \leq N_{\kappa_y} \text{ where } i \in \mathbb{N} \\ & \text{subject to } \mathcal{M}(\kappa_x, \kappa_y, \kappa_z) \in \mathcal{C} \\ 0, & \text{otherwise.} \end{cases} \quad (9.26)$$

The construction of the k -space center sampling is schematically shown in Figure 9.3 for $N_s = 4$. The possible k -space central regions for $j \in \{1, \dots, 4\}$ are shown for the 2-D case in Figure 9.3(a) and for the 3-D case in Figure 9.3(b).

The introduction of the mapping $j(t, s)$ allows to represent a wide range of possible central pattern variations. Conventional choices such as a static pattern, sampling all time steps and velocity encodings in the same way, can be formulated with by constant $c \in \mathbb{Z}$ as

$$j_S(t, s) = c, \quad (9.27)$$

independent of t and s . The sampling strategy with variations in time dimension is obtained by choosing

$$j_T(t, s) = c(t). \quad (9.28)$$

The novel I-VT sampling strategy proposes variations in both time and velocity encoding direction, which obey two constraints:

1. Two subsequent time steps in the same encoding never share the same central lines and
2. all k -space central lines must be sampled in each time step.

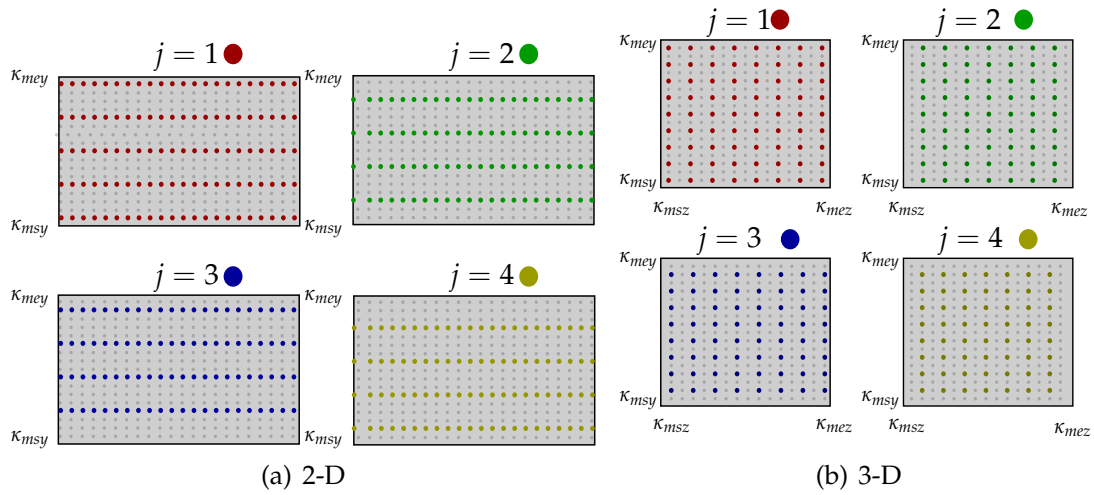


Figure 9.3: Illustration of the central region generated with the proposed I-VT sampling strategy: Variations for $j \in \{1, \dots, N_s\}$ for the (a) 2-D and (b) 3-D case. The four different colours express the acquired k -space samples for the four variations. The smaller black dots represent non-sampled k -space points.

This introduces mappings $j(t, s)$ such that

$$1. \quad j(t_i, s) \neq j(t_k, s) \text{ for } |t_i - t_k| = 1 \text{ and} \quad (9.29)$$

$$2. \quad j(t, s_i) \neq j(t, s_k), \quad \forall \quad s_i, s_k \in \{1, \dots, N_s\}. \quad (9.30)$$

These constraints assure both high incoherence and the shared coil sensitivity calculation. The patterns fulfilling those constraints are referred to as interleaved velocity encoding temporal (I-VT) patterns.

The regular permutations $j_P(t, s)$ interleave the sampling in s direction and offer cyclic shifts in time domain as

$$j_P(t, s) = \text{mod}(t + s, N_s). \quad (9.31)$$

This mapping automatically obeys the two constraints formulated in Eqs. (9.29-9.30). Another option are random permutations

$$j_P(t, s) = \text{rand}(1, \dots, N_s), \quad (9.32)$$

such that Eqs. (9.29-9.30) hold.

The four mentioned mapping functions are schematically illustrated in Figure 9.4.

9.2.3 Peripheral Decreased Density Sampling

The proposed sampling of the center can in principle be combined with any incoherent choice for the periphery such as the Poisson-disc distribution. In the following, the proposed MICCS pattern from Section 4.3.2 will be used with the same offsets for central and peripheral region $\mathbf{o}_P = \mathbf{o}_C$ to assure smooth transitions. While the pattern construction was illustrated schematically so far, an exemplary 2-D problem with $N_{k_y} = 256$ and the obtained patterns are shown in Figure 9.5.

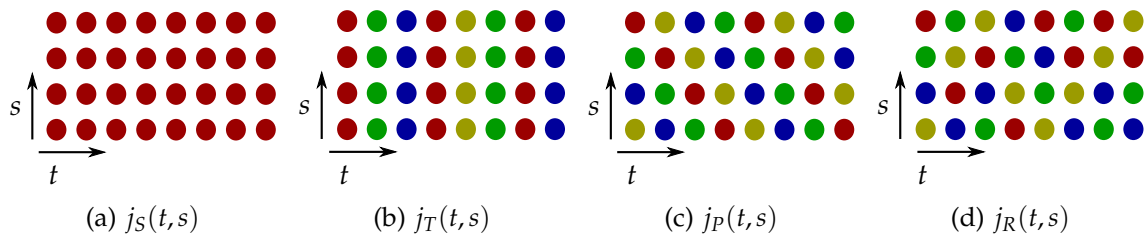


Figure 9.4: Schematic results in the ts plane for four mapping functions: Static mapping $j_S(t,s)$, temporal variation $j_T(t,s)$, regular permutations $j_P(t,s)$ and random permutations $j_R(t,s)$.

The point spread functions over time and velocity encoding dimension for the four described variants are illustrated using a 3-D plot and a 2-D projection in Figure 9.6.

The proposed I-VT sampling strategy exploits s and t directions to add incoherence, but also enables shared calculation of the coil sensitivity profiles. Typically, the central lines of k -space are externally acquired and used for the calculation of coil profiles. Using the proposed pattern, the central lines can be collected interleaved over all encodings. Further benefits of this sampling strategy become evident later in this thesis.

9.3 Implementation

All developed reconstruction algorithms are implemented into the previously explained IterRecon framework described in Section 4.5. The parts relevant for the PCI data reconstructions are framed in red in Figure 9.7. The computational complexity for the evaluation of the data fidelity term for each encoding and each time step corresponds to the complexity calculated for the static case, as the Fourier transforms are calculated independently for each encoding and time step. The total cost thus equals $O(N_p N_\gamma N \log N)$ for each evaluation of the data fidelity term.

The run times for the current implementation on a standard notebook with 8.0 GB RAM using a i3-2328M CPU with 2.2GHz are given in Table 9.1. These are again measured for the entire reconstruction, but without taking the data I/O and the calculation of the coil sensitivities into account. The MuFloCoS algorithm requires for example for a 2-D carotid data set with matrix size $N = 256 \times 256$, 11 temporal phases and 4 velocity encodings with $N_\gamma = 10$ coils, performing $N_i = 10$ iterations around 25 minutes.

9.4 Summary and Conclusion

The joint iterative reconstruction problem for PCI was presented. In contrast to the conventional case, all encodings are reconstructed simultaneously, enabling multi-dimensional regularizers such as second order temporal Fourier transforms. Furthermore, the novel PCI sampling strategy, called I-VT sampling, was motivated

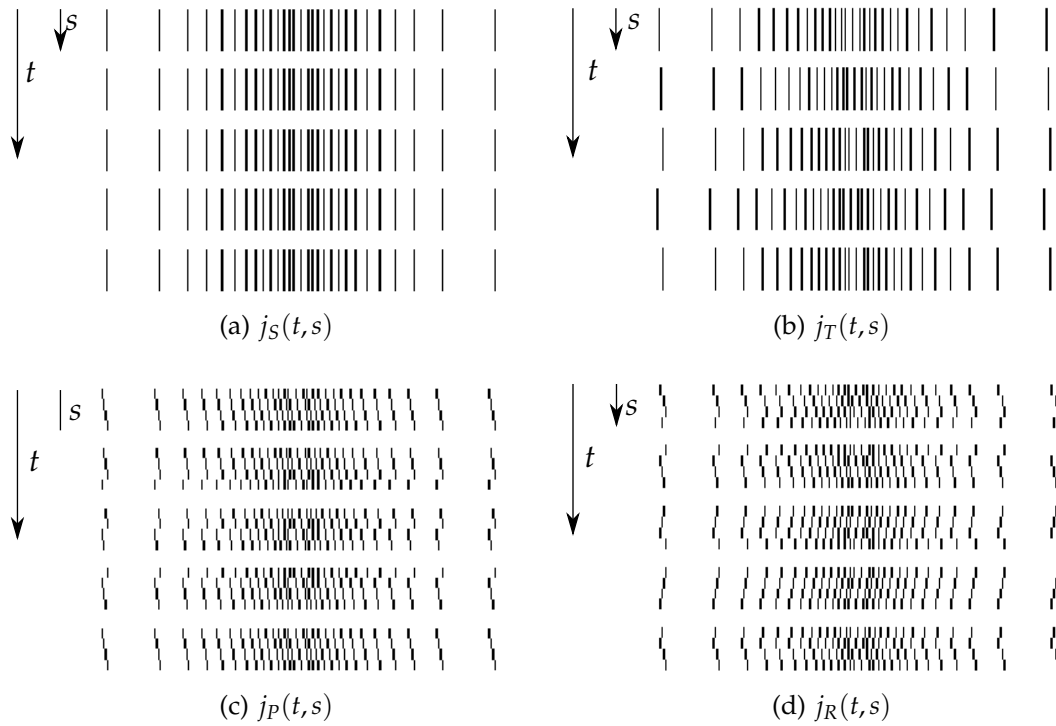


Figure 9.5: Exemplary 2-D patterns for $N_{k_y} = 256$ are shown using the same parameters a, b for the inverse root sampling in the periphery, but varying in the mapping $j(t, s)$ used for the central k -space region.

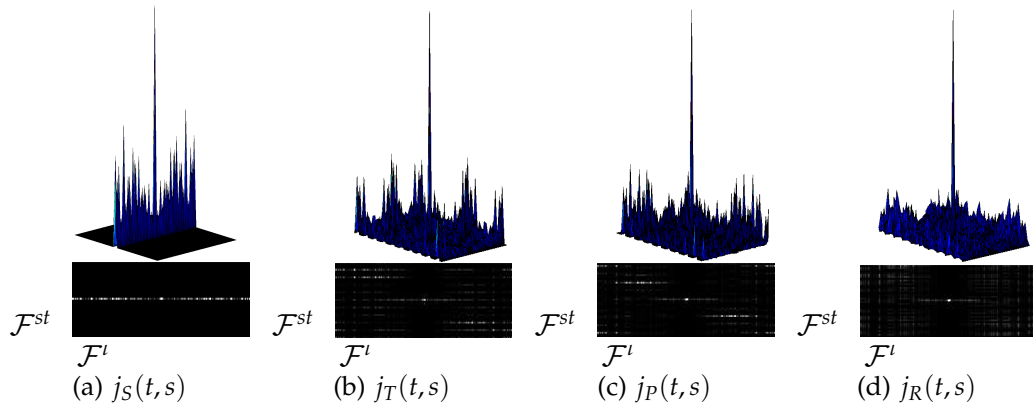


Figure 9.6: The point spread functions (PSF) for the four discussed mapping functions are depicted. All PSFs are shown in 3-D and in a 2-D projection below.

and detailed. It includes variation in all available dimensions, especially as well over velocity encodings, which is not yet used in the state of the art detailed in Section 7. The implementation of the joint reconstruction and the I-VT sampling was described, including the presentation of the developed PCI part of the IterRecon framework.

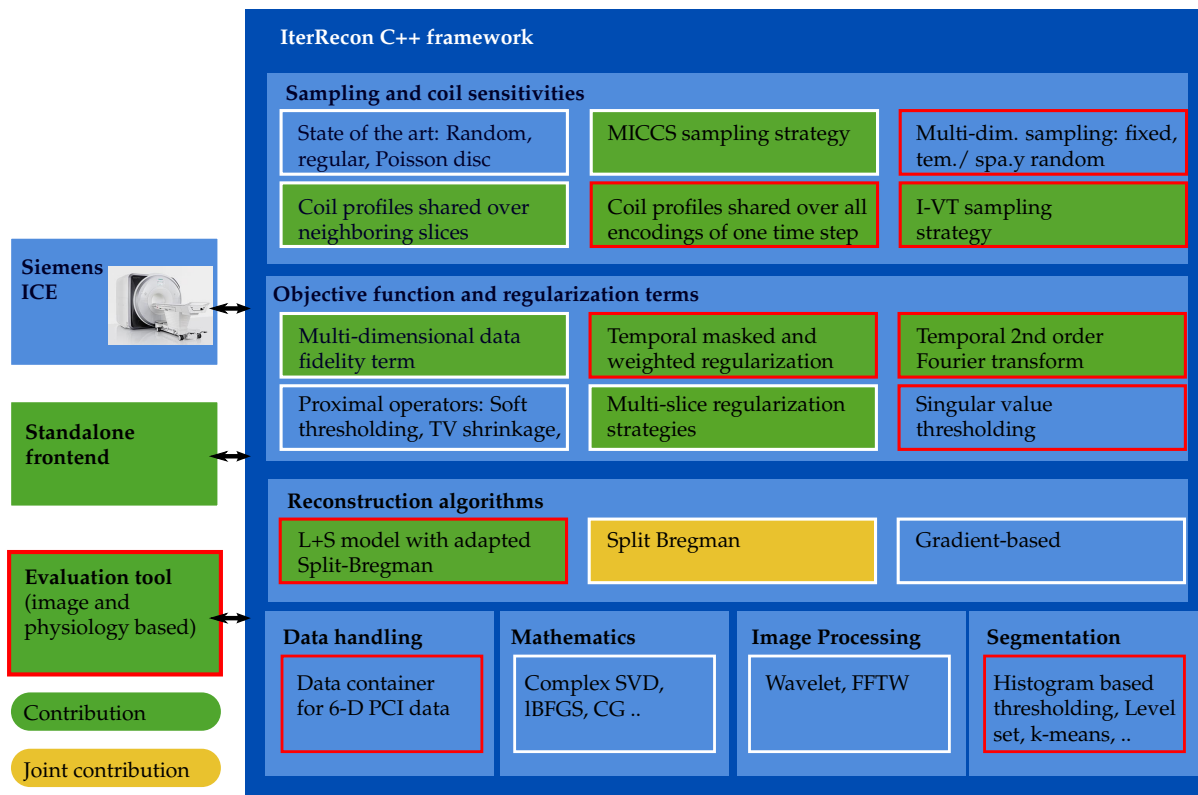


Figure 9.7: Illustration of the IterRecon framework highlighting the elements for PCI reconstruction in red. The joint contributions are marked in yellow, the contributions of this thesis in green.

Application	Algorithm	N	N_p	N_γ	$N_i/N_j/N'_i$	Run time [sec]
Carotids	MuFloCoS	256×256	44	11	10/ - / -	1519.4
Carotids	LoSDeCoS	256×256	44	11	-/5/3	988.6
Carotids	S-CS _{veFT-W}	256×256	44	11	10/ - / -	885.4

Table 9.1: The run times for the considered algorithms for the PCI data are given with the corresponding parameters.

Multi-dimensional Flow-Preserving Compressed Sensing (MuFloCoS)

10.1 Motivation	117
10.2 MuFloCoS	118
10.3 Implementation and Experiments.	124
10.4 Results	129
10.5 Discussion	134
10.6 Summary and Conclusion	141

This chapter presents an iterative reconstruction algorithm for PCI data, called multi-dimensional, flow-adapted Compressed Sensing (MuFloCoS). The MuFloCoS approach proposes an adaptive vessel masked and temporally weighted (TMW) L_1 regularization which exploits spatio-temporal correlations while maintaining the temporal flow fidelity using the anatomy based sub-division. In this chapter, the MuFloCoS algorithm will be motivated and developed. The implementation, the experimental setup using the data presented in Chapter 8 are explained and the results are presented and discussed.

10.1 Motivation

For carotid PCI, the dynamic changes originate mainly from blood flow effects, either directly or indirectly induced by vessel wall motion due to its pulsatile nature. In addition, their spatial extent is limited to the vessel proximity. Further possible origins of movement, patient-, cardiac-, and breathing motion can be neglected for this application. The temporal resolution of derived physiological parameters with clinical relevance, such as volumetric flow, peak velocity or wall shear stress depends to a high degree on the temporal fidelity of the reconstruction. A well suited temporal regularization should thus exploit the anatomical correlation in the static tissue parts to offer volumes with clinically accepted image quality while maintaining the temporal fidelity in vessel proximity.

Two basic requirements exist for the use of this prior knowledge:

- A joint reconstruction algorithm, which reconstructs all volumes for all time steps as well as velocity encodings simultaneously to allow for exploiting correlations spanning over different images along all dimensions.
- A stable dynamic sub-division of the image volume into vessels and static tissue is required.

The necessary information for this subdivision is intrinsically available in PCI with the anatomical images. The proposed MuFloCoS algorithm exploits the significant spatio-temporal correlation in the dynamic acquisition while preserving the temporal flow resolution with a temporal masked and weighted (TMW) L_1 regularization strategy employing vessel masks.

Two versions of this algorithm have been developed. The first version, called MDFCS, corresponds in parts to the publications [Hutt 13b] and [Hutt 13a], the second version will be referred to by MuFloCoS and was presented in [Hutt 14d]. MuFloCoS extends MDFCS by a fully interleaved and incoherent sampling. Furthermore, the TMW- L_1 regularization strategy is refined by adding additional weighting and masking with a static and dynamic mask for a stable and automatic differentiation into static and non-static tissue during the reconstruction. In contrast to further proposed methods, not only the spatial and temporal dimension, but also the PCI inherent velocity encoding dimension is included in all steps of the algorithm.

10.2 MuFloCoS

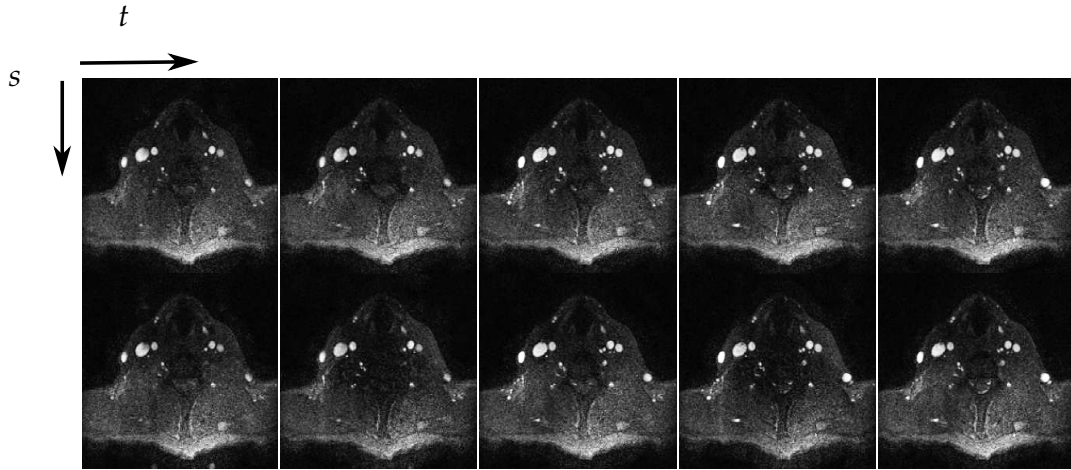
The novel MuFloCoS approach is presented in detail here. It consists of four main points: (i) The multi-dimensional joint iterative Newton-based reconstruction and (ii) the interleaved I-VT pattern were already explained in Sections 9.1 and 9.2. (iii) The vessel-masked and temporal weighted TMW regularization will be detailed in Section 10.2.1 and finally (iv) the domain sub-division using the anatomical image will be explained in Section 10.2.2.

10.2.1 Vessel Masked and Temporal Weighted L_1 Regularization

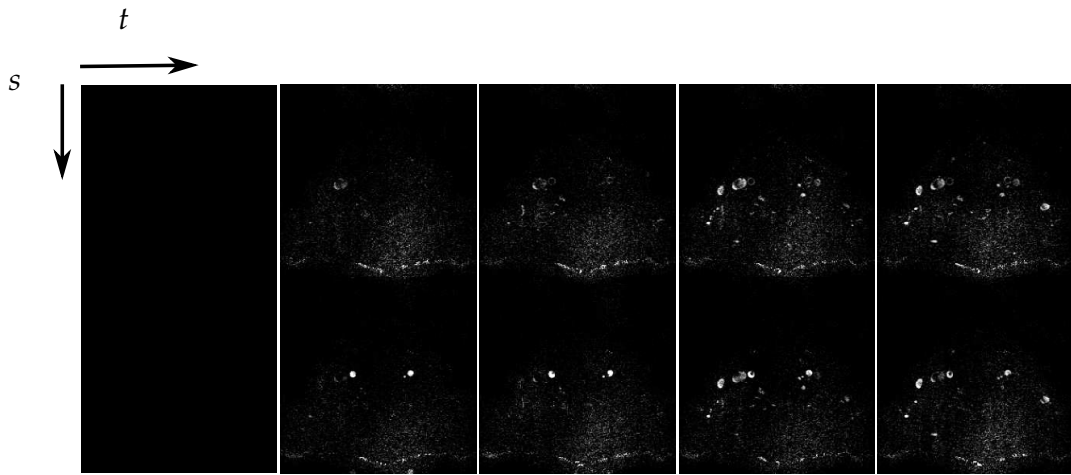
The significant spatio-temporal correlations of PCI can be observed exemplarily in the first five time steps for the velocity compensated scan and the through-plane velocity encoded scan in Figure 10.1(a). Those can be modelled using finite differences (FD) ∇_t with different step length in time direction. For each temporal time point t and encoding s , the FD $\nabla_t^{t,s,t_j} \mathbf{x}$, with $\nabla_t^{t,s,t_j} \mathbf{x} \in \mathbb{C}^N$ to phase t_j with $j \in \{1, \dots, N_t\}$ is calculated voxel wise as

$$(\nabla_t^{t,s,t_j} \mathbf{x})_i = x_i^{t_j,s} - x_i^{t,s}. \quad (10.1)$$

Figure 10.1(b) illustrates the FD $\nabla_t^{t,s,t_j} \mathbf{x}$ for $t = 1$ and $t_j \in \{2, \dots, 5\}$ for the velocity compensated ($s = 1$) and through-plane encoded ($s = 2$) scans. To assess the proposed sparsity assumption quantitatively, the coefficients of the FD images



(a) Exemplary PCI dataset



(b) Finite differences with growing timestep

Figure 10.1: Illustration and justification of the weighted and masked temporal regularization strategy. (a) The magnitude of the flow-compensated ($s = 1$) and through-plane encoded ($s = 2$) images is shown for $t \in \{1, \dots, 5\}$. (b) The finite differences over time between $t = 1$ and $t_j \in \{2, \dots, 5\}$ are depicted.

$\left| (\nabla_t^{t,s,t_j} \mathbf{x})_\iota \right|$ for $\iota \in \{1, \dots, N\}$ are depicted sorted by magnitude in Figure 10.2 for $\nabla_t^{1,1,2} \mathbf{x}$, $\nabla_t^{1,1,4} \mathbf{x}$, $\nabla_t^{1,2,2} \mathbf{x}$ and $\nabla_t^{1,2,4} \mathbf{x}$. Three observations can be made and will motivate the algorithmic choices detailed below. (i) In general, it can be observed, that the significant high contributions are concentrated within few pixels in the coefficient plot. This corresponds well to the difference images in Figure 10.1(b), where the main contributions to the finite differences are clearly concentrated at the vessels, which show velocity changes over time, while the background has relatively low contribution. (ii) There is a substantial difference between the flow compensated and encoded images. While the flow-encoded scans show the described enhancement of vessels in the temporal phases with high flow, this is less clearly observable in the compensated scans. The zooms into the highest 0.1% of the coefficients show a more significant contribution of the velocity-encoded scan.

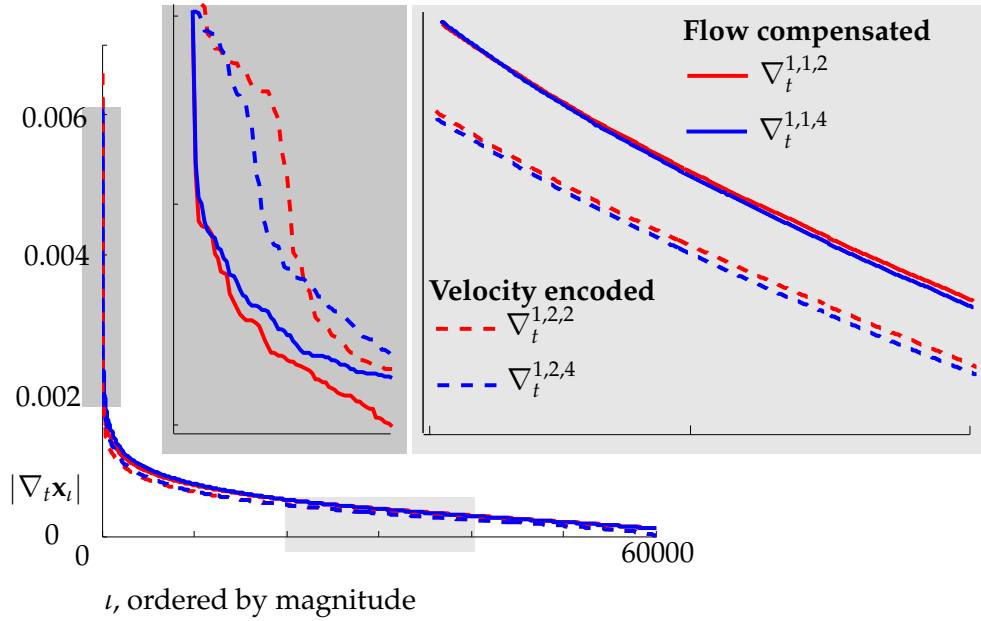


Figure 10.2: Finite difference coefficients $\left|(\nabla_t^{t,s,t_j} \mathbf{x})_i\right|$ ordered by magnitude show the sparsity of the used differences for $t_j = 2$ and $t_j = 4$. The straight lines depict the coefficients for the velocity-compensated, the dotted lines for the velocity-encoded scans. The zooms illustrated the 0.1% highest and the evolution of the middle third of the coefficients.

The lower coefficients reveal the inverse situation. Overall, the coefficients for the flow-encoded scans are more compressed in the highest values. (iii) Finally, the concentration of contributions to the vessels decrease for more distant time steps. However, the general importance of the differentiation in vessels and background remains valid for a certain range of subsequent time steps. Based on those observations, the MuFloCoS algorithm includes three features into the temporal finite difference regularization:

- A vessel-mask limiting the regularization to background areas to preserve the dynamics within the vessels,
- different treatment for the flow compensated and velocity encoded scans, and
- a temporal weighting in time direction, including a range of time steps but attributing higher importance to closer frames.

The difference terms are arranged for all step sizes in a common vector $\nabla_t^{t,s} \mathbf{x} \in \mathbf{C}^{NN_t}$ as:

$$\nabla_t^{t,s} \mathbf{x} = \begin{pmatrix} \nabla_t^{t,s,1} \mathbf{x} \\ \vdots \\ \nabla_t^{t,s,N_t} \mathbf{x} \end{pmatrix}. \quad (10.2)$$

The concatenated vector for all flow encodings $\nabla_t^t \mathbf{x} \in \mathbf{C}^{NN_p}$ and for all encodings and all time steps $\nabla_t \mathbf{x} \in \mathbf{C}^{NN_p N_t}$ equal

$$\nabla_t^t \mathbf{x} = \begin{pmatrix} \nabla_t^{t,1} \mathbf{x} \\ \vdots \\ \nabla_t^{t,N_s} \mathbf{x} \end{pmatrix} \quad \text{and} \quad \nabla_t \mathbf{x} = \begin{pmatrix} \nabla_t^1 \mathbf{x} \\ \vdots \\ \nabla_t^{N_t} \mathbf{x} \end{pmatrix}. \quad (10.3)$$

The weighting function $w(t, t_j)$ is realized either with a box function $w_B(t, t_j)$ or a Gaussian kernel $w_G(t, t_j) = \frac{-1}{\sqrt{2\pi}} e^{-\frac{(t_j-t)^2}{\sigma^2}}$, centred at position t with standard deviation $\sigma \in \mathbb{R}$, determining the extent of the influence of neighbouring phases. Thereby the vector $\mathbf{w}^t \in \mathbb{R}^{NN_t}$ equals

$$\mathbf{w}^t = \underbrace{(w(t, 1), \dots, w(t, 1))}_{N \text{ times}}, \dots, \underbrace{(w(t, N_t), \dots, w(t, N_t))}_{N \text{ times}}. \quad (10.4)$$

It is used to form the weighting matrix for time step t , $\mathbf{W}^t \in \mathbb{R}^{NN_s \times NN_p}$, as well as the complete weighting matrix $\mathbf{W} \in \mathbb{R}^{NN_p \times NN_p N_t}$ with

$$\mathbf{W}^t = \begin{pmatrix} \mathbf{w}^t & & \\ & \ddots & \\ & & \mathbf{w}^t \end{pmatrix} \quad \text{and} \quad \mathbf{W} = \begin{pmatrix} \mathbf{W}^1 & & \\ & \ddots & \\ & & \mathbf{W}^{N_t} \end{pmatrix}. \quad (10.5)$$

Finally, the vessel masks $\mathbf{b}^t \in \mathbb{R}^N$ are involved. Those equal

$$b_i^t = \begin{cases} 1, & \text{for voxels within a vessel and} \\ 0, & \text{for background voxels.} \end{cases} \quad (10.6)$$

Their calculation is detailed in Section 10.2.2. To limit the regularization to the background areas, the masks are subtracted from the unity vector $\mathbf{1}_N - \mathbf{b}^t$, such that voxels within vessels are multiplied with 0 and do not contribute to the value of the regularization. The differentiation between compensated and encoded acquisitions is modelled by weighting all voxels of the compensated scan with 1, meaning that the regularization considers them. The masks are arranged in the diagonal matrices $\mathbf{B}^t = \text{diag}(\mathbf{b}^t) \in \mathbb{R}^N$, and composed to form matrices $\mathbf{M}^t \in \mathbb{R}^{NN_s \times NN_s}$. These are used in the assemblage of the entire mask matrix $\mathbf{M} \in \mathbf{C}^{NN_p \times NN_p}$ and are given as

$$\mathbf{M}^t = \begin{pmatrix} \mathbf{1} & & & \\ & \mathbf{1} - \mathbf{B}^t & & \\ & & \ddots & \\ & & & \mathbf{1} - \mathbf{B}^t \end{pmatrix} \quad \text{and} \quad \mathbf{M} = \begin{pmatrix} \mathbf{M}^1 & & \\ & \ddots & \\ & & \mathbf{M}^{N_t} \end{pmatrix}. \quad (10.7)$$

The temporal differences $\nabla_t \mathbf{x}$ are multiplied with the mask matrix \mathbf{M} and the weighting matrix \mathbf{W} , which results in the temporal masked and weighted regularization term

$$\text{TMW}(\mathbf{x}) = \|\mathbf{M}\mathbf{W}\nabla_t \mathbf{x}\|_{L_1}. \quad (10.8)$$

The objective function including the regularization weight λ_{tmw} equals

$$\mathcal{L}_{\text{Muf}}(\mathbf{x}) = \underbrace{H(\mathbf{x})}_{\text{Data fidelity term}} + \underbrace{\lambda_{\text{tmw}} \text{TMW}(\mathbf{x})}_{\text{Regularization}} \quad (10.9)$$

$$= \underbrace{\frac{1}{2} \|\mathbf{E}\mathbf{x} - \mathbf{m}\|_{L_2}^2}_{\text{Data fidelity term}} + \underbrace{\lambda_{\text{tmw}} \|\mathbf{M}\mathbf{W}\nabla_t \mathbf{x}\|_{L_1}}_{\text{Regularization}}. \quad (10.10)$$

This leads to the following minimization problem:

$$\hat{\mathbf{x}} = \underset{\mathbf{x}}{\text{argmin}} \mathcal{L}_{\text{Muf}}(\mathbf{x}). \quad (10.11)$$

The TMW- L_1 regularization penalizes non-similarity to neighbouring temporal phases but differentiates between static and flow affected areas in order to avoid temporal blurring.

10.2.2 Anatomy Based Sub Division

During the iterative reconstruction the volume, defined by its voxel set T with $T = \{\iota = 1, \dots, N\}$ is divided into a static part consisting of the voxel set S and a part affected by flow induced motion D with $T = S \cup D$ and $S \cap D = \emptyset$ to allow guidance of the temporal regularization to the static parts. This is important to avoid temporal blurring. The goal is therefore to obtain dynamic masks $\mathbf{b}^t \in [0, 1]^N$ as described in Eq. (10.6) with the property

$$b_i^t = \begin{cases} 1, & \text{if } \iota \in D \text{ and} \\ 0, & \text{if } \iota \in S. \end{cases} \quad (10.12)$$

As the sub-division correlates mainly with the vessel anatomy in the chosen application, b_i^t is referred to as vessel mask. The selected differentiation feature is the occurrence of flow as it is inherent in the PCI technique through the anatomical images \mathbf{a}^t as explained in Section 7.2.2. The proposed interleaved and incoherent pattern leading to distributed incoherent artefacts in s and t direction allows an approximation of \mathbf{a}^t , which is used to generate the masks \mathbf{b}^t . This information is then available for the temporal regularization and directs it to the known locations of correlation. Beside the approximation of the typical PCI anatomical map \mathbf{a}^t , as described in Eq. (7.7), a static approximation $\bar{\mathbf{a}}$ calculated as the anatomical image over all phases is used

$$\bar{a}_i = \sqrt{\sum_{s=2}^{N_s} \frac{1}{N_t} \left(\sum_{t=1}^{N_t} (\mathbf{x}^{t,1})_i - \sum_{t=1}^{N_t} (\mathbf{x}^{t,s})_i \right)^2}. \quad (10.13)$$

During the reconstruction, both are calculated based on the actual image estimate $\mathbf{x}_i^{t,s}$ for iteration $i \in \{1, \dots, N_i\}$. The first necessary estimate used during the first iteration, referred to by \mathbf{x}^0 corresponds to the conventionally reconstructed raw data vector using the SoS method: $\mathbf{x}^0 = \mathcal{S}(\mathbf{m})$. By updating the masks in each iteration, the algorithm adapts to the improving image quality over iterations. MuFloCoS

uses a combination of both static and dynamic images, which is crucial for the stability and robustness of the algorithm particularly for the first iterations which are heavily influenced by aliasing artefacts. This is illustrated with a 9.0 times under sampled data set in Figure 10.3. The obtained static masks for the first 4 iterations and the last iteration are shown in Figure 10.3(a), the dynamic images for time step 2 in Figure 10.3(b). The aliasing artefacts in the first dynamic masks are visible, while the static images allow clear depiction of the vessels with the first iteration. This is possible through the use of the I-VT pattern with variations in both temporal and velocity encoding direction. The combined use of these interleaved sampled k -space reconstructions allows to generate the high quality anatomical images.

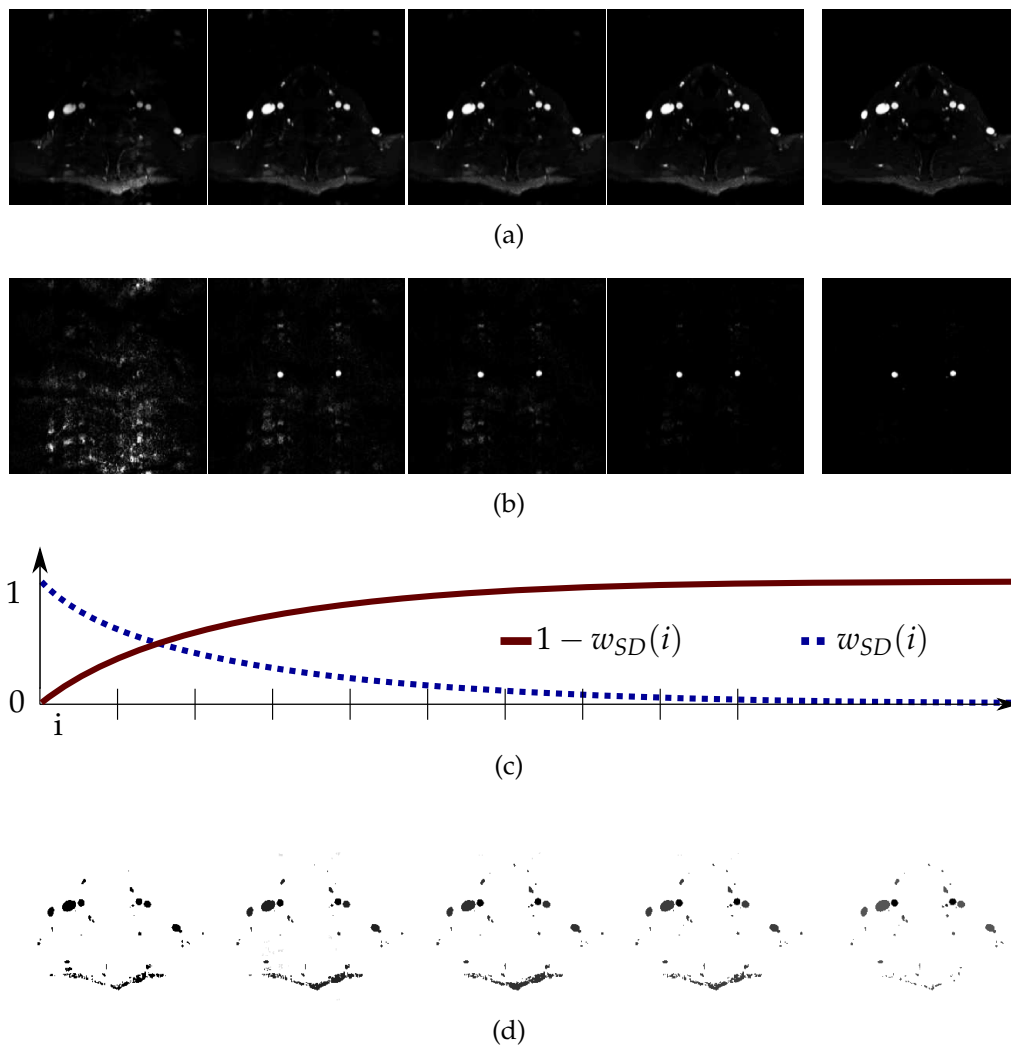


Figure 10.3: The generation of the adaptive vessel masks as a combination of the static and dynamic anatomical images is illustrated. The (a) static images $\bar{\mathbf{a}}$ and (b) dynamic images \mathbf{a}^t for the first 4 and the last iteration are depicted. (c) The evolution of their respective influence is shown depending on the parameter $w_{SD}(i)$. (d) The final vessel masks \mathbf{b}^t for $t = 2$ are visualized.

The sub-division is entirely based on this intrinsically obtained anatomical images $\bar{\mathbf{a}}$ and \mathbf{a}^t by applying a binary threshold α_m . The obtained static masks $\bar{\mathbf{b}}^i$ and dynamic masks $\check{\mathbf{b}}^i$ for voxel i equal

$$\bar{b}_i^i = \begin{cases} 1, & \text{if } \bar{a}_i^t > \alpha_m \\ 0, & \text{otherwise} \end{cases} \quad \text{and} \quad \check{b}_i^i = \begin{cases} 1, & \text{if } a_i^t > \alpha_m \\ 0, & \text{otherwise} \end{cases}. \quad (10.14)$$

The influence of the static and dynamic anatomical image approximation changes smoothly with the parameter $w_{SD}(i)$ depending only on the iteration step i with

$$\mathbf{b}^t = \frac{1}{2} \left(w_{SD}(i) \bar{\mathbf{b}} + (1 - w_{SD}(i)) \check{\mathbf{b}}^t \right), \quad \text{where} \quad w_{SD}(i) = 1/i^\beta. \quad (10.15)$$

The evolution of $w_{SD}(i)$ over iteration steps is visualized in Figure 10.3(c). Figure 10.3(d) illustrates the final vessel masks \mathbf{b}^t .

10.3 Implementation and Experiments

This section describes the details of the MuFloCoS algorithm implementation as well as the experimental setup.

10.3.1 MuFloCoS Implementation Details

The algorithm is included into the described C++ reconstruction framework. The linked version directly processes the raw data after acquisition using the inline data processing pipeline. The MuFloCoS algorithm seeks to find a solution $\hat{\mathbf{x}}$ for the problem as stated in Eq. (10.9).

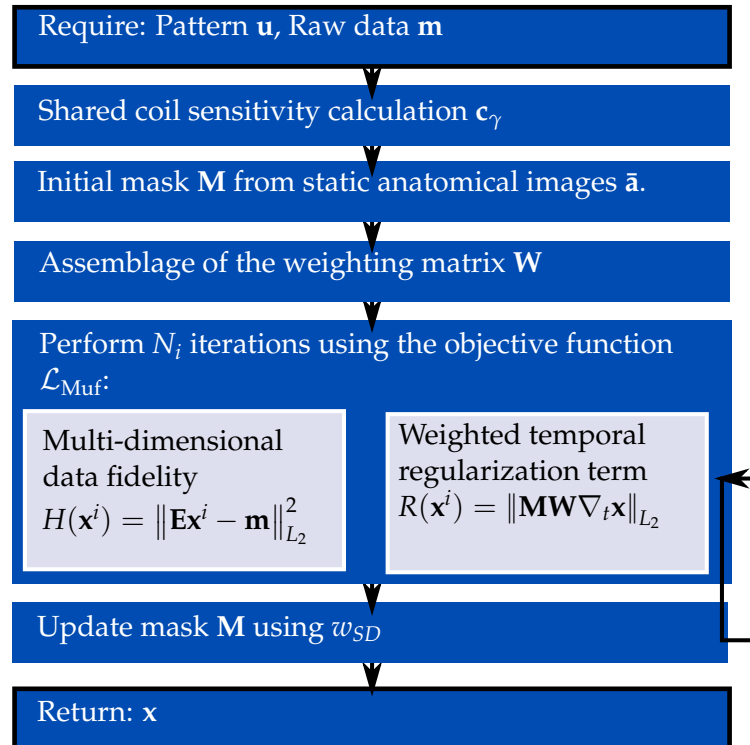
The complete MuFloCoS algorithm is represented in the flow chart in Figure 10.4 as well as in a detailed step overview in Algorithm 10.1. The preprocessing steps 1 through 2 include shared coil profile calculation, initialization of the vessel mask, calculation of the temporal weights and assembling of the encoding matrix. Then, the iterative process is started.

Considering the size of the optimization problem with NN_p unknowns, a limited-memory BFGS solver [Noce 80] is used. Replacement with further solvers such as the conjugate gradient method is possible without introducing structural changes. For all gradient-based solvers, evaluation of both the objective function and its gradient are required within each iteration to determine with direction and step size. Finally, the vessel mask matrix is updated. The parameters were chosen equally for all datasets and experiments as $N_i = 10$, $\alpha_m = 0.1 \max_i \bar{a}_i$, $\sigma = 1.8$ and $\lambda_{tmw} = 0.004$. The $\epsilon = 0.001$ ensures computational efficiency, as the differences are calculated only in the relevant kernel of $w(t, t_j)$.

For the proposed TMW regularization, as described in the methods section and given in Algorithm 10.1, the finite differences are multiplied with the weighting matrix and subsequently the mask matrix, resulting in a total of $N^2 N_p^2 N_t + N^2 N_p^2$ multiplications. The computational effort thus adds up to $O(N^2 N_p^2 N_t)$. Regarding the calculation of the anatomical images with $N_{s-1} N_t$ required subtractions and

Algorithm 10.1 MuFloCoS algorithm (theoretical)**Require:** $\mathbf{m}, \mathbf{u}, \mathcal{L}_{\text{Muf}}, \nabla \mathcal{L}_{\text{Muf}}, w(t, t_j), \epsilon, \lambda_{\text{tmw}}, N_i, w_{\text{SD}}(i)$ **INPUT:** \mathbf{x}^0

- 1: Calculate combined coil profiles \mathbf{c}_γ^t
 - 2: Obtain direct reconstruction with $\mathcal{S}(\mathbf{m}^{t,s})$
 - 3: Calculate $\bar{\mathbf{a}}^t$ and $\bar{\mathbf{b}}^t$
 - 4: Initialize mask matrix \mathbf{M}
 - 5: Assemble weighting matrix \mathbf{W}
 - 6: Assemble encoding matrix \mathbf{E} with $e_{(\gamma,\kappa),\iota}^{t,s} = u_\kappa^{t,s} e^{i\mathbf{k}_\kappa^{t,s} \mathbf{r}_\iota} c_{(\gamma,\iota)}^t$
 - 7: **for all** $i = 1$ to N_i **do**
 - 8: Perform optimizer step with the objective function $\mathcal{L}_{\text{Muf}}(\mathbf{x}^{i-1})$ and its gradient $\nabla \mathcal{L}_{\text{Muf}}(\mathbf{x}^{i-1})$
 - 9: Calculate the data fidelity term $H(\mathbf{x}^{i-1})$
 - 10: Assemble FD vector $\nabla^t = (\nabla_t^1, \dots, \nabla_t^{N_t})$
 - 11: Calculate $R(\mathbf{x}^i) = \|\mathbf{M}\mathbf{W}\nabla_t \mathbf{x}^{i-1}\|_{L_1}$
 - 12: Update \mathbf{x}^i
 - 13: Update $\bar{\mathbf{a}}, \mathbf{a}^t, \bar{\mathbf{b}}, \mathbf{b}^t$
 - 14: Combine $\bar{\mathbf{b}}$ and \mathbf{b}^t to $\check{\mathbf{b}}^t$ using $w_{\text{SD}}(i)$
 - 15: Update mask matrix \mathbf{M}
 - 16: **end for**
- OUTPUT:** \mathbf{x}^{N_i}

**Figure 10.4:** Schematic representation of the MuFloCoS algorithm

multiplications, the total computational cost adds up to $O(N^2N_p^2N_t)$. The implementation, however, differs from this theoretically calculated complexity, as the weighting matrix is not calculated a priori, but evaluated for all vector elements as shown in Algorithm 10.2. The complexity thus lays within $O(NN_sN_t^2)$ for the evaluation of the TMW regularization term. The squared consideration of the number of time steps is due to the theoretical calculation of the finite differences with all possible step length. The introduction of the Gaussian weighting and the ϵ fixes the number of used temporal steps to $N'_t < N_t$. The following calculations, are, however, given for the worst case of $N'_t = N_t$. The evaluation of the multi-dimensional data fidelity term lays within $O(N_pN_\gamma N \log N)$ as discussed in Section 9.3. In total, the complexity of the per-iteration complexity, considering again a limited number of function evaluations, is bounded by $O(N_pN_\gamma N \log N + NN_sN_t^2)$. For N_i iterations of the linearly scaled LBFGS algorithm, the total complexity lays within $O(N_iN_pN_\gamma N \log N + N_iNN_sN_t^2)$.

Algorithm 10.2 MuFloCoS algorithm (implemented)

Require: $\mathbf{m}, \mathbf{u}, \mathcal{L}_{\text{Muf}}, \nabla \mathcal{L}_{\text{Muf}}, w(t, t_j), \epsilon, \lambda_{\text{tmw}}, N_i, w_{\text{SD}}(i)$
INPUT: \mathbf{x}^0

- 1: Calculate combined coil profiles \mathbf{c}_γ^t
 - 2: Obtain direct reconstruction with $\mathcal{S}(\mathbf{m}^{t,s})$
 - 3: Calculate $\bar{\mathbf{a}}^t$ and $\bar{\mathbf{b}}^t$
 - 4: Initialize mask matrices \mathbf{M}^t as column vectors \mathbf{m}^t
 - 5: **for all** $i = 1$ to N_i **do**
 - 6: Perform optimizer step with the obj. function $\mathcal{L}_{\text{Muf}}(\mathbf{x}^{i-1})$ and its gradient $\nabla \mathcal{L}_{\text{Muf}}(\mathbf{x}^{i-1})$
 - 7: Calculate the data fidelity term $H(\mathbf{x}^{i-1})$ as illustrated in Figure 4.4
 - 8: **for all** $s = 1, \dots, N_s$ **do**
 - 9: **for all** $t = 1, \dots, N_t$ **do**
 - 10: **for all** $t_j = 1, \dots, N_t$ **do**
 - 11: **for all** $\iota = 1, \dots, N$ **do**
 - 12: **if** $s = 1$ **then**
 - 13: $h = h + w(t, t_j)(\nabla_t^{t_j, s})_\iota$
 - 14: **else**
 - 15: $h = h + (1 - (\mathbf{m}^t)_\iota)w(t, t_j)(\nabla_t^{t_j, s})_\iota$
 - 16: **end if**
 - 17: **end for**
 - 18: **end for**
 - 19: **end for**
 - 20: **end for**
 - 21: Update \mathbf{x}^i
 - 22: Update $\bar{\mathbf{a}}, \mathbf{a}^t, \bar{\mathbf{b}}, \check{\mathbf{b}}^t$
 - 23: Combine $\bar{\mathbf{b}}$ and $\check{\mathbf{b}}^t$ to \mathbf{b}^t using $w_{\text{SD}}(i)$
 - 24: Update mask vectors \mathbf{m}^t
 - 25: **end for**
- OUTPUT:**
- \mathbf{x}^{N_i}
-

Reconstruction method	ΔQ [%]	ΔQ^i [%]	ΔQ^o [%]
Reference	2.72 ± 0.10	-0.73 ± -0.16	-1.16 ± 0.10
MuFloCoS	3.31 ± 0.07	2.45 ± 0.73	2.23 ± 0.46

Table 10.1: Quantitative evaluation of the phantom data. The flow deviations ΔQ in the slices and between neighbouring slices regarding both inflow ΔQ^i and outflow ΔQ^o are calculated for all slices in the phantom experiment. The deviations are given in percent.

10.3.2 Quantitative and Physiological Evaluation of the TMW Regularization

The fully sampled phantom data sets were reconstructed with the conventional SoS technique to obtain a reference volume. The I-VT pattern with acceleration factor 9 was applied retrospectively and the under sampled data was reconstructed using our proposed MuFloCoS method. Table 10.1 presents the deviation results for the reference reconstruction and for MuFloCoS in percent, which are all below 4%.

Quantitative flow parameters obtained with the proposed reconstruction algorithm are compared to previously reported literature values and to the results of different state of the art iterative algorithms to ensure the validity of the proposed method for enhanced image quality and quantification purposes. Six reconstructions were therefore performed: the fully sampled data set was reconstructed using the SoS technique to obtain a Reference. The remaining five reconstructions were performed using an acceleration factor of 9.0 for different iterative techniques all reconstructed using the proposed I-VT sampling. Furthermore, the same formulation of the data fidelity term in Eq. (10.9) was used for all reconstructions, the algorithms thus varied in the choice of the regularization. All emerging optimization problems were solved using the same LBFGS method with $N_i = 10$ which has been shown to be very stable and especially well suited for large optimization problems as the present. The considered algorithms are

- **Iterative SENSE (ISENSE)** without regularization, corresponding to $\lambda_{\text{tmw}} = 0$ in Eq. (10.9).
- **Spatially L_1 regularized CS** with spatial regularization. State of the art L_1 Compressed Sensing algorithm, regularized in the present case with wavelet decomposition and TV, in combination with the data fidelity term to reconstruct under sampled k -space data. This method was proposed by several authors, including for example Lustig et al. [Lust07] with wavelets and by Hsiao et al. [Hsia12] and Holland et al. [Holl10] with TV, wavelets and curvelets as well for PCI. It will be referred to by $S\text{-CS}_{\text{TV-W}}$ in the following sections.
- **kt-SPARSE SENSE** was proposed specifically for dynamic MRI by Otazo et al. [Ota10] and includes temporal regularization which is in most cases temporal Fourier transform. This is typically combined with a spatial regularization component, such as Wavelets in the study by Lustig et al. [Lust06],

or with PCA by Kim et al. [Kim 12a]. It will be referred to by $S\text{-CS}_{W\text{-vtFT}}$ in the following sections.

- **The MDFCS algorithm** previously proposed by Hutter et al. [Hutt 13b]. A box function instead of the Gaussian weighting is used and the vessel mask is obtained uniquely based on the dynamic images.
- **The proposed MuFloCoS algorithm** with $\lambda_{\text{tmw}} = 0.004$.

The sparsity weights for $S\text{-CS}_{\text{TV-W}}$ and $S\text{-CS}_{W\text{-vtFT}}$ were optimized individually for each technique regarding NRMSE over the parameter space $\lambda_t, \lambda_w, \lambda_f \in [10^{-5}, 10^{-3}]$ as described in Section 11.3.2. The resulting values $\lambda_t = 0.00001$ and $\lambda_w = 0.00003$ for $S\text{-CS}_{\text{TV-W}}$ and $\lambda_f = 0.00002$ and $\lambda_w = 0.00001$ for $S\text{-CS}_{W\text{-vtFT}}$ were used for all data sets.

10.3.3 Comparison Against State of the Art in CS for Carotid PCI

The aim of this experiment is the comparison of MuFloCoS against the only known further state of the art algorithm proposed for the same application, in-vivo imaging of the carotid arteries, the method by Tao et al. [Tao 13]. The key algorithmic elements are

- **R**: A pattern which is fully sampled in the central region and randomly under sampled in the periphery. The same percentage of central lines as in the study of Tao et al. (20 / 192) were used for the present data sets (26 / 256). The pattern was not varied over encodings but includes random variations over time.
- **L₁yf**: L₁ minimization in the yf-space for each encoding separately was proposed as regularization.

Different reconstructions, stated in Table 10.2, evaluating these components against the corresponding MuFloCoS parts, the I-VT sampling and the TMW regularization were evaluated for acceleration factor 3 as proposed in the study of Tao et al. and factor 9 as used for MuFloCoS. To ensure fair comparison, the weights were optimized regarding NRMSE for each of these experiments, but kept fixed over all data sets.

10.3.4 Parameter and Robustness

The influence, stability and robustness of different algorithmic aspects and parameter choices are evaluated based on quantitative image measures and reconstruction parameters. For Experiment II, three elements were investigated: The regularization weight λ_{tmw} , the sampling strategy and the use of the shared coil profile calculation. The parameter λ_{tmw} was varied between 0.0005 and 0.0125, the sampling pattern was chosen to be fixed for all phases and temporal phases or interleaved and permuted with regular permutations with length 1 or interleaved and permuted as proposed by the I-VT sampling strategy of MuFloCoS. The basis pattern parameters $\mathbf{o}_c, \mathbf{d}_c, a$ and b were chosen identical for both. Furthermore, the

Reconstruction method	Regularization	
	L ₁ yf	TMW
R3	TAO3	R+TMW3
R9	TAO9	R+TMW9
I-VT3	I-VT+L ₁ yf3	MuFloCoS3
I-VT9	I-VT+L ₁ yf9	MuFloCoS9

Table 10.2: The different elements from the study by Tao et al. and the presented MuFloCoS algorithm are shown. This includes the random and I-VT sampling pattern, evaluated for both acceleration $\xi = 3$ and $\xi = 9$ as well as the L₁yf and the TMW regularization strategy.

influence of the internal coil sensitivity calculation was evaluated by using either the shared version or by acquiring an external reference scan, both resulting in a total of 16 used reference lines. Feasible acceleration factors for this application are determined, the used acceleration factor was therefore varied between 3, 6, 9, 12 and 15. The reconstructions were performed with fixed $\lambda_{\text{tmw}} = 0.004$.

The deviation is calculated for the volumetric flow $Q_v(t)$ and for the peak velocity $V_p(t)$. The TNRMSE for the mean velocity $V_m(t)$ equals $\text{TNRMSE}(Q_v(t))$ by definition of these values. Those results are illustrated with Bland-Altman diagrams for graphical illustration of all data sets and for each combination between MuFloCoS and state of the art methods. The results are ordered by the absolute values for the volumetric flow and the peak velocity of the data sets. This illustration aids to identify any systematic errors or outliers.

10.4 Results

In this section, the results for all presented experiments are given and illustrated.

10.4.1 Quantitative and Physiological Evaluation

The quantitative results for the image based measures of the study with 18 data sets are shown in Table 10.3 for MuFloCoS and the four comparison methods. The NRMSE of MuFloCoS is significantly reduced compared to the iterative SENSE reconstruction and all further considered methods. Statistically, the NRMSE has been improved by 47.6% compared to ISENSE, by 19.12% in comparison to S-CS_{W-VTFT} and by 19.12% compared to S-CS_{TV-W}. The same is valuable for the structural similarity SSIM, which was improved by 3.39% compared to the best comparison method S-CS_{TV-W}. The Contrast to Noise Ratio between the vessel and the background could be improved for all data sets, in the mean by at least 24.24% and up to 54.69%. Table 10.4 shows the mean deviation from the physiological parameters for each reconstruction technique. One data set (P16) was excluded from the calculation of physiological parameters, as the overall image

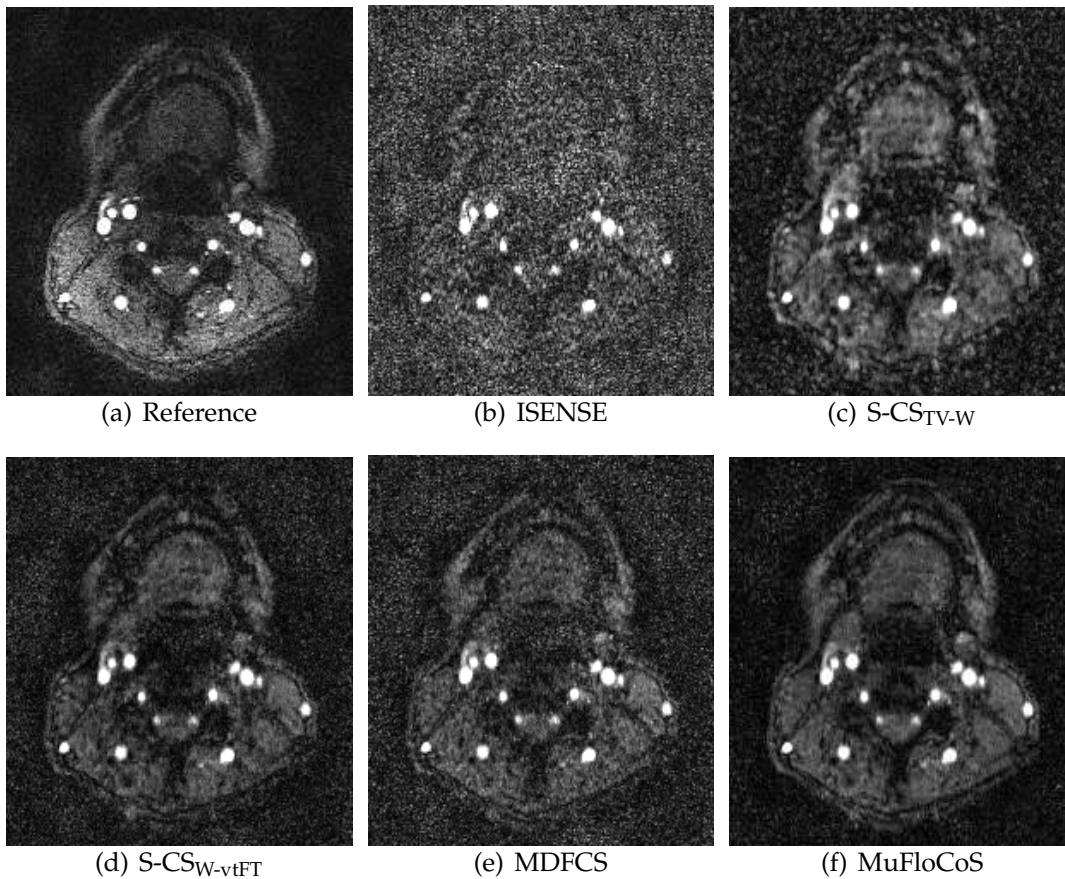


Figure 10.5: Magnitude reconstruction results for the through-plane encoding for volunteer P2 at peak systole: (a) Reference (b) ISENSE (c) $S\text{-CS}_{TV-W}$ (d) $S\text{-CS}_{W-vtFT}$ (e) MDFCS and (f) MuFloCoS.

quality even for the reference did not allow for a stable evaluation. A significant improvement was achieved for the peak velocity with 49.40% lower TNRMSE compared to $S\text{-CS}_{W-vtFT}$, 35.11% lower TNRMSE compared to MDFCS and 43.33% lower TNRMSE compared to $S\text{-CS}_{TV-W}$. Figure 10.5 and 10.6 illustrate two representative results for peak systole. The magnitude result for $s = 4$ is, in the upper row, shown for the reference, ISENSE, and $S\text{-CS}_{TV-W}$ and in the lower row for $S\text{-CS}_{W-vtFT}$, MDFCS and MuFloCoS. Representative time curves are shown in Figure 10.7, displaying the volumetric flow in the first row, the mean velocity in the second row and the peak velocity in the last row for all reconstruction results. The curves of the reference and MuFloCoS are very similar, while the other methods except $S\text{-CS}_{TV-W}$ tend to overestimate volumetric flow and mean velocity in both cases. The most significant difference is visible in the peak velocity plots, which is heavily disturbed for comparison methods but well preserved for MuFloCoS. Especially the $S\text{-CS}_{TV-W}$ method, which produced a lower error in volumetric flow significantly underestimated the Peak Velocity. The Bland-Altman diagram for the best comparison method $S\text{-CS}_{W-vtFT}$ is given in Figure 10.8. No outlier or systematic bias is visible in the MuFloCoS result, whereas the values for the other methods are spread for both volumetric flow and peak velocity. Figure 10.10 illus-

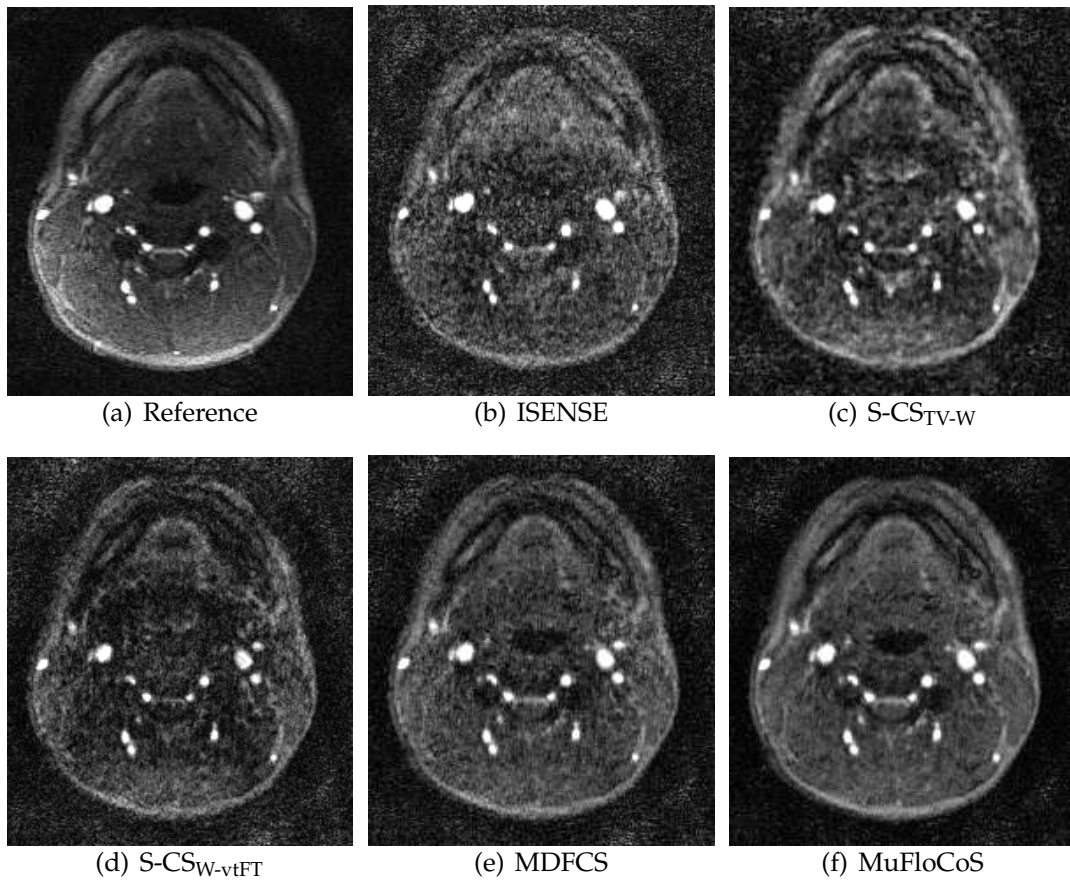


Figure 10.6: Magnitude reconstruction results for the through-plane encoding for volunteer P7 at peak systole: (a) Reference (b) ISENSE (c) CS_{wt} (d) CS_{kt} (e) MDFCS and (f) MuFloCoS.

trates the 3D result for peak systole and early diastole at three selected locations as depicted in Figure 8.2.

10.4.2 Comparison against Carotid PCI State of the Art

The results for this experiment are given in Table 10.5. Very good results were achieved for an acceleration factor of 3 with the original method proposed by Tao et al. [Tao 13], resulting in a SSIM of 0.939 ± 0.039 , a NRMSE of 0.057 ± 0.012 and a TNRMSE of the volumetric flow of 0.098 ± 0.042 for the random pattern. The results using the same regularization but the proposed I-VT sampling further increase image quality and the accuracy of the physiological values with a NRMSE of 0.042 ± 0.010 and TNRMSE of the peak velocity of 0.172 ± 0.069 . For the higher factor of 9, however, the proposed MuFloCoS algorithm outperforms this method, particularly with respect to the TNRMSE of the physiological values and the NRMSE. However, the method of Tao et al. shows some advantages regarding the SSIM value and the CNR. Comparing the results using the L_{1yt} regularization in combination with either the random or the I-VT pattern, the I-VT

Reconstruction method	NRMSE	SSIM	CNRVT	CNRVB
Reference	0.0 ± 0.0	1.0 ± 0.0	5.921 ± 2.7112	8.312 ± 2.333
ISENSE	0.105 ± 0.029	0.774 ± 0.126	4.341 ± 1.204	5.142 ± 1.403
S-CS _{TV-W}	0.068 ± 0.022	0.856 ± 0.070	5.200 ± 1.515	6.492 ± 1.714
S-CS _{W-vtFT}	0.068 ± 0.019	0.867 ± 0.078	5.060 ± 1.464	6.318 ± 1.759
MDFCS	0.074 ± 0.028	0.831 ± 0.098	5.315 ± 1.506	6.554 ± 1.683
MuFloCoS	0.055 ± 0.015	0.885 ± 0.064	6.084 ± 1.615	7.954 ± 1.998

Table 10.3: Quantitative image and physiology-based evaluation for the in-vivo study comparing MuFloCoS to the reference and further iterative methods.

Reconstruction method	TN(Q_v)	TN(V_p)
Reference	0.0 ± 0.0	0.0 ± 0.0
ISENSE	0.135 ± 0.068	0.228 ± 0.115
S-CS _{TV-W}	0.085 ± 0.039	0.150 ± 0.096
S-CS _{W-vtFT}	0.108 ± 0.059	0.168 ± 0.047
MDFCS	0.113 ± 0.058	0.131 ± 0.075
MuFloCoS	0.096 ± 0.045	0.085 ± 0.054

Table 10.4: Quantitative image and physiology-based evaluation for the in-vivo study comparing MuFloCoS to the reference and further iterative methods.

pattern delivers more accurate flow results and better NRMSE, but lower SSIM and CNR.

10.4.3 Robustness and Acceleration Studies

Image results for different λ_{tmw} values are shown in Figure 10.11 with a zoom to the right carotid artery. The data fidelity term as well as the TMW regularization term for selected choices of λ_{tmw} are illustrated in Figure 10.12(a) and 10.12(b). This reconstruction resulted in the values illustrated in Table 10.6. The respective images for $s = 4$ for early diastole ($t_3 = 136$ ms) and difference images to the complete MuFloCoS method are shown for the fixed pattern and the version with external coil sensitivities in Figure 10.13 along with the corresponding difference images to the normal MuFloCoS in the lower row. Volumetric flow and mean velocity are illustrated in Figure 10.14. Reconstruction specific parameters including the data fidelity term and the regularization term over time are illustrated in the lower row of Figure 10.13(c). Both the data fidelity and the L_1 norm show a similar behaviour for the variants with and without the shared coil sensitivities, but higher values for the variant without the interleaved and shifted pattern). Results of varying acceleration factors of 3, 6, 9, 12 and 15 and fixed λ_{tmw} can be seen for

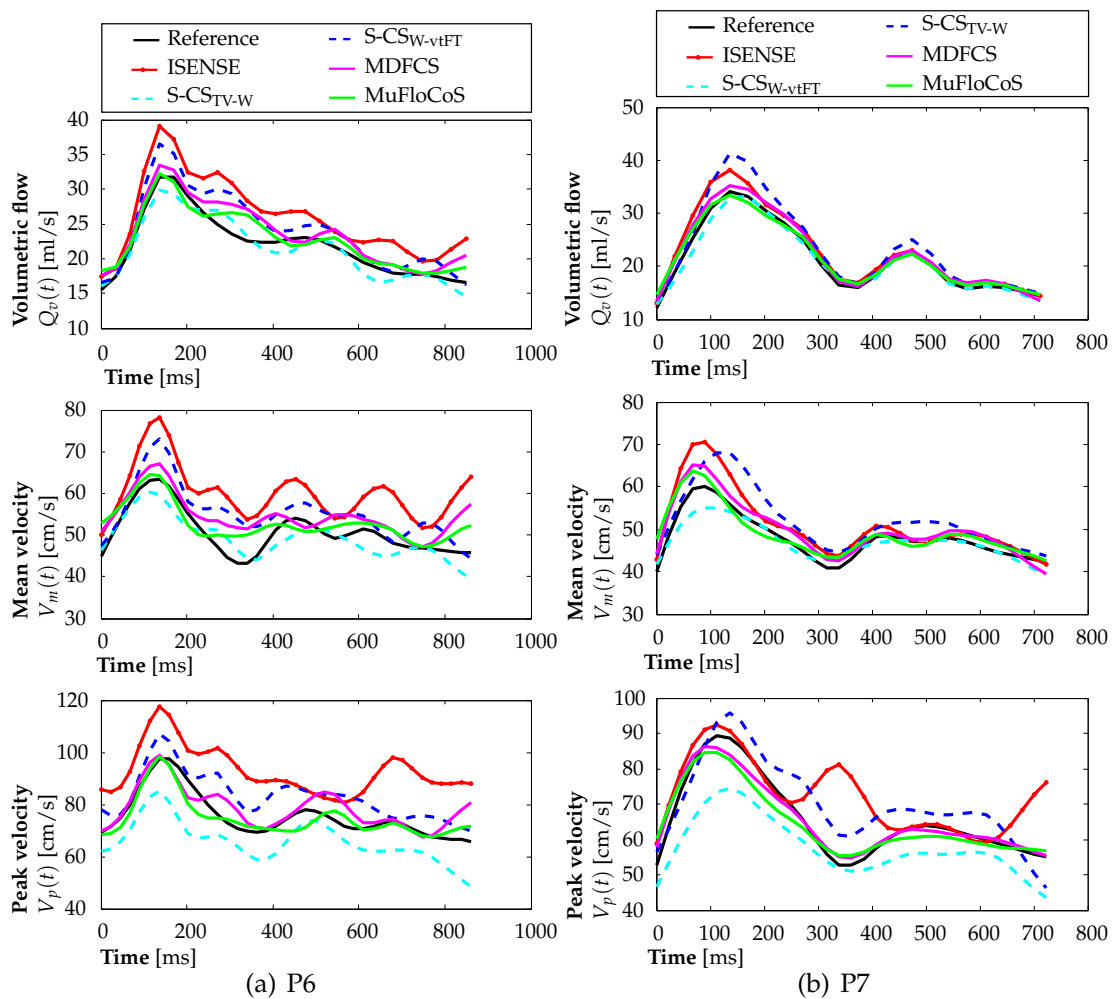


Figure 10.7: Volumetric flow, mean velocity profile and peak velocity profiles illustrated for volunteers P6 and P7.

$s = 4$ for the entire image and a zoom in Figure 10.16. The corresponding curves for volumetric flow are illustrated in Figure 10.17(a), the peak velocity in Figure 10.17(b).

10.4.4 Patient Cases

The two patient cases, described in Chapter 8 were examined. The under sampled data was reconstructed with MuFloCoS and evaluated with a special focus on the pathology detection by analysing the peak velocities in the CCA and ICA at three positions in the CCA, in close proximity to the stenosis and post-stenotic in the ICA. For patient 1, the corresponding peak velocity plots are illustrated in Figure 10.18. A clear difference is visible between the velocities in the pre-stenotic CCA and after the stenosis in the ICA. Especially on the right side, where the high-degree stenosis has been diagnosed, a sharp increase in peak velocity is observable, which correlates well with the reduced lumen at this position. The difference between the high-grade stenosis on the right side to the low-grade stenosis on the

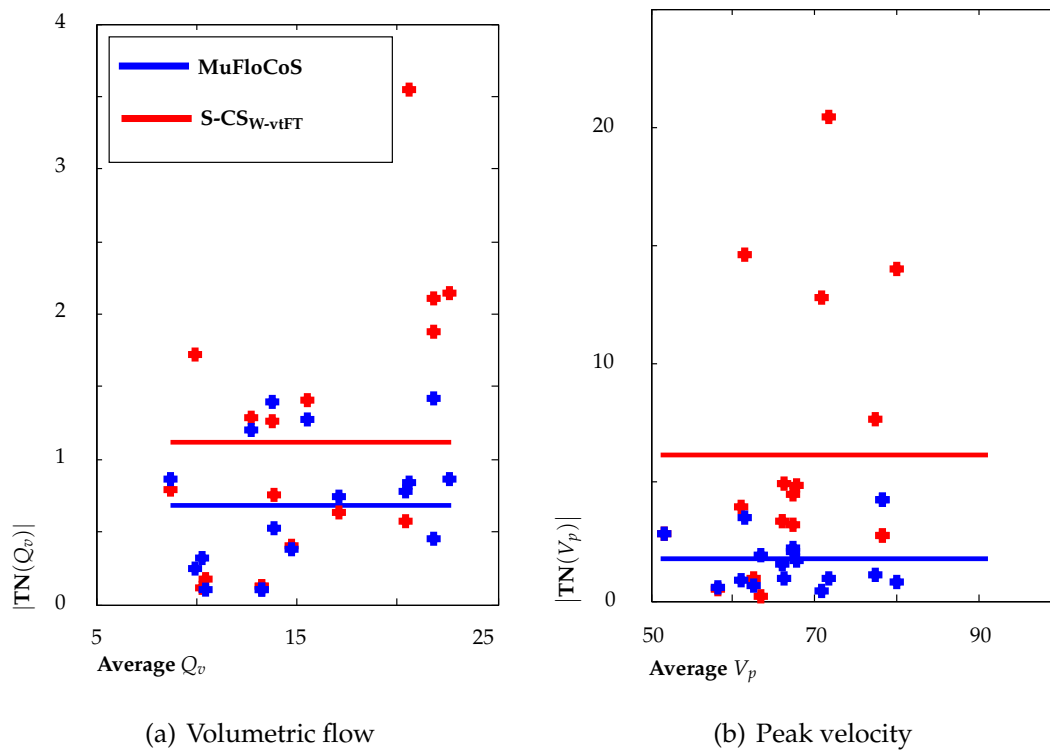


Figure 10.8: Bland-Altman diagram for (a) volumetric flow and (b) peak velocity for the in-vivo study for MuFloCoS and S-CS_{W-vtFT}.

left side is well visible in the difference of the peak velocities. The results for patient 2 in Figure 10.19 indicate the unilateral stenosis diagnosed with DCE-MRI. The stenotic profile in the ICA is corrupted by aliasing due to the high velocities. No correction was applied to this, but could be done by unwrapping.

10.5 Discussion

Iterative reconstruction with the proposed MuFloCoS method was successful for all phantom and in-vivo experiments and produced comparable and consistent results. The high noise level both in the background and the tissue of the image reconstructed with iterative SENSE was significantly reduced with the iterative methods. While all methods managed to recover the image structures, the quality of the images as well as the accuracy of the physiological parameters were objectively better for MuFloCoS. The image quality allowed in summary good visualization of the anatomy and corresponds to that of the fully sampled reference image.

10.5.1 Quantitative Evaluation

The inter and intra-slice deviations in the phantom-experiment were all under 4%, which illustrates the capability of MuFloCoS to preserve the flow values over the

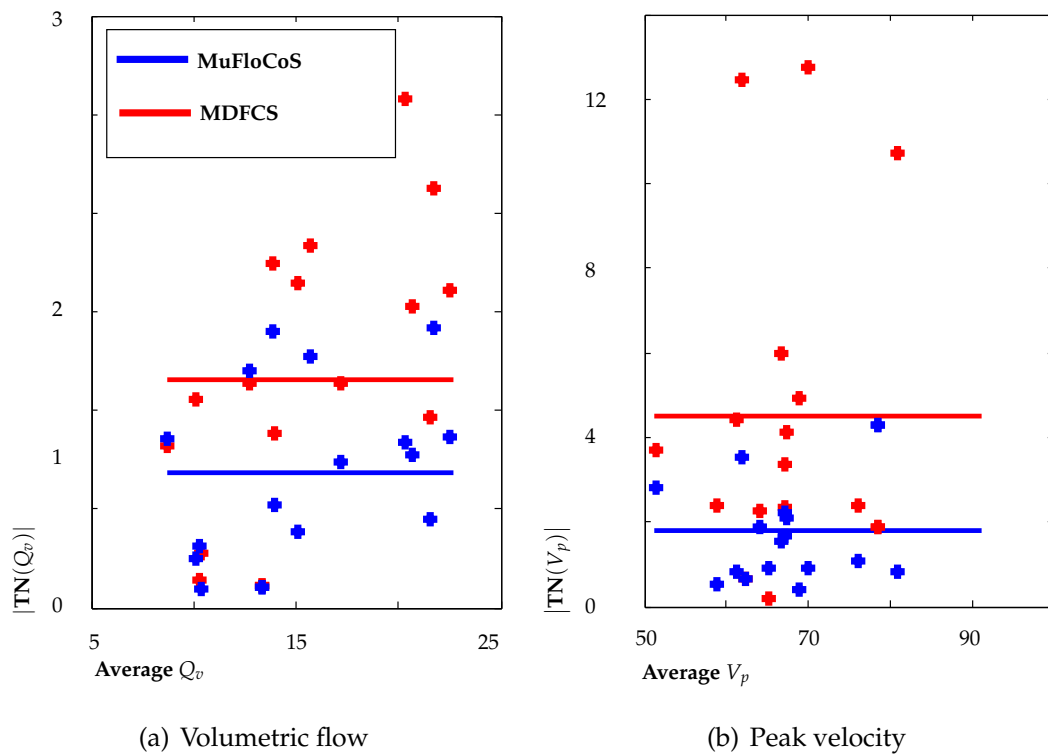


Figure 10.9: Bland-Altman diagram for (a) volumetric flow and (b) peak velocity for the in-vivo study for MuFloCoS and MDFCS.

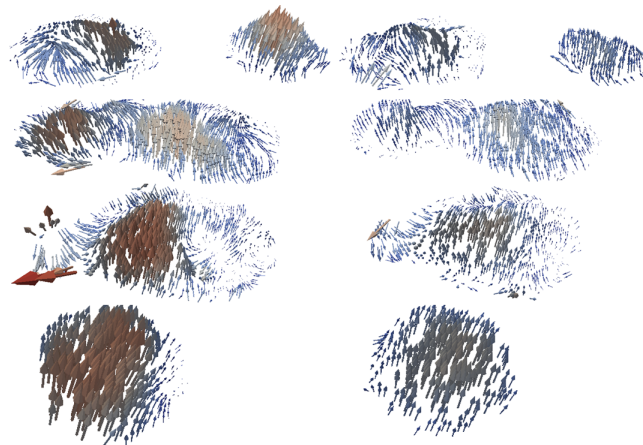


Figure 10.10: 3-D velocity vector field from the left carotid bifurcation region illustrated with 3-D vectors at four different locations for peak systole and early diastole.

entire dataset. Concerning the in-vivo data, both the evaluation of the flow parameters showed good preservation of flow parameters and had a significantly reduced deviation compared to the further methods in both the phantom experiment and the volunteer study, see Table 10.1, Table 10.3 and Table 10.4 for the quantitative results.

The MuFloCoS volumetric flow $Q_v(t)$ and the mean velocity $V_m(t)$ as well as the peak velocity $V_p(t)$ over time, see Figure 10.7, were in good agreement with

Reconstruction method	NRMSE	SSIM	CNRVT	CNRVB
Reference	0.0 ± 0.0	1.0 ± 0.0	5.921 ± 2.7112	8.312 ± 2.333
TAO $\xi = 3$	0.057 ± 0.012	0.939 ± 0.039	6.265 ± 1.674	8.068 ± 2.177
TAO $\xi = 9$	0.082 ± 0.017	0.936 ± 0.044	6.212 ± 1.285	9.117 ± 1.919
I-VT+L ₁ yf $\xi = 3$	0.042 ± 0.010	0.954 ± 0.031	6.326 ± 1.700	8.130 ± 2.166
I-VT+L ₁ yf $\xi = 9$	0.058 ± 0.017	0.884 ± 0.070	5.261 ± 1.346	6.710 ± 1.572
MuFloCoS 9	0.055 ± 0.015	0.885 ± 0.064	6.084 ± 1.615	7.954 ± 1.998

Table 10.5: Quantitative image-based evaluation for the in-vivo study comparing MuFloCoS against the results of carotid PCI state of the art.

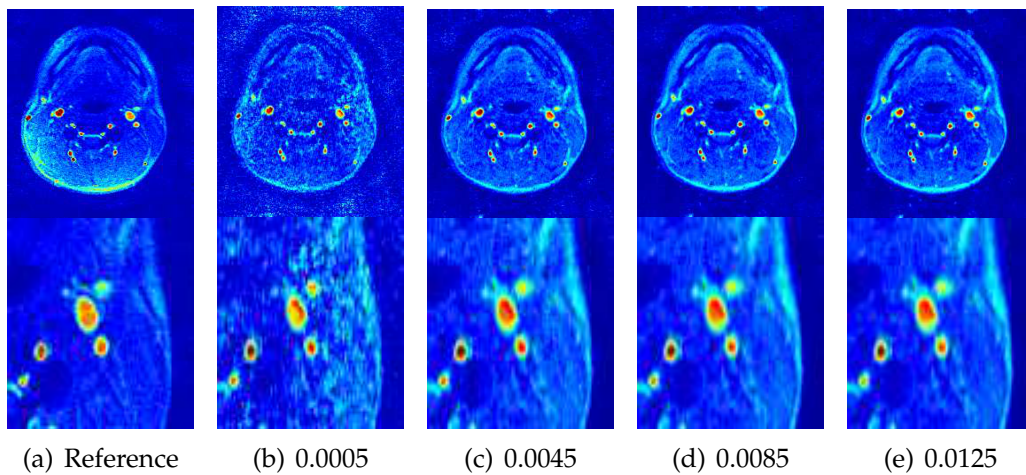


Figure 10.11: Image results for a representative volunteer using different λ_{tmw} and zooms to the right ICA for, from left to right, the reference and MuFloCoS with $\lambda_{tmw} = [0.0005, 0.0045, 0.0085, 0.0125]$.

the fully sampled directly reconstructed data sets in the CCA. Improvements to further state of the art methods showed improvements in NRMSE, SSIM but especially in the peak velocity, which is an important diagnostic value in the classification of stenosis. This indicates that both temporal and spatial resolution are well preserved. Volumetric flow and mean velocity corresponded well to previously reported values for the volumetric flow rate in Long et al. [Long 01] and for the mean velocity in Ringgaard et al. [Ring 04]. The patient cases and the respective peak velocity profiles in Figure 10.18 and Figure 10.19 confirmed the CT findings and allowed even to differentiate between high and low-grade stenosis.

The improvement compared to MDFCS shows the positive influence of the combined static and dynamic anatomical images as well as the Gaussian weighting. The comparison against state of the art for CS methods applied to carotid PCI indicated the improvements achieved with MuFloCoS regarding both image and physiology based measures and especially its availability for higher acceleration factors.

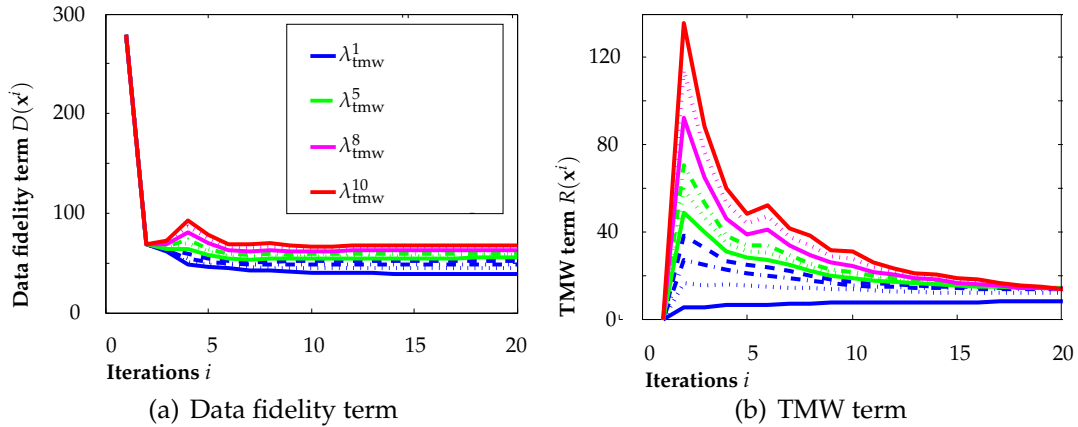


Figure 10.12: Reconstruction parameter results for a representative volunteer using different λ_{tmw} . (a) The evolution of the data fidelity term and (b) the temporal masked and weighted term are depicted for 20 iteration steps.

Measure	NRMSE	SSIM	CNRVB	TN(Q_v)	TN(V_p)
Reference	0.0	1.0	7.733	0.0	0.0
MuFloCoS	0.055 ± 0.022	0.848 ± 0.101	7.601 ± 1.018	0.074 ± 0.005	0.058 ± 0.010
Static pattern	0.059 ± 0.059	0.856 ± 0.100	6.703 ± 1.509	0.074 ± 0.005	0.081 ± 0.045
Ext. coil maps	0.058 ± 0.058	0.841 ± 0.107	7.371 ± 1.362	0.057 ± 0.007	0.054 ± 0.018

Table 10.6: Quantitative image based evaluation for different MuFloCoS variants.

10.5.2 Evaluation of I-VT, Shared Coil Profiles and TMW

The benefits of the masked temporal regularization and the I-VT pattern to exploit the inherent data correlation both in velocity encoding and temporal direction become evident with the results of their respective influence. The shared coil profile calculation led to a very slight change in the results for NRMSE from 0.055 to 0.058 while it contributed to the final acceleration in substantial amount by allowing real under sampling by factor four in the central k -space. Its influence, illustrated in Figure 10.13(b), was barely visible in the difference image where the main deviations occur outside the object. The influence of the interleaved and shifted pattern was substantially higher, as shown in Table 10.6 and in image 10.13(c). The L_1 norm plot in Figure 10.14 on the left illustrates that the higher similarity at the beginning due to the same sampling, expressed through low L_1 difference values, increased with iterations and converged at higher values than the I-VT pattern variant. This can be explained by the property of the I-VT pattern to allow a better minimization for the whole objective function in Eq. (10.9) including data fidelity term and regularization term. The NRMSE decreased from 0.059 to 0.055 compared to the shifted and interleaved pattern.

Experiment III illustrated furthermore that the proposed TMW- L_1 regularization offers a very stable regularization option. Different choices of the weighting factor λ_{tmw} led to comparable results both in terms of visual impression and in

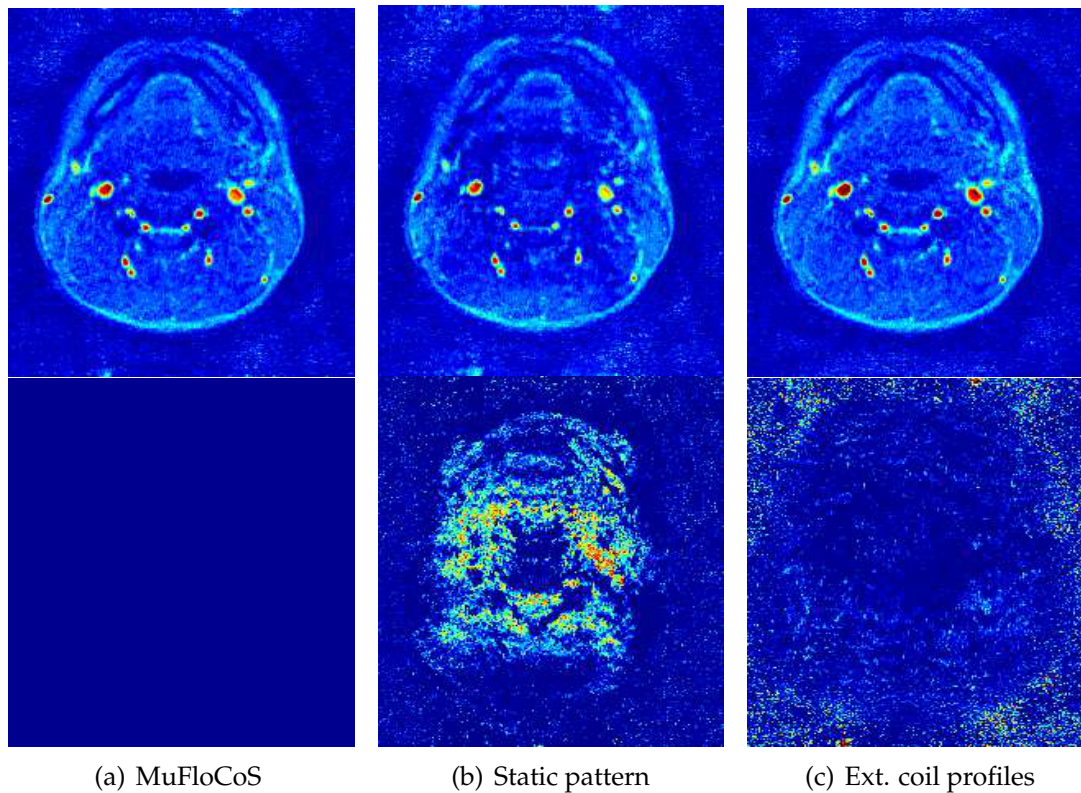


Figure 10.13: Image results for the through-plane encoding comparing the reference and MuFloCoS (a) with the I-VT pattern and the shared coil profiles, (b) without the I-VT pattern and (c) with external coil profiles. The lower row illustrates the difference to MuFloCoS scaled by a factor of 10.

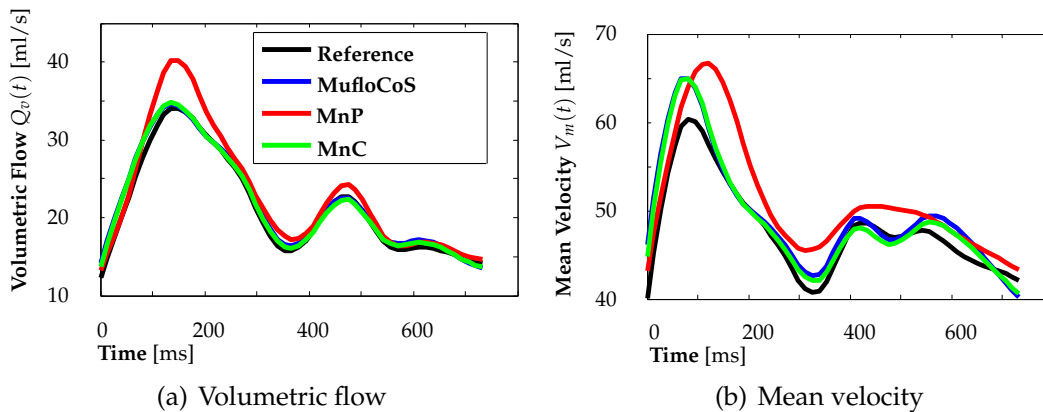


Figure 10.14: Physiological parameters for MuFloCoS with the I-VT pattern and the shared coil profiles, without the I-VT pattern and with external coil profiles. (a) Volumetric flow $Q_v(t)$ and (b) mean velocity $V_m(t)$ are shown.

the physiological parameter estimation. Figures 10.12(a) and 10.12(b) illustrated even a convergence for both the data fidelity term, as well as for the TMW- L_1 term independent of λ_{tmw} . For λ_{tmw} in the range of $[0.0015, 0.0125]$, the term converged to the same value after 20 iterations. No critical bound was obtained, the changes

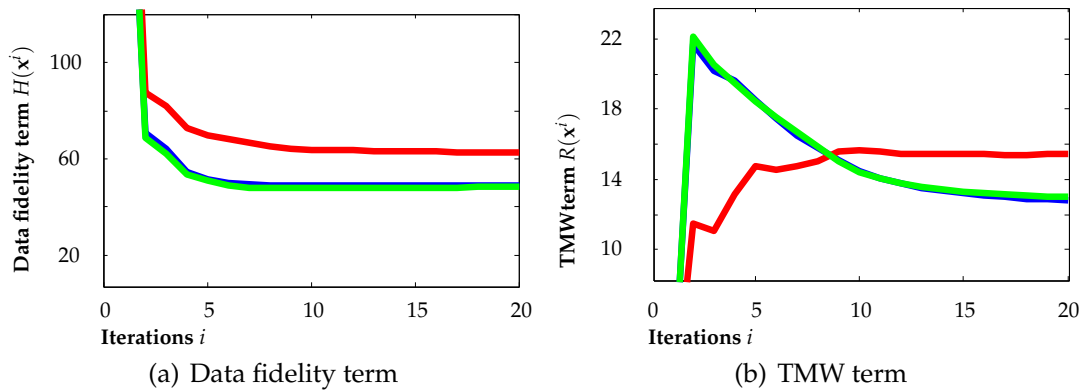


Figure 10.15: Reconstruction results for MuFloCoS with the I-VT pattern and the shared coil profiles, without the I-VT pattern and with external coil profiles. (a) The evolution of the data fidelity term and (b) the evolution of the TMW- L_1 term are depicted for 20 iteration steps.

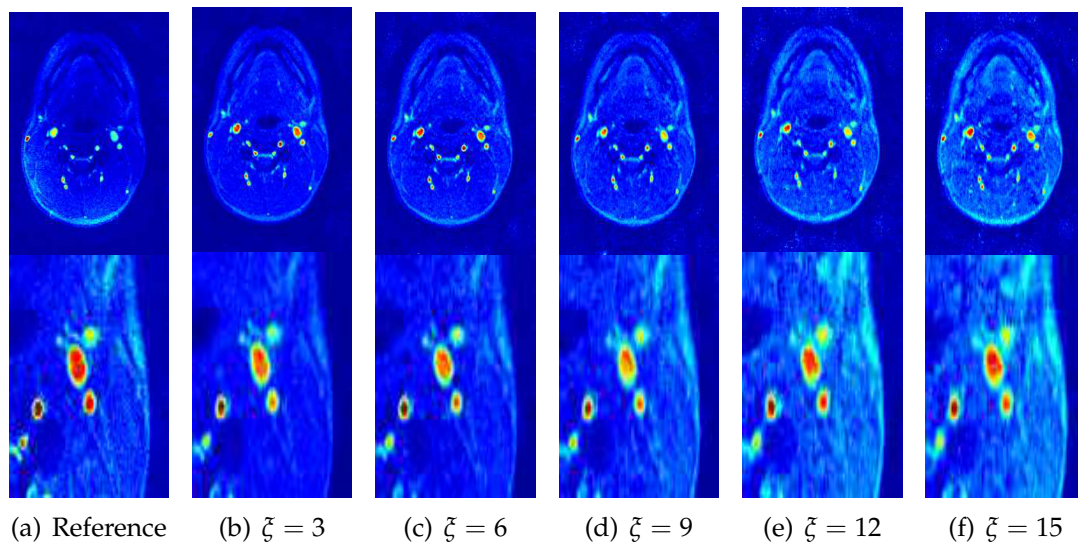


Figure 10.16: Image results for a representative volunteer for different acceleration factors $\xi = 1, \xi = 3, \xi = 6, \xi = 9, \xi = 12$ and $\xi = 15$.

with growing λ_{tmw} are smooth as seen in Figure 10.11. All reconstructions for the 18 volunteers were performed with a fixed $\lambda_{\text{tmw}} = 0.0040$ and produced comparable results, the parameter can therefore be assumed to be robust in a wide range and stable over different data sets.

Experiment II illustrated furthermore the acceleration capacities of MuFloCoS. Even for high factors, such as 15, resulting in using only around 6.7% of the data, good physiological results could be achieved. This acceleration is significantly higher than feasible with currently clinically used methods, which can achieve an acceleration of 2-4 (25-50% of the data) in this application. The performed study had the limitation that the reference values were calculated based on the fully sampled PC MRI scans. This provided a reliable reference for the physiological values. Further prospective sampled studies need to be done in the future. A further ex-

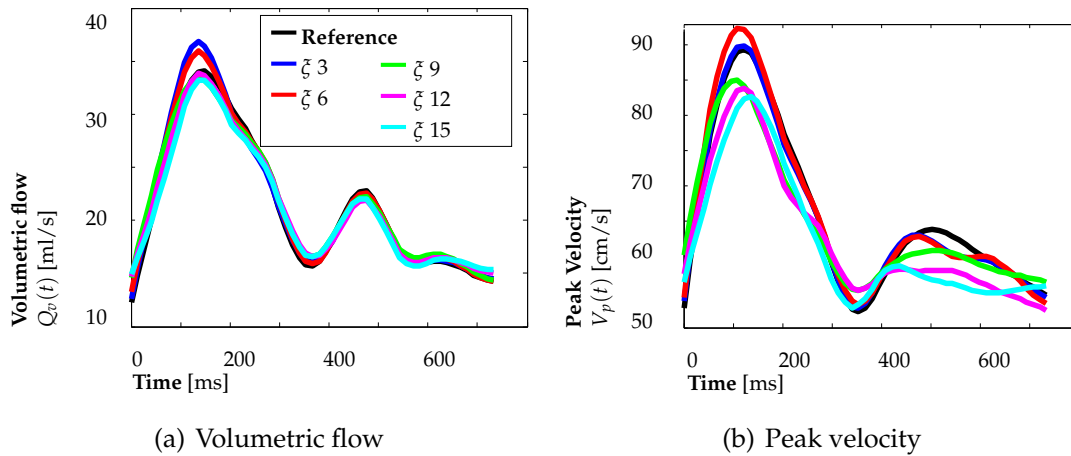


Figure 10.17: Physiological parameters for a representative volunteer for different acceleration factors $\zeta = 3$, $\zeta = 6$, $\zeta = 9$, $\zeta = 12$ and $\zeta = 15$. (a) Volumetric flow $Q_v(t)$ and (b) peak velocity $V_p(t)$.

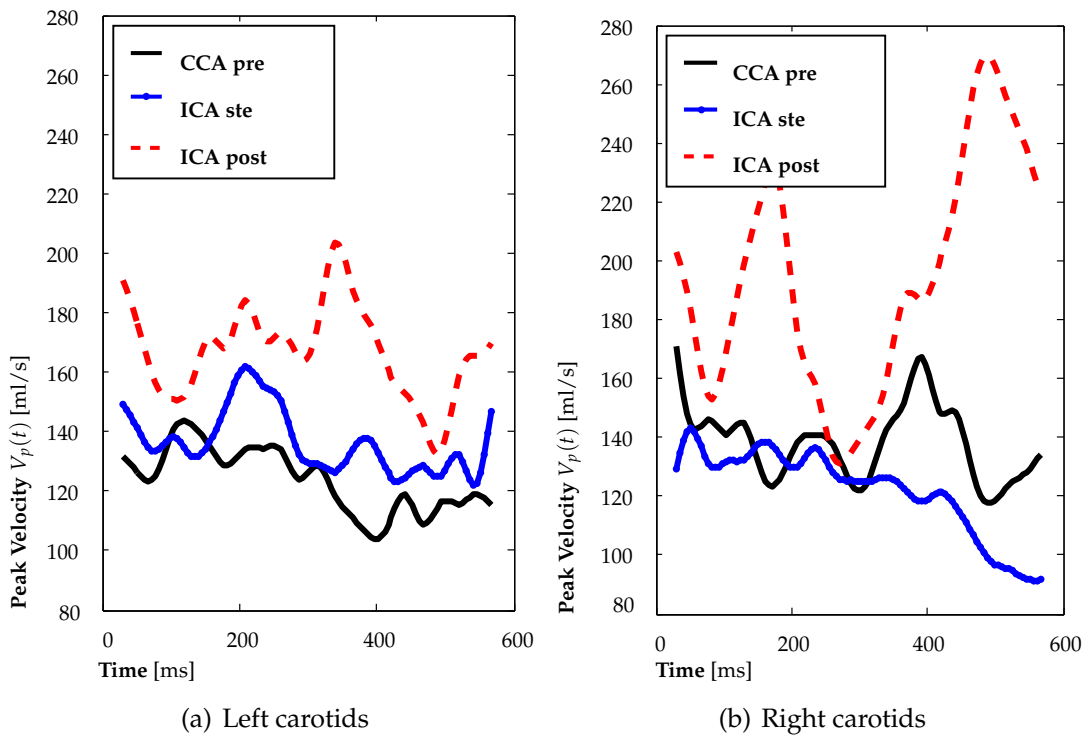


Figure 10.18: Peak velocity profiles for patient 1 from the PCI scan, accelerated with factor $\zeta = 9.0$ and reconstructed using MuFloCoS.

tension could be direct comparison with a different modality such as a flow meter or Doppler ultra sound.

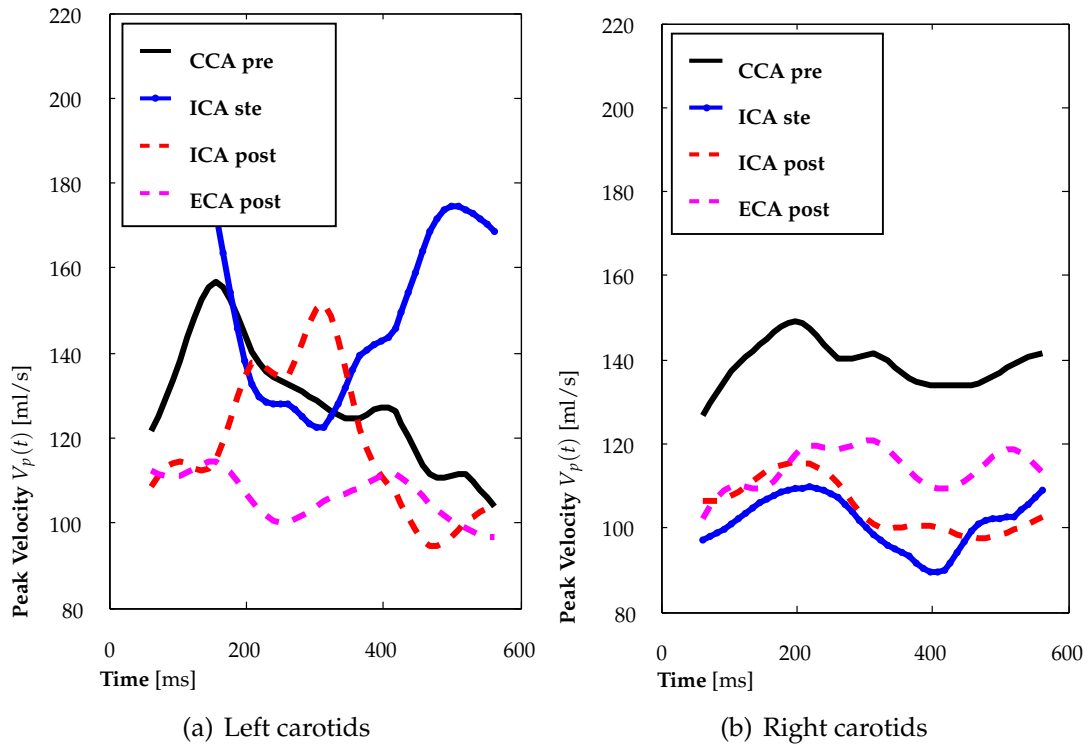


Figure 10.19: Peak velocity profiles for patient 2 from the PCI scan, accelerated with factor $\zeta = 9.0$ and reconstructed using MuFloCoS.

10.6 Summary and Conclusion

Acceleration factors of $\zeta = 9.0$ in volunteers have been successfully applied to PCI, leading to a significant speed up of the acquisition. The acquisition time for good temporal and spatial resolution in the carotid artery region can be significantly reduced. For the concrete example of the patient data acquisition using three three-directional 2D slices pre- and post-stenosis in the CCA and ICA, the acquisition time could be reduced from 8 minutes 24 seconds to 56 seconds. This significant reduction can be an important step in the clinical acceptance of this technique. This saved time could also be invested in a higher spatial and/or temporal resolution allowing to visualize especially pathological hemodynamic situations with better accuracy. The proposed method is not limited to the introduced masked and weighted temporal regularization, but is easily expendable to different regularizers such as TV, wavelet or more PCI specific constraints as divergence free flow fields or phase constraint. Only intrinsic properties of the PCI acquisition were exploited which makes the proposed method ideally suited to be applied to different body regions imaged with PCI.

Low Rank Sparse Decomposition based Compressed Sensing (LoSDeCoS)

11.1 Motivation	143
11.2 LoSDeCoS	144
11.3 Implementation and Experiments.	151
11.4 Results	155
11.5 Discussion	159
11.6 Summary and Conclusion	162

11.1 Motivation

Recently, the low rank sparse decomposition model, called L+S model, originally presented in the context of video compression, was adapted to dynamic and multi-slice MRI [Cand 11], [Maju 12],[Yin 12], [Trem 12]. In this approach the image information is modelled by two components called L and S. Thereby L is assumed to have a low rank and S to be sparse. The concept is particularly well suited for dynamic MRI, where L represents the static background and S the dynamic signal such as the heart motion [Otaz 13]. The advantages of this concept are the enforced sparsity of S compared to the global matrix as well as the possibility to apply more specific regularizers. Whereas all L+S models proposed so far uniquely focus on temporal dynamics, the novel Low rank and Sparse Decomposition Compressed Sensing (LoSDeCoS) method, presented in this chapter, extends this concept. A common vector space for both the temporal and the velocity encoding directions is constructed. Correlations in both directions can thus be exploited to accelerate the acquisition. In PCI, the final set of volumes contains information from N_t different time points and N_s velocity encodings, resulting in $N_p = N_t N_s$ volumes from the same anatomical position. Thus, the data exhibits correlation not only between space and time, but also between space and flow encoding. In addition,

dynamic and directional changes are limited to specific areas - the vessels - within the volume. Therefore, the L+S model is well suited for this application. A Split-Bregman algorithm [Aelt 10] was adapted to resolve the resulting minimization problem with different regularization terms.

The experiments include different sparsity assumptions, combined with both sparsity based Compressed Sensing (S-CS) and the novel LoSDeCoS algorithm to assess the influence of the L+S model for PCI allowing comparison on a fair basis. Furthermore, the data was reconstructed with fixed parameters for a fully sampled reference, ISENSE, S-CS and LoSDeCoS to evaluate the proposed approach. The described algorithm was presented in an earlier version in [Hutt 13e] and corresponds to [Hutt 14c].

11.2 LoSDeCoS

In this section, the LoSDeCoS algorithm is described in detail focusing on the used low rank and sparsity assumptions and the adapted unconstrained Split Bregman algorithm. With LoSDeCoS, as with MuFloCoS, the entire PCI data set is reconstructed simultaneously using the common vector $\mathbf{x} \in \mathbb{C}^{NN_p}$. Here, the image vector \mathbf{x} is further written as the sum of two vectors \mathbf{l} and $\mathbf{s} \in \mathbb{C}^{NN_p}$, representing the column wise notation of the matrices $\mathbf{L} \in \mathbb{C}^{N \times N_p}$ and $\mathbf{S} \in \mathbb{C}^{N \times N_p}$:

$$\mathbf{x} = \mathbf{l} + \mathbf{s}, \quad (11.1)$$

where \mathbf{s} is the sparse component and \mathbf{l} the low rank component of the common vector \mathbf{x} .

11.2.1 Influence of the Sampling on the Rank Minimization

Sampling strategies based on the relation between sparsity and incoherence have been well investigated in the theory of Compressed Sensing [Cand 08]. For the used low rank model in the st -vector space, the sampling strategy in s and t -dimension is of particular interest. Figure 11.1 illustrates an under sampled, directly reconstructed and rank limited PCI data set using two different patterns. The result with the static pattern, shown in Figure 11.1(a) and denoted by its center mapping $j_S(t, s)$ in Section 9.2, is given in Figure 11.1(b). The outcome of the reconstruction with the proposed I-VT sampling strategy ($j_R(t, s)$), recalled in Figure 11.1(c), is depicted in Figure 11.1(d). While the results obtained with the fixed pattern include a significant amount of aliasing, the I-VT pattern based reconstruction permits the recovery of the main structural elements of the PCI dataset by just limiting the rank. Taking these observations into account, the used under sampling strategy for LoSDeCoS involves both intra-volume and inter-volume variations in the I-VT sampling.

11.2.2 Low Rank Assumption

Similar to the sparsity assumptions, a transform L is required to formulate the low rank assumption in the adapted space, for PCI the st -vector space. Therefore,

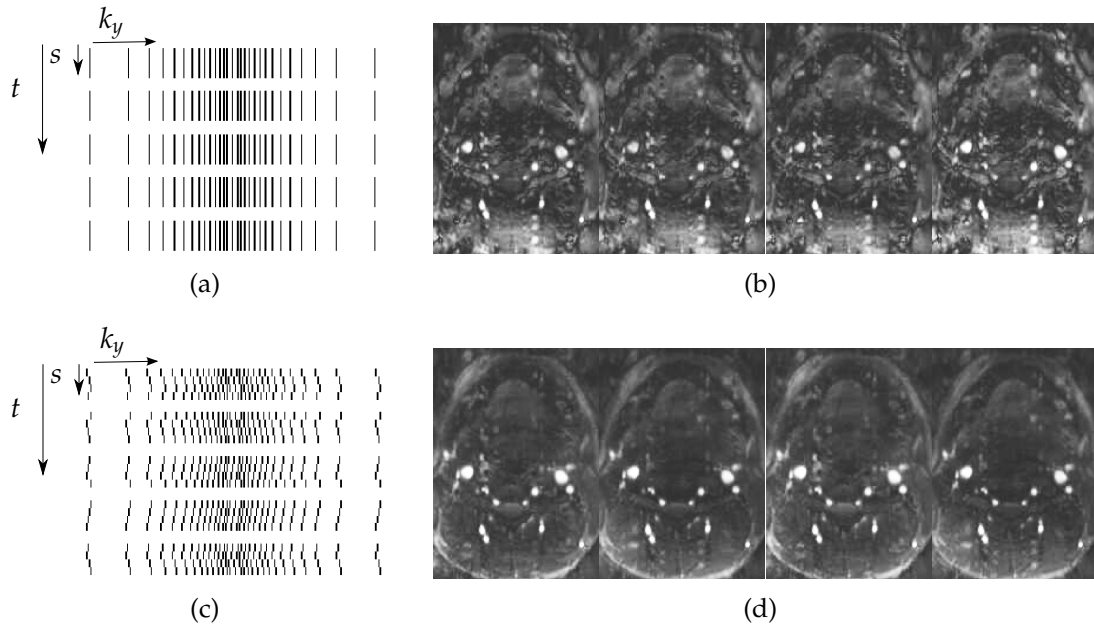


Figure 11.1: Illustration of the I-VT sampling pattern in comparison to a fixed pattern for the reconstruction of an under sampled and directly reconstructed rank-limited PCI dataset. (a) Illustration of the fixed pattern for all t and s and (b) reconstruction results using the fixed pattern showing a significant amount of aliasing. (c) I-VT pattern showing variations in both t and s direction and (d) reconstruction results with the I-VT pattern.

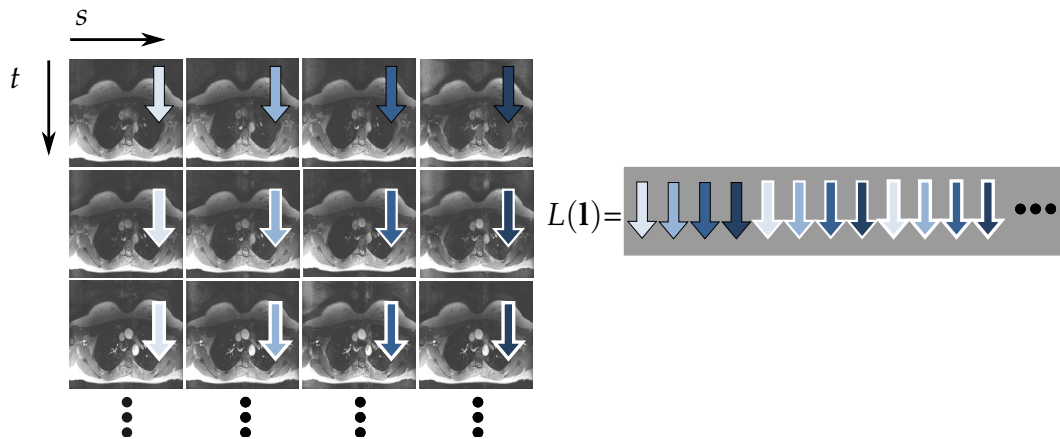


Figure 11.2: Vectorization of the individual volumes for all time steps and velocity encodings and composition of the st -matrix.

the vectorized individual volumes of the low rank part $\mathbf{I}^{t,s}$ are arranged as column vectors in a joint st -matrix. This is obtained using the transform $L : \mathbb{C}^{NN_p} \mapsto \mathbb{C}^{N \times N_p}$ as illustrated in Figure 11.2 and formulated as

$$L(\mathbf{I}) = \begin{bmatrix} \mathbf{I}_1^{1,1} & \mathbf{I}_1^{1,N_s} & \dots & \mathbf{I}_1^{N_t,1} & \mathbf{I}_1^{N_t,N_s} \\ \vdots & \vdots & \dots & \vdots & \vdots \\ \mathbf{I}_N^{1,1} & \mathbf{I}_N^{1,N_s} & \dots & \mathbf{I}_N^{N_t,1} & \mathbf{I}_N^{N_t,N_s} \end{bmatrix}. \quad (11.2)$$

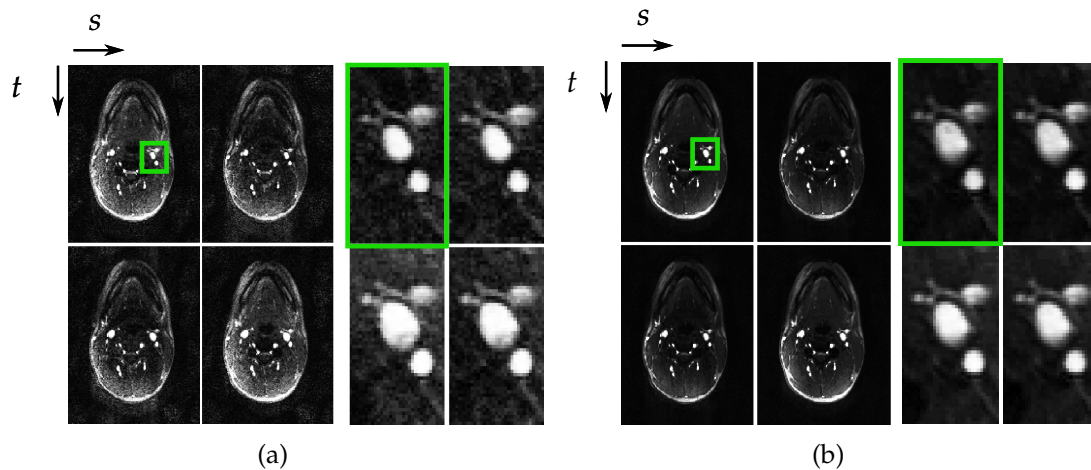


Figure 11.3: Low rank assumption illustrated on a fully sampled carotid dataset with $N_t = 11$ time steps and $N_s = 4$ velocity encodings. Reference reconstruction with a zoom to the right CCA for velocity encodings $s=1$ and $s=3$ and time step $t=1$ and $t=2$ using (a) all singular values and (b) only the two largest singular value. The images and a zoom to the ICA/ECA are illustrated for both cases.

The i^{th} -row in the st -matrix represents the image intensity for voxel i in all time steps and velocity encodings. If the PCI data is seen as a multidimensional tensor with the dimensions time t , velocity encoding s and image domain i , three tensor unfoldings are possible [Trza 13]. Relevant for the present case of the same anatomical position sampled for each time step and encoding is mainly the $st - i$ unfolding as presented above.

Figure 11.3 illustrates the rank compressibility with a fully sampled and directly reconstructed carotid data set with $N_p = 44$. Reconstruction results using all singular values are shown in Figure 11.3(a) and the results considering only the two biggest singular values are depicted in Figure 11.3(b) with a zoom to the right CCA. The information loss with decreasing number of singular values, and therefore decreasing rank is depicted. While Figure 11.3(a) shows all details including the temporal and directional changes in the flow pattern, Figure 11.3(b) suffers from a reduced depiction of the temporal dynamics as can be well observed by looking at the size of the CCA. Size changes between the depicted time steps due to arterial filling is visible in the case with all singular values, but not with reduced rank. The image quality concerning the surrounding tissue is well preserved in both reconstructions.

11.2.3 Rank Minimization Using the Nuclear Norm

Be $\mathbf{X} \in \mathbb{C}^{N \times M}$, where $N, M \in \mathbb{R}$, a matrix with entries $x_{ij} \in \mathbb{C}$ and eigenvalues $\lambda_i \in \mathbb{C}$. Its rank is denoted by $r = \text{rank}(\mathbf{X})$ where $r \in \mathbb{Z}$ and corresponds to the number of singular values above zero. The singular values are obtained by the singular value decomposition:

$$\mathbf{X} = \mathbf{U}\mathbf{\Sigma}\mathbf{V}^*, \quad (11.3)$$

consisting of the matrix $\Sigma \in \mathbb{R}^{N \times M}$ with the singular values $\sigma_i \in \mathbb{C}^{\min\{N,M\}}$ ordered by magnitude and two unitary matrices $\mathbf{U} \in \mathbb{C}^{N \times N}$ and $\mathbf{V}^* \in \mathbb{C}^{M \times M}$. The operator norm is defined as the largest singular value of \mathbf{X} : $\|\mathbf{X}\| = \sigma_1$. The trace $\text{trace}(\mathbf{X})$ is defined as the sum of the diagonal elements, which equals the sum of the eigenvalues λ_i :

$$\text{trace}(\mathbf{X}) = \sum_{i=1}^N x_{ii} = \sum_{i=1}^N \lambda_i. \quad (11.4)$$

The trace, defined only for quadratic matrices, i.e. $N = M$, induces the inner product $\langle \mathbf{X}, \mathbf{Y} \rangle = \text{trace}(\mathbf{X}\mathbf{Y}^*)$, which makes the space of the complex matrices $\mathbf{X} \in \mathbb{C}^{N \times M}$ a Hilbert space. Another norm of interest is the Frobenius norm $\|\mathbf{X}\|_F$

$$\|\mathbf{X}\|_F = \sqrt{\langle \mathbf{X}, \mathbf{X} \rangle} = \sqrt{\sum_{i=1}^{\min\{N,M\}} \sigma_i^2}, \quad (11.5)$$

and the nuclear norm, or Schatten-1 norm, $\|\mathbf{X}\|_*$, which equals the sum of the singular values σ_i of \mathbf{X} :

$$\|\mathbf{X}\|_* = \sum_{i=1}^{\min\{N,M\}} \sigma_i. \quad (11.6)$$

The problem of rank minimization, written for a matrix $\mathbf{X} \in \mathbb{C}^{N \times M}$ equals

$$\min \text{rank}(\mathbf{X}) \text{ subject to } \mathcal{A}(\mathbf{X}) = \mathbf{b}, \quad (11.7)$$

where $\mathcal{A} : \mathbb{C}^{N \times M} \mapsto \mathbb{C}^{N'}$ and $\mathbf{b} \in \mathbb{C}^{N'}$. This problem is NP-hard and not convex [Vand 96], relaxation methods are thus required. A well known relaxation technique, applicable for quadratic and positive semi definite \mathbf{X} replaces the rank by the trace of \mathbf{X} :

$$\min \text{trace}(\mathbf{X}) \text{ subject to } \mathcal{A}(\mathbf{X}) = \mathbf{b}. \quad (11.8)$$

The convex minimization problem in Eq. (11.8) corresponds for quadratic matrices to the relaxation of the sparsity assumptions to the L_1 norm, as

$$\text{trace}(\mathbf{X}) = \sum_{i=1}^N \lambda_i. \quad (11.9)$$

Minimizing the number of eigenvalues $\lambda_i > 0$ leads thus to a low rank matrix \mathbf{X} [Faze 02].

This heuristic is, however, not applicable for the present case of a non-quadratic matrix $\mathbf{X} \in \mathbb{C}^{N \times M}$ with $N > M$. Generalization is possible using the nuclear norm [Boyd 04], resulting in the following minimization problem:

$$\hat{\mathbf{X}} = \text{argmin} \|\mathbf{X}\|_* \text{ subject to } \mathcal{A}(\mathbf{X}) = \mathbf{b}. \quad (11.10)$$

It can be proven, that the nuclear norm minimizes the convex hull of the rank for matrices with $\|\mathbf{X}\| \leq 1$ [Faze 02]. Thereby, the convex hull of a $\text{rank}(\mathbf{X})$ is defined as the largest convex function

$$g(\mathbf{X}) \text{ subject to } g(\mathbf{X}) \leq \text{rank}(\mathbf{X}) \quad \forall \quad \mathbf{X} \in \mathbb{C}^{N \times M}. \quad (11.11)$$

The quality of the nuclear norm as a lower convex bound can be shown for matrices with $\text{rank}(\mathbf{X}) \leq r'$:

$$\|\mathbf{X}\| \leq \|\mathbf{X}\|_F \leq \|\mathbf{X}\|_* \leq \sqrt{r'} \|\mathbf{X}\|_F \leq r' \|\mathbf{X}\|. \quad (11.12)$$

Which results in

$$\|\mathbf{X}\|_* \leq r' \Leftrightarrow \|\mathbf{X}\|_* \leq \text{rank}(\mathbf{X}), \quad (11.13)$$

for matrices with $\|\mathbf{X}\| \leq 1$ [Rech 10]. It can be shown that the nuclear norm is in fact the best suited lower bound [Faze 02].

A condition for the treated problem in Eq. (11.10), where the nuclear norm guarantees to retrieve the \mathbf{X} with rank r , is formulated using the r -Restricted isometry property (rRIP). Thereby, the r -restricted isometry constant is defined as the smallest $\delta_r(\mathcal{A}) \in \mathbb{R}$ such that

$$(1 - \delta_r) \|\mathbf{X}\|_F^2 \leq \|\mathcal{A}(\mathbf{X})\|_{L_2}^2 \leq (1 + \delta_r) \|\mathbf{X}\|_F^2. \quad (11.14)$$

The theorem has been formulated analogously to the known RIP for sparsity assumptions in Eq. (3.45) and states: Be \mathbf{X}_0 a matrix of rank r , be \mathbf{X}_* the solution of $\mathcal{A}(\mathbf{X}) = \mathcal{A}(\mathbf{X}_0)$. If a constant $\delta_r(\mathcal{A})$ with $\delta_r(\mathcal{A}) \in \mathbb{R}$ and $\delta_r(\mathcal{A}) < 1/10$ exists, then holds $\mathbf{X}_* = \mathbf{X}_0$ [Rech 10].

The search for suited $\delta_r(\mathcal{A})$ for specific \mathcal{A} is NP-hard itself, there are, however statistical proofs exists for specific transforms \mathcal{A} including random transforms [Rech 10].

11.2.4 Objective Function

In addition to the data fidelity term in Eq. (9.9), the objective function \mathcal{L}_{Los} includes all regularization terms, formulating the low rank and sparsity assumptions used within the reconstruction:

$$\begin{aligned} \mathcal{L}_{\text{Los}}(\mathbf{s}, \mathbf{l}) = & \underbrace{\frac{1}{2} \|\mathbf{E}(\mathbf{s} + \mathbf{l}) - \mathbf{m}\|_{L_2}^2}_{\text{Data fidelity term}} + \underbrace{\lambda_t \|\nabla(\mathbf{s})\|_{L_{2,1}}}_{\text{Total variation}} + \underbrace{\lambda_w \|\mathbf{W}(\mathbf{s})\|_{L_1}}_{\text{Wavelet decomposition}} \\ & + \underbrace{\lambda_f \|\mathcal{F}_{t,s}^v(\mathbf{s})\|_{L_1}}_{\text{Temporal Fourier Transform}} + \underbrace{\lambda_n \|\mathbf{L}(\mathbf{l})\|_*}_{\text{Nuclear Norm}}. \end{aligned} \quad (11.15)$$

The parameters $\lambda_t, \lambda_w, \lambda_f \in \mathbb{R}$ regulate the influence of the sparsity terms, $\lambda_n \in \mathbb{R}$ respectively the weight of the rank term.

The minimization problem for LoSDeCoS thus equals

$$(\hat{\mathbf{s}}, \hat{\mathbf{l}}) = \underset{(\mathbf{s}, \mathbf{l})}{\text{argmin}} \mathcal{L}_{\text{Los}}(\mathbf{s}, \mathbf{l}). \quad (11.16)$$

The sparsity of the sparse matrix \mathbf{s} in a transform domain $\Phi(\mathbf{s})$, expressed as the number of non-zero entries $\|\Phi(\mathbf{s})\|_{L_0}$, is commonly approximated by the L_1 norm. The investigated sparsity transforms for LoSDeCoS include isotropic total variation (TV), wavelet decomposition and temporal Fourier transform as described in Section 9.1.

11.2.5 Minimization Using the Split Bregman Algorithm

The wide range of algorithms for the minimization of the nuclear norm with constraints were proposed, including interior point methods [Liu 09b], iteratively re-weighted least squares approaches [Forn 11] and fixed point algorithms [Gold 11]. The present algorithm solves the objective function in Eq. (11.15) coupling L_2 , L_1 and nuclear norm terms using the unconstrained Split Bregman algorithm. The unconstrained Split Bregman algorithm was presented in Section 4.4.3. The coupling of the individual sub-problems is performed with additional variables \mathbf{d}_x , \mathbf{d}_y , \mathbf{d}_z , \mathbf{d}_w , \mathbf{d}_f and \mathbf{d}_n . They are equal to the actual values of the corresponding regularization terms $\mathbf{d}_x = (\nabla_x \mathbf{s})$, $\mathbf{d}_y = (\nabla_y \mathbf{s})$, $\mathbf{d}_z = (\nabla_z \mathbf{s})$, $\mathbf{d}_w = W(\mathbf{s})$, $\mathbf{d}_f = \mathcal{F}_{t,s}^v(\mathbf{s})$ and $\mathbf{d}_n = L(\mathbf{1})$. Furthermore, variables for the residual errors \mathbf{b}_x , \mathbf{b}_y , \mathbf{b}_z , \mathbf{b}_w , \mathbf{b}_f and $\mathbf{b}_n \in \mathbb{C}^N$ are defined.

The algorithm is initialized with $\mathbf{s}, \mathbf{1}, \mathbf{d}_x, \mathbf{d}_y, \mathbf{d}_z, \mathbf{d}_w, \mathbf{d}_n, \mathbf{d}_f, \mathbf{b}_x, \mathbf{b}_y, \mathbf{b}_z, \mathbf{b}_n, \mathbf{b}_f = \mathbf{0}$ and, directly resulting, $\mathbf{x} = \mathbf{0}$. The minimization problem equals

$$\begin{aligned}
 & (\hat{\mathbf{s}}, \hat{\mathbf{1}}, \hat{\mathbf{d}}_x, \hat{\mathbf{d}}_y, \hat{\mathbf{d}}_z, \hat{\mathbf{d}}_w, \hat{\mathbf{d}}_f, \hat{\mathbf{d}}_n) = \\
 & \underset{\mathbf{s}, \mathbf{1}, \mathbf{d}_x, \mathbf{d}_y, \mathbf{d}_z, \mathbf{d}_w, \mathbf{d}_f, \mathbf{d}_n}{\operatorname{argmin}} \quad \frac{\mu}{2} \|\mathbf{E}(\mathbf{s} + \mathbf{1}) - \mathbf{m}\|_{L_2}^2 \\
 & \quad + \lambda_t \left(\|\mathbf{d}_x, \mathbf{d}_y, \mathbf{d}_z\|_{L_2} + \lambda_w \|\mathbf{d}_w\|_{L_1} + \lambda_f \|\mathbf{d}_f\|_{L_1} + \lambda_n \|L(\mathbf{1})\|_* \right) \\
 & \quad + \frac{\alpha \lambda_t}{2} \left(\|\mathbf{d}_x - \nabla_x \mathbf{s}\|_{L_2}^2 + \|\mathbf{d}_y - \nabla_y \mathbf{s}\|_{L_2}^2 + \|\mathbf{d}_z - \nabla_z \mathbf{s}\|_{L_2}^2 \right) \\
 & \quad + \frac{\alpha \lambda_w}{2} \|\mathbf{d}_w - W(\mathbf{s})\|_{L_2}^2 \\
 & \quad + \frac{\alpha \lambda_f}{2} \|\mathbf{d}_f - \mathcal{F}_{t,s}^v(\mathbf{s})\|_{L_2}^2 + \frac{\alpha \lambda_n}{2} \|\mathbf{d}_n - L(\mathbf{1})\|_{L_2}^2. \tag{11.17}
 \end{aligned}$$

The first Split Bregman step, as specified in Eq. (4.45), equals for the stated problem

$$\begin{aligned}
 & (\hat{\mathbf{s}}, \hat{\mathbf{1}}, \hat{\mathbf{d}}_x, \hat{\mathbf{d}}_y, \hat{\mathbf{d}}_z, \hat{\mathbf{d}}_w, \hat{\mathbf{d}}_f, \hat{\mathbf{d}}_n) = \\
 & \underset{\mathbf{s}, \mathbf{1}, \mathbf{d}_x, \mathbf{d}_y, \mathbf{d}_z, \mathbf{d}_w, \mathbf{d}_f, \mathbf{d}_n}{\operatorname{argmin}} \quad \frac{\mu}{2} \|\mathbf{E}(\mathbf{s} + \mathbf{1}) - \mathbf{m}\|_{L_2}^2 \\
 & \quad + \lambda_t \left(\|\mathbf{d}_x, \mathbf{d}_y, \mathbf{d}_z\|_{L_2} + \lambda_w \|\mathbf{d}_w\|_{L_1} + \lambda_f \|\mathbf{d}_f\|_{L_1} + \lambda_n \|L(\mathbf{1})\|_* \right) \\
 & \quad + \frac{\alpha \lambda_t}{2} \left(\|\mathbf{d}_x - \nabla_x \mathbf{s} - \mathbf{b}_x^j\|_{L_2}^2 + \|\mathbf{d}_y - \nabla_y \mathbf{s} - \mathbf{b}_y^j\|_{L_2}^2 + \|\mathbf{d}_z - \nabla_z \mathbf{s} - \mathbf{b}_z^j\|_{L_2}^2 \right) \\
 & \quad + \frac{\alpha \lambda_w}{2} \|\mathbf{d}_w - W(\mathbf{s}) - \mathbf{b}_w^j\|_{L_2}^2 \\
 & \quad + \frac{\alpha \lambda_f}{2} \|\mathbf{d}_f - \mathcal{F}_{t,s}^v(\mathbf{s}) - \mathbf{d}_f^j\|_{L_2}^2 + \frac{\alpha \lambda_n}{2} \|\mathbf{d}_n - L(\mathbf{1}) - \mathbf{d}_n^j\|_{L_2}^2. \tag{11.18}
 \end{aligned}$$

The second Split Bregman step, formulated in its general form in Eq.(4.46), is for the concrete problem given as

$$\mathbf{b}_x^{j+1} = \mathbf{b}_x^j + \nabla_x \mathbf{s}^{j+1} - \mathbf{d}_x^{j+1}, \quad (11.19)$$

$$\mathbf{b}_y^{j+1} = \mathbf{b}_y^j + \nabla_y \mathbf{s}^{j+1} - \mathbf{d}_y^{j+1}, \quad (11.20)$$

$$\mathbf{b}_z^{j+1} = \mathbf{b}_z^j + \nabla_z \mathbf{s}^{j+1} - \mathbf{d}_z^{j+1}, \quad (11.21)$$

$$\mathbf{b}_w^{j+1} = \mathbf{b}_w^j + W(\mathbf{s}^{j+1}) - \mathbf{d}_w^{j+1}, \quad (11.22)$$

$$\mathbf{b}_f^{j+1} = \mathbf{b}_f^j + \mathcal{F}_{t,s}^v(\mathbf{s}^{j+1}) - \mathbf{d}_f^{j+1} \text{ and} \quad (11.23)$$

$$\mathbf{b}_n^{j+1} = \mathbf{b}_n^j + L(\mathbf{l}^{j+1}) - \mathbf{d}_n^{j+1}. \quad (11.24)$$

In each Split Bregman iteration j , where $j \in \{1, \dots, N_j\}$, three steps are performed, the first formulated in Eq. (11.25) as an L_2 minimization of the data fidelity term and the L_2 terms for each of the chosen regularization terms. This L_2 minimization problem is minimized with N_i iterations of the IBFSG algorithm [Noce 06] with

$$(\mathbf{s}^{j+1}, \mathbf{l}^{j+1}) = \underset{(\mathbf{s}, \mathbf{l})}{\operatorname{argmin}} \mathcal{L}_{\text{Los-L2}}(\mathbf{s}, \mathbf{l}) \quad (11.25)$$

where

$$\begin{aligned} \mathcal{L}_{\text{Los-L2}}(\mathbf{s}, \mathbf{l}) = & \frac{\mu}{2} \|\mathbf{E}(\mathbf{s} + \mathbf{l}) - \mathbf{m}\|_{L_2}^2 \\ & + \frac{\alpha \lambda_t}{2} \left(\|\mathbf{d}_x^j - \nabla_x(\mathbf{s}) - \mathbf{b}_x^j\|_{L_2}^2 + \|\mathbf{d}_y^j - \nabla_y(\mathbf{s}) - \mathbf{b}_y^j\|_{L_2}^2 + \|\mathbf{d}_z^j - \nabla_z(\mathbf{s}) - \mathbf{b}_z^j\|_{L_2}^2 \right) \\ & + \frac{\alpha \lambda_w}{2} \|\mathbf{d}_w^j - W(\mathbf{s}^j) - \mathbf{b}_w^j\|_{L_2}^2 \\ & + \frac{\alpha \lambda_f}{2} \|\mathbf{d}_f^j - \mathcal{F}_{t,s}^v(\mathbf{s}) - \mathbf{b}_f^j\|_{L_2}^2 + \frac{\alpha \lambda_n}{2} \|\mathbf{d}_n^j - L(\mathbf{l}) - \mathbf{b}_n^j\|_{L_2}^2. \end{aligned} \quad (11.26)$$

In the second step, the regularization terms are minimized with tailored strategies using the results from the first step $\mathbf{s}^{j+1}, \mathbf{l}^{j+1}$:

$$\begin{aligned} (\mathbf{d}_x^{j+1}, \mathbf{d}_y^{j+1}, \mathbf{d}_z^{j+1}) = & \underset{\mathbf{d}_x, \mathbf{d}_y, \mathbf{d}_z}{\operatorname{argmin}} \frac{\alpha \lambda_t}{2} \|\mathbf{d}_x - \nabla_x(\mathbf{s}^{j+1}) - \mathbf{b}_x^j\|_{L_2}^2 + \frac{\alpha \lambda_t}{2} \|\mathbf{d}_y - \nabla_y(\mathbf{s}^{j+1}) - \mathbf{b}_y^j\|_{L_2}^2 \\ & + \frac{\alpha \lambda_t}{2} \|\mathbf{d}_z - \nabla_z(\mathbf{s}^{j+1}) - \mathbf{b}_z^j\|_{L_2}^2 + \lambda_t \|\mathbf{d}_x, \mathbf{d}_y, \mathbf{d}_z\|_{L_2}, \end{aligned} \quad (11.27)$$

$$(\mathbf{d}_w^{j+1}) = \underset{\mathbf{d}_w}{\operatorname{argmin}} \frac{\alpha \lambda_w}{2} \|\mathbf{d}_w - W(\mathbf{s}^{j+1}) - \lambda_w \mathbf{b}_w^j\|_{L_2}^2 + \|\mathbf{d}_w\|_{L_1}, \quad (11.28)$$

$$(\mathbf{d}_f^{j+1}) = \underset{\mathbf{d}_f}{\operatorname{argmin}} \frac{\alpha \lambda_f}{2} \|\mathbf{d}_f - \mathcal{F}_{t,s}^v(\mathbf{s}^{j+1}) - \mathbf{b}_f^j\|_{L_2}^2 + \lambda_f \|\mathbf{d}_f\|_{L_1} \text{ and} \quad (11.29)$$

$$(\mathbf{d}_n^{j+1}) = \underset{\mathbf{d}_n}{\operatorname{argmin}} \frac{\alpha \lambda_n}{2} \|\mathbf{d}_n - L(\mathbf{l}^{j+1}) - \mathbf{b}_n^j\|_{L_2}^2 + \lambda_n \|\mathbf{d}_n\|_{L_1}. \quad (11.30)$$

The isotropic TV in Eq. (11.27) is minimized using the generalized shrinkage formula formulated with s_1 and the wavelet transform using the soft thresholding s_2 as presented in Section 4.4.3. The temporal vtFTsub problem in Eq. (11.29) is equivalently solved using soft thresholding, which results in

$$(\mathbf{d}_f^{j+1}) = s_2 \left(\mathbf{s}^{j+1}, \mathbf{b}_f^j, \frac{1}{\alpha} \right), \quad (11.31)$$

where

$$(\mathbf{d}_f^{j+1})_l = \frac{(\mathcal{F}_{t,s}^v(\mathbf{s}^{j+1}))_l}{|(\mathcal{F}_{t,s}^v(\mathbf{s}^{j+1}))_l|} \left(|(\mathcal{F}_{t,s}^v(\mathbf{s}^{j+1}))_l| - \frac{1}{\alpha} \right)_+. \quad (11.32)$$

Finally, the nuclear norm in Eq. (11.30) is minimized using singular value thresholding [Cai 10]

$$(\mathbf{d}_n^{j+1}) = s_3 \left(\mathbf{s}^{j+1}, \mathbf{b}_n^j, \frac{1}{\alpha} \right), \quad (11.33)$$

with

$$\mathbf{d}_n^{j+1} = \mathbf{U} \bar{\Sigma}^j \mathbf{V}^* \quad (11.34)$$

with $\bar{\Sigma}^j = \text{diag}((\sigma - (\frac{1}{\alpha})^j)_+)$.

11.3 Implementation and Experiments

Details about the implementation of the LoSDeCoS algorithm and the performed experiments are given below.

11.3.1 LoSDeCoS Implementation Details

The LoSDeCoS algorithm was implemented into the previously explained Iter-Recon framework. The flow chart in Figure 11.4 and Algorithm 11.1 illustrate the LoSDeCoS method.

The complexity of LoSDeCoS is analysed first for one iteration of the Split Bregman algorithm, consisting of the L_2 minimization step and the shrinkage steps. The L_2 step with N_i iterations and the objective function $\mathcal{L}_{\text{Los-L2}}$ includes the evaluation of the data fidelity term, which lays within $O(N_i N_p N_\gamma N \log N)$ as discussed in Section 9.3. For each penalty term two subtractions as well as the evaluation of the transform are required. The transform costs for TV, and wavelet are within $O(N_p N)$ and for temporal Fourier transform within $O(N_s N N_t \log N_t)$. The SVD calculation for the matrix of size $N \times N_p$ lies within $O(4N^2 N_p + 8N N_p^2 + 9N_p^3)$ if calculation of \mathbf{V} and \mathbf{U} is required. The total cost for N_j Bregman iterations thus lies within $O(N_j (N_p N \log N_t + N^2 N_p + N N_p^2 + N_p^3 + N_i N_p N_\gamma N \log N))$.

11.3.2 Sparsity and Parameter Study

Different experiments were performed to evaluate the performance of the novel LoSDeCoS algorithm regarding the fidelity compared to fully sampled reference acquisitions in terms of image quality, NRMSE, SSIM and SNR, as well as accuracy in the calculation of physiological values.

Different analyses were conducted based on the volunteer and patient data to compare the results achieved with LoSDeCoS to state of the art methods and to evaluate the robustness of the proposed method with respect to parametrization. Improvements compared to reconstruction without the L+S model were analysed qualitatively and quantitatively. The fully sampled reference data was reconstructed (Reference) using SoS. The data was then retrospectively under sampled

Algorithm 11.1 LoSDeCoS algorithm**Require:** $\mathbf{u}, \mathbf{m}, \lambda_t, \lambda_w, \lambda_f, \lambda_n, \mathcal{L}_{\text{Los-L2}}, N_i, N_j$ **INPUT:** $\mathbf{s}^0, \mathbf{l}^0$

- 1: Calculate combined coil profiles \mathbf{c}_γ^t
 - 2: **for all** $j = 1$ to N_j **do**
 - 3: $\mathbf{s}^0 = \mathbf{s}^{j-1}$
 - 4: $\mathbf{l}^0 = \mathbf{l}^{j-1}$
 - 5: **for all** $i = 1$ to N_i **do**
 - 6: Perform optimizer step with the obj. function $\mathcal{L}_{\text{Los-L2}}(\mathbf{s}^{i-1}, \mathbf{l}^{i-1})$ and its gradient $\nabla \mathcal{L}_{\text{Los-L2}}(\mathbf{s}^{i-1}, \mathbf{l}^{i-1})$
 - 7: Calculate the data fidelity term $H(\mathbf{s}^{i-1}, \mathbf{l}^{i-1})$ as illustrated in Figure 4.4
 - 8: Evaluate the TV penalty term $TV_i(\mathbf{s}^{i-1})$
 - 9: Perform wavelet decomposition and evaluate the L_1 wavelet penalty term $WV(\mathbf{s}^{i-1})$
 - 10: Update $\mathbf{s}^i, \mathbf{l}^i$
 - 11: **end for**
 - 12: Set $\mathbf{s}^j = \mathbf{s}^{N_i}$
 - 13: Set $\mathbf{l}^j = \mathbf{l}^{N_i}$
 - 14: Perform the shrinkage operations
 - 15: $(\mathbf{d}_x^j, \mathbf{d}_y^j, \mathbf{d}_z^j) = s_1(\mathbf{s}^j, \mathbf{b}_x^{j-1}, \mathbf{b}_y^{j-1}, \mathbf{b}_z^{j-1}, \frac{1}{\alpha})$
 - 16: $\mathbf{d}_w^j = s_2(\mathbf{s}^j, \mathbf{b}_w^{j-1}, \frac{1}{\alpha})$
 - 17: $\mathbf{d}_f^j = s_2(\mathbf{s}^j, \mathbf{b}_f^{j-1}, \frac{1}{\alpha})$
 - 18: $\mathbf{d}_n^j = s_3(\mathbf{l}^j, \mathbf{b}_n^{j-1}, \frac{1}{\alpha})$
 - 19: Update the residual errors
 - 20: $\mathbf{b}_x^j = \mathbf{b}_x^{j-1} + \nabla_x \mathbf{s}^j - \mathbf{d}_x^j$
 - 21: $\mathbf{b}_y^j = \mathbf{b}_y^{j-1} + \nabla_y \mathbf{s}^j - \mathbf{d}_y^j$
 - 22: $\mathbf{b}_z^j = \mathbf{b}_z^{j-1} + \nabla_z \mathbf{s}^j - \mathbf{d}_z^j$
 - 23: $\mathbf{b}_w^j = \mathbf{b}_w^{j-1} + W(\mathbf{s}^j) - \mathbf{d}_w^j$
 - 24: $\mathbf{b}_f^j = \mathbf{b}_f^{j-1} + \mathcal{F}_{t,s}^v(\mathbf{s}^j) - \mathbf{d}_f^j$
 - 25: Perform tensor unfolding with the transform \mathbf{L}
 - 26: $\mathbf{b}_n^j = \mathbf{b}_n^{j-1} + L(\mathbf{l}^j) - \mathbf{d}_n^j$
 - 27: **end for**
- OUTPUT:** $\mathbf{x}^{N_j} = \mathbf{s}^{N_j} + \mathbf{l}^{N_j}$

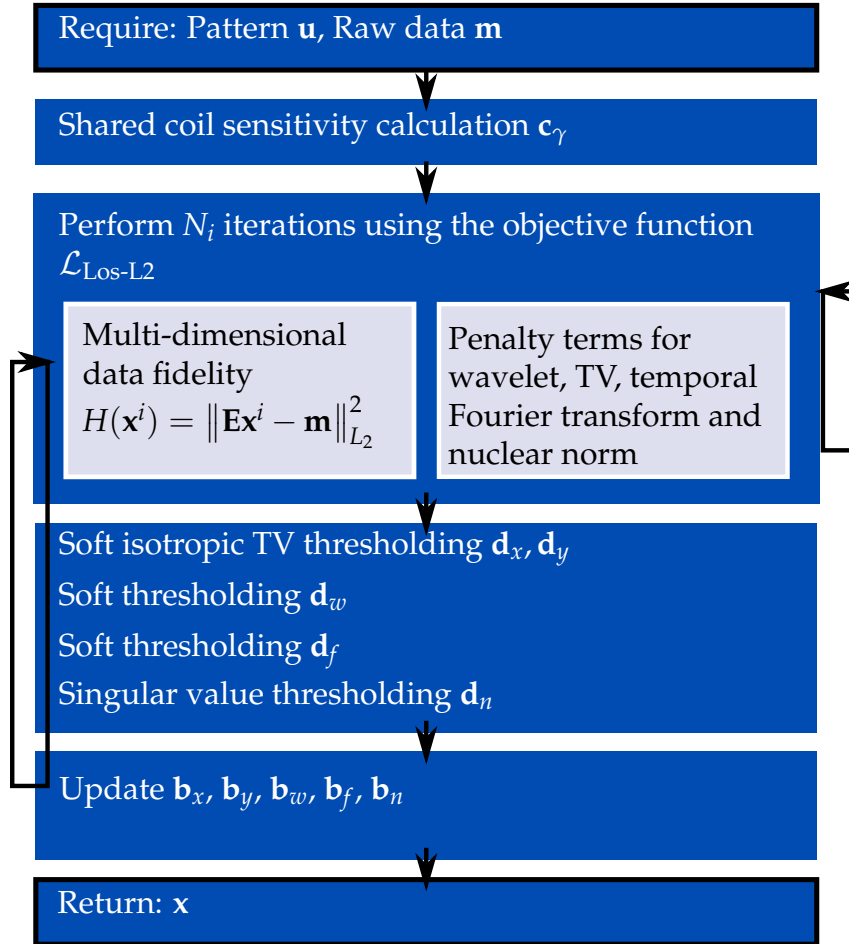


Figure 11.4: Flow chart diagram of the LoSDeCoS algorithm including preprocessing, minimization and post processing steps.

using an acceleration factor of $\zeta = 9$, which corresponds to 29/25 lines out of 256/224, and reconstructed with different reconstruction settings.

The used reconstructions differ in the employed regularization, the use of the low rank assumption and the chosen minimization algorithm. The first iterative experiment was the unregularized SENSE algorithm (ISENSE). Furthermore, reconstructions including uniquely sparsity constraints, referred to by S-CS and the proposed method including low rank and sparse assumptions LoSDeCoS were performed. For S-CS, the following objective function was used:

$$\begin{aligned}
 \mathcal{L}_{\text{Los}}(\mathbf{x}) = & \underbrace{\frac{1}{2} \|\mathbf{E}\mathbf{x} - \mathbf{m}\|_{L_2}^2}_{\text{Data fidelity term}} + \underbrace{\lambda_t \|\nabla(\mathbf{x})\|_{L_{2,1}}}_{\text{Total variation}} + \underbrace{\lambda_w \|\mathbf{W}(\mathbf{x})\|_{L_1}}_{\text{Wavelet decomposition}} \\
 & + \underbrace{\lambda_f \|\mathcal{F}_{t,s}^v(\mathbf{x})\|_{L_1}}_{\text{Temporal Fourier Transform}} . \tag{11.35}
 \end{aligned}$$

For the proposed LoSDeCoS algorithm including both low rank and sparse terms, solved with the Split Bregman method, the respective L_2 problem reads

$$\begin{aligned}
 \mathcal{L}_{\text{Los-L2}}(\mathbf{s}, \mathbf{l}) &= \frac{\mu}{2} \|\mathbf{E}(\mathbf{s} + \mathbf{l}) - \mathbf{m}\|_{L_2}^2 \\
 &+ \lambda_t^{SB} \|(\mathbf{d}_x, \mathbf{d}_y, \mathbf{d}_z)\|_{L_2} + \lambda_w^{SB} \|\mathbf{d}_w\|_{L_1} + \lambda_f^{SB} \|\mathbf{d}_f\|_{L_1} + \lambda_n^{SB} \|\mathbf{l}\|_* \\
 &+ \frac{\alpha \lambda_t^{SB}}{2} \left(\|\mathbf{d}_x - \nabla_x \mathbf{s} - \mathbf{b}_x^j\|_{L_2}^2 + \|\mathbf{d}_y - \nabla_y \mathbf{s} - \mathbf{b}_y^j\|_{L_2}^2 + \|\mathbf{d}_z - \nabla_z \mathbf{s} - \mathbf{b}_z^j\|_{L_2}^2 \right) \\
 &+ \frac{\alpha \lambda_w^{SB}}{2} \|\mathbf{d}_w - W(\mathbf{s}) - \mathbf{b}_w^j\|_{L_2}^2 + \frac{\alpha \lambda_f^{SB}}{2} \|\mathbf{d}_f - \mathcal{F}_{t,s}^v(\mathbf{s}) - \mathbf{d}_f^j\|_{L_2}^2 \\
 &+ \frac{\alpha \lambda_n^{SB}}{2} \|\mathbf{d}_n - L(\mathbf{l}) - \mathbf{d}_n^j\|_{L_2}^2, \tag{11.36}
 \end{aligned}$$

with $\mu = 1.0$ and $\alpha = 2.0$ and the weights $\lambda_t^{SB}, \lambda_w^{SB}, \lambda_f^{SB}, \lambda_n^{SB} \in \mathbb{R}$ to differentiate them from the weights $\lambda_t, \lambda_w, \lambda_f, \lambda_n$ used for the S-CS algorithm.

The regularization weights need to be carefully chosen to allow for a fair comparison between the S-CS and LS-CS methods. Three variants can be thought of:

- Use of the same weights for both the sparse and the sparse + low rank method.
- Find optimal weights such that $\text{NRMSE}(\mathbf{x})$ is minimized.
- Choose weights such that the difference between the data fidelity term of the L+S model and of the sparsity based algorithm is minimized.

The parameters were optimized using the low $\text{NRMSE}(\mathbf{x})$ method for the following experiments. Combinations of the included sparsity transforms wavelet, TV and temporal Fourier transform were performed with the parameters optimized using a grid search over $\lambda_t, \lambda_w, \lambda_f = [0.00001, \dots, 0.0002]$. First, an experiment involving three different combinations of sparsity transforms, was performed to evaluate the influence of these regularization terms. For each combination, the data was reconstructed with both S-CS and LoSDeCoS to analyse influence of the low rank component in a fixed setting. This results in the reconstructions S-CS_{TV-W}, S-CS_{TV-vtFT}, S-CS_{W-vtFT} for the sparsity based version and LoSDeCoS_{TV-W}, LoSDeCoS_{TV-vtFT}, LoSDeCoS_{W-vtFT} for the novel LoSDeCoS version. Specifically for TV, additional reconstruction were performed to assess the inferior results obtained for the combinations including TV. These included the evaluation of the TV regularization for different λ_t . The impact of the low rank regularization weight λ_n was assessed with another experiment, keeping λ_t, λ_w and λ_f fixed and varying λ_n between 0.00001 and 0.1. The number of iterations N_j and N_i for LoSDeCoS and N_i for S-CS was the focus of the next experiment, analysing the errors over the first $N_i = 15$ or respectively $N_i \cdot N_j = 15$ iterations for fixed $\lambda_t, \lambda_w, \lambda_f, \lambda_n$ values. Finally, the results obtained from these experiments were used to provide a broader comparison.

Method	NRMSE	SSIM	CNRVT	CNRVB
Reference	0.0	1.0	5.58	6.40
ISENSE	0.078	0.67	4.46	5.29
S-CS _{W-vtFT}	0.051	0.76	3.64	4.81
LoSDeCoS _{W-vtFT}	0.033	0.87	5.09	5.72
S-CS _{TV-vtFT}	0.051	0.78	4.54	5.51
LoSDeCoS _{TV-vtFT}	0.038	0.87	5.46	6.61
S-CS _{TVW}	0.052	0.87	4.82	6.01
LoSDeCoS _{TVW}	0.043	0.86	5.87	6.53

Table 11.1: Quantitative evaluation for different regularization combinations in the S-CS and the LoSDeCoS algorithm.

11.4 Results

The results for the sparsity and parameter study as well as for the comparison study are given in this section.

11.4.1 Sparsity and Parameter Study

The results of the sparsity transform study are shown in Table 11.1. The SSIM and NRMSE show improved values for all S-CS and LoSDeCoS variants compared to ISENSE. Comparing S-CS and LoSDeCoS, the NRMSE was reduced and the CNR improved for all LoSDeCoS variants compared to the respective S-CS reconstructions. For example, the NRMSE was reduced from 0.078 in the non-regularized version to 0.033 for LoSDeCoS_{W-vtFT} and to 0.051 for S-CS_{W-vtFT}. This corresponds to an error reduction of 57% for LoSDeCoS against 34% for S-CS. The comparison of the sparsity variants reveals the lowest NRMSE (0.033) for S-CS_{W-vtFT} compared to S-CS_{TV-vtFT} and S-CS_{TVW} (0.038 and 0.043). In contrary, the CNR is higher for the latter. The deviations over encodings and time steps are visualized in Figure 11.5, showing the NRMSE for all 6 combinations and the unregularized SENSE over 11 time steps for each of the four velocity encodings. In each case, the direct comparison between the S-CS and the LoSDeCoS methods reveals a reduced error for LoSDeCoS reconstructions compared to S-CS. The lowest error, combined with low inter-encoding deviations is obtained for the LoSDeCoS_{W-vtFT} algorithm.

The results of the TV reconstruction reveal a trade off between the NRMSE and the TNRMSE for PCI data. While the NRMSE drops significantly with growing TV weight, the TNRMSE grows, which corresponds to the visible under-estimation of the velocity within the vessels as depicted in Figure 11.8 and in the image results in Figure 11.9 shown in colour scale to better illustrate the differences. Figure 11.9(a) gives the result for $\lambda_t = 0.0001$, Figure 11.9(b) for $\lambda_t = 0.0005$ and finally Figure 11.9(c) depicts the absolute magnitude difference between both.

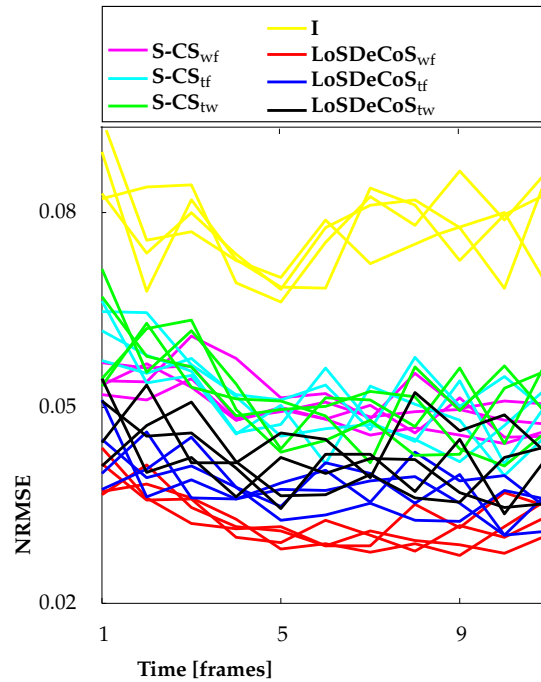


Figure 11.5: (a) Normalized NRMSE, SSIM, CNRVB and CNRVT plotted against λ_n in a logarithmic scale.

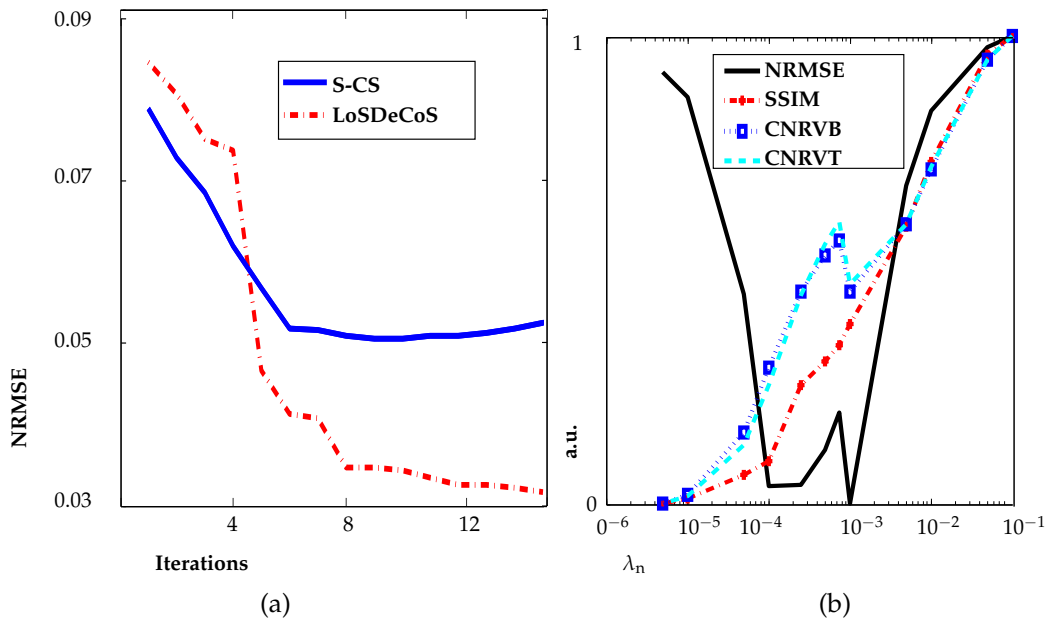


Figure 11.6: (a) NRMSE for S-CS and LoSDeCoS over the first 15 iterations and (b) normalized NRMSE, SSIM, CNRVB and CNRVT plotted against λ_n in a logarithmic scale.

The influence of the number of iterations is illustrated in Figure 11.6(a), showing the evolution of the NRMSE for $S-CS_{W-vtFT}$ and $LoSDeCoS_{W-vtFT}$ for the first 15 iterations. While $S-CS_{W-vtFT}$ reaches a minimum of around 0.05 for $i = 9$ and retains a relatively stable error for more iterations, $LoSDeCoS_{W-vtFT}$ converges to a lower error of just above 0.03. To ensure a fair comparison $N_i \cdot N_j = 9$ iterations

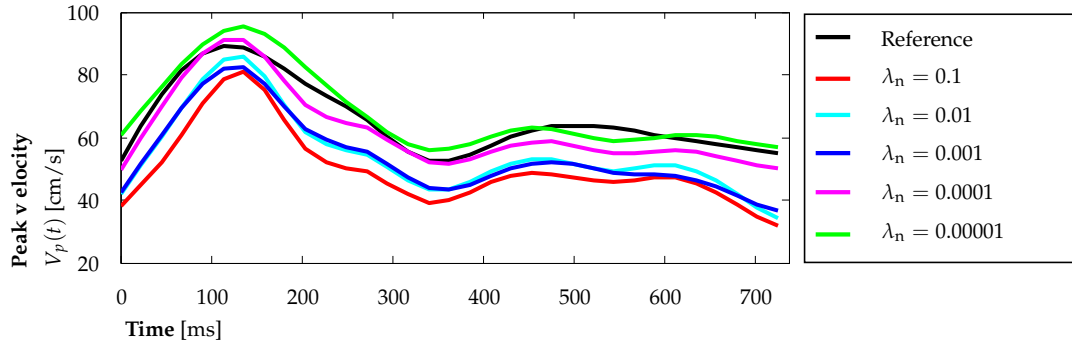


Figure 11.7: Peak velocity over time calculated for different nuclear norm weights λ_n .

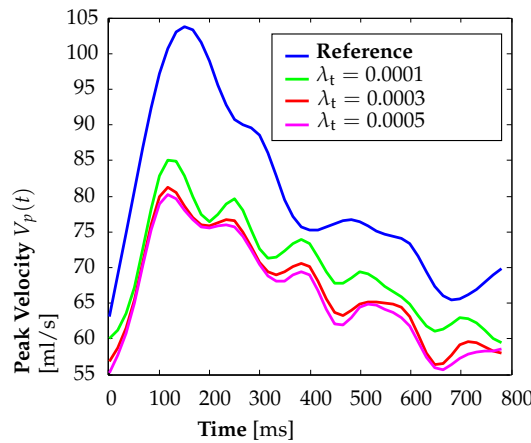


Figure 11.8: Peak flow evaluation for different TV weights from 0.0001 to 0.0005.

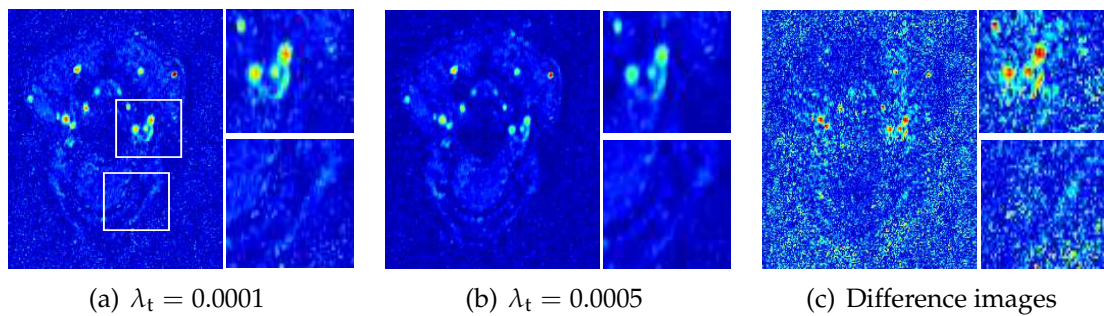


Figure 11.9: Results and difference image for TV weights from 0.0001 to 0.0005.

were used for all comparisons. Figure 11.6(b) illustrates the effects of the nuclear norm weight λ_n . The NRMSE, SSIM, CNRVB and CNRVT values were normalized to values between 0 and 1 and are shown against the chosen weights in a logarithmic scale. It can be observed that an increasing influence of the nuclear norm leads to an increase in CNR and SSIM. It should be noted that the NRMSE reaches a relatively stable minimum for $\lambda_n \in [0.0001, 0.001]$, while the errors for smaller and larger λ_n values are about a factor 10 larger. Figure 11.7 illustrates as well the effects of high values of λ_n , showing the peak velocities over time for the reference and different λ_n choices. For all depicted values of λ_n , the shape of the profile was qualitatively comparable. However, growing λ_n correlates with an

Method	NRMSE	SSIM	CNRVT	CNRVB
Reference	0.0	1.0	7.145 ± 2.115	8.640 ± 2.593
ISENSE	0.087 ± 0.019	0.78 ± 0.114	4.767 ± 1.460	5.843 ± 1.512
S-CS _{W-vtFT}	0.064 ± 0.018	0.85 ± 0.068	5.425 ± 1.775	6.663 ± 1.957
LoSDeCoS _{W-vtFT}	0.041 ± 0.012	0.91 ± 0.040	6.174 ± 1.767	7.315 ± 1.940

Table 11.2: Quantitative evaluation of the in-vivo volunteer data for LoSDeCoS_{W-vtFT}, S-CS_{W-vtFT} and ISENSE.

Method	NRMSE	SSIM	CNRVT	CNRVB
Reference	0.0	1.0	6.082 ± 1.198	7.165 ± 1.979
ISENSE	0.126 ± 0.019	0.955 ± 0.019	3.331 ± 1.092	3.826 ± 1.226
S-CS _{W-vtFT}	0.094 ± 0.021	0.976 ± 0.008	4.121 ± 1.252	5.013 ± 1.380
LoSDeCoS _{W-vtFT}	0.072 ± 0.012	0.989 ± 0.003	4.861 ± 1.018	6.034 ± 1.423

Table 11.3: Quantitative evaluation of the in-vivo patient data.

under estimation of the absolute velocities. As a result of these parameter studies a value of $\lambda_n = 0.001$ was chosen to obtain both valid velocity values and good NRMSE, SSIM and CNR values.

11.4.2 Comparison

The results for the comparison between different reconstruction algorithms for all volunteers are reported in Table 11.2. The results for the patients are given in Table 11.3. Exemplary image results are shown for volunteer P7 in Figure 11.10. These results illustrate the reduced noise level in LoSDeCoS_{W-vtFT} compared to ISENSE and S-CS_{W-vtFT}. Furthermore, the small vessels in proximity of the CCA, indicated by arrows, are better depicted. The L+S decomposition in Figure 11.12 shows a good depiction of the structures and the background with a very low noise level for the low rank component and a separation of dynamically varying and background tissue for the sparse part. The quantitative results in Table 11.2 show a reduction of the NRMSE from 0.087 (ISENSE) to 0.041 for LoSDeCoS_{W-vtFT}. Compared to the S-CS_{W-vtFT} result (0.064), an NRMSE improvement of 35% as well as an SSIM increase by 6.7 % are achieved. The standard deviation over all datasets for LoSDeCoS_{W-vtFT} is very low with 0.04 for SSIM and 0.012 for the NRMSE.

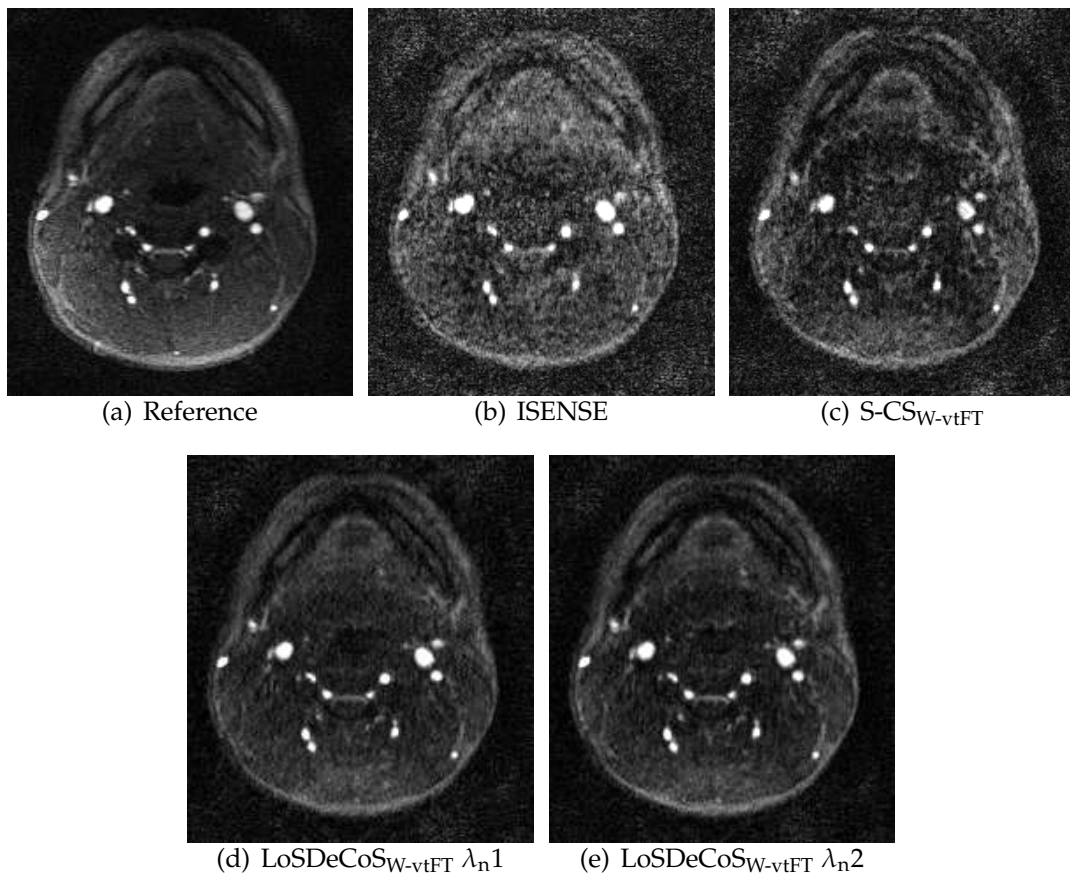


Figure 11.10: Magnitude reconstruction results for the through-plane encoding for volunteer P7 at peak systole: (a) Reference (b) ISENSE (c) $S\text{-}CS_{W\text{-}vtFT}$ (d) $LoSDeCoS_{W\text{-}vtFT}$ with $\lambda_{n1} = 0.001$ and (e) $LoSDeCoS_{W\text{-}vtFT}$ with $\lambda_{n2} = 0.0001$.

11.5 Discussion

11.5.1 Parameter Choices and Comparison

The results of the sparsity experiment illustrate the advantages of the L+S model compared to a reconstruction relying uniquely on sparsity in a well defined setting with the same choice of weights, iterations numbers and acceleration. The case of wavelet-TV combination, where the difference was less significant, indicates that the success of the L+S model partially relies on the use of temporal sparsity transforms such as vtFT. The smoothing effect of TV regularization leads to increased CNR both in the tissue and background, but this effect is counteracted by the higher NRMSE, showing that the smoothing does not represent the true image contents, which are of importance for the calculation of physiological values.

The experiments with different influences of the nuclear norm in Figure 11.6(a) and Figure 11.7 reveal an interesting trade-off between image quality and accuracy. An increasing influence of the low rank part generates a measurable improved image quality (high SSIM, high CNR) but a less accurate reconstruction of the reference (as indicated in the NRMSE) and an under estimation of the physi-

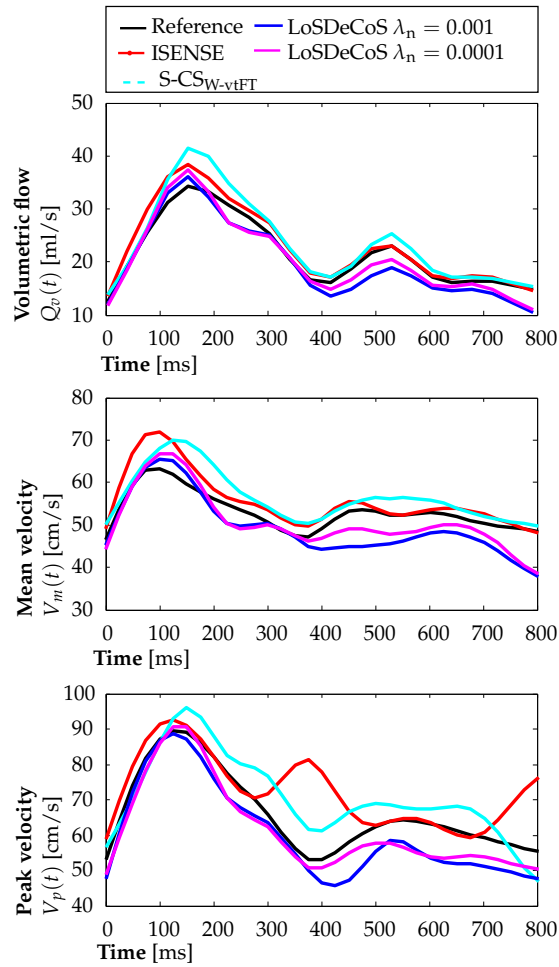


Figure 11.11: Volumetric flow, mean velocity profile and peak velocity profiles illustrated for volunteer P7.

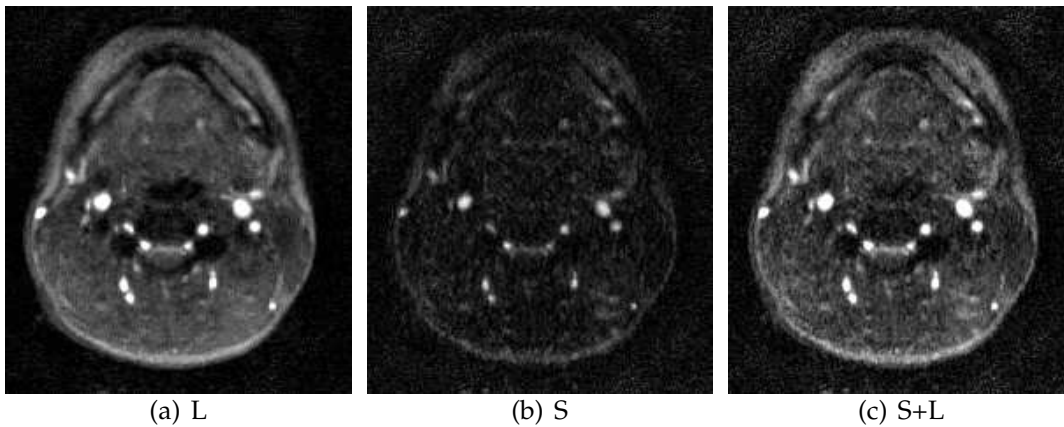


Figure 11.12: Magnitude reconstruction results for the sparse and low rank part as well as for the combination of both for volunteer P7 at peak systole: (a) Sparse part S, (b) low rank part L and (c) combination of both S+L .

ological values. This effect is easily understood by the model assumptions themselves. The L part, representing the low rank background components, is modelled

to be smooth, with minor changes between velocity encodings and time steps as velocity-spatio-temporal correlations are assumed. The S part, on the other hand, contains the dynamics over time, and by decreasing their influence compared to the background (corresponding to increasing λ_n), the images tend to be smoother over time and across velocity encodings, which explains the under estimation of physiological values as well as the growing NRMSE. The observable NRMSE minimum between 0.0001 and 0.001, where both effects are balanced, indicate a stable and optimal parameter choice.

The comparison results show that LoSDeCoS_{W-vtFT} provides accurate reconstruction results even for a high under sampling factor of 9. This factor is the net reduction, as no external acquisition of low resolution data for coil profiles is required. The low standard deviations in the volunteer study, combined with the possibility to use fixed parameters for all volunteers further indicate the stability and robustness of the technique.

11.5.2 Limitations

The scope of this study was to show the benefit of variations in the sampling strategy in both t and s directions, combined with the interleaved center acquisition to obtain coil sensitivity information from the data itself. The proposed pattern provides good artifact and image content separation, illustrated both in the reconstruction results and the low rank experiment in Figure 11.1. However, further pattern choices are possible.

The presented study focused on specific parameters, relevant for the L+S decomposition model such as the nuclear norm weight and evaluated three different regularizations in multiple combinations. Further parameter combinations could be evaluated, including different choices for the thresholding parameters and regularization weights.

Retrospective under sampling was chosen for these experiments to be able to compare the results with the fully sampled reference. This may be a limitation in terms of ignoring additional effects that might be encountered with prospective under sampling such as eddy currents. Nevertheless, the direct comparison with the reference values extracted from the same data set for all time steps and encodings is relevant for PCI for two reasons. First, the calculation of accurate velocity values relies on the combination of different encodings and/or time steps, and the accuracy of all of them should be of highest interest, which can only be achieved with a fully sampled scan acquired in the same physiological state. Second, no further method is able to acquire non-invasive anatomy-mapped 3-D velocity fields as a reference. Velocity values obtained with US or Fractional Flow Reserve may be beneficial for comparison in the future, but would not represent a suitable reference for the chosen application. Furthermore, the use of different regularizations, ranging from very general to more specific assumptions, can be integrated into the Split Bregman algorithm framework. The incorporation of flow or phase related assumptions such as proposed by Zhao et al. [Zhao 12] might be useful.

11.6 Summary and Conclusion

It was demonstrated that the proposed LoSDeCoS reconstruction method was capable of significantly accelerating the Phase Contrast acquisition by allowing an acceleration of at least factor 9, decreasing acquisition time from about 9 minutes in the carotid artery bifurcation to below 1 minute. The image quality and the CNR are well preserved, which was shown by comparison to the fully sampled reference data sets in a volunteer study. Moreover, the diagnostic value of the LoSDeCoS reconstruction method was demonstrated in two patient cases. Furthermore, the study has shown that the use of dedicated sparsity transforms is advantageous in combination with the L+S model.

The LoSDeCoS method is by no means restricted to the shown application, but can also be employed for different body regions or even acquisition types with multiple contrasts.

Part IV

Summary and Outlook

Summary

The focus of this work is the acceleration of non-contrast-enhanced Magnetic Resonance Angiography (nceMRA) examinations. These can be divided into two groups of methods, (i) morphological acquisitions using Time of Flight (TOF) and magnetization-prepared balanced Steady State Free Precession (mp-bSSFP) and (ii) functional acquisitions with Phase Contrast Imaging (PCI). While the first group provides non-invasive alternatives to established clinical techniques, PCI has the unique advantage to provide three-directional velocity fields simultaneously to the morphological information which is not yet clinical standard. All these nceMRA techniques suffer from long acquisition times, which limit at present its wider clinical use. Hence, acceleration is a problem of major interest and with great potential impact. The techniques presented in this thesis focus on decreasing imaging times by under sampling k -space below the Nyquist criteria and reconstructing the Sub-Nyquist data with adapted Compressed Sensing (CS) and parallel MRI (pMRI) based techniques.

The first part of this thesis focuses on the theoretical and methodological background. In Chapter 1, the human vessel system along with the relevant vascular diseases and common angiographic techniques is presented. NceMRA acquisitions are introduced as fully non-invasive alternatives to commonly used CTA, ceMRA, DSA and US methods and the carotid artery bifurcation, the peripheral arteries as well as the renal vasculature are targeted as applications for the developed techniques.

The relevant bases of MRI physics are presented in Chapter 2 concentrating on the used acquisition techniques TOF for the peripheral arteries, mp-bSSFP for the renal arteries and PCI for the carotid bifurcation.

Compressed Sensing and parallel MRI techniques are in the focus of Chapter 3. First, signal processing background to the MRI reconstruction, detailing the finite, discrete nature of MRI sampling and its limits resulting in aliasing and reduced resolution, is given. The approach to limit the number of phase encoding steps is introduced to accelerate the acquisition. Second, established pMRI methods for MRI acquisition relying on spatial encoding with multiple coils are presented and the method used within this thesis, SENSE, is formulated as a linear problem. Third, CS, as a concept to obtain signals from sub-sampled measurements using transform sparsity assumptions and non-linear reconstruction algorithms is introduced and motivated for MRI. The principles of incoherence and sparsity with their corresponding application in MR acquisition are explained. Finally, the joint pMRI-CS problem is presented and relevant state of the art reported.

Part II focuses on methods, experiments and results for morphological nceMRA reconstruction techniques. The novel Multi-Coil Compressed Sensing (MICCS) sampling pattern is introduced as a Cartesian analytical sampling scheme combining the requirements for pMRI and CS in Chapter 4. The used objective function is developed with its data fidelity term and sparsity constraints. The Split Bregman algorithm is adapted to the present problem as a promising alternative to traditional gradient based algorithms as it allows for incorporation of specific minimization strategies.

Subject of Chapters 5 and 6 is the application of the proposed methodical elements to two applications, the visualization of the renal and peripheral arteries. They differ in the dimensionality, as peripheral TOF is due to physiological reasons an ECG triggered 2-D application and 3-D renal angiography with mp-bSSFP are respiratory triggered 3-D acquisitions. However, they share common challenges and the need for significant acceleration while maintaining excellent image quality to allow for their wider clinical usage. Chapter 5 reports the results obtained for the proposed MICCS pattern evaluation, compared to five further sampling options with the same number of acquired lines. Clear advantages of the MICCS strategy especially regarding the vessel sharpness and the significantly reduced NRMSE are observed. The reconstruction results of the adapted Split Bregman solver in combination with the MICCS sampling proves the ability of the novel method to produce excellent image quality and vessel sharpness even for a high under sampling factor of 12. This corresponds to a reduction of the acquisition time by 83%, which allows a wider use of the TOF acquisition for the visualization of the peripheral vasculature.

The application of the proposed algorithm to free-breathing renal acquisitions is shown in Chapter 6 in combination with a dedicated organ-based evaluation strategy. The study of possible acceleration factors reveal stable results even for higher factors, reducing the effective scan time from over 8 minutes to less than 1 minute. The combination with the Split Bregman algorithm shows advantages in the measured quantitative values both regarding NRMSE, SSIM and the vessel sharpness. Finally, the comparison to the clinically established methods SENSE and GRAPPA, using the same acceleration factor of 6, demonstrates the superior performance of the iterative methods.

The focus of Part III are methods for the acceleration of PCI acquisitions. Chapter 7 presents the multi-dimensionality and the required processing pipeline from moving spins to physiological values as challenges of PCI and focuses on their implications on the reconstruction. The dynamic nature of the data and the need for multiple velocity encodings increase the computational effort but provide as well possibilities for dedicated sampling and regularization strategies. The need to process the reconstructed volumes further increases the importance of the temporal and spatial accuracy of the complex reconstructed volumes.

The visualization of the region around the carotid bifurcation is chosen as targeted application and presented in Chapter 8. The high prevalence of stenosis and calcifications in the carotids with implications on further important cardiovascular diseases such as strokes raises the clinical importance of this application. But it

also provides an excellent example of the challenges of PCI, as the small vessel diameters combined with high blood flow velocities increase the need for high spatial and temporal resolution, which in consequence leads to long acquisition times and the need for dedicated acceleration strategies. Phantom and in-vivo volunteer data from 18 volunteers, acquired to evaluate the robustness and accuracy regarding clinical values as well as physiological flow conservation laws are presented. Furthermore two patient cases with severe ICA stenosis are acquired to show the diagnostic usefulness of the proposed algorithms in presence of pathologies.

The joint iterative reconstruction problem for PCI is presented in Chapter 9 as well as the novel interleaved velocity encoding temporal sampling strategy, called I-VT, which exploits all available dimensions. The developed PCI part of the IterRecon framework is introduced, which includes a wide range of sampling, regularization, optimization and evaluation possibilities.

Chapter 10 presents a novel regularization strategy, called temporal masked and weighted L_1 regularization (TMW), which focuses on exploiting intrinsic properties of PCI to provide a regularization yielding good image quality combined with high accuracy of the temporal evolution of the calculated physiological values. Specific methodological elements are the calculation of the vessel masks from a combination of dynamic and static images to obtain a more robust algorithm as well as the masked and temporally weighted regularization. Over all data sets, the results show a significantly improved image quality as well as accuracy of the physiological values. Furthermore, different variants and choices of the regularization parameter detail specific advantages of the proposed method. The results of patient cases, accelerated from over 3 minutes to less than 1 minute correspond well to the diagnostic information available from CTA or ceMRA results. Finally, the application of the low rank sparse decomposition on the PCI data is motivated and developed in the LoSDeCoS algorithm in Chapter 11. LoSDeCoS extends the concept of low rank sparse decomposition, previously presented for dynamic MRI to the multi-dimensional case by proposing a joint temporal encoding vector space. The nuclear norm is presented along with its justification to approximate the low rank case. Furthermore, the influence of the sampling pattern on the rank compressibility is demonstrated. The unconstrained Split Bregman algorithm is adapted to incorporate the different sparsity transforms and the nuclear norm. The results demonstrate the capability of LoSDeCoS to reconstruct highly under sampled PCI data with good image quality and high Contrast to Noise Ratio. Evaluation of the results in comparison to gradient based algorithms is provided for different sparsity assumption combinations.

In Chapter 13 ideas on future work as well as combinations with further methods are discussed.

Outlook

This chapter presents ideas for future work in both morphological and functional nceMRA. The discussions from previous chapters are recalled and directions for further research are presented.

Sampling Strategy and Coil Sensitivity Calculation

The proposed analytical MICCS pattern can be extended to incorporate further sampling strategies such as Poisson distribution based approaches. Furthermore, the combined coil sensitivity strategy, presented in the context of the I-VT pattern, could be improved by sharing the coil sensitivity information not only over velocity encoding, but over adjacent time steps as well.

Regularization strategies

Further regularizations than the presented total variation and wavelet for the static nceMRA data sets can be used. These include for peripheral TOF the proposed vessel specific types such as vessel prior knowledge as shown in [Hutt 12b] and by Stinson et al. [Stin 13]. Furthermore, multi-slice regularization can be thought of as presented in [Hutt 13c]. But further, more general assumptions such as ridgelets, curvelets as proposed by Al Zubi et al. [AlZu 11] can be of benefit for the chosen application. For the renal acquisition, the discussion of the NRMSE over the y-coordinate revealed an increased influence of the total variation regularized Split Bregman algorithm in the slices within the kidneys. This result could be used to design adapted regularization terms.

The different ways to incorporate the velocity encoding dimension within the temporal Fourier term were discussed in Chapter 9, the vector based method was chosen for the conducted experiments. However, investigation of different combinations can be beneficial, for example in combination with the group sparsity approach presented by Huang et al. [Huan 09]. Specific flow based sparsity assumptions such as the divergence free condition as proposed for non-iterative reconstruction by Busch et al. [Busc 12] and the different treatment for phase and magnitude terms as shown by Zhao et al. [Zhao 12] may be of interest.

Combining MuFloCoS and LoSDeCoS

The masked and temporal weighted regularization strategy proposed in MuFloCoS has shown to improve the accuracy of both image quality and physiological parameters. Incorporating this into the low rank sparse decomposition proposed

in LoSDeCoS could further accelerate the acquisition and improve the reconstruction results.

Dynamic Morphological nceMRA

The presented morphological nceMRA examinations are applications. Dynamic acquisitions to evaluate not only the vessel lumen, but also the blood flow dynamics in certain heart phases could be incorporated. These applications provide the bridge to the presented PCI algorithms. For these, the temporal as well as the flow encoding dimension are fully taken into account. The incorporation of temporal regularization to dynamic morphological nceMRA into the framework is thus prepared.

Processing Pipeline for PCI Data

Considering the processing pipeline for PCI data in Chapter 7, this thesis focused on the reconstruction presented in step (B) of Figure 7.1. While a couple of steps in the pipeline, such as the calculation of anatomical and phase difference images (C) and the calculation of velocity maps (E) are straight forward, other steps would benefit from further work. One example is the vessel segmentation step (D), where state of the art segmentation algorithms could be considered. Examples are given by Sundareswaran et al. and Odille et al. For step (F), the calculation of physiological values, the volumetric flow, mean and peak velocity were considered. While these are important clinical measures, further derived quantities such as wall shear stress as proposed by Stalder et al. [Stal08], which are of interest in current research could be implemented.

Prospective Subsampling and Clinical Evaluation

Peripheral TOF data sets from 10 volunteers, 3-D bSSFP renal data sets from 10 and PCI data sets from 18 volunteers were acquired and used for the evaluation. Furthermore, the diagnostic usability of the produced results was assessed in two PCI patient data sets. The retrospective under sampling approach was used throughout the experiments to provide reliable references for the evaluation of the image based and physiological measures. There is, however, a need for prospective experiments to translate the gain in acquisition speed to practice and to be able to evaluate further patient cases with an increased spatial or temporal resolution. This could further demonstrate the benefits of the accelerated reconstruction and generate new information for the clinical work flow.

Framework

The presented algorithms were implemented within the presented C++ framework, which offers access to the manufacturer's pipeline allowing to incorporate data from the scanner and operates as a standalone platform for further evaluations. The current implementation allows reconstruction in reasonable times for evaluating different algorithms. It allow to reconstruct 3-D renal volumes of size

$N = 192 \times 68 \times 156$ with $N_\gamma = 10$ coils in around 19 minutes, which is a reasonable reconstruction time for performing evaluations. Increasing the reconstruction speed is possible using acceleration strategies and implementation on graphical processing units (GPUs) as proposed for example by Nam et al. and Smith et al. [Nam 13] and [Smit 12].

List of Figures

1.1	Human vascular system	4
1.2	Reconstruction algorithm pipeline	6
1.3	Organization of the thesis	10
2.1	Spins and magnetic fields	14
2.2	RF pulse and spins in the laboratory and rotating frame	15
2.3	Sequence diagrams for echo generation mechanisms	17
2.4	Sequence diagram illustrating the Steady State	18
2.5	Sequence diagram for spatial localization	19
2.6	Cartesian, radial and spiral k -space trajectories	21
2.7	Flow-related enhancement for Time-of-Flight contrast	22
2.8	Illustration of the mp-SSFP contrast generation	23
2.9	Gradients for Phase Contrast MRI	24
3.1	Line phantom used in the illustration of aliasing and resolution loss	30
3.2	Aliasing and resolution loss	31
3.3	Influence of the sampling width and spacing	34
3.4	Multi-coil setup	35
3.5	Principle of Compressed Sensing	39
3.6	Wavelet and total variation coefficients	41
4.1	Illustration of k -space division and the MICCS pattern	52
4.2	Exemplary MICCS pattern construction	53
4.3	Interleaved coil profile acquisition	54
4.4	SENSE encoding operator illustration	56
4.5	IterRecon framework	62
4.6	Gradient based and Split Bregman algorithm	63
5.1	Acquisition and evaluation range for the peripheral data	69
5.2	Pattern study design	70
5.3	Pattern study results	71
5.4	Algorithm study results	75
5.5	MIPs using the MICCS pattern and the Split Bregman algorithm	76
6.1	Acquisition and evaluation range for the renal data	79
6.2	Image reconstruction results for the renal acceleration study	84
6.3	Vessel sharpness results for the renal acceleration study	85
6.4	Results for the algorithm study	86
6.5	Results for the comparison study against clinical methods	87
6.6	Results for the comparison study against clinical methods	88
6.7	NRMSE over the y coordinates for renal reconstructions	88

7.1	PCI processing pipeline	92
7.2	Subset of a representative PCI data set	94
7.3	Illustration of the anatomical and phase difference images	95
8.1	Phantom experiment setup	100
8.2	Carotid volunteer experiment setup	101
8.3	Diagnostic CTA information for patient I	102
8.4	Diagnostic nceMRA and ceMRA information for patient II	102
9.1	Temporal Fourier transform for a PCI data set	110
9.2	Second order temporal Fourier transform for a PCI data set	110
9.3	I-VT sampling strategy central k -space region	113
9.4	Mapping functions in the ts plane	114
9.5	Exemplary 2-D I-VT patterns	115
9.6	Point Spread Functions for four mapping functions	115
9.7	IterRecon framework for PCI data	116
10.1	Finite differences with different step length for a PCI data set	119
10.2	Finite different coefficients for a PCI data set	120
10.3	Combined static and dynamic vessel mask generation	123
10.4	Schematic representation of the MuFloCoS algorithm	125
10.5	Comparative reconstruction results for the carotid in-vivo study	130
10.6	Image results for volunteer P7	131
10.7	Comparative flow profiles for two representative volunteers	133
10.8	Bland-Altman diagram comparing MuFloCoS and $S-CS_{W-vtFT}$	134
10.9	Bland-Altman diagram comparing MuFloCoS and MDFCS	135
10.10	3-D velocity vector reconstruction results	135
10.11	Image results for different TMW regularization weights	136
10.12	Flow profile results for different TMW regularization weights	137
10.13	Image results for different MuFloCoS variants	138
10.14	Flow profiles for different MuFloCoS variants	138
10.15	Reconstruction results for different MuFloCoS variants	139
10.16	Results for different acceleration factors	139
10.17	Flow profiles for different acceleration factors	140
10.18	Peak velocity profiles for patient 1	140
10.19	Peak velocity profiles for patient 2	141
11.1	Influence of the I-VT sampling on rank limited reconstructions	145
11.2	Vectorization of the PCI data	145
11.3	Illustration of rank limited reconstructions for PCI data	146
11.4	Flow chart for the LoSDeCoS algorithm	153
11.5	Evaluation of the influence of the nuclear norm weight	156
11.6	NRMSE for $S-CS$ and LoSDeCoS	156
11.7	Influence of the nuclear norm weight on the peak velocity	157
11.8	Peak flow evaluation for different TV weights	157
11.9	Image results for different TV weights	157
11.10	Image results for volunteer P7	159

11.11 Comparative flow profiles for volunteer P7 160
11.12 Decomposition results for volunteer P7 160

List of Symbols

Abbreviations

bSSFP	Balanced Steady State Free Precession	21
CCA	Common Carotid Artery	3
ce	Contrast-enhanced	5
CNRVB	Contrast to Noise Ratio vessel-background	69
CNRVT	Contrast to Noise Ratio vessel-tissue	69
CS	Compressed Sensing	1
ECA	External Carotid Artery	3
FID	Free induction delay	16
GB _{TV}	Gradient based method with total variation	73
GB _W	Gradient based method with wavelet	73
GB _{TV-W}	Gradient based method with total variation and wavelet	73
I-VT	Interleaved Velocity-encoding Temporal sampling	111
ICA	Internal Carotid Artery	3
ISENSE	Unregularized iterative SENSE algorithm	73
LRA	Main left renal artery	78
MICCS	Multi-Coil Compressed Sensing sampling	47
MIP	Maximum intensity projections	73
MRA	Magnetic Resonance Angiography	1
MRI	Magnetic Resonance Imaging	2
nce	Non-contrast-enhanced	1
NRMSE	Normalized Root Mean Squared Error	68
pMRI	Parallel MRI	1
RF	Radio frequency pulses	14
RRA	Main right renal artery	78
PCI	Phase Contrast Imaging	21
SB _{TV}	Split Bregman based method with total variation	73
SB _W	Split Bregman based method with wavelet	73
SB _{TV-W}	Split Bregman based method with total variation and wavelet	73
S-CS	Sparsity based Compressed Sensing	144
SOS	Sum of Squares	34
TMW	Temporal Masked and Weighted regularization	118
TOF	Time of Flight	21
VSI	Vessel sharpness index	69
vtFT	Velocity encoding temporal Fourier transform	111
SSIM	Structured Similarity	68

Symbols

Basics

N	Number of image voxels	28
N_x	Number of image voxels in x direction	28
N_y	Number of image voxels in y direction	28
N_z	Number of image voxels in z direction	28
l_x	Discrete voxel coordinate in x direction	28
l_y	Discrete voxel coordinate in y direction	28
l_z	Discrete voxel coordinate in z direction	28
l	Voxel index for the 3-D volume	28
ρ_l	Spin density at voxel l	28
\mathcal{M}	Mapping from 3-D to 2-D coordinates	29
\mathcal{M}^{-1}	Mapping from 2-D to 3-D coordinates	29
\mathbf{r}_l	Spatial position of voxel l	29
N_k	Number of k -space samples	29
N_{k_x}	Number of k -space samples in frequency-encoding (x) direction	29
N_{k_y}	Number of k -space samples in the first phase-encoding (y) direction	29
N_{k_z}	Number of k -space samples in the second phase-encoding (z) direction	29
κ_x	Discrete k -space index in frequency-encoding (x) direction	29
κ_y	Discrete k -space index in the first phase-encoding (y) direction	29
κ_z	Discrete k -space index in the second phase-encoding (z) direction	29
κ	k -space point for the 3-D volume	29
k_κ	Frequency of the κ th point	29
N_γ	Number of parallel receive coils	33
γ	Coil index	33
\mathcal{S}	Sum of Squares reconstruction	34
\mathbf{m}_γ	k -space vector for channel γ	36
\mathbf{m}	k -space vector for all channels	36
\mathbf{E}	Encoding matrix	37
ζ	Acceleration factor	38
\mathbf{x}	Image space vector	39
$\mathbf{x}^{t,s}$	Image space vector for time step t and velocity encoding s	93
$\mathbf{m}^{t,s}$	k -space vector for time step t and velocity encoding s	93

Iterative reconstruction

$\mathcal{L}(x)$	Objective function	42
N_i	Number of IBFGS iterations	42
τ	Stabilization constant for the TV term	56
$TV_i(\mathbf{x})$	Isotropic Total Variation	50
W	Wavelet Decomposition	51
$WV(\mathbf{x})$	Wavelet L_1 operator	51

N_j	Number of Split Bregman iterations	61
-------	--	----

Sampling

\mathbf{u}	2-D sampling	51
$N_{k_{cy}}$	k -space center size	51
\mathbf{d}_c	Distance factor for the MICCS sampling	52
\mathbf{o}_c	Offset factor for the MICCS sampling	52
a, b	Parameter for the MICCS sampling	52

Static nceMRA

\mathcal{L}_{UC}	Unconstrained objective function	51
λ_t	Weight for the total variation term	51
λ_w	Weight for the wavelet term	51
\mathbf{d}_x	Split variable for the TV in x direction	59
\mathbf{d}_y	Split variable for the TV in y direction	59
\mathbf{d}_w	Split variable for the wavelet term	59
μ	Weight for the data fidelity term	60
α	Weight for the regularization terms	60
\mathbf{b}_x	Residual error for the TV in x direction	60
\mathbf{b}_y	Residual error for the TV in y direction	60
\mathbf{b}_w	Residual error for the wavelet term	60
\mathcal{L}_{L_2}	Objective function for the L_2 sub problem	60
N'_i	Number of iterations for the L_2 sub problem	60
\mathbf{z}	TV coupling variable	61
λ_t^{SB}	Weight for the total variation term in the SB algorithm	65
λ_w^{SB}	Weight for the wavelet term in the SB algorithm	65
VSI_a	Aortic sharpness	78
VSI_{ra}	Renal artery sharpness	78
\mathbf{a}_{pr}	Axial pre-aortic position	78
\mathbf{a}_{po}	Axial post-aortic position	78
\mathbf{ra}_r	Axial position orthogonal to the RRA	78
\mathbf{ra}_l	Axial position orthogonal to the LRA	78

PCI

v	Encoding velocity	25
N_t	Number of temporal phases	93
N_s	Number of velocity encodings	93
N_p	Problem size	93
χ	Vessel	95
$\mathbf{l}^{\chi,t}$	Lumen of vessel χ	95

Q_v	Volumetric flow	96
V_p	Peak velocity	96
V_m	Mean velocity	96
Q	Total flow	104
ΔQ_l	Deviation in the in/outflow of slice l	104
ΔQ_l^i	Inter-slice deviation in the inflow	104
ΔQ_l^o	Inter-slice deviation in the outflow	104
$\mathbf{u}^{t,s}$	3-D s-t sampling	108
$\mathcal{F}_{t,s}^v(\mathbf{x})$	Velocity encoding temporal Fourier transform	111
$j(t,s)$	Mapping for the I-VT sampling	112

LoSDeCoS

\mathbf{s}	Sparse matrix component	144
\mathbf{l}	Low rank matrix component	144
L	Low rank transform	144
r	Rank of a matrix	146
σ_i	Singular values ordered by magnitude	147
$\text{tr}(\mathbf{X})$	Trace of the matrix \mathbf{x}	147
$\ \mathbf{X}\ _F$	Frobenius norm of the matrix \mathbf{X}	147
$\ \mathbf{X}\ _*$	Nuclear norm of the matrix \mathbf{X}	147
\mathcal{L}_{Los}	Objective function for LoSDeCoS	148
λ_f	Weight for the temporal Fourier transform term	148
λ_n	Weight for the nuclear norm	148
\mathbf{d}_z	Split variable for the TV in z direction	149
\mathbf{d}_f	Split variable for the temporal Fourier transform	149
\mathbf{d}_n	Split variable for the nuclear norm	149
\mathbf{b}_z	Residual error for the TV in z direction	149
\mathbf{b}_f	Residual error for the temporal Fourier transform	149
\mathbf{b}_n	Residual error for the nuclear norm	149
$\mathcal{L}_{\text{Los-L2}}$	Objective function for the L_2 step of LoSDeCoS	150
s_3	Singular value thresholding	151
λ_f^{SB}	Weight for the temporal Fourier term in the SB algorithm	154
λ_n^{SB}	Weight for the nuclear norm term in the SB algorithm	154

MuFloCoS

$\nabla_t^{t,t_j,s}$	Difference vector between temporal step t and t_j .	118
\mathbf{b}^t	Vessel mask	121
\mathbf{M}	Vessel mask matrix	121
$w(t, t_j)$	Temporal weighting function	121
$w_B(t, t_j)$	Box weighting function	121
$w_G(t, t_j)$	Gaussian weighting function	121
σ	Standard deviation for the Gaussian weighting function	121

\mathbf{W}	Weighting matrix	121
\mathcal{L}_{Muf}	Objective function for MuFloCoS	122
T	Index set of the entire volume	122
D	Index set of the flow dynamic affected part	122
S	Index set of the static part	122
$\bar{\mathbf{a}}$	Static anatomical image	122
$\check{\mathbf{a}}^t$	Dynamic anatomical image	122
$\bar{\mathbf{b}}$	Static binary mask	124
$\check{\mathbf{b}}^t$	Dynamic binary mask	124
$w_{SD}(i)$	Weighting function for the dynamic and static masks	124
β	Weighting parameter for the dynamic and static masks	124
α_m	Threshold for the anatomical images	124
λ_{tmw}	Weight for the TMW- L_1 regularization.	122
ϵ	Threshold for the TMW- L_1 term.	124

List of Tables

2.1	Characteristic T_1/T_2 values	16
2.2	Properties of nceMRA methods	21
4.1	Run times for the static nceMRA algorithms	63
5.1	Quantitative results for the peripheral pattern study	72
5.2	Quantitative results for the peripheral pattern study	72
5.3	Reconstruction parameters for the peripheral in-vivo study	73
5.4	Quantitative results for the peripheral algorithm study	74
5.5	Quantitative results for the peripheral algorithm study	75
6.1	Acceleration achieved within the acceleration study	79
6.2	Quantitative results for the renal acceleration study	80
6.3	Quantitative results for the renal algorithm study	81
6.4	Quantitative results for the renal comparison study	82
9.1	Run times for the PCI algorithms	116
10.1	Quantitative evaluation of the phantom experiments	127
10.2	Experimental setup for the comparison of Tao et al. and MuFloCoS .	129
10.3	Comparative image quality results for the in-vivo carotid study . . .	132
10.4	Comparative physiological results for the in-vivo carotid study . . .	132
10.5	Quantitative results for the comparison with Tao et al.	136
10.6	Comparative reconstruction results for different MuFloCoS variants .	137
11.1	Quantitative results for the S-CS and LoSDeCoS algorithms	155
11.2	Quantitative volunteer evaluation	158
11.3	Quantitative patient evaluation	158

Bibliography

- [Acar 94] R. Acar and C. R. Vogel. "Analysis of Bounded Variation Penalty Methods for Ill-Posed Problems". *Inverse Problems*, Vol. 10, pp. 1217–1229, Aug 1994.
- [Aelt 10] J. Aelterman, H. Luong, B. Goossens, A. Pižurica, and W. Philips. "COMPASS: a Joint Framework for Parallel Imaging and Compressive Sensing in MRI". In: IEEE, Ed., *IEEE International Conference on Image Processing (ICIP 2010), Hong Kong, China, Sep. 26-29*, pp. 1653–1656, 2010.
- [Afon 11] M. V. Afonso, J. M. Bioucas-Dias, and M. A. T. Figueiredo. "An Augmented Lagrangian Approach to the Constrained Optimization Formulation of Imaging Inverse Problems.". *IEEE Transactions on Image Processing*, Vol. 20, No. 3, pp. 681–695, Mar 2011.
- [Akca 11] M. Akcakaya, P. Hu, M. L. Chuang, T. H. Hauser, L. H. Ngo, W. J. Manning, V. Tarokh, and R. Nezafat. "Accelerated noncontrast-enhanced pulmonary vein MRA with distributed compressed sensing". *Journal of Magnetic Resonance Imaging*, Vol. 33, No. 5, pp. 1248–1255, May 2011.
- [Al Q 09] M. Al-Qaisi, D. Nott, D. King, S. Kaddoura, and M. Hamady. "Imaging of peripheral vascular disease". *Reports on Medical Imaging*, Vol. 2, pp. 25–34, Mar 2009.
- [Alpe 05] N. Alperin, A. Sivaramakrishnan, and T. Lichtor. "Magnetic resonance imaging-based measurements of cerebrospinal fluid and blood flow as indicators of intracranial compliance in patients with Chiari malformation". *Journal of Neurosurgery*, Vol. 103, No. 1, pp. 46–52, Jul 2005.
- [AlZu 11] S. AlZubi, N. Islam, and M. Abbod. "Multiresolution Analysis Using Wavelet, Ridgelet, and Curvelet Transforms for Medical Image Segmentation". *Journal of Biomedical Imaging*, Vol. 2011, pp. 4:1–4:18, Jan 2011.
- [Atki 94] D. Atkinson, M. Brant-Zawadzki, G. Gillan, D. Purdy, and G. Laub. "Improved MR angiography: magnetization transfer suppression with variable flip angle excitation and increased resolution.". *Radiology*, Vol. 190, No. 3, pp. 890–894, Mar 1994.
- [Balt 05] C. Baltés, S. Kozerke, M. Hansen, K. Pruessmann, J. Tsao, and P. Boesiger. "Accelerating cine phase-contrast flow measurements using k-t BLAST and k-t SENSE.". *Magnetic Resonance in Medicine*, Vol. 54, No. 6, pp. 1430–1438, Dec 2005.
- [Barg 02] A. V. Barger, W. F. Block, Y. Toropov, T. M. Grist, and C. A. Mistretta. "Time-resolved contrast-enhanced imaging with isotropic resolution and broad coverage using an undersampled 3D projection trajectory". *Magnetic Resonance in Medicine*, Vol. 48, No. 2, pp. 297–305, Aug 2002.

- [Bart06] E. Bartlett, T. Walters, S. Symons, and A. Fox. “Quantification of Carotid Stenosis on CT Angiography”. *American Journal of Neuroradiology*, Vol. 27, No. 1, pp. 13–19, Jan 2006.
- [Baue13] S. Bauer, M. Markl, D. Foll, M. Russe, Z. Stankovic, and B. Jung. “K-t GRAPPA accelerated phase contrast MRI: Improved assessment of blood flow and 3-directional myocardial motion during breath-hold”. *Journal of Magnetic Resonance Imaging*, Vol. 38, No. 5, pp. 1054–1062, Nov 2013.
- [Beer05] P. Beerbaum, H. Korperich, J. Gieseke, P. Barth, M. Peuster, and H. Meyer. “Blood flow quantification in adults by phase-contrast MRI combined with SENSE—a validation study”. *Journal of Cardiovascular Magnetic Resonance*, Vol. 7, No. 2, pp. 361–369, Jan 2005.
- [Blai04] M. Blaimer, F. Breuer, M. Mueller, R. M. Heidemann, M. A. Griswold, and P. M. Jakob. “SMASH, SENSE, PILS, GRAPPA: how to choose the optimal method.”. *Topics in magnetic resonance imaging*, Vol. 15, No. 4, pp. 223–236, Aug 2004.
- [Bloc07] K. T. Block, M. Uecker, and J. Frahm. “Undersampled radial MRI with multiple coils. Iterative image reconstruction using a total variation constraint”. *Magnetic Resonance in Medicine*, Vol. 57, No. 6, pp. 1086–1098, Jun 2007.
- [Blum08] T. Blumensath and M. E. Davies. “Iterative Thresholding for Sparse Approximations”. *Journal of Fourier Analysis and Applications*, Vol. 14, No. 5, pp. 629–654, Dec. 2008.
- [Boyd04] S. Boyd and L. Vandenberghe. *Convex Optimization*. Cambridge University Press, New York, USA, 2004.
- [Breg67] L. Bregman. “The relaxation method of finding the common points of convex sets and its application to the solution of problems in convex programming”. *USSR Computational Mathematics and Mathematical Physics*, Vol. 7, pp. 200–217, Nov 1967.
- [Busc12] J. Busch, D. Giese, L. Wissmann, and S. Kozerke. “Divergence-free reconstruction for accelerated 3D phase-contrast flow measurements.”. *Journal of Cardiovascular Magnetic Resonance*, Vol. 14 Suppl 1, p. W38, Feb 2012.
- [Caba12] J. Caballero, D. Rueckert, and J. Hajnal. “Dictionary Learning and Time Sparsity in Dynamic MRI”. In: N. Ayache, H. Delingette, P. Golland, and K. Mori, Eds., *Lecture Notes in Computer Science (15th International Conference for Medical Image Computing and Computer-Assisted Intervention (MICCAI 2012))*, Nice, France, Oct 1-5, pp. 256–263, Springer, 2012.
- [Cai10] J. Cai, E. Candès, and Z. Shen. “A Singular Value Thresholding Algorithm for Matrix Completion”. *SIAM Journal on Optimization*, Vol. 20, No. 4, pp. 1956–1982, Mar 2010.
- [Cand08] E. J. Candès and M. B. Wakin. “An Introduction To Compressive Sampling”. *IEEE Signal Processing Magazine*, Vol. 25, No. 2, pp. 21–30, Mar 2008.

- [Cand 11] E. Candès, X. Li, Y. Ma, and J. Wright. “Robust principal component analysis?”. *Journal of the ACM*, Vol. 58, No. 3, pp. 11:1–11:37, Jun 2011.
- [Carr 12] J. Carr and T. Carroll. *Magnetic Resonance Angiography: Principles and Applications*. Springer, New York, USA, 2012.
- [Caw109] P. J. Cawley, J. H. Maki, and C. M. Otto. “Cardiovascular Magnetic Resonance Imaging for Valvular Heart Disease: Technique and Validation”. *Circulation*, Vol. 119, No. 3, pp. 468–478, Jan 2009.
- [Chan 13] T. Chang, M. Nadar, J. Gühring, M. Zenge, K. Block, P. Schmitt, and E. Mueller. “Non-Contrast-Enhanced 4D MRA Using Compressed Sensing Reconstruction”. May 2013. US Patent App. 13/284,143.
- [Chen 01] S. S. Chen, D. L. Donoho, Michael, and A. Saunders. “Atomic decomposition by basis pursuit”. *SIAM Review*, Vol. 45, No. 1, pp. 129–155, Mar 2001.
- [Chen 06] C. Cheng, D. Tempel, R. van Haperen, A. van der Baan, F. Grosveld, M. J. Daemen, R. Krams, and R. de Crom. “Atherosclerotic Lesion Size and Vulnerability Are Determined by Patterns of Fluid Shear Stress”. *Circulation*, Vol. 113, No. 23, pp. 2744–2753, Jun. 2006.
- [Chen 10] L. Chen, M. C. Schabel, and E. V. DiBella. “Reconstruction of dynamic contrast enhanced magnetic resonance imaging of the breast with temporal constraints”. *Magnetic Resonance Imaging*, Vol. 28, No. 5, pp. 637–45, Jun 2010.
- [Chro 01] B. A. Chronik and B. K. Rutt. “Simple linear formulation for magnetostimulation specific to MRI gradient coils”. *Magnetic Resonance in Medicine*, Vol. 45, No. 5, pp. 916–919, May 2001.
- [Coll 07] R. Collins, G. Cranny, J. Burch, R. Aguiar-Ibanez, D. Craig, K. Wright, E. Berry, M. Gough, J. Kleijnen, and M. Westwood. “A systematic review of duplex ultrasound, magnetic resonance angiography and computed tomography angiography for the diagnosis and assessment of symptomatic, lower limb peripheral arterial disease”. *Health Technology Assessment Journal*, Vol. 11, No. 20, pp. 1–184, May 2007.
- [Craw 92] A. P. Crawley, M. S. Cohen, E. K. Yucel, B. Poncelet, and T. J. Brady. “Single-shot magnetic resonance imaging: applications to angiography”. *Cardiovascular Interventional Radiology*, Vol. 15, No. 1, pp. 32–42, Jan-Feb 1992.
- [Cuku 09] T. Cukur, M. Lustig, and D. G. Nishimura. “Improving non-contrast-enhanced steady-state free precession angiography with compressed sensing”. *Magnetic Resonance in Medicine*, Vol. 61, No. 5, pp. 1122–1131, May 2009.
- [Daly 13] S. Daly and M. Leahy. “Go with the flow: A review of methods and advancements in blood flow imaging.”. *Journal on Biophotonics*, Vol. 6, No. 3, pp. 217–255, Jun 2013.

- [Daub 04] I. Daubechies, M. Defrise, and C. De Mol. "An iterative thresholding algorithm for linear inverse problems with a sparsity constraint". *Communications of Pure and Applied Mathematics*, Vol. 57, No. 11, pp. 1413–1457, Nov 2004.
- [Dono 06] D. Donoho. "Compressed sensing". *IEEE Transactions on Information Theory*, Vol. 52, No. 4, pp. 1289–1306, Apr 2006.
- [Doyl 95] M. Doyle, E. G. Walsh, G. G. Blackwell, and G. M. Pohost. "Block regional interpolation scheme for k-space (BRISK): a rapid cardiac imaging technique". *Magnetic Resonance in Medicine*, Vol. 33, No. 2, pp. 163–170, Feb 1995.
- [Doyl 99] M. Doyle, E. Kortright, A. S. Anayiotos, A. M. Elmahdi, E. G. Walsh, A. R. Fuisz, and G. M. Pohost. "Rapid velocity-encoded cine imaging with turbo-BRISK". *Journal of Cardiovascular Magnetic Resonance*, Vol. 1, No. 3, pp. 223–232, Jan 1999.
- [Faze 02] M. Fazel. *Matrix Rank Minimization with Applications*. PhD thesis, Elec. Eng. Dept, Stanford University, 2002.
- [Feng 13] L. Feng, R. Grimm, and K. T. Block. "Golden-angle radial sparse parallel MRI: Combination of compressed sensing, parallel imaging, and golden-angle radial sampling for fast and flexible dynamic volumetric MRI". *Magnetic Resonance in Medicine*, Vol. -, No. -, 2013.
- [Foo 95] T. K. Foo, M. A. Bernstein, A. M. Aisen, R. J. Hernandez, B. D. Collick, and T. Bernstein. "Improved ejection fraction and flow velocity estimates with use of view sharing and uniform repetition time excitation with fast cardiac techniques.". *Radiology*, Vol. 195, No. 2, pp. 471–8, May 1995.
- [Forn 11] M. Fornasier, H. Rauhut, and R. Ward. "Low-rank Matrix Recovery via Iteratively Reweighted Least Squares Minimization". *SIAM Journal on Optimization*, Vol. 21, No. 4, pp. 1614–1640, Dec. 2011.
- [Gamp 08] U. Gamper, P. Boesiger, and S. Kozerke. "Compressed sensing in dynamic MRI.". *Magnetic Resonance in Medicine*, Vol. 59, No. 2, pp. 365–373, Feb 2008.
- [Gibs 94] W. G. Gibson, R. S. Cobbold, and K. W. Johnston. "Principles and design feasibility of a Doppler ultrasound intravascular volumetric flowmeter". *IEEE Transactions on Biomedical Engineering*, Vol. 41, No. 9, pp. 898–908, Sep 1994.
- [Gies 12] D. Giese, T. Schaeffter, and S. Kozerke. "Highly undersampled phase-contrast flow measurements using compartment-based k-t principal component analysis". *Magnetic Resonance in Medicine*, Vol. 69, No. 2, pp. 434–443, Apr 2012.
- [Gloc 10] J. F. Glockner, N. Takahashi, A. Kawashima, D. A. Woodrum, D. W. Stanley, N. Takei, M. Miyoshi, and W. Sun. "Non-contrast renal artery MRA using an inflow inversion recovery steady state free precession technique (Inhance): comparison with 3D contrast-enhanced MRA.". *Journal of Magnetic Resonance Imaging*, Vol. 31, No. 6, pp. 1411–1418, Jun 2010.

- [Glov 92] G. H. Glover and J. M. Pauly. "Projection reconstruction techniques for reduction of motion effects in MRI.". *Magnetic Resonance in Medicine*, Vol. 28, No. 2, pp. 275–289, Dec 1992.
- [Gold 09] T. Goldstein and S. Osher. "The Split Bregman Method for L1-Regularized Problems". *SIAM Journal on Imaging Sciences*, Vol. 2, pp. 323–343, Apr 2009.
- [Gold 11] D. Goldfarb and S. Ma. "Convergence of Fixed-Point Continuation Algorithms for Matrix Rank Minimization". *Foundations of Computational Mathematics*, Vol. 11, No. 2, pp. 183–210, Apr. 2011.
- [Gonz 11] R. González, J. Hirsch, M. Lev, P. Schaefer, and L. Schwamm, Eds. *Acute Ischemic Stroke, Imaging and Intervention*. Springer, New York, USA, 2nd Ed., Oct 2011.
- [Gray 01] H. Gray. *Anatomy, descriptive and surgical*. Barleby, New York, USA, 20. Ed., 2001.
- [Grei 03] A. Greiser and M. von Kienlin. "Efficient k-space sampling by density-weighted phase-encoding". *Magnetic Resonance in Medicine*, Vol. 50, No. 6, pp. 1266–1275, Dec 2003.
- [Gris 02] M. A. Griswold, P. N. Jakob, R. M. Heidemann, M. Nittka, V. Jellus, J. Wang, B. Kiefer, and A. Haase. "Generalized Autocalibrating Partially Parallel Acquisitions (GRAPPA)". *Magnetic Resonance in Medicine*, Vol. 47, pp. 1202–1210, Jun 2002.
- [Haac 99] E. Haacke, R. Brown, M. Thompson, and R. Venkatesan. *Magnetic Resonance Imaging: Physical Principles and Sequence Design*. Wiley, New York, USA, 1999.
- [Hage 06] W. W. Hager and H. Zhang. "A survey of nonlinear conjugate gradient methods". *Pacific journal of Optimization*, Vol. 2, No. 1, pp. 35–58, Jan 2006.
- [Herb 06] C. U. Herborn, D. M. Watkins, V. M. Runge, J. M. Gendron, M. L. Montgomery, and L. G. Naul. "Renal arteries: comparison of steady-state free precession MR angiography and contrast-enhanced MR angiography". *Radiology*, Vol. 239, No. 1, pp. 263–268, Apr 2006.
- [Hest 52] M. R. Hestenes and E. Stiefel. "Methods of conjugate gradients for solving linear systems". *Journal of research of the National Bureau of Standards*, Vol. 49, pp. 409–436, Dec 1952.
- [Hoge 04] W. S. Hoge, B. Madore, W. E. Kyriakos, and D. H. Brooks. "On the Regularization of SENSE and Space-RIP in Parallel MR Imaging.". In: IEEE, Ed., *6th IEEE International Symposium on Biomedical Imaging (ISBI 2009)*, Arlington, USA, Apr 15–18, pp. 241–244, 2004.
- [Hoge 05] W. S. Hoge, D. H. Brooks, B. Madore, and W. E. Kyriakos. "A tour of accelerated parallel MR imaging from a linear systems perspective". *Concepts in Magnetic Resonance Part A*, Vol. 27A, No. 1, pp. 17–37, Sep 2005.

- [Holl 10] D. Holland, D. Malioutov, A. Blake, A. Sederman, and L. Gladden. "Reducing data acquisition times in phase-encoded velocity imaging using compressed sensing". *Journal of Magnetic Resonance*, Vol. 203, No. 2, pp. 236 – 246, Apr 2010.
- [Hsia 12] A. Hsiao, M. Lustig, M. T. Alley, M. Murphy, F. P. Chan, R. J. Herfkens, and S. S. Vasanawala. "Rapid pediatric cardiac assessment of flow and ventricular volume with compressed sensing parallel imaging volumetric cine phase-contrast MRI". *American Journal of Roentgenology*, Vol. 198, No. 3, pp. W250–259, Mar 2012.
- [Huan 09] J. Huang and T. Zhang. "The Benefit of Group Sparsity". Tech. Rep., Jan 2009.
- [Huan 12] J. Huang, C. Chen, and L. Axel. "Fast Multi-contrast MRI Reconstruction.". In: N. Ayache, H. Delingette, P. Golland, and K. Mori, Eds., *MICCAI (1)*, pp. 281–288, Springer, 2012.
- [Hule 13] J. Hulet, A. Greiser, J. Mendes, C. McGann, G. Treiman, and D. Parker. "Highly accelerated cardiac cine phase-contrast mri using an under-sampled radial acquisition and temporally constrained reconstruction". *Journal of Magnetic Resonance Imaging*, Vol. 0, No. 0, pp. 00–00, 2013.
- [Hutt 11a] J. Hutter, R. Grimm, C. Forman, J. Hornegger, and P. Schmitt. "Inverse root sampling pattern for iterative reconstruction in non-CE MR angiography". In: *Proceedings of the annual conference of the ESMRMB (ESMRMB 2011), Leipzig, Germany, 6-8 Oct 2011*, 2011.
- [Hutt 11b] J. Hutter, J. Hornegger, and P. Schmitt. "Vessel prior-knowledge regularization for MR angiography". In: *Proceedings of the annual conference of the ESMRMB (ESMRMB 2011), Leipzig, Germany, 6-8 Oct 2011*, 2011.
- [Hutt 12a] J. Hutter, R. Grimm, and C. Forman. "Highly accelerated non-contrast enhanced MRA of the renal arteries using iterative reconstruction". In: J. Pipe, Ed., *Proceedings of the 21st annual meeting of the ISMRM, Melbourne, Australia, May 5–11, 2012*.
- [Hutt 12b] J. Hutter, R. Grimm, C. Forman, J. Hornegger, and P. Schmitt. "Vessel Adapted Regularization for Iterative Reconstruction in MR Angiography". In: J. Pipe, Ed., *Proceedings of the 21st annual meeting of the ISMRM, Melbourne, Australia, May 5–11, 2012*.
- [Hutt 12c] J. Hutter, H. Hofmann, R. Grimm, A. Greiser, M. Saake, J. Hornegger, and P. Schmitt. "Prior-Based Automatic Segmentation of the Carotid Artery Lumen in TOF MRA (PASCAL)". In: N. Ayache, H. Delingette, P. Golland, and K. Mori, Eds., *Lecture Notes in Computer Science (15th International Conference for Medical Image Computing and Computer-Assisted Intervention (MICCAI 2012)), Nice, France, Oct 1-5*, pp. 511–518, 2012.
- [Hutt 13a] J. Hutter, A. Greiser, R. Grimm, C. Forman, J. Hornegger, and P. Schmitt. "Highly undersampled time resolved phase-contrast MRA with flow-adapted compressed sensing reconstruction". In: G. E. Gold, Ed., *Proceedings of the 21st annual meeting of the ISMRM, Salt Lake City, USA, Apr 20-26, 2013*.

- [Hutt 13b] J. Hutter, A. Greiser, R. Grimm, C. Forman, J. Hornegger, and P. Schmitt. "Multi-Dimensional Flow-Adapted Compressed Sensing (MDFCS) for time-resolved velocity-encoded Phase Contrast MRA". In: IEEE, Ed., *10th IEEE International Symposium on Biomedical Imaging (ISBI 2013), San Francisco, USA, Apr 7–11*, pp. 13 – 16, 2013.
- [Hutt 13c] J. Hutter, R. Grimm, M. Ciocan, J. Hornegger, and P. Schmitt. "Iterative Multi-Slice Compressed Sensing Reconstruction for Peripheral MRA". In: *Proceedings of the annual conference of the ESMRMB (ESMRMB 2013), Toulouse, France, 3-5 Oct 2013*, 2013.
- [Hutt 13d] J. Hutter and P. Schmitt. "Sampling pattern for iterative magnetic resonance image reconstruction". Feb. 28 2013. US Patent App. 13/592,675.
- [Hutt 13e] J. Hutter, P. Schmitt, G. Aandal, A. Greiser, C. Forman, R. Grimm, J. Hornegger, and A. Maier. "Low-rank and Sparse Matrix Decomposition for Compressed Sensing reconstruction of Magnetic Resonance 4D Phase Contrast blood flow imaging (LoSDeCoS 4D-PCI)". In: K. Mori, I. Sakuma, Y. Sato, C. Barillot, and N. Navab, Eds., *Lecture Notes in Computer Science (16th International Conference for Medical Image Computing and Computer-Assisted Intervention (MICCAI 2013))*, Nagoya, Japan, Sep 22-26, pp. 558–565, 2013.
- [Hutt 14a] J. Hutter, P. Schmitt, R. Grimm, C. Forman, and J. Hornegger. "Highly Accelerated 2-D peripheral TOF using the MICCS pattern". -, Vol. Manuscript for Magnetic Resonance in Medicine, No. -, 2014.
- [Hutt 14b] J. Hutter, P. Schmitt, R. Grimm, C. Forman, and J. Hornegger. "Highly Accelerated Free-Breathing SSFP Renal Angiography using Split Bregman based Compressed Sensing". -, Vol. Manuscript for Magnetic Resonance in Medicine, No. -, 2014.
- [Hutt 14c] J. Hutter, P. Schmitt, M. Saake, A. Stübinger, R. Grimm, C. Forman, J. Hornegger, and A. Greiser. "Accelerated Velocity-Encoded Phase Contrast MRI using a Split Bregman based Compressed Sensing Reconstruction with Low Rank and Sparse Matrix Model (LoSDeCoS)". *Submitted to Magnetic Resonance in Medicine*, Vol. -, No. -, 2014.
- [Hutt 14d] J. Hutter, P. Schmitt, M. Saake, A. Stübinger, R. Grimm, C. Forman, A. Maier, J. Hornegger, and A. Greiser. "Multi-Dimensional Flow-Preserving Compressed Sensing (MuFloCoS) for Time-Resolved Velocity-Encoded Phase Contrast MRA". *Submitted to IEEE Transactions on Medical Imaging*, Vol. -, No. -, 2014.
- [Jin 05] Y. Jin, E. Angelini, and A. Laine. "Wavelets in Medical Image Processing: Denoising, Segmentation, and Registration". In: J. Suri, D. Wilson, and S. Laxminarayan, Eds., *Handbook of Biomedical Image Analysis*, pp. 305–358, Springer, New York, USA, 2005.
- [Juer 63] J. Juergens. "Chronic occlusive arterial disease of the extremities.". *Circulation*, Vol. 27, No. , pp. 964–9, May 1963.
- [Jung 08a] B. Jung, M. Honal, P. Ullmann, J. Hennig, and M. Markl. "Highly k-t-space-accelerated phase-contrast MRI". *Magnetic Resonance in Medicine*, Vol. 60, No. 5, pp. 1169–1177, Nov 2008.

- [Jung 08b] B. Jung, P. Ullmann, M. Honal, S. Bauer, J. Hennig, and M. Markl. "Parallel MRI with extended and averaged GRAPPA kernels (PEAK-GRAPPA): optimized spatiotemporal dynamic imaging". *Journal of Magnetic Resonance Imaging*, Vol. 28, No. 5, pp. 1226–1232, Nov 2008.
- [Jung 09] H. Jung, K. Sung, K. S. Nayak, E. Y. Kim, and J. C. Ye. "k-t FOCUSS: a general compressed sensing framework for high resolution dynamic MRI". *Magnetic Resonance in Medicine*, Vol. 61, No. 1, pp. 103–116, Jan 2009.
- [Kand 08] K. Kandarpa. *Peripheral Vascular Interventions*. LWW medical book collection, Wolters Kluwer Health/Lippincott Williams & Wilkins, Philadelphia, USA, 2008.
- [Kato 04] M. Katoh, A. Buecker, M. Stuber, R. W. Guenther, and E. Spuentrup. "Free-breathing renal MR angiography with steady-state free-precession (SSFP) and slab-selective spin inversion: initial results". *Kidney Int*, Vol. 66, No. 3, pp. 1272–1278, Sep 2004.
- [Keil 13] B. Keil, J. N. Blau, S. Biber, P. Hoecht, V. Tountcheva, K. Setsompop, C. Triantafyllou, and L. L. Wald. "A 64-channel 3T array coil for accelerated brain MRI". *Magnetic Resonance in Medicine*, Vol. 70, No. 1, pp. 248–258, Jul 2013.
- [Kell 01] P. Kellman, F. H. Epstein, and E. R. McVeigh. "Adaptive sensitivity encoding incorporating temporal filtering (TSENSE)". *Magnetic Resonance in Medicine*, Vol. 45, No. 5, pp. 846–852, May 2001.
- [Kim 12a] D. Kim, H. Dyvorne, R. Otazo, L. Feng, D. Sodickson, and V. Lee. "Accelerated phase-contrast cine MRI using k-t SPARSE-SENSE". *Magnetic Resonance in Medicine*, Vol. 67, pp. 1054–1064, Apr 2012.
- [Kim 12b] S.-E. Kim and D. L. Parker. "Time-of-Flight Angiography". In: J. C. Carr and T. J. Carroll, Eds., *Magnetic Resonance Angiography: Principles and Applications*, Springer, Berlin / Heidelberg, Germany, 2012.
- [KNNa 89] K.N.Nayak and D. Nishimura. "Randomized Trajectories for Reduced Aliasing Artifact". In: *Proceedings of the 6th Annual meeting of the ISMRM, Sydney, Australia, Apr 18-24, 1989*.
- [Knob 13] V. Knobloch, P. Boesiger, and S. Kozerke. "Sparsity transform k-t principal component analysis for accelerating cine three-dimensional flow measurements". *Magnetic Resonance in Medicine*, Vol. 70, No. 1, pp. 53–63, Jul 2013.
- [Knol 12] F. Knoll, C. Clason, K. Bredies, M. Uecker, and R. Stollberger. "Parallel imaging with nonlinear reconstruction using variational penalties". *Magnetic Resonance in Medicine*, Vol. 7, No. 1, pp. 34–41, Jan 2012.
- [Kwak 12] Y. Kwak, S. Nam, K. V. Kissinger, B. Goddu, L. Goepfert, W. M. V. Tarokh, and R. Nezafat. "Accelerated phase contrast imaging using compressed sensing with complex difference sparsity.". *Journal of Cardiovascular Magnetic Resonance*, Vol. 14 Suppl 1, p. W24, Feb 2012.

- [Lai 11] P. Lai, T. Zhang, M. Lustig, S. Vasanawala, and A. C. Brau. "Improving Compressed Sensing Parallel Imaging using Autocalibrating Parallel Imaging Initialization with Variable Density Tiled Random k-space Sampling". In: C. Reinhold, Ed., *Proceedings of the 19th annual meeting of the ISMRM, Montreal, Canada, May 7-13, 2011*.
- [Lanz 09] R. S. Lanzman, A. Voiculescu, C. Walther, A. Ringelstein, X. Bi, P. Schmitt, S.-M. Freitag, S. Won, A. Scherer, and D. Blondin. "ECG-gated nonenhanced 3D steady-state free precession MR angiography in assessment of transplant renal arteries: comparison with DSA.". *Radiology*, Vol. 252, No. 3, pp. 914–921, Sep 2009.
- [Lein 05] T. Leiner, A. G. Kessels, P. J. Nelemans, G. B. Vasbinder, M. W. de Haan, P. E. Kitslaar, K. Y. Ho, J. H. Tordoir, and J. M. van Engelshoven. "Peripheral arterial disease: comparison of color duplex US and contrast-enhanced MR angiography for diagnosis". *Radiology*, Vol. 235, No. 2, pp. 699–708, May 2005.
- [Lew 10] C. Lew, M. T. Alley, D. M. Spielman, R. Bammer, and F. P. Chan. "Breathheld autocalibrated phase-contrast imaging". *Journal of Magnetic Resonance Imaging*, Vol. 31, No. 4, pp. 1004–1014, Apr 2010.
- [Li 01] D. Li, J. C. Carr, S. M. Shea, J. Zheng, V. S. Deshpande, P. A. Wielopolski, and J. P. Finn. "Coronary arteries: magnetization-prepared contrast-enhanced three-dimensional volume-targeted breath-hold MR angiography". *Radiology*, Vol. 219, No. 1, pp. 270–277, Apr 2001.
- [Lin 04] F.-H. Lin, K. K. Kwong, J. W. Belliveau, and L. L. Wald. "Parallel imaging reconstruction using automatic regularization". *Magnetic Resonance in Medicine*, Vol. 51, No. 3, pp. 559–567, Mar 2004.
- [Liu 09a] B. Liu, K. King, M. Steckner, J. Xie, J. Sheng, and L. Ying. "Regularized sensitivity encoding (SENSE) reconstruction using Bregman iterations.". *Magnetic Resonance in Medicine*, Vol. 61, No. 1, pp. 145–152, Jan 2009.
- [Liu 09b] Z. Liu and L. Vandenberghe. "Interior-Point Method for Nuclear Norm Approximation with Application to System Identification.". *SIAM Journal on Matrix Analysis Applications*, Vol. 31, No. 3, pp. 1235–1256, Aug 2009.
- [Long 01] Q. Long, X. Xu, K. Ramnarine, and P. Hoskins. "Numerical investigation of physiologically realistic pulsatile flow through arterial stenosis.". *J Biomech*, Vol. 34, No. 10, pp. 1229–42, Oct 2001.
- [Lust 06] M. Lustig, J. M. Santos, D. L. Donoho, and J. M. Pauly. "kt SPARSE: High frame rate dynamic MRI exploiting spatio-temporal sparsity". In: *Proceedings of the 14th annual meeting of the ISMRM, Seattle, USA, May 6–12, p. 2420, 2006*.
- [Lust 07] M. Lustig, D. Donoho, and J. M. Pauly. "Sparse MRI: The application of compressed sensing for rapid MR imaging". *Magnetic Resonance in Medicine*, Vol. 58, No. 6, pp. 1182–1195, Dec 2007.

- [Lust 08] M. Lustig, D. L. Donoho, J. M. Santos, and J. M. Pauly. "Compressed Sensing MRI". *IEEE Signal Processing Magazine*, Vol. 25, No. 2, pp. 72–82, Mar 2008.
- [Lust 10] M. Lustig and J. Pauly. "SPIRiT: Iterative self-consistent parallel imaging reconstruction from arbitrary k-space". *Magnetic Resonance in Medicine*, Vol. 64, No. 2, pp. 457–471, Aug 2010.
- [Mado 04] B. Madore. "UNFOLD-SENSE: a parallel MRI method with self-calibration and artifact suppression". *Magnetic Resonance in Medicine*, Vol. 52, No. 2, pp. 310–320, Aug 2004.
- [Maju 11] A. Majumdar and R. Ward. "Joint reconstruction of multiecho MR images using correlated sparsity". *Magnetic Resonance Imaging*, Vol. 29, No. 7, pp. 899 – 906, Sep 2011.
- [Maju 12] A. Majumdar and R. Ward. "Nuclear norm-regularized SENSE reconstruction.". *Magnetic Resonance in Medicine*, Vol. 30, No. 2, pp. 213–21, Feb 2012.
- [Maki 07] J. H. Maki, G. J. Wilson, W. B. Eubank, D. J. Glickerman, S. Pipavath, and R. M. Hoogeveen. "Steady-state free precession MRA of the renal arteries: breath-hold and navigator-gated techniques vs. CE-MRA.". *Journal of Magnetic Resonance Imaging*, Vol. 26, No. 4, pp. 966–973, Oct 2007.
- [Mall 93] S. Mallat and Z. Zhang. "Matching Pursuit With Time-Frequency Dictionaries". *IEEE Transactions on Signal Processing*, Vol. 41, pp. 3397–3415, Dec 1993.
- [Mark 01] M. Markl and J. Hennig. "Phase contrast MRI with improved temporal resolution by view sharing: k-space related velocity mapping properties.". *Magnetic Resonance Imaging*, Vol. 19, No. 5, pp. 669–76, Jun 2001.
- [Mark 11] M. Markl, P. J. Kilner, and T. Ebbers. "Comprehensive 4D velocity mapping of the heart and great vessels by cardiovascular magnetic resonance". *Journal of Cardiovascular Magnetic Resonance*, Vol. 13, p. 7, Jan 2011.
- [Mark 12] M. Markl and J. Leupold. "Gradient echo imaging". *Journal of Magnetic Resonance Imaging*, Vol. 35, No. 6, pp. 1274–1289, May 2012.
- [McKi 05] A. M. McKinney, S. O. Casey, M. Teksam, L. T. Lucato, M. Smith, C. L. Truwit, and S. Kieffer. "Carotid bifurcation calcium and correlation with percent stenosis of the internal carotid artery on CT angiography". *Neuroradiology*, Vol. 47, No. 1, pp. 1–9, Jan 2005.
- [Mich 06] H. J. Michaely, K. A. Herrmann, H. Kramer, O. Dietrich, G. Laub, M. F. Reiser, and S. O. Schoenberg. "High-resolution renal MRA: comparison of image quality and vessel depiction with different parallel imaging acceleration factors". *Journal of Magnetic Resonance Imaging*, Vol. 24, No. 1, pp. 95–100, Jul 2006.

- [Mohr 10] O. K. Mohrs, S. E. Petersen, T. Schulze, M. Zieschang, H. Kießig, P. Schmitt, S. Bergemann, and H.-U. Kauczor. "High-resolution 3D unenhanced ECG-gated respiratory-navigated MR angiography of the renal arteries: comparison with contrast-enhanced MR angiography.". *American Journal of Roentgenology*, Vol. 195, No. 6, pp. 1423–1428, Dec 2010.
- [Nam 13] S. Nam, M. Akcakaya, T. Basha, C. Stehning, W. Manning, V. Tarokh, and R. Nezafat. "Compressed sensing reconstruction for whole-heart imaging with 3D radial trajectories: A graphics processing unit implementation". *Magnetic Resonance in Medicine*, Vol. 69, No. 1, pp. 91–102, 2013.
- [Nata 95] B. K. Natarajan. "Sparse Approximate Solutions to Linear Systems". *SIAM Journal on Computation*, Vol. 24, No. 2, pp. 227–234, Apr 1995.
- [Naza 79] L. Nazareth. "A Relationship between the BFGS and Conjugate Gradient Algorithms and Its Implications for New Algorithms". *SIAM Journal on Numerical Analysis*, Vol. 16, No. 5, pp. 794–800, Oct 1979.
- [Nien 14] H. Nien and J. Fessler. "A convergence proof of the split Bregman method for regularized least-squares problems". *CoRR*, Vol. -, No. -, Feb 2014.
- [Noce 06] J. Nocedal and S. Wright. *Numerical Optimization*. *Springer Series in Operations Research and Financial Engineering*, Springer, New York, 2nd Ed., 2006.
- [Noce 80] F. Nocedal. "Updating quasi-Newton matrices with limited storage". *Mathematics of computation*, Vol. 35, No. 151, pp. 773–782, Jul 1980.
- [Ooij 13] P. van Ooij, A. Guedon, H. A. Marquering, J. J. Schneiders, C. B. Majoie, E. van Bavel, and A. J. Nederveen. "k-t BLAST and SENSE accelerated time-resolved three-dimensional phase contrast MRI in an intracranial aneurysm". *Magnetic Resonance in Physics, Biology and Medicine*, Vol. 26, No. 3, pp. 261–270, Jun 2013.
- [Orga 13] W. H. Organization. "Fact sheet on Cardiovascular diseases (CVDs)". Tech. Rep. 317, World Health Organization, Mar 2013.
- [Oshe 92] R. Osher and E. Fatemi. "Nonlinear Total Variation Based Noise Removal Algorithms". *Physica D*, Vol. 60, No. 1–2, pp. 259–268, Nov 1992.
- [Otaz 10] R. Otazo, D. Kim, L. Axel, and D. Sodickson. "Combination of compressed sensing and parallel imaging for highly accelerated first-pass cardiac perfusion MRI.". *Magnetic Resonance in Medicine*, Vol. 64, No. 3, pp. 767–776, Sep 2010.
- [Otaz 11] R. Otazo, P. Storey, D. Kim, D. K. Sodickson, and V. S. Lee. "Highly-Accelerated Dynamic Non-Contrast MRA Using a Combination of Compressed Sensing and Parallel Imaging ". In: C. Reinhold, Ed., *Proceedings of the 19th annual meeting of the ISMRM, Montreal, Canada, May 7-13, 2011*.

- [Otaz 13] R. Otazo, D. Sodickson, and E. Candès. “Low-rank + sparse (L+S) reconstruction for accelerated dynamic MRI with separation of background and dynamic components”. pp. 88581Z–88581Z–8, 2013.
- [Pelc 91] N. Pelc, M. Bernstein, A. Shimakawa, and G. Glover. “Encoding strategies for three-direction phase-contrast MR imaging of flow”. *Journal of Magnetic Resonance Imaging*, Vol. 1, No. 4, pp. 405–413, Jul-Aug 1991.
- [Peng 10] H. H. Peng, S. Bauer, T. Y. Huang, H. W. Chung, J. Hennig, B. Jung, and M. Markl. “Optimized parallel imaging for dynamic PC-MRI with multidirectional velocity encoding”. *Magnetic Resonance in Medicine*, Vol. 64, No. 2, pp. 472–480, Aug 2010.
- [Picc 11] D. Piccini, A. Littmann, S. Nielles-Vallespin, and M. O. Zenge. “Spiral phyllotaxis: The natural way to construct a 3D radial trajectory in MRI”. *Magnetic Resonance in Medicine*, Vol. 66, No. 4, pp. 1049–1056, Apr 2011.
- [Pike 94] G. B. Pike, C. H. Meyer, T. J. Brosnan, and N. J. Pelc. “Magnetic resonance velocity imaging using a fast spiral phase contrast sequence”. *Magnetic Resonance in Medicine*, Vol. 32, No. 4, pp. 476–483, Oct 1994.
- [Pivz 06] A. Pižurica, A. Wink, E. Vansteenkiste, W. Philips, and J. Roerdink. “A Review of Wavelet Denoising in MRI and Ultrasound Brain Imaging”. *Current Medical Imaging Reviews*, Vol. 2, No. 2, pp. 247–260, May 2006.
- [Plon 11] G. Plonka and J. Ma. “Curvelet-Wavelet Regularized Split Bregman Iteration for Compressed Sensing”. *International Journal of Wavelets, Multiresolution and Information Processing*, Vol. 9, No. 1, pp. 79–110, Jan 2011.
- [Prin 09] M. R. Prince, H. L. Zhang, G. H. Roditi, T. Leiner, and W. Kucharczyk. “Risk factors for NSF: a literature review”. *Journal of Magnetic Resonance Imaging*, Vol. 30, No. 6, pp. 1298–1308, Dec 2009.
- [Prue 06] K. P. Pruessmann. “Encoding and reconstruction in parallel MRI”. *NMR in Biomedicine*, Vol. 19, No. 3, pp. 288–299, May 2006.
- [Prue 99] K. P. Pruessmann, M. Weiger, M. B. Scheidegger, and P. Boesiger. “SENSE: sensitivity encoding for fast MRI”. *Magnetic Resonance in Medicine*, Vol. 42, No. 5, pp. 952–962, Nov 1999.
- [Qu 07] P. Qu, J. Luo, B. Zhang, J. Wang, and G. X. Shen. “An improved iterative SENSE reconstruction method”. *Concepts in Magnetic Resonance Part B: Magnetic Resonance Engineering*, Vol. 31B, pp. 44–50, Feb 2007.
- [Rama 11] S. Ramani and J. A. Fessler. “Parallel MR Image Reconstruction Using Augmented Lagrangian Methods.”. *IEEE Transactions on Medical Imaging*, Vol. 30, No. 3, pp. 694–706, Mar 2011.
- [Ravi 11] S. Ravishankar and Y. Bresler. “MR Image Reconstruction From Highly Undersampled k-Space Data by Dictionary Learning”. *IEEE Transactions on Medical Imaging*, Vol. 30, No. 5, pp. 1028–1041, May 2011.

- [Rech 10] B. Recht, M. Fazel, and P. A. Parrilo. "Guaranteed Minimum-Rank Solutions of Linear Matrix Equations via Nuclear Norm Minimization". *SIAM Review*, Vol. 52, No. 3, pp. 471–501, Aug. 2010.
- [Rich 04] Y. Richter, A. Groothuis, P. Seifert, and E. Edelman. "Dynamic flow alterations dictate leukocyte adhesion and response to endovascular interventions". *The Journal of Clinical Investigation*, Vol. 113, pp. 1607–1614, Jun 2004.
- [Riff 13] P. Riffel, U. I. Attenberger, S. Kannengiesser, M. D. Nickel, C. Arndt, M. Meyer, S. O. Schoenberg, and H. J. Michaely. "Highly accelerated T1-weighted abdominal imaging using 2-dimensional controlled aliasing in parallel imaging results in higher acceleration: a comparison with generalized autocalibrating partially parallel acquisitions parallel imaging". *Investigative Radiology*, Vol. 48, No. 7, pp. 554–561, Jul 2013.
- [Ring 04] S. Ringgaard, S. Oyre, and E. Pedersen. "Arterial MR Imaging Phase-Contrast Flow Measurement: Improvements with Varying Velocity Sensitivity during Cardiac Cycle". *Radiology*, Vol. 232, No. 1, pp. 289–294, Jul 2004.
- [Roem 90] P. B. Roemer, W. A. Edelstein, C. E. Hayes, S. P. Souza, and O. M. Mueller. "The NMR phased array.". *Magnetic Resonance in Medicine*, Vol. 16, No. 2, pp. 192–225, Nov 1990.
- [Rubi 10] R. Rubinstein, A. Bruckstein, and M. Elad. "Dictionaries for Sparse Representation Modeling". *Proceedings of the IEEE*, Vol. 98, No. 6, pp. 1045–1057, June 2010.
- [Rubi 12] G. Rubin and N. Rofsky. *CT and MR Angiography: Comprehensive Vascular Assessment*. Wolters Kluwer Health, 2012.
- [Sant 13] C. Santelli, T. Schaeffter, and S. Kozerke. "Radial k-t SPIRiT: Autocalibrated parallel imaging for generalized phase-contrast MRI". *Magnetic Resonance in Medicine*, Vol. -, No. -, pp. -, Nov 2013.
- [Sche 11] O. Scherzer. *Inverse Problems - Methods*. Springer, Berlin, Germany, 2011.
- [Sher 11] M. Sherif, M. Abdel-Wahab, H. Beurich, B. Stoecker, D. Zachow, V. Geist, R. Toelg, and G. Richardt. "Haemodynamic evaluation of aortic regurgitation after transcatheter aortic valve implantation using cardiovascular magnetic resonance". *Eurointervention*, Vol. 7, No. 1, pp. 57–63, May 2011.
- [Sigf 12] A. Sigfridsson, S. Petersson, C. J. Carlhall, and T. Ebbers. "Four-dimensional flow MRI using spiral acquisition". *Magnetic Resonance in Medicine*, Vol. 68, No. 4, pp. 1065–1073, Oct 2012.
- [Sigo 11] M. Sigovan, M. D. Hope, P. Dyverfeldt, and D. Saloner. "Comparison of four-dimensional flow parameters for quantification of flow eccentricity in the ascending aorta". *Journal of Magnetic Resonance Imaging*, Vol. 34, No. 5, pp. 1226–1230, Nov 2011.

- [Smit 12] D. S. Smith, J. C. Gore, T. E. Yankeelov, and E. B. Welch. "Real-Time Compressive Sensing MRI Reconstruction Using GPU Computing and Split Bregman Methods". *International Journal of Biomedical Imaging*, Vol. 2012, p. 864827, Jan 2012.
- [Sodi 97] D. K. Sodickson and W. J. Manning. "Simultaneous acquisition of spatial harmonics (SMASH): fast imaging with radiofrequency coil arrays.". *Magnetic Resonance in Medicine*, Vol. 38, No. 4, pp. 591–603, Oct 1997.
- [Stad 09] A. Stadlbauer, W. van der Riet, S. Globits, G. Crelier, and E. Salomonowitz. "Accelerated phase-contrast MR imaging: comparison of k-t BLAST with SENSE and Doppler ultrasound for velocity and flow measurements in the aorta". *Journal of Magnetic Resonance Imaging*, Vol. 29, No. 4, pp. 817–24, Apr. 2009.
- [Stal 08] A. F. Stalder, M. F. Russe, A. Frydrychowicz, J. Bock, J. Hennig, and M. Markl. "Quantitative 2D and 3D phase contrast MRI: optimized analysis of blood flow and vessel wall parameters.". *Magnetic Resonance in Medicine*, Vol. 60, No. 5, pp. 1218–1231, Nov 2008.
- [Stin 13] E. Stinson, E. Borisch, C. Johnson, J. Trzasko, P. Young, and S. Riederer. "Vascular masking for improved unfolding in 2D SENSE-accelerated 3D contrast-enhanced MR angiography". *Journal of Magnetic Resonance Imaging*, Vol. -, pp. -, - 2013.
- [Stor 12] P. Storey, R. Otazo, R. P. Lim, S. Kim, L. Fleysler, N. Oesingmann, V. S. Lee, and D. K. Sodickson. "Exploiting sparsity to accelerate noncontrast MR angiography in the context of parallel imaging". *Magnetic Resonance in Medicine*, Vol. 67, No. 5, pp. 1391–1400, May 2012.
- [Tao 13] Y. Tao, G. Rilling, M. Davies, and I. Marshall. "Carotid blood flow measurement accelerated by compressed sensing: Validation in healthy volunteers". *Magnetic Resonance Imaging*, Vol. 31, No. 9, pp. 1485 – 1491, Nov 2013.
- [Thom 04] R. B. Thompson and E. R. McVeigh. "Flow-gated phase-contrast MRI using radial acquisitions". *Magnetic Resonance in Medicine*, Vol. 52, No. 3, pp. 598–604, Sep 2004.
- [Thun 03] P. Thunberg, M. Karlsson, and L. Wigstrom. "Accuracy and reproducibility in phase contrast imaging using SENSE". *Magnetic Resonance in Medicine*, Vol. 50, No. 5, pp. 1061–1068, Nov 2003.
- [Thun 12] P. Thunberg, K. Emilsson, P. Rask, and A. Kahari. "Flow and peak velocity measurements in patients with aortic valve stenosis using phase contrast MR accelerated with k-t BLAST". *European Journal of Radiology*, Vol. 81, No. 9, pp. 2203–2207, Sep 2012.
- [Toni 09] P. Tonino, B. D. Bruyne, N. Pijls, U. Siebert, F. Ikeno, M. van 't Veer, V. Volker, G. Manoharan, T. Engström, K. Oldroyd, P. V. Lee, P. McCarthy, and W. Fearon. "Fractional Flow Reserve versus Angiography for Guiding Percutaneous Coronary Intervention". *The New England Journal of Medicine*, Vol. 360, No. 3, pp. 213–224, Jan 2009.

- [Trem 12] B. Tremoulheac, D. Atkinson, , and S. Arridge. "Motion and Contrast Enhancement Separation Model Reconstruction from Partial Measurements in Dynamic MRI". In: *(Proceedings) MICCAI Workshop on Sparsity Techniques in Medical Imaging, Oct 5, Nice, France, Oct 2012*.
- [Trza 13] J. D. Trzasko and A. Manduca. "A Unified Tensor Regression Framework for Calibrationless Dynamic, Multi-Channel MRI Reconstruction". In: G. E. Gold, Ed., *Proceedings of the 21st annual meeting of the ISMRM, Salt Lake City, USA, Apr 20-26, 2013*.
- [Tsao 05] J. Tsao, S. Kozerke, P. Boesiger, and K. P. Pruessmann. "Optimizing spatiotemporal sampling for k-t BLAST and k-t SENSE: application to high-resolution real-time cardiac steady-state free precession.". *Magnetic Resonance in Medicine*, Vol. 53, No. 6, pp. 1372–1382, Jun 2005.
- [U Ki 09] J. U-King-Im, V. Young, and J. Gillard. "Carotid-artery imaging in the diagnosis and management of patients at risk of stroke.". *Lancet Neurology*, Vol. 8, No. 6, pp. 569–80, Jun 2009.
- [Ueck 08] M. Uecker, T. Hohage, K. T. Block, and J. Frahm. "Image reconstruction by regularized nonlinear inversion–joint estimation of coil sensitivities and image content.". *Magnetic Resonance in Medicine*, Vol. 60, No. 3, pp. 674–682, Sep 2008.
- [Ueck 09] M. Uecker. *Nonlinear Reconstruction Methods for Parallel Magnetic Resonance Imaging*. PhD thesis, Georg-August-Universität Göttingen, 2009.
- [Ufla 06] R. Uflacker. *Atlas of Vascular Anatomy: An Angiographic Approach*. Lippincott Williams & Wilkins, Philadelphia, USA, 2nd ed. Ed., 2006.
- [Usma 11] M. Usman, C. Prieto, T. Schaeffter, and P. G. Batchelor. "k-t Group sparse: a method for accelerating dynamic MRI". *Magnetic Resonance in Medicine*, Vol. 66, No. 4, pp. 1163–1176, Oct 2011.
- [Vaal 93] J. J. van Vaals, M. E. Brummer, W. T. Dixon, H. H. Tuijthof, H. Engels, R. C. Nelson, B. M. Gerety, J. L. Chezmar, and J. A. den Boer. "Keyhole method for accelerating imaging of contrast agent uptake". *Journal of Magnetic Resonance Imaging*, Vol. 3, No. 4, pp. 671–675, Jul-Aug 1993.
- [Vand 96] L. Vandenberghe and S. Boyd. "Semidefinite Programming". *SIAM Review*, Vol. 38, No. 1, pp. 49–95, Mar 1996.
- [Veli 10] J. Velikina, K. Johnson, W. Block, and A. Samsonov. "Design of Temporally Constrained Compressed Sensing Methods for Accelerated Dynamic MRI". In: *Proceedings of the Joint Annual Meeting ISMRM - ESM-RMB, Stockholm, Sweden, May 1–7, p. 4865, 2010*.
- [Wang 04] Z. Wang, A. Bovik, H. Sheikh, and E. Simoncelli. "Image Quality Assessment: From Error Visibility to Structural Similarity". *IEEE Transactions on Image Processing*, Vol. 13, No. 4, pp. 600–612, Apr 2004.
- [Wang 09] H. Wang, D. Liang, and L. Ying. "Pseudo 2D random sampling for compressed sensing MRI". In: IEEE, Ed., *IEEE Conference Proceedings of the IEEE Engineering in Medicine and Biology Society, Minneapolis, Sept 3–6, pp. 2672–2675, 2009*.

- [Whea 12] A. J. Wheaton and M. Miyazaki. "Non-contrast enhanced MR angiography: physical principles". *Journal of Magnetic Resonance Imaging*, Vol. 36, No. 2, pp. 286–304, Aug 2012.
- [Wiks 07] J. Wikström, L. J. S., Karacagil, and H. Ahlström. "Correlation of femoral artery flow velocity waveform with ipsilateral iliac artery stenoses assessed with magnetic resonance imaging". *Acta Radiologica*, Vol. 48, No. 4, pp. 422–430, May 2007.
- [Wort 12] P. W. Worters, M. Saranathan, A. Xu, and S. S. Vasanawala. "Inversion-recovery-prepared dixon bSSFP: initial clinical experience with a novel pulse sequence for renal MRA within a breathhold". *Journal of Magnetic Resonance Imaging*, Vol. 35, No. 4, pp. 875–881, Apr 2012.
- [Wrig 14] K. L. Wright, G. R. Lee, P. Ehse, M. A. Griswold, V. Gulani, and N. Seiberlich. "Three-dimensional through-time radial GRAPPA for renal MR angiography". *Journal of Magnetic Resonance Imaging*, Vol. -, pp. -, - 2014.
- [Wrig 97] G. Wright. "Magnetic resonance imaging". *IEEE Signal Processing Magazine*, Vol. 14, No. 1, pp. 56–66, Jan 1997.
- [Wytt 07] R. Wyttenbach, A. Braghetti, M. Wyss, M. Alerci, L. Briner, P. Santini, L. Cozzi, M. D. Valentino, M. Katoh, C. Marone, P. Vock, and A. Gallino. "Renal artery assessment with nonenhanced steady-state free precession versus contrast-enhanced MR angiography.". *Radiology*, Vol. 245, No. 1, pp. 186–195, Oct 2007.
- [Ye 07] J. C. Ye, S. Tak, Y. Han, and H. W. Park. "Projection reconstruction MR imaging using FOCUSS". *Magnetic Resonance in Medicine*, Vol. 57, No. 4, pp. 764–775, Apr 2007.
- [Yell 83] J. Yellott. "Spectral consequences of photoreceptor sampling in the rhesus retina". *Science*, Vol. 221, No. 4608, pp. 382–385, Jul 1983.
- [Yin 12] X. Yin, B.W., K. Ramamohanarao, A. Baghai-Wadji, and D. Abbott. "Exploiting sparsity and low-rank structure for the recovery of multi-slice breast MRIs with reduced sampling error.". *Medical & Biological Engineering & Computing*, Vol. 50, No. 9, pp. 991–1000, Sep 2012.
- [Zhao 12] F. Zhao, D. Noll, J. Nielsen, and F. Fessler. "Separate Magnitude and Phase Regularization via Compressed Sensing.". *IEEE Transactions on Medical Imaging*, Vol. 31, No. 9, pp. 1713–1723, Sep 2012.

